JESSE SAARI

Defect, Phase, and Interface Engineering of Titanium Dioxide Thin Films Grown by Atomic Layer Deposition for Solar Fuel Production

JESSE SAARI

Defect, Phase, and Interface Engineering of Titanium Dioxide Thin Films Grown by Atomic Layer Deposition for Solar Fuel Production

ACADEMIC DISSERTATION
To be presented, with the permission of
the Faculty of Engineering and Natural Sciences
of Tampere University,
for public discussion in the Auditorium B1096
of the Pinni B Building, Kanslerinrinne 1, 33014 Tampere,
on 9 December 2022, at 12 o'clock.

ACADEMIC DISSERTATION
Tampere University, Faculty of Engineering and Natural Sciences
Finland

Responsible supervisor and Custos	Professor Mika Valden Tampere University Finland	
Supervisor	Doctor of Science (Technology) Harri Ali-Löytty Tampere University Finland	
Pre-examiners	Doctor of Philosophy Lionel Santinacci Center for Interdisciplinary Nanoscience of Marseille France	Doctor of Philosophy Ville Miikkulainen Aalto University Finland
Opponent	Associate Professor Riikka Puurunen Aalto University Finland	

The originality of this thesis has been checked using the Turnitin OriginalityCheck service.

Cover design: Roihu Inc.

HIILINEUTRAALI PAINOTUOTE

ClimateCalc CC-000025/FI
PunaMusta Printing

Carbon dioxide emissions from printing Tampere University dissertations have been compensated.

PREFACE

The Thesis' experimental research was carried out using the facilities of the Surface Science Group and the Photonics Laboratory at Tampere University. In addition to essential research infrastructure, Surface Science Group provided an inspiring and supportive atmosphere during the whole dissertation project and my years as a research assistant before that.

First, I would like to express my gratitude to the Head of the Surface Science Group, my responsible supervisor Professor Mika Valden for believing in me since my first application letter for a summer research assistant position and then guiding me through my university studies including the B.Sc. and M.Sc. Theses. Secondly, I would like to sincerely thank my supervisor Dr. Harri Ali-Löytty for mentoring me in the dissertation research and publication processes. I really liked our fruitful discussions and I appreciate that it was always easy to come and knock on the door to have a quick talk regarding everything between the research and life in general. I feel that we were a very good and productive team.

Thirdly, I would like to thank my colleagues in the Surface Science Group who have contributed to the Thesis research and the positive team spirit in the group. Especially, many thanks to Dr. Kimmo Lahtonen for introducing me into electron spectroscopy and atomic layer deposition during my early years in the group. I think we worked really well together with all that research, maintenance, and procurement work related to the electron spectroscopy systems and the atomic layer deposition reactor. I want to thank Dr. Markku Hannula and M.Sc. Lauri Palmolahti for all the good discussions, friendship, and also activities outside of work. Thank you, Markku, for kindly helping me with the hands-on laboratory and electron spectroscopy work. I feel that with Lauri, we were a great team, and we became pretty experienced in organizing laboratory tours for students. These are such fun memories.

Regarding X-ray diffraction and reflectivity measurement expertise, I would like to express my gratitude to Dr. Antti Tukiainen. I want to thank Dr. Minttu Maria Kauppinen and Professor Henrik Grönbeck from Chalmers University of Technology for nice and productive collaboration related to computational analysis. Moreover, for supporting the Thesis research, I would like to thank Dr. Mari

Tampere, September 2022

Jesse Saari

ABSTRACT

Constantly growing need for energy is causing inevitable problems that the humankind must solve in the near future. Global energy consumption is rising due to population and economic growth, and burning of fossil fuels, such as oil, coal, and natural gas, is accounted for global warming. Therefore, supplying this massive energy demand by using sustainable and carbon-neutral energy sources at the expense of fossil fuel power sector is needed. Solar power is one of the most promising sustainable energy technologies. However, due to challenges caused by diurnal cycle and intermittency of sunlight, development of solar energy storage technologies is highly important. Photoelectrochemical technology aims at storing solar energy into chemical form, i.e., solar fuels by splitting water molecules to hydrogen and oxygen or driving reduction of water and carbon dioxide to methanol, methane or other hydrocarbons and their derivatives. Despite great progress, photoelectrodes in photoelectrochemical solar fuel reactors still lack the required efficiency and stability for commercial viability.

This Thesis provides insights into atomic-level structure, charge carrier dynamics, and crystallization of TiO_2 thin films grown by atomic layer deposition, and their performance as photoelectrode coatings. The results show that mass densities, precursor traces, and oxide defects of amorphous TiO_2 can be varied in a desirable way by the atomic layer deposition growth temperature when using tetrakis(dimethylamido)titanium(IV) and H_2O precursors at 100–200 °C. The growth temperature of 100 °C results in TiO_2 with low mass density and precursor traces that inhibit crystallization up to 375 °C and stabilize the anatase phase. TiO_2 grown at 200 °C, instead, exhibits high concentration of oxide defects and distinctly higher mass density facilitating electrical conductivity and direct crystallization into rutile at an exceptionally low post deposition annealing temperature of 250 °C. The photoelectrochemical analysis for TiO_2/Si photoelectrodes revealed that crystallization is necessary to achieve desired chemical stability, and the lower the crystallization temperature the thinner the interfacial SiO_2 layer and the better the photocurrent onset potential. The results of this Thesis on TiO_2 thin films grown by atomic layer deposition are applicable to tailoring of protective photoelectrode coatings for economically viable photoelectrochemical solar fuel production.

TIIVISTELMÄ

Jatkuva energiantarpeen kasvu aiheuttaa vääjäämättä ongelmia, jotka ihmiskunnan on lähitulevaisuudessa ratkaistava. Kasvava väestö ja talous nostavat maailmanlaajuista energiankulutusta ja fossiilisten polttoaineiden, kuten öljyn, kivihiilen ja maakaasun, käyttöä pidetään selityksenä ilmaston lämpenemiseen. Näin ollen valtava energiantarve pitäisi kattaa ympäristöä säästävillä ja hiilineutraaleilla energianlähteillä pienentäen fossiilisiin polttoaineisiin perustuvan energiasektorin osuutta. Aurinkoenergia on yksi lupaavimmista ympäristöä säästävistä energiamuodoista. Auringonvalon vuorokautisen vaihtelun ja epäsäännöllisyyden aiheuttamien haasteiden takia aurinkoenergian varastointiteknologioiden kehitys on erittäin tärkeää. Valosähkökemiallisella kennolla aurinkoenergia voidaan varastoida kemialliseen muotoon aurinkopolttoaineiksi esimerkiksi hajottamalla vettä vedyksi ja hapeksi tai muodostamalla vedestä ja hiilidioksidista metanolia, metaania tai muita hiilivetyjä ja niiden johdannaisia. Merkittävästä edistyksestä huolimatta, sovelluksen tehokkuus ja vakaus eivät ole vielä riittävällä tasolla.

Tämä väitöskirja keskittyy atomikerroskasvatettujen TiO_2-ohutkalvojen atomitason rakenteen, varauksenkuljettajien dynamiikan ja kiteytymisen ymmärtämiseen sekä TiO_2-kalvon käyttöön suojaavana fotoelektrodipinnoitteena. Tulokset osoittavat, että amorfisen TiO_2-ohutkalvon tiheyttä, lähtöainejäämiä ja oksidihilavirheitä voidaan hallita atomikerroskasvatuksen lämpötilan avulla (100–200 °C), kun käytetään tetrakis(dimetyyliamido)titaani- ja H_2O-lähtöaineita. Matalampi kasvatuslämpötila (100 °C) johtaa lähtöainejäämiin ja pienempään tiheyteen hidastaen kiteytymistä (375 °C) ja stabiloiden anataasifaasin. Sen sijaan korkeampi kasvatuslämpötila (200 °C) johtaa oksidihilavirheisiin ja tiheämpään rakenteeseen parantaen sähköistä johtavuutta ja mahdollistaen kiteytymisen rutiiliksi poikkeuksellisen matalassa lämpötilassa (250 °C). Toiminnallisuustestien perusteella kiteytymisen aikaansaava jälkilämmitys on välttämätön kemiallisesti stabiilin TiO_2-fotoelektrodipinnoitteen valmistamiseksi. Lisäksi matalampi kiteytymislämpötila Si-fotoelektrodeilla mahdollistaa paremman SiO_2-rajapintakerroksen ja valovirran kynnysjännitteen. Väitöskirjassa esitetyt tulokset atomikerroskasvatettuihin TiO_2-ohutkalvoihin liittyen edistävät taloudellisesti kannattavan TiO_2-pinnoitteita hyödyntävän aurinkopolttoainereaktorin kehitystyötä.

CONTENTS

ABBREVIATIONS AND SYMBOLS

ALD	Atomic layer deposition
ALE	Atomic layer epitaxy
am.-TiO_2	Amorphous TiO_2
ARXPS	Angle-resolved X-ray photoelectron spectroscopy
BE	Binding energy
CA	Contact angle
CB	Conduction band
CBM	Conduction band minimum
CE	Counter electrode
CLS	Core-level shift
CO_2RR	Carbon dioxide reduction reaction
c-TiO_2	Crystalline TiO_2
CVD	Chemical vapor deposition
DFT	Density functional theory
DRAM	Dynamic random-access memory
EBSD	Electron backscatter diffraction
EL	Electroluminescent
EPR	Electron paramagnetic resonance
ESCA	Electron spectroscopy for chemical analysis
GIXRD	Grazing incidence X-ray diffraction
GPC	Growth-per-cycle
HER	Hydrogen evolution reaction
HEC	Hydrogen evolution catalyst
HF	Hydrofluoric acid
IMFP	Inelastic mean free path
MIS	Metal–insulator–semiconductor
ML	Molecular layering
NHE	Normal hydrogen electrode
NIR	Near-infrared
n-Si	n-type silicon

n^+-Si	Highly doped n-type silicon
$N_{subs.}$	Substitutional nitrogen
OER	Oxygen evolution reaction
OEC	Oxygen evolution catalyst
PDA	Post deposition annealing
PEC	Photoelectrochemical
PEM	Proton-exchange membrane
PREIN	Photonics Research and Innovation platform (the Academy of Finland Flagship Programme)
p-Si	p-type silicon
p^+-Si	Highly doped p-type silicon
PV	Photovoltaic
RCA SC	Radio Corporation of America Standard Clean
RE	Reference electrode
RHE	Reversible hydrogen electrode
sccm	Standard cubic centimeters per minute
SEM	Scanning electron microscopy
SESSA	Simulation of Electron Spectra for Surface Analysis
STH	Solar-to-hydrogen
Syngas	Synthesis gas (a mixture of carbon monoxide (CO) and hydrogen (H_2))
TAF	Technology Academy Finland
TAS	Transient absorption spectroscopy
TDMAT	Tetrakis(dimethylamido)titanium(IV) ($Ti(N(CH_3)_2)_4$)
$TiCl_4$	Titanium tetrachloride
TRL	Technology readiness level
TTIP	Titanium isopropoxide ($Ti(OCH(CH_3)_2)_4$)
UHV	Ultra-high vacuum
UV	Ultraviolet
VB	Valence band
VBM	Valence band maximum
VESTA	Visualization for electronic and structural analysis
WE	Working electrode
XPS	X-ray photoelectron spectroscopy
XRR	X-ray reflectivity

A	Absorbance
Al Kα	Characteristic aluminum Kα X-ray electromagnetic radiation
e$^-$	Electron
E_g	Band gap
E_{onset}	Photocurrent onset potential in a photoelectrochemical cell
$E_{ph.min}$	Required minimum photopotential for photoelectrochemical water splitting reaction
eV	Electron volt (1 eV = 1.6022×10^{-19} J)
$h\nu$	Photon energy (the Planck constant h times the frequency of light ν)
h$^+$	Hole (charge carrier)
I	XPS peak intensity (the intensity of photoelectrons)
I_{op}	Operating current in a photoelectrochemical cell
$I-E/V$	Current−voltage (characteristics)
III–V	Multijunction solar cell consisting of elements from the periodic table groups III and V
M	Molar concentration
N	Number of atoms per unit volume
O_2^{2-}	Interstitial peroxo species
pH	Commonly used scale to present acidic, neutral, or alkaline nature of an aqueous solution (pH = $-\log_{10}$[H$^+$])
R	Reflectance
S	Photoemission spectroscopy constant
t	Thickness of a thin film
T	Transmittance
Ti^{3+}	Oxygen vacancy-induced Ti^{3+} defect
Ti^{3+} 3d	Electronic gap states of TiO$_2$ occupied by the excess electrons of Ti^{3+} defects
Ti$_{5/6/7c}$	Penta-/hexa-/heptacoordinated Ti ion
V_{bias}	Applied bias voltage in a photoelectrochemical cell
α	Absorption coefficient
η_{HER}	Overpotential loss related to the hydrogen evolution reaction
$\eta_{ionic\ cond}$	Overpotential loss related to ionic conductivity
η_{OER}	Overpotential loss related to the oxygen evolution reaction
η_{sep}	Overpotential loss related to charge carrier separation
η_{trans}	Overpotential loss related to charge carrier transport

λ Inelastic mean free path

Φ_{ox} Self-oxidation potential

Φ_{red} Self-reduction potential

$\Phi(\mathrm{H^+/H_2})$ Reduction potential of hydrogen

$\Phi(\mathrm{H_2O/O_2})$ Oxidation potential of water

$\Phi(\mathrm{O_2/H_2O})$ Reduction potential of water

LIST OF ORIGINAL PUBLICATIONS

Publication **I**   **Saari, J.**, Ali-Löytty, H., Kauppinen, M.M., Hannula, M., Khan, R., Lahtonen, K., Palmolahti, L., Tukiainen, A., Grönbeck, H., Tkachenko, N.V., Valden, M. Tunable Ti^{3+}-Mediated Charge Carrier Dynamics of Atomic Layer Deposition-Grown Amorphous TiO_2. *J. Phys. Chem. C* 126 (2022) 4542–4554.

Publication **II**   **Saari, J.**, Ali-Löytty, H., Lahtonen, K., Hannula, M., Palmolahti, L., Tukiainen, A., Valden, M. Low-Temperature Route to Direct Amorphous to Rutile Crystallization of TiO_2 Thin Films Grown by Atomic Layer Deposition. *J. Phys. Chem. C* 126 (2022) 15357–15366.

Publication **III** **Saari, J.**, Ali-Löytty, H., Honkanen, M., Tukiainen, A., Lahtonen, K., Valden, M. Interface Engineering of TiO_2 Photoelectrode Coatings Grown by Atomic Layer Deposition on Silicon. *ACS Omega* 6 (2021) 27501–27509.

Publication **IV** Ali-Löytty, H., Hannula, M., **Saari, J.**, Palmolahti, L., Bhuskute, B.D., Ulkuniemi, R., Nyyssönen, T., Lahtonen, K., Valden, M. Diversity of TiO_2: Controlling the Molecular and Electronic Structure of Atomic-Layer-Deposited Black TiO_2. *ACS Appl. Mater. Interfaces* 11 (2019) 2758–2762.

AUTHOR'S CONTRIBUTION

This Thesis compiles four peer-reviewed publications and additional unpublished results covering insights into modification and properties of titanium dioxide thin films grown by atomic layer deposition (ALD) and their use in applications, particularly in photoelectrochemical (PEC) solar fuel reactors. The author's detailed contribution is as follows.

Publication **I**   The publication presents a comprehensive X-ray photoelectron spectroscopy (XPS) and computational study providing atomic-level insights into the formation of intrinsic titanium (Ti^{3+} ions), oxygen, and nitrogen defects within amorphous TiO_2 (am.-TiO_2) grown by ALD using tetrakis(dimethylamido)titanium(IV) (TDMAT) and H_2O precursors. The effects of ALD growth temperature on defect concentrations and charge carrier dynamics of am.-TiO_2 are also discussed. The author prepared the samples for the experiments, participated in the XPS measurements, carried out ellipsometry, and analyzed the data. The author wrote the first version of the manuscript and was responsible for the publication process.

Publication **II**   The publication highlights how crystallization of amorphous TiO_2 can be controlled via ALD growth temperature-induced differences in mass density, and intrinsic nitrogen and titanium defects. The author prepared the samples, participated in the XPS measurements, carried out scanning electron microscopy (SEM) imaging, and analyzed the data. The author wrote the first version of the manuscript and was responsible for the publication process.

Publication **III** The publication focuses on comparing the effect of Si pretreatment and post deposition annealing (PDA) temperature on interfacial SiO_2 formation and its influence on the performance of TiO_2/Si photoanodes in solar water splitting. The author prepared the samples, performed most of the contact angle (CA) measurements, X-ray photoelectron spectroscopy, the PEC measurements, and SEM imaging as well as the data analysis. The author wrote the first version of the manuscript and was responsible for the publication process.

Publication **IV** The publication demonstrates how photoelectrochemical stability and performance of an ALD-grown TiO_2 thin film can be improved by post deposition annealing-induced crystallization. The author participated in preliminary research and preparations regarding the atomic layer deposition process and characterization of TiO_2 thin films. The author was partly responsible for carrying out the ALD depositions and took part in commenting and proofreading the manuscript.

The chapter 4 also includes additional and unpublished XPS and PEC results from the experiments carried out by the author.

1 INTRODUCTION

One of the most important challenges that humankind must solve is to fulfill the growing need for energy by using sustainable and carbon-neutral energy sources. Global energy consumption is inevitably rising due to population and economic growth and supplying this energy demand with fossil fuels is unsustainable. Burning of fossil fuels, such as oil, coal, and natural gas, increases massively atmospheric carbon dioxide (CO_2) which is the main reason for the imbalanced greenhouse effect and global warming. [1–3] During the recent years, there has been a distinctly increasing and positive trend in use of renewable energy, especially wind and solar power. Unfortunately, that is still not enough since the growth should come even more at the expense of coal power sector. [4] Sunlight is a decentralized and sustainable natural resource that can be harnessed, e.g., by photovoltaic (PV) or photoelectrochemical cells. As an example, the global energy demand of 20 TW could be produced by covering 0.16% of Earth's surface with solar panels of 10% efficiency. [5] Although the scenario is infeasible, the calculation shows the potential of solar energy [6]. However, due to the challenges caused by diurnal cycle and intermittency of sunlight, storage technologies for solar energy have to be developed [5,6].

   An attractive method to store solar energy is to convert it into chemical energy through artificial photosynthesis providing solar fuels, with high-energy density and good transportation options [6,7]. In artificial photosynthesis, solar fuels can be produced for example by using a PEC cell or photovoltaic-driven electrolysis to split water molecules to hydrogen and oxygen, or splitting of carbon dioxide and water molecules together can be directed to produce methanol, methane or other hydrocarbons and their derivatives [3,7,8]. The first process generates the most energetically dense solar fuel, hydrogen, via simple electrochemical reactions. In the latter technology, liquid solar fuels, e.g., methanol or ethanol, can be produced. However, in dealing with carbon dioxide there are several challenges, such as energy losses in capturing CO_2 and complexity of electrochemical reactions for conversion of CO_2 into solar fuels. [3,6,9,10] Instead of producing directly, e.g., methanol, another feasible approach is to produce a mixture of hydrogen and carbon monoxide

(CO), known as synthesis gas (syngas) [11]. This carbon-neutral syngas can be then used as a feedstock to produce methanol, synthetic fuels, or other industrially important chemicals via well-established Fischer–Tropsch technology. [3,6,9–12] Although, water splitting is slightly simpler approach to solar fuel production, there are no large-scale and cost-effective solutions available. So far, the highest solar-to-hydrogen (STH) efficiency of a PEC cell is reported to be 19.3% [13,14]. Based on the theory and modelling the maximum STH efficiency of a PEC device is 31.1% but in fact, due to the practical issues it is limited to around 25% [15]. In terms of efficiency, an alternative system consisting of a photovoltaic cell and an electrolyzer can potentially be better and achieves STH efficiency of 30% nowadays (the theoretical limit around 41%) but material and peripheral device costs are likely higher compared to the PEC approach [14,16–18].

Figure 1 presents a schematic illustration of the PEC cell and PV-electrolysis concepts for solar fuel production. The photovoltaic-driven electrolysis where the PV cell and the electrolyzer are separate components is currently more mature and has a higher technology readiness level (TRL) than the integrated PEC architecture. This Thesis focuses on the PEC technology which could enable lower material costs compared to PV-electrolysis. However, despite the high disruptive potential, the TRL of PEC cells is still low. [18–20] To have commercially viable PEC cells, there are still many issues to study and solve, such as stability of photoelectrodes, efficiency (e.g., product selectivity, surface reaction kinetics, charge carrier dynamics, exploitation of near-infrared (NIR) wavelengths) and scale-up [6,10,21,22].
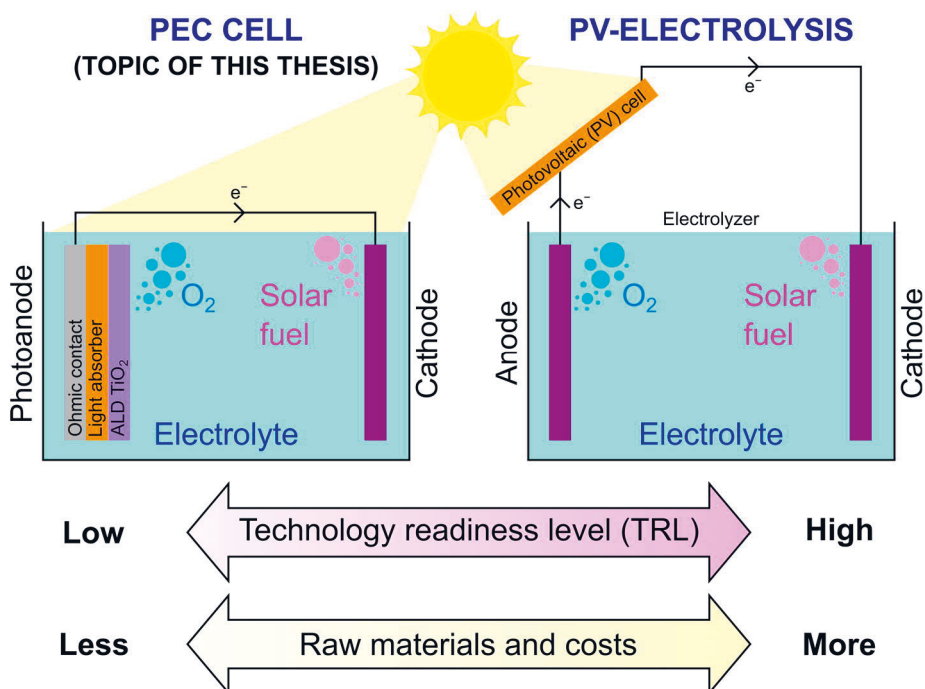
Figure 1. A schematic illustration of the PEC cell and PV-electrolysis concepts and a comparison of these solar fuel production technologies in terms of technology readiness and costs. This Thesis focuses on the PEC technology where ALD-grown TiO_2 can serve as a photoelectrode protection layer against corrosion in acidic or alkaline aqueous electrolyte. The figure was composed based on the refs. [14,18,23].

From the fundamental point of view, semiconductor materials for PEC cell photoelectrodes require certain properties for driving electrochemical reactions, such as, suitable band gap to absorb sunlight to generate electron–hole pairs and a sufficient voltage as well as favourable potentials for valence band maximum (VBM) and conduction band minimum (CBM) with respect to redox potentials of reactants in the electrolyte. Furthermore, semiconductor materials should be stable against corrosion in aqueous electrolytes, exhibit a low recombination rate and high mobility of the charge carriers as well as a facile charge transfer through semiconductor–electrolyte interface. [6,19,21,24]

The first discovery of the photoelectrochemical water splitting was introduced by Fujishima and Honda in 1972 by using n-type rutile TiO_2, and since then Earth-abundant, non-toxic and chemically stable TiO_2-based materials have been of wide interest in various photocatalytic applications [25–28]. However, due to the relatively large band gap (E_g = 3.0–3.2 eV) of TiO_2, the absorption of sunlight is limited to

ultraviolet (UV) wavelength range covering only around 5% of the solar spectrum and thus reducing dramatically the efficiency of the PEC cell [29–33]. To overcome this inherent limitation, several means, such as nitrogen doping or structural disorder have been reported to extend the light absorption from UV to the visible-light wavelength range, or even to form visually black TiO_2 [27,34–37].

Protecting highly efficient light absorbers, such as Si, GaAs, GaP, and III–V multijunction solar cells, with chemically stable TiO_2 is another potential approach to develop commercially viable PEC cells [13,14,19,24]. Particularly, atomic layer deposition is regarded as a promising thin film deposition method for photoelectrodes since ALD can provide high-quality and pinhole-free coatings with excellent controllability, uniformity and conformality [20,38–41]. Depending on the photoelectrode design, both amorphous and crystalline TiO_2 have been reported to serve as a protection layer for semiconductor materials that are intrinsically unstable under PEC conditions [13,40–44]. However, there are still doubts about sufficient chemical stability of am.-TiO_2 thin films, both in acidic and alkaline environments [42,45,46]. Crystalline anatase and rutile TiO_2, instead, are chemically stable but grain boundaries and defects in polycrystalline structure may lead to degradation of the device, for example, via pinhole-mediated corrosion [43,47,48]. In addition to stability, charge transfer properties should be optimized. For instance, am.-TiO_2 can provide enhanced charge transfer thanks to intrinsic Ti^{3+} defects [49]. Furthermore, the growth of detrimental SiO_2 in TiO_2/Si photoelectrodes limits the post deposition annealing temperatures if crystallization of am.-TiO_2 is needed [50]. Thus, in-depth understanding of different TiO_2 phases and how to tune the diverse properties of titanium dioxide are essential when optimizing the performance of protective TiO_2 photoelectrode coatings in photoelectrochemical solar fuel reactors.

1.1   Research objectives and scope of the Thesis

The aim of this Thesis is to provide atomic-level insights into ALD-grown amorphous TiO_2 thin films and to understand of how to tune and optimize the charge transfer properties and chemical stability of protective ALD TiO_2 photoelectrode coatings in photoelectrochemical solar fuel reactors. The work serves as an advancement towards cost-effective solar fuel production utilizing photoelectrochemical cells to store solar energy into chemical form, for instance, as hydrogen or carbon-neutral methane or methanol. The specific objectives of the Thesis are as follows:

1. To study the effect of atomic layer deposition growth temperature on intrinsic defects and charge carrier dynamics of amorphous TiO_2 thin films that could be used as electronically conductive and protective PEC photoelectrode coatings.

2. To understand the role of intrinsic titanium, oxygen, and nitrogen defects within am.-TiO_2 on crystallization upon post deposition annealing treatment in air. The crystallization temperature, phase, and grain size are important properties when optimizing protective crystalline TiO_2 photoelectrode coatings.

3. To compare the effects of standard silicon surface pretreatments and post deposition annealing temperature on the growth of interfacial SiO_2 in ALD TiO_2/Si photoelectrodes. A thick interfacial SiO_2 layer is detrimental to the PEC device performance and thus its thickness should be limited.

4. To demonstrate and rationalize the performance improvement of ALD TiO_2/Si photoanodes by optimizing the chemical stability and charge transfer properties via selecting the ALD growth temperature and post deposition annealing treatment.

Besides the in-depth understanding of ALD-grown TiO_2, the Thesis aims at introducing solar fuel production as a technology and its significance for sustainable future. Moreover, the Thesis highlights X-ray photoelectron spectroscopy as a versatile research method to study a substrate–thin-film interface morphology as well as amorphous, chemical, and electronic structure of materials.

1.2   Outline of the Thesis

This Thesis introduces the basic principles of photoelectrochemical solar fuel production and different approaches to use both amorphous and crystalline TiO_2 as protective photoelectrode coatings in photoelectrochemical solar fuel reactors. Furthermore, atomic layer deposition of TiO_2 thin films and properties of TiO_2 are discussed comprehensively before focusing on XPS as a research method to provide in-depth understanding of atomic-level composition and electronic structure as well as chemistry and morphology of TiO_2 thin films. Finally, the results related to the

research objectives of the Thesis are presented and discussed in detail. The Thesis is divided into following chapters:

Chapter 2

The chapter provides an introduction to solar fuel production as a concept and to the basic principles of photoelectrochemical cells including structure, materials as well as physics and chemistry behind solar water splitting and CO_2 reduction reactions. The use of ALD-grown amorphous and crystalline TiO_2 as protective photoelectrode coatings is extensively discussed.

Chapter 3

The chapter focuses on atomic layer deposition technique, and particularly, ALD of TiO_2 in terms of different precursors and substrates. Furthermore, characteristics of different TiO_2 phases and their properties are discussed, mainly from the PEC application point of view. The second half of the chapter includes the introduction and experimental details of XPS and PEC analysis, and how these methods can be used to gain in-depth understanding of interfacial, molecular, and electronic structure of ALD TiO_2 and the PEC performance of ALD TiO_2/Si photoanodes.

Chapter 4

This chapter focuses on describing the key findings of the Thesis research and reflects the importance of the results in the context of the ALD, XPS, TiO_2 and PEC research fields. The results address the research questions related to effects of ALD growth temperature on intrinsic defects within am.-TiO_2 and on crystallization kinetics of am.-TiO_2 thin films. Furthermore, Si wafer cleaning methods and post deposition annealing are studied and considered in terms of an interfacial SiO_2 layer thickness and the PEC performance of ALD TiO_2/Si photoanodes.

Chapter 5

The chapter concludes the main results of the Thesis and provides an outlook for the research related to the ALD-grown TiO_2 thin films and PEC solar fuel reactors.

Original publications

The Thesis research in detail is described in the four original publications at the end of this Thesis. Publication **I** focuses on atomic-level insights into the formation and controlling of intrinsic titanium, oxygen, and nitrogen defects within ALD-grown am.-TiO_2 via the ALD growth temperature. Publication **II** discusses roles of mass density, and intrinsic oxide defects and TDMAT precursor traces on the

crystallization of ALD-grown am.-TiO$_2$ thin films upon PDA in air. Publication **III** studies the effects of Si cleaning pretreatments and PDA temperature on the interfacial SiO$_2$ formation and the performance of ALD TiO$_2$/Si photoanodes. Publication **IV** demonstrates how the PEC stability and performance of ALD-grown am.-TiO$_2$ coatings can be improved by post deposition annealing-induced crystallization.

2 SOLAR FUEL PRODUCTION

As many innovations the inspiration for artificial photosynthesis arises from nature. In the natural photosynthesis, plants utilize sunlight to produce carbohydrates and oxygen from water and carbon dioxide [51]. Analogously, artificial photosynthesis mimics this process by converting solar energy into the chemical bonds of solar fuel molecules (e.g., H_2, CH_3OH) by using engineered photocatalyst materials [6,7]. However, artificial photosynthesis pursues solar fuel production that is much more efficient compared to the biological photosynthesis occurring in the nature [7]. Due to the energy costs for self-repairing of biological system and light saturation at low sunlight intensities, the efficiency of biological photosynthesis is typically below 1%. The most efficient artificial photosynthesis systems, instead, have demonstrated solar-to-hydrogen efficiencies of 20–30%. [7,13,14,16,52,53] This chapter introduces solar fuel production as a concept, the basic principles of photoelectrochemical cells and the use of ALD-grown amorphous or crystalline TiO_2 as protective photoelectrode coatings.

2.1 Basic principles of photoelectrochemical solar fuel production

The energy conversion of solar energy into chemical bonds in artificial photosynthesis is based on chemical reactions carried out in photoelectrochemical cell by utilizing semiconductor light absorbers and catalyst materials [54]. The first application related to photoelectrochemical water splitting was introduced by Fujishima and Honda in 1972 by using n-type rutile TiO_2 as a photocatalyst [25]. After these experiments, many different semiconductor materials have been studied but none of them has fulfilled all the requirements for cost-effective solar fuel production [6].

First requirement relates to efficient absorption of photons emitted by the Sun and the formation electron–hole pairs via excitation of electrons from a valence band (VB) to a conduction band (CB). When light hits a semiconductor surface, some of the photons will be reflected and the rest will propagate into the semiconductor

where they can transmit through the medium or become absorbed. [19] In practice, the reflectance R and the transmittance T can be measured by UV–vis–NIR spectrophotometer, and the absorbance A or the absorption coefficient α can be approximated as follows

$$A = -\log_{10}\left(\frac{T}{1-R}\right) = \frac{\alpha \times t}{\ln(10)} \qquad (1)$$

where t is the thickness of the material [6,21]. The light absorption and the formation of electron–hole pairs as a phenomenon depends on the electronic structure of a material, and consequently the band gap of a semiconductor [6]. Since majority (74%) of solar energy falls within the wavelength range of 300–1000 nm [55], corresponding to photon energies of 4.13–1.24 eV, semiconductor materials with band gap values in this range make an efficient light absorber for a PEC photoelectrode [19]. Figure 2 illustrates how the band gaps of TiO_2, Si, and a III–V dual-junction solar cell materials (GaInP/GaInAs) correspond with the solar spectrum.
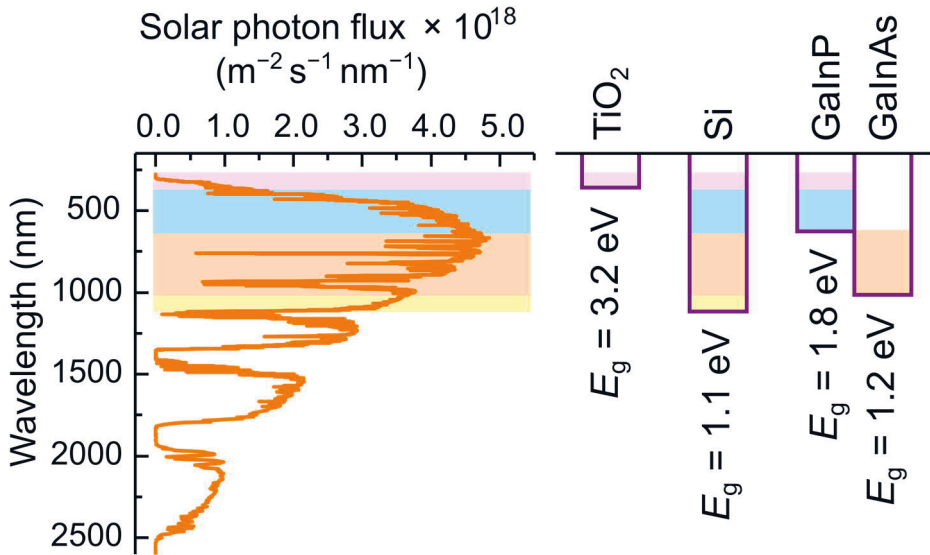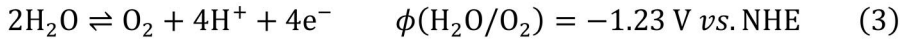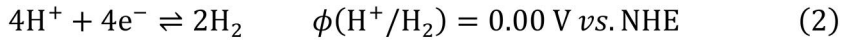

Figure 2. A schematic illustration of sunlight absorption of TiO_2, Si, and a III–V dual-junction solar cell (GaInP/GaInAs) with the different band gap energies. The solar photon flux is based on the hemispherical global total spectral irradiance (reference air mass 1.5 spectra ASTM G-173-03) [56].

As shown in Figure 2, compared to TiO₂ with the relatively large band gap of 3.2 eV, Si and GaInP/GaInAs dual-junction solar cell can absorb remarkably larger portion of the solar photon flux. While both Si and GaInP/GaInAs dual-junction solar cell can absorb wide fraction of solar spectrum, an advantage of dual-junction cell is a larger cell voltage that is the sum of the sub-junction voltages [57]. Furthermore, light absorption can be extended to the NIR wavelength range with addition of a narrow gap semiconductor material (e.g., Ge or GaInAs alloy) to a multijunction solar cell or by plasmonic nanostructures [14,22,58].

After photoexcitation of an electron to a conduction band, either an external bias or an internal built-in potential steers electrons in the CB and holes in the VB to the surface of a photocathode and photoanode, respectively. This charge carrier separation and transport is essential to photovoltage and photocurrent generated for driving reduction and oxidation reactions to produce solar fuels. [19] In water splitting reaction to produce hydrogen, the reduction and oxidation half-reactions in acidic aqueous electrolyte (pH = 0) can be written as

$$4H^+ + 4e^- \rightleftharpoons 2H_2 \qquad \phi(H^+/H_2) = 0.00 \text{ V } vs. \text{ NHE} \qquad (2)$$

$$2H_2O \rightleftharpoons O_2 + 4H^+ + 4e^- \qquad \phi(H_2O/O_2) = -1.23 \text{ V } vs. \text{ NHE} \qquad (3)$$

where $\Phi(H^+/H_2)$ and $\Phi(H_2O/O_2)$ are reduction and oxidation potentials for hydrogen and water, respectively, and in respect of normal hydrogen electrode (NHE) [59]. Thus, thermodynamically the water splitting reaction requires a potential of 1.23 V minimum. The amount of excess potential required to drive the reaction at a given rate, i.e., overpotential, depends on the catalytic activity of the electrode surfaces. [6] The water redox potentials $\Phi(H^+/H_2)$ and $\Phi(O_2/H_2O)$ set requirements for band alignment of a semiconductor. If no external bias is used, the CB should be more negative than $\Phi(H^+/H_2)$ and the VB more positive than $\Phi(O_2/H_2O)$ to enable the photoelectrochemical water splitting reaction [19].

Producing carbon-neutral solar fuels via a CO₂ reduction reaction (CO₂RR) is more complicated process compared to water splitting but it is based on similar requirements for semiconductor band alignment. The reduction potentials for CO₂RR to produce, for instance, CO, formic acid (HCOOH), methane (CH₄) or methanol (CH₃OH) are rather close to $\Phi(H^+/H_2)$ and several semiconductors can provide the CB potential negative enough. However, the selectivity towards a desired product and the competition with the hydrogen evolution reaction (HER) are still problems to be solved. [3,60] Moreover, one of the issues related to reaction

pathways that has been under debate considers whether the formation CO_2 anion radical ($CO_2 \cdot^-$) is the initial and the rate-determining step or not. This reduction reaction has significantly more negative potential (-1.48 V *vs.* RHE [60]) compared to the conduction bands of the most common semiconductors, which may hamper an efficient and bias-free CO_2RR. [3,9] Figure 3 presents the VB and CB positions of TiO_2, Si, and a III–V dual-junction solar cell (GaInP/GaInAs) together with the water redox potentials $\Phi(H^+/H_2)$ and $\Phi(O_2/H_2O)$, and the potentials related to CO_2RR at pH = 0. Self-oxidation and self-reduction potentials Φ_{ox} and Φ_{red}, respectively, are discussed in detail in the next subchapter.
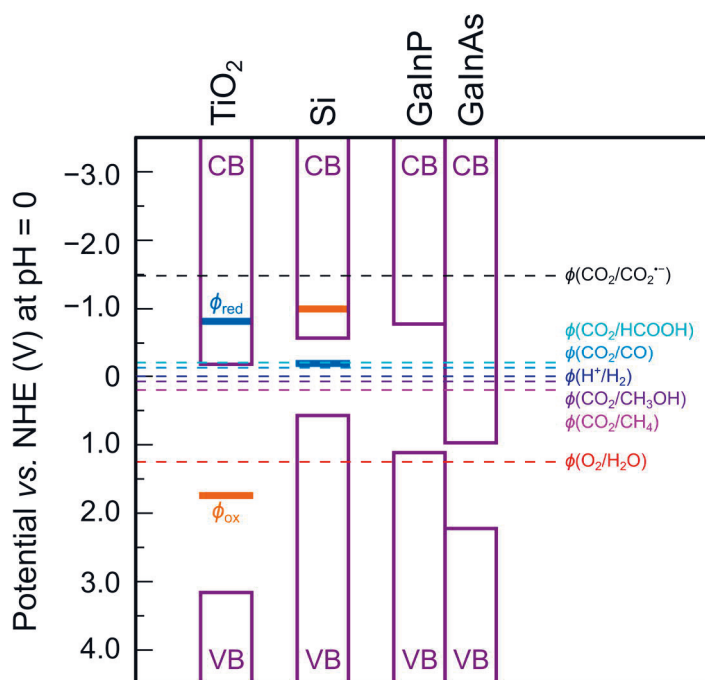
Figure 3. The VB and CB positions of TiO_2, Si, and a III–V dual-junction solar cell (GaInP/GaInAs), and the water redox potentials $\Phi(H^+/H_2)$ and $\Phi(O_2/H_2O)$, and the potentials related to CO_2RR in respect of NHE at pH = 0. The figure was composed based on the ref. [59]. The potential values were positioned based on the refs. [3,13,14,60,61]. The self-oxidation and self-reduction potentials Φ_{ox} and Φ_{red}, respectively, for TiO_2 and Si were placed based on the calculations in the ref. [59].

In addition to absorption of sunlight and favourable band alignment with respect to redox potentials, there are still several aspects related to a PEC cell design and components that affect remarkably the performance of the photoelectrochemical cell.

2.2   Structure and materials of photoelectrochemical cells

The main component of the PEC cell is the semiconductor photoelectrode. Metal oxide semiconductor materials formed from Earth-abundant metals, such as TiO_2 and Fe_2O_3, are low-cost, stable, and non-toxic photocatalysts and thus promising materials for photoelectrodes in PEC cell. However, limitations on charge transport and absorption of the solar spectrum reduce the efficiency of metal oxide-based PEC applications. [6,20] An alternative approach and more efficient in terms of sunlight absorption is to couple a narrow band gap light absorber, e.g., Si or GaAs with a wide band gap photocatalyst, such as TiO_2, that can protect the unstable light absorber against corrosion and absorb the UV region of the solar spectrum [40–42,54,62]. The most efficient but the most expensive monolithic tandem PEC devices utilize III–V multijunction solar cells to absorb efficiently almost the whole solar spectrum as illustrated in Figure 2 [13,14]. Nevertheless, also these semiconductor materials need protective coating against corrosion [6,13,14]. The vulnerability to corrosion and thermodynamic instability under photoelectrochemical conditions can be evaluated by analyzing the self-oxidation Φ_{ox} and self-reduction Φ_{red} potentials of a semiconductor material relative to $\Phi(H^+/H_2)$ and $\Phi(O_2/H_2O)$ in the case of water splitting reaction [24,59]. If Φ_{ox} is smaller than $\Phi(O_2/H_2O)$ the semiconductor will oxidize itself and suffer photocorrosion. If the self-oxidation potential is between the VB and $\Phi(O_2/H_2O)$, the self-oxidation depends on the reaction kinetics and consumption rate of holes for oxygen evolution reaction (OER) at the solid/liquid interface. A semiconductor with Φ_{ox} more positive than $\Phi(O_2/H_2O)$ and the VBM exhibits inherent thermodynamic stability against oxidation under PEC solar fuel production conditions. Analogously, a semiconductor is stable or will reduce itself depending on the position of Φ_{red}. [24] As an example, the self-oxidation and self-reduction potentials for TiO_2, and Si at pH = 0, are presented in Figure 3. Compared to more efficient light absorber, silicon, TiO_2 exhibits good stability against photocorrosion both when used for the OER and especially for HER. Therefore, TiO_2 is often added as a protective coating on Si or on other unstable semiconductor photoelectrodes [13,14,24,40–43,63–65]. Moreover, Pourbaix diagrams are another way to predict thermodynamic stability of materials in aqueous electrolytes with different pH [19,59,66,67]. In addition to the self-reduction and self-oxidation potentials, pH of the electrolyte may affect dissolution properties, and thus the stability of a photoelectrode. For instance, Si will passivate itself with SiO_2 in acidic electrolyte but under alkaline conditions Si will dissolve continuously [19,24,68,69]. Despite

great progress in the PEC field, finding a proper protection against severe dissolution or photocorrosion of semiconductor photoelectrode materials in practice has remained one of the main challenges to be solved [13,14,19,24].

Outlines of three different PEC cell configurations and corresponding current *versus* voltage (I–E) curves are depicted in Figure 4. Figure 4a depicts a simple PEC cell consisting of a photoanode connected via an external circuit to a cathode that can be HER active metal, such as, platinum. However, this single photoelectrode PEC cell design typically requires an external potential to drive solar fuel production reactions efficiently. [19] Figure 4b demonstrates the effect of an applied bias (V_{bias}) and a resulting operating current (I_{op}) of a PEC cell. Generally, the higher the I_{op}, the better the performance, and thus lowering onset potentials of I–E curves is of major interest. [54,70] A bias-free PEC cell, instead, can be achieved by using a tandem configuration, either with an external circuit (Figure 4c) or as a monolithic device (Figure 4d), comprising of a photoanode and a photocathode with a Z-scheme band alignment [3,13,19,70]. I–E curves and an operating bias-free photocurrent of a tandem PEC cell are illustrated in Figure 4e [70].
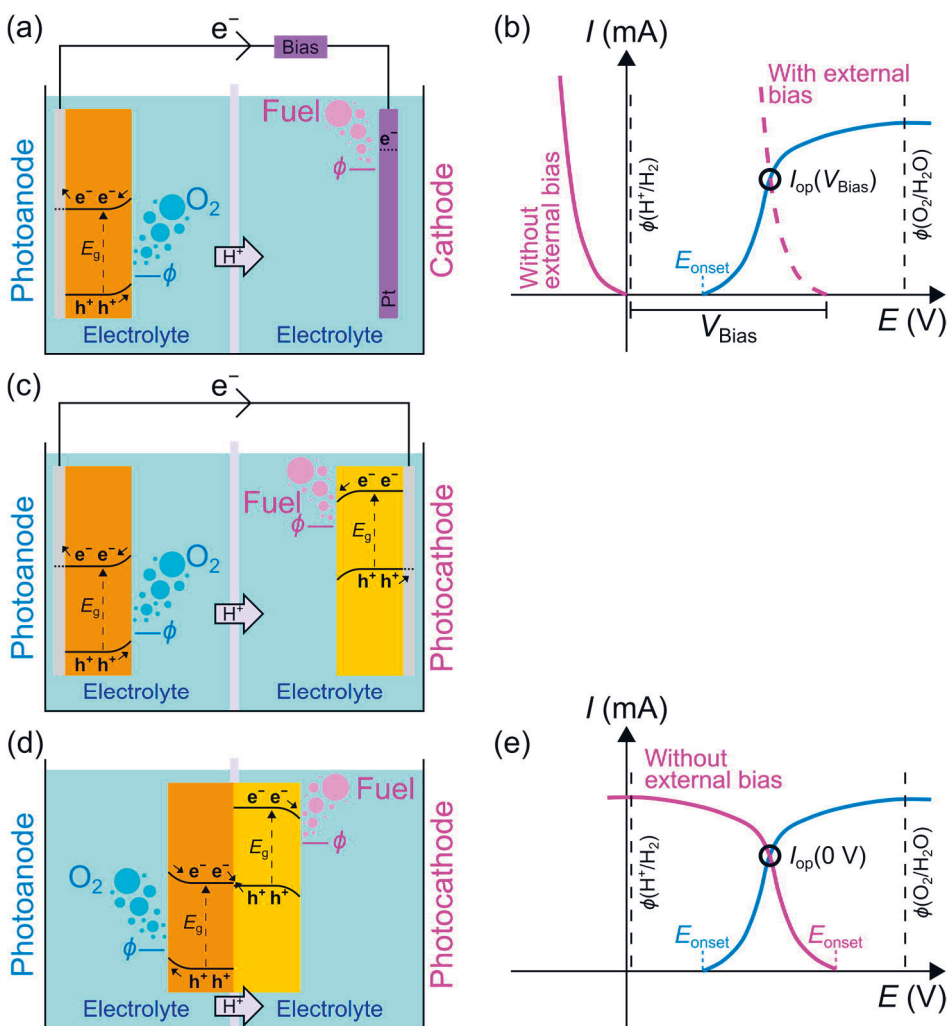
Figure 4. Schematic illustrations of PEC cell configurations comprising of (a) a photoanode and a Pt cathode, (c) a photoanode and a photocathode connected with an external circuit, and (d) a Z-scheme monolithic tandem cell. Characteristic $I–E$ curves related to configurations (a), and (c, d) are presented in (b) and (e), respectively. The representation of the $I–E$ curves is based on the refs. [54,70].

The choice of an electrolyte is also one significant aspect affecting the chemical stability and efficiency of a PEC cell. In general, alkaline electrolytes enhance OER, while HER prefers acids, and these are also the most studied environments for the water splitting reactions. [19,24] Commonly the electrolyte is the same for both electrodes but thanks to development of ion-selective bipolar membranes, having different pH conditions in the photoanode and photocathode sides may also be

14

possible [19,24,71–73]. In Figure 4a, Figure 4c, and Figure 4d a proton-exchange membrane (PEM) is used to let H^+ ions to pass from anode to cathode side [3]. Furthermore, a membrane will reduce crossover-induced back reactions of produced gases and formation of dangerous mixtures of oxygen and fuels [3,19].

As discussed in the previous subchapter, the photoelectrochemical water splitting reaction requires thermodynamically the potential of 1.23 V minimum [6]. However, the potential is de facto larger due to the several overpotential losses occurring in PEC cell. To enhance the OER and HER reaction kinetics, electrocatalyst-dependent overpotentials, η_{OER} and η_{HER}, need to be considered. A good ion transport between the electrodes is essential to reduce losses related to the ionic conductivity ($\eta_{ionic\ cond}$). Moreover, solid-state losses concerning charge carrier separation of electrons and holes, and their transport from one electrode to another can cause additional overpotentials, η_{sep} and η_{trans}, respectively. [6,19] Considering these overpotential losses a minimum band gap or more precisely a useable photopotential exhibited by semiconductor photoelectrodes in a bias-free PEC cell can be calculated by the following equation

$$E_{ph,min} = 1.23\ eV + \eta_{OER} + \eta_{HER} + \eta_{ionic\ cond} + \eta_{sep} + \eta_{trans} \qquad (4)$$

where $E_{ph.min}$ is the required minimum photopotential and can be estimated to be >2 eV [6,19,23,74].

To lower the overpotential losses and to enhance reaction kinetics, typically electrocatalysts are added on PEC photoelectrode surfaces [3,6,19,54,60]. These co-catalysts are essential for reducing losses by lowering activation energies for surface reactions and by improving charge separation of electrons and holes generated by light absorber [21]. Moreover, co-catalysts can have a positive effect on the stability of a photoelectrode by steering the holes and the electrons from a semiconductor material towards its surface to be consumed for the OER and HER instead of self-oxidation or self-reduction of a light absorber i.e., photocorrosion, as discussed earlier [3,54,68]. As an example, some potential electrocatalysts for the HER are Pt, MoS_2, and NiMo-based materials whereas the more challenging OER can be promoted, e.g., by IrO_2, RuO_2 or Ni-based (such as Earth-abundant Ni–Fe) co-catalysts [13,19,40,41,75–79]. Regarding CO_2 reduction reaction, by choosing the electrocatalyst, selectivity towards a desired product can be controlled to some extent but further research is still needed [60,80]. If an electrocatalyst exhibits a weak CO binding energy, the main product is most likely CO that desorbs from the surface before forming other products. In contrast, if CO adsorbs strongly on a surface, it

can more likely react further to produce, e.g., methane or methanol. Furthermore, surface oxophilicity and thus favoring of C−O bond breakage is reported to lead to methane whereas less oxophilic surface prefers methanol production. [80] So far, Earth-abundant and low-cost Cu-based electrocatalysts are the most studied and the most promising for production of hydrocarbons and alcohols via CO_2RR [60,80,81].

2.3   Protective TiO_2 photoelectrode coatings

Severe dissolution or photocorrosion of semiconductor photoelectrode materials is a major issue to be solved when developing commercially viable PEC cells. Titanium dioxide is proven to be a good material choice for protective photoelectrode coatings thanks to its intrinsic chemical stability and the favourable self-oxidation and self-reduction potentials [24]. Interestingly, depending on a fabrication method and a phase of TiO_2, several strategies for using TiO_2 as a protective coating have been reported. ALD-grown ultra-thin (≤ 2 nm) amorphous TiO_2 coatings used in metal−insulator−semiconductor (MIS) photoanodes allow tunneling of photogenerated holes from a semiconductor light absorber to a metal electrocatalyst surface. If am.-TiO_2 thickness of 2 nm is exceeded (2.5–12 nm), instead of direct tunneling mechanism, TiO_2 bulk-limited conduction dominates and increases the required overpotential for water oxidation reaction. [41,64] However, if a photoanode with a buried p⁺n-Si junction is used to increase the interfacial hole density and charge carrier transport in Ir/am.-TiO_2/SiO_2/Si MIS photoanode structure, remarkably high photovoltages can be achieved, and those have been reported to be less dependent on TiO_2 protection layer thickness [63,65]. Another approach of using ALD-grown am.-TiO_2 as a protective coating is relying on Ti^{3+} defects-induced conductivity enabling hole transport even through a thicker am.-TiO_2 coating (4–143 nm) [40]. This intriguing phenomenon based on a polaron hopping mechanism is however highly dependent on ALD precursor choice [32,49,82]. Moreover, computational studies have proposed that hole conduction may also occur through O−O peroxy linkages within am.-TiO_2 [44,83]. Besides enhanced conduction, a careful fabrication and choice of an electrocatalyst in terms of work function and metal/am.-TiO_2 interface is required to induce a proper band bending and contact [49,84]. In addition to ultra-thin or conductive ALD-grown am.-TiO_2, a thicker crystalline TiO_2 (c-TiO_2) thin film (ALD-grown or sputtered) can also serve as a protective coating and exhibit sufficient charge carrier transport properties in case of a suitable band alignment with the photoelectrode [13,43,50,85]. It is reported

that n-type c-TiO$_2$ with an applied bias is capable to transport electrons from the OER via the conduction band to the valence band of Si photoanode, and thus can behave like an ohmic contact [43]. Compared to other strategies, here the TiO$_2$ protective coating is designed to conduct electrons into the photoanode, instead of transporting the holes to the photoanode surface [24]. In fact, similar conduction mechanism has also been suggested for the ALD-grown am.-TiO$_2$ photoelectrode coating, despite the conductivity mediated by Ti^{3+} defect states [86]. As a protective photocathode coating, instead, n-type crystalline TiO$_2$ can conduct photogenerated electrons from the CB of Si to the photocathode surface to drive the HER thanks to a beneficial CB band alignment of TiO$_2$ with Si [87,88].

Figure 5 shows schematic illustrations of the discussed strategies to use different protective TiO$_2$ photoelectrode coatings and to facilitate the charge carrier transport properties on Si photoelectrodes. The same strategies can also be used for other semiconductor photoelectrodes, for instance, in the latest record-breaking III–V dual-junction PEC cell, c-TiO$_2$ was used as a photocathode coating thanks to its beneficial band alignment [13,14]. Furthermore, another interesting but less studied approach to benefit from different crystalline TiO$_2$ phases and their band alignments relates to fabrication of anatase–rutile phase junction structures. This phase junction structure can enhance electron–hole separation and outperform pristine single-phase anatase and rutile, especially, in PEC applications where TiO$_2$ serves as a photoanode itself. It is proposed that the anatase–rutile phase junction steers the electrons from rutile to anatase via conduction bands and holes vice versa via valence bands, and thus rutile should be the choice at the electrolyte–TiO$_2$ interface. [30,89]
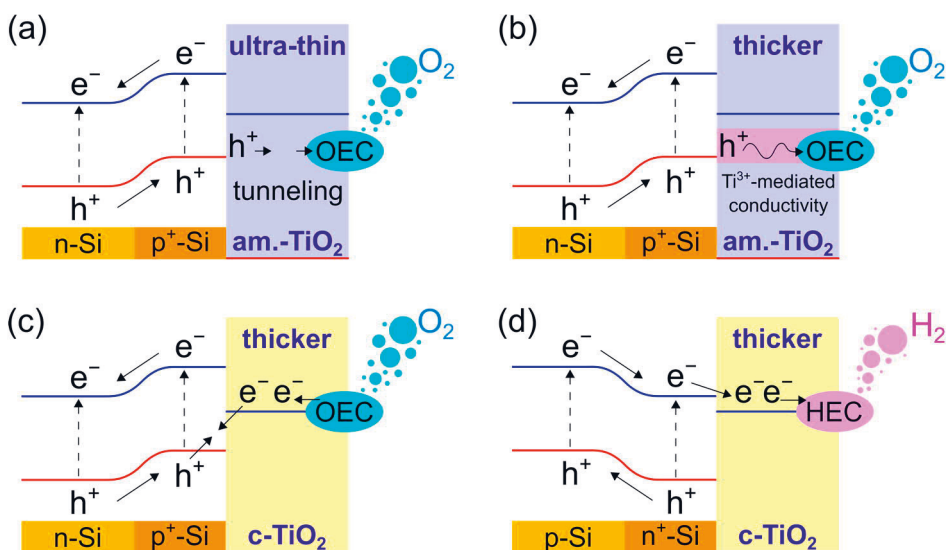
Figure 5. Schemes of widely studied strategies to use (a, b) amorphous and (c, d) crystalline TiO_2 as a protective coating for Si photoelectrodes and to facilitate the charge carrier transport between a light absorber and an oxygen evolution catalyst (OEC) or a hydrogen evolution catalyst (HEC). The blue and the red lines represent the CB and the VB, respectively. (a) In a MIS photoanode holes from the VB can tunnel through an ultra-thin am.-TiO_2 coating to OEC. (b) Ti^{3+} defects-induced conductivity can enable hole transport from the VB to OEC even through a thicker am.-TiO_2 coating. (c) The CB of c-TiO_2 can conduct electrons from an electrolyte/OEC to the VB of Si where they recombine with holes (an applied bias needed). (d) In a photocathode c-TiO_2 can steer electrons from the CB of Si to HEC via its CB. The figure was composed based on the schemes presented in the refs. [19,24,63].

Albeit am.-TiO_2 is regarded as rather stable under various aqueous electrolyte conditions, its chemical stability has been still under debate [24,45,46]. Some articles have reported that ALD-grown amorphous TiO_2, without an additional electrocatalyst, dissolves in acidic electrolyte but exhibits stable behaviour under alkaline conditions [45,46]. Contrarily, there are also studies showing instability of plain ALD-grown am.-TiO_2 upon PEC water splitting in alkaline solution [42]. Adding an electrocatalyst on am.-TiO_2, however, can reduce photocorrosion and thus be, at least partly, the reason for reported good stability of electrocatalyst/am.-TiO_2/photoanode structures [3,24,40,41,46,54]. Polycrystalline anatase and rutile TiO_2, instead, have shown to be intrinsically stable, also without an electrocatalyst [45,46,48,68]. However, an unfortunate failure of protection may still occur due to fissures at grain boundaries in polycrystalline structure that can let an electrolyte to a photoelectrode–TiO_2 interface leading to etching of the photoelectrode [47,48,50,68].

TiO$_2$ is clearly a potential material and there are several strategies how to use it to tackle the one of the paramount challenges, long-term stability of PEC cells [19,24,90]. However, there is still no general consensus on which of the strategies is the best and optimization of protective coating fabrication procedures is ongoing research [19,24]. Although TiO$_2$ coatings fabricated by sputtering-based methods are widely studied and shown to serve as protection for photoelectrodes, atomic layer deposition-grown TiO$_2$ is regarded as the best candidate for pinhole-free, controllable, and conformal coating, and thus maybe the most promising material for PEC photoelectrode protection [13,19,24,38–41,43,68,91].

3 ATOMIC LAYER DEPOSITION AND ANALYSIS METHODS FOR TiO$_2$ THIN FILMS ON PHOTOELECTRODES

Over the past few decades, the atomic layer deposition method, providing high-quality nanoscale coatings has shown its competence in many high technology and industrial applications, such as, microelectronics, and solar energy conversion applications [20,38,92]. Regarding the history of ALD, the early research of sequential gas–solid surface reactions for thin film fabrication was conducted rather simultaneously in Finland and in the Soviet Union [93]. In the 1960s, Valentin B. Aleskovskii and Stanislav I. Kolt'sov developed a method named as molecular layering (ML) [94,95]. They studied and reported thin film growth of TiO$_2$ from titanium tetrachloride (TiCl$_4$) and H$_2$O on silica gel and on single crystal Si(111) surfaces [96–99]. However, in the 1970s in Finland Tuomo Suntola invented a similar kind of technique to grow polycrystalline ZnS thin films for electroluminescent (EL) display panels [93]. And in 1977, together with Jorma Antson, they were granted an international patent on this novel thin film deposition method, called as atomic layer epitaxy (ALE) [93,100]. Nowadays the technique is typically utilized to grow other than epitaxial thin films and better known as atomic layer deposition [101]. As an inventor of this successful ALD technology, Tuomo Suntola, was awarded Millennium Technology Prize by Technology Academy Finland (TAF) in 2018 [102].

Thanks to pinhole-free, conformal, and highly controllable thin films, atomic layer deposition is accounted an ideal choice for fabricating protective coatings, both on 2D and 3D PEC photoelectrodes [19,20,24]. This chapter focuses on basic principles of the ALD method and characteristics of different TiO$_2$ phases. Furthermore, the chapter includes the introduction and experimental details of XPS and PEC analysis, and how these methods can be used to gain in-depth understanding of interfacial, molecular, and electronic structure of ALD TiO$_2$ and its properties in terms of PEC performance.

3.1 Fundamentals of atomic layer deposition method for TiO$_2$ thin film growth

The most prominent key features that differentiate ALD from many other thin film deposition methods are self-limiting surface reactions and non-overlapping pulsing sequence of precursors [38,103]. This leads to possibility to grow highly uniform and conformal thin films ideally with a submonolayer thickness control even on high aspect ratio structures [38,103,104]. Figure 6 presents a schematic illustration of an ALD thin-film growth process, generally known as an ALD cycle. As an example, the ALD cycle depicts the growth process of TiO$_2$ on a Si substrate using TDMAT and H$_2$O as precursors.
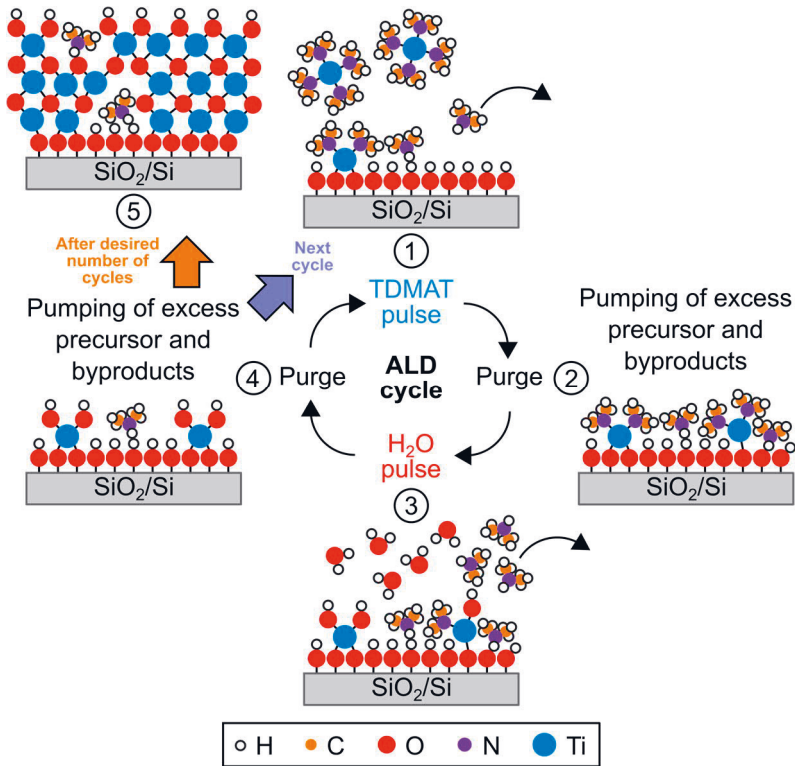
Figure 6. A schematic illustration of the ALD cycle using TDMAT and H$_2$O as precursors to grow TiO$_2$ thin film on SiO$_2$/Si substrate. The ALD cycle consists of four steps: (1) the TDMAT precursor pulse, (2) the purge of the excess unreacted TDMAT precursor and reaction byproducts, (3) the H$_2$O precursor pulse, and (4) the purge of the excess H$_2$O and reaction byproducts. (5) The number of ALD cycles defines the thickness of the resulting thin film.

The ALD cycle consists of four steps. During the first precursor pulse, TDMAT is introduced into the reaction chamber to react with initially OH-terminated SiO_2 surface sites. TDMAT molecules are chemisorbed via ligand exchange reactions with OH surface groups until monolayer saturation is reached, i.e., all the OH adsorption sites have been reacted, or steric hindrance limits the adsorption. After the TDMAT pulse the reaction chamber is purged and excess unreacted TDMAT and volatile dimethylamine ($HN(CH_3)_2$) reaction byproducts are removed. Then the TDMAT-saturated surface is exposed to the second precursor pulse, H_2O, that react with the remaining dimethylamide ($-N(CH_3)_2$) ligands resulting in OH-terminated monolayer of TiO_2 followed by the purging step. This ALD cycle can be repeated desired number of times to obtain the target thin-film thickness [38,103–106] Even though ALD is often described to form an ideal and pure monolayer of material on each ALD cycle, in practice, less than a monolayer is typically obtained and reaction byproducts may be re-adsorbed and appear as impurities in a grown thin film [38,106,107].

Some of the main concepts related to ALD are "growth per cycle" (GPC) and an ALD window. As mentioned above, in a well behaving ALD process, one ALD cycle yields certain amount of material onto a surface depending on the number of available chemisorption sites and this thickness of material is designated as GPC. [38,104] In practice, GPC is typically determined by measuring a thin-film thickness by ellipsometer and dividing the result by the number of cycles. The GPC can also slightly vary during the growth process. For instance, a substrate may hinder the initial growth but after the first full monolayer has been formed, the GPC is increased if the as-grown material provides more chemisorption sites compared to the substrate [38]. In some cases, this substrate-inhibited growth mechanism can lead to island growth, and thus increased surface roughness and even higher GPC after the full monolayer is completed [38,108,109]. However, the change in the GPC can also be vice versa with different substrate and ALD material combinations [38,110,111]. These substrate- and ALD material-dependent growth mechanisms are summarized in Figure 7.
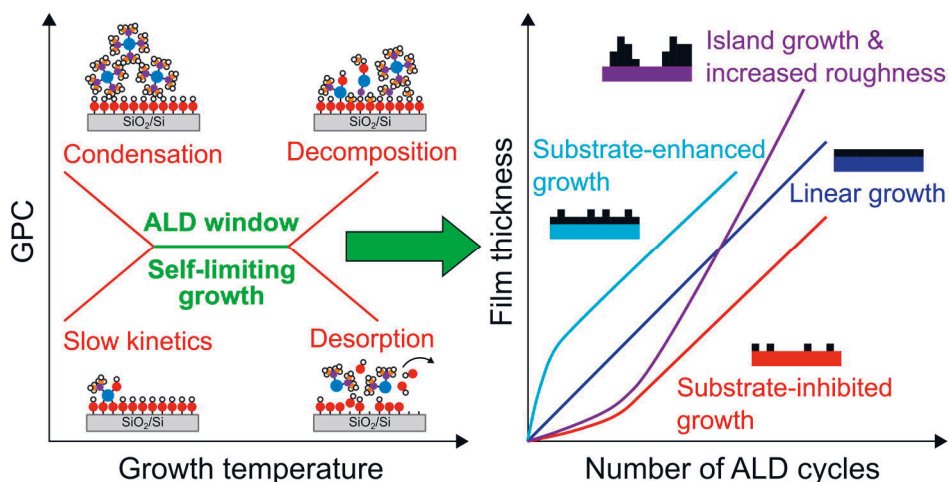
Figure 7. A basic concept of ALD window, i.e., a growth temperature range where an ALD process for certain precursors exhibits self-limiting growth and a stable GPC. If the temperature range is exceeded decomposition of precursors or desorption of chemisorbed reaction surface species may interfere the film growth. A low growth temperature, instead, can lead to condensation of precursors or incomplete surface reactions. Even within the ALD window the GPC may slightly vary due to the substrate-induced effects that can also affect the morphology of a resulted thin film. The representations of the ALD window and the substrate effects are based on the refs. [38,101,103,104] and the refs. [38,107–109], respectively.

An ALD window as a concept means a temperature range where an ALD process works ideally in a self-saturating manner, and the GPC remains rather constant if the temperature is changed within the ALD window [38,103,104]. Figure 7 illustrates a fundamental dependency of the ALD growth temperature on the GPC and the ALD window. At low growth temperatures thermal energy may be not sufficient to result in complete surface reactions, and the slow reaction kinetics leads to the lower GPC. Furthermore, a low temperature can cause precursor to condensate onto substrate surface which can be observed as a high GPC value. If the growth temperature is too high, instead, a precursor decomposes inducing a chemical vapor deposition (CVD)-like growth and an increased GPC. However, a high temperature may also lead to desorption of reactive surface species and a low GPC. If these undesirable phenomena can be avoided in some temperature range, the ideal ALD process and the constant GPC is likely to occur within that temperature window. [38,101,103,104] However, it should be noted that the optimal temperature range for ALD process depends on precursor choice, and moreover, even within the ALD window the GPC can slightly vary if the growth temperature affects chemisorption sites or reaction pathways [107,112].

Furthermore, in addition to the growth temperature, precursor pulse and purge times are of importance to achieve the optimized ALD growth. Typically, saturation curve studies at constant temperature are conducted to confirm long enough precursor pulse and purge times for surface saturation and for preventing precursor pulses to overlap, respectively. [38,112] The pulse and purge times should not be too long either since the duration of the deposition should be feasible in practice and desorption of reactive surface species should be minimized [112,113]. Since several factors and parameters affect the ALD process, a fully ideal ALD growth is de facto often really difficult to achieve, and thus non-ideal features contributing to ALD thin films have to be often accepted to some extent [112].

3.1.1   Structure and properties of TiO$_2$ phases

In general, titanium dioxide as an Earth-abundant, non-toxic, and chemically stable semiconductor material has remained for decades one of the most studied and applied oxides in many different fields from photocatalysis to dielectric and optical applications [26–28,114–118]. The main four phases of TiO$_2$ are amorphous, anatase, rutile, and brookite. Anatase and rutile polymorphs are the most common, whereas utilization of brookite has remained limited due to the challenges in its synthesis. [29,119,120] During the last ten years, there has been an increasing interest towards amorphous TiO$_2$ demonstrating exceptional charge carrier transport and visible-light absorption properties induced by oxide defects within disordered am.-TiO$_2$ structure [32,34,40,49,121,122]. Besides these phases, also other less studied polymorphs exist. For instance, TiO$_2$-II, can exhibit even higher refractive index than rutile. [29,123,124]

Regarding the structure of the crystalline TiO$_2$, well-ordered Ti–O$_6$ octahedras are the fundamental building blocks forming the different polymorphs and an arrangement of these octahedras determines the TiO$_2$ phase [29,125]. In anatase four edge-shared and four corner-shared octahedras surround the center octahedron whereas in rutile there are two edge-shared and eight corner-shared octahedras and the brookite structure comprises of three edge-shared and six corner-shared octahedras around the center Ti–O$_6$ [125]. The metastable anatase phase exhibits less-constrained structure and thus it is the most common TiO$_2$ polymorph and requires typically lower formation temperatures. Rutile, instead, is the thermodynamically stable TiO$_2$ phase but the high fabrication temperature (>400 °C, often even 600–800 °C) is the widely known challenge in its use. [29,115,126]

However, liquid-based synthesis, such as hydrothermal method, enables formation of rutile (as well as anatase) nanocrystals at temperatures ≤ 200 °C or even at the room temperature [29,125,127–129]. Lowering the formation temperature of the rutile thin film may be possible for example by inducing disordered oxygen sublattice, i.e., oxygen vacancies, which can allow easier rearrangement of ions to more constrained rutile structure [29,89,130,131]. Furthermore, atomic layer deposition of TiO_2 on substrates with a rutile-structured seed layer, e.g., SnO_2, RuO_2, or IrO_2, have been reported to facilitate epitaxial rutile TiO_2 growth at 250–350 °C [117,126,131–133]. Fundamentally, amorphous TiO_2 structure, instead, lacks long-range order and consists of randomly connected Ti–O_6 octahedras (Ti_{6c} and O_{3c} coordinated ions) and under- and over-coordinated ions (e.g., Ti_{5c}, Ti_{7c}, O_{2c}, and O_{4c}) with broad distributions of bond lengths and angles [32,134,135].

The enhanced charge carrier transport and visible-light absorption properties of am.-TiO_2 are generally attributed to oxide defects, i.e., oxygen vacancies and Ti^{3+} ions which are easier to generate within am.-TiO_2 structure compared to c-TiO_2 [32,34,122,136]. The formation of oxygen vacancy leads to three pentacoordinated Ti ions (Ti_{5c}). Moreover, the oxygen vacancy induces two unpaired excess electrons initially carried by surrounding Ti_{5c} ions, i.e., Ti^{3+} defects [137,138]. These Ti^{3+} defects induce Coulombic attractive and repulsive forces that distort the bond lengths and angles between surrounding ions, as illustrated in Figure 8a. Consequently, phonons originated from this structural deformation and vibration of ions are coupled with the excess electrons forming quasiparticles, known as electron polarons. [82,139,140] Commonly accepted electron conductivity mechanism of TiO_2 is described with polarons, i.e., electrons of Ti^{3+} ions, that can hop to an adjacent Ti^{4+} ion converting it to a Ti^{3+} ion, as visualized in Figure 8b. This phenomenon is typically referred as polaron hopping mechanism. [32,49,82,139,140] Hole conduction, instead, has been proposed to occur via oxygen vacancies, hole polarons or O−O peroxy linkages [32,44,83,136,141,142]. In addition to electron conductivity, visible-light absorption is also mediated by Ti^{3+} defects [34]. Due to the Jahn−Teller effect-induced splitting of Ti 3d orbitals, the excess electrons of Ti^{3+} defects occupy Ti^{3+} $3d_{xy}$ electronic states within the TiO_2 band gap [137,143,144]. These electrons of the in-gap states can absorb photons of the visible-light wavelength range and enable the fabrication of visible-light active black TiO_2 [34,35,37,122,145].
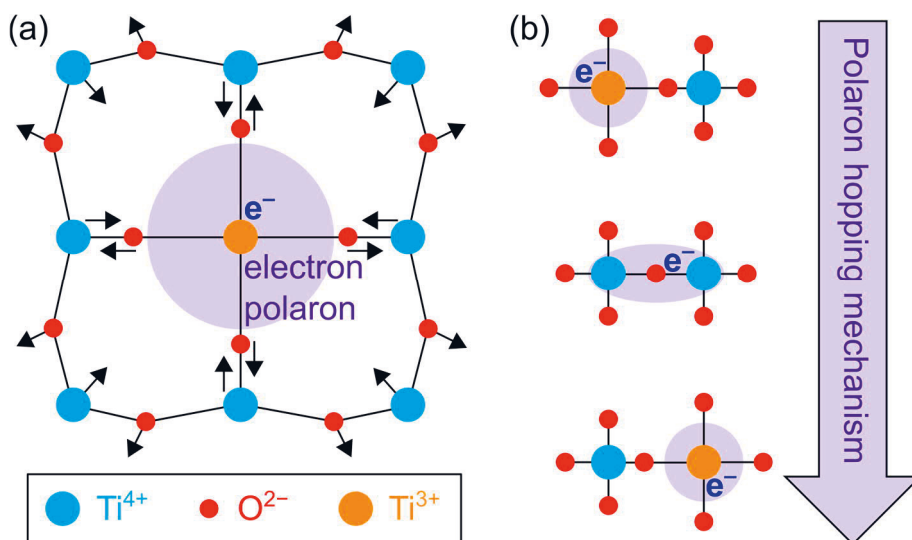
Figure 8. Schematic illustrations of (a) a small electron polaron and (b) polaron hopping mechanism inducing Ti^{3+} defects-mediated enhanced conductivity of TiO_2. An excess electron carried by Ti^{3+} defect induces phonons via Coulombic attractive and repulsive forces deforming the bond lengths and angles of the surrounding ions. This electron–phonon coupling is known as an electron polaron. The excess electron can hop from a localized state (polaron) to an adjacent Ti ion via an intermediate delocalized state. Enhanced conductivity of TiO_2 is commonly attributed to this polaron hopping mechanism. The figures were composed based on the representations in the refs. [82,139,140].

As elucidated above, TiO_2 materials exhibit diverse set of properties depending on the phase and the atomic- and the electronic-level structure. Thus, every TiO_2 phase has its own advantages and potential from applications perspective. As a photocatalyst, anatase TiO_2 (E_g = 3.2 eV) is often described to be more active than rutile, although rutile should exhibit narrower band gap of 3.0 eV [28,29]. However, recent research has elucidated that due to the difference in dynamics of electrons and holes, anatase facilitates reduction reactions whereas rutile shows higher photocatalytic activity towards oxidation reactions [146]. Since the discovery of black TiO_2 materials in 2011 produced through hydrogenation, those have accounted as highly beneficial and potential, e.g., for photocatalytic applications [122,147]. However, due to conflicting results and lack of comprehensive understanding related to photocatalytic activity of black TiO_2, its real significance in many applications has remained rather vague [122]. Rutile TiO_2 exhibiting high refractive index (>2.6) and anisotropic nature, is of interest in optics [29,114,115,148]. Furthermore, low-temperature (≤400 °C) rutile TiO_2 with high dielectric constant is a promising material of choice for dynamic random-access memory (DRAM) capacitors

[126,131]. As a protective photoelectrode coating, pinhole-free and continuous am.-TiO$_2$ with oxide defects-mediated enhanced conductivity has shown to provide facile hole transport [40,49,84]. Defect-free crystalline TiO$_2$, instead, can exhibit high-transparency and reduced charge carrier recombination compared to am.-TiO$_2$ [13,149]. In-depth understanding of these TiO$_2$ phases and how to control the diverse properties of titanium dioxide are the key means to optimize the protective TiO$_2$ photoelectrode coatings.

3.1.2 Effect of precursors and substrate pretreatment on ALD TiO$_2$ coatings

Precursors used in ALD processes have several requirements, i.a., a precursor should evaporate at a relatively low temperature, be reactive towards surface species but not itself, and exhibit a sufficient thermal stability to enable the characteristic self-limiting ALD process at certain temperature range. Furthermore, the reaction byproducts should be volatile and not interfere with the growth process. Besides these must-have properties, precursors are also desired to be non-toxic, highly pure, easy to synthesize and work with, and as cheap as possible. Typical ALD precursors serving as metal sources (e.g., Ti, Al, Cu) comprise of metal ion surrounded by different types of ligands. Depending on ligands, precursors can be classified as inorganic or metalorganic reactants, and homoleptic or heteroleptic if a compound includes only one type of ligand or two or more different, respectively. [104,112,117,150]

The most commonly used metal precursors for TiO$_2$ ALD process in general and in the PEC field are inorganic halide titanium tetrachloride (TiCl$_4$), metalorganic alkoxide titanium isopropoxide (TTIP), and metalorganic alkylamide TDMAT that are mainly used with water as a co-reactant and the oxygen source [13,40,41,48–50,105,112,117,151–154]. TiCl$_4$+H$_2$O process is rather comprehensively studied and known of its wide ALD window allowing direct deposition of am.-TiO$_2$ and crystalline anatase, or even rutile at temperatures around 400 °C or higher [31,117]. However, the reaction byproduct, hydrochloric acid (HCl) may cause damage to a substrate, a growth thin film, or parts of the ALD reactor, and hence other ALD TiO$_2$ processes are often preferred [104,105,117]. TTIP+H$_2$O process, instead, does not produce corrosive byproducts but studies have revealed that the process is likely to result in TiO$_2$ coating with fissures between grains or incorporated alkoxide ligands which can lead to deleterious degradation of the protective TiO$_2$ photoelectrode coating [48,50,117,152]. Due to the above-mentioned issues, TDMAT+H$_2$O process is in many cases regarded as the most promising of these

ALD processes [48,50]. Since the ligand exchange through the Ti–N(CH$_3$)$_2$ bond breakage requires rather small amount of energy, TDMAT has significantly high reactivity towards water and surface OH groups, and thus proposed to enable the ALD growth as low temperature as 50 °C [105,117,155]. However, the thermal decomposition, reported to start at temperatures >180–200 °C, challenges the self-limiting ALD process and complicates to grow crystalline TiO$_2$ thin films [105,117,156,157]. Despite the limited thermal stability, the high substrate temperature of 250–300 °C combined with a short TDMAT pulse or a long H$_2$O purge time have been proposed to enable crystalline anatase or mixed-phase anatase/brookite–rutile TiO$_2$ thin film growth with the linear ALD growth behavior [153,158]. Furthermore, formation of small rutile and brookite crystallites within mostly amorphous structure has been reported during the growth at 200–250 °C [159]. Am.-TiO$_2$ thin films grown by using TDMAT+H$_2$O process can also be postannealed to obtain crystalline TiO$_2$ thin films but the increase in a thickness of detrimental interfacial oxides should be taken into account [19,50,152]. Regarding Ti^{3+} defects-mediated conductivity, TDMAT-grown am.-TiO$_2$ has been the most typical and reported choice, and has shown to outperform, for instance, am.-TiO$_2$ deposited by using TiCl$_4$+H$_2$O process [40,49,84].

Substrate surface chemistry can have a significant effect on an initial ALD growth that can steer crystallinity and morphology of a grown thin film [103,112,160–162]. Metal oxides, such as TiO$_2$, can grow easily on oxide surfaces, for example, on native oxide silicon with natural surface hydroxyl groups [103,112]. However, a substrate pretreatment prior to ALD growth may be desired to remove native oxide layer or to form a thin oxide layer in a controlled and reproducible manner [50,108,151,163,164]. Hydrofluoric acid (HF) etching is a typical chemical pretreatment to eliminate native SiO$_2$ on Si substrate resulting in an H-terminated surface [151,163,164]. These Si–H surface groups induce hydrophobic behaviour and are rather stable at commonly used ALD growth temperatures (≤300 °C) leading to slower precursor adsorption and inhibited initial ALD growth [108,160,164–168]. Other frequently used Si pretreatments are RCA SC-1 and SC-2 (Radio Corporation of America Standard Clean) which provide removal of organic surface impurities with the SC-1 solution (NH$_4$OH–H$_2$O$_2$–H$_2$O) and elimination of alkali ions and metallic contaminants with the SC-2 treatment (HCl–H$_2$O$_2$–H$_2$O). [169] Both of these treatments produce a thin silicon oxide layer with a high density of surface hydroxyl groups and hydrophilicity. [160,168–170] Due to the distinct difference in wettability and in functional surface groups between HF- and RCA-treated Si surfaces, ALD can result in very different TiO$_2$ surface morphologies depending on

the pretreatment of choice. Due to the sparsely existing OH groups on HF-treated Si surface the $TiCl_4+H_2O$ process results in immediate crystallization and island growth-induced small grain size and increased surface roughness. In contrast, the RCA-treated Si surface with the high density of OH groups promotes initial growth of flat and amorphous TiO_2 which crystallizes into larger grains after a specific film thickness is exceeded. [160,161,171] The nucleation of crystals and the grain size can also be affected by adding an interfacial layer prior to ALD of TiO_2. For instance, Al_2O_3 with a high surface energy has shown to induce large crystallites. [162,171] The TDMAT+H_2O process, instead, has been reported to grow as a flat and amorphous thin film both on HF- and RCA-treated Si surfaces at growth temperatures ≤150 °C, and the thin films exhibit relatively large grain size after postannealing-induced crystallization [48,50,152].

Therefore, when designing an optimized PEC photoelectrode with the protective ALD TiO_2 coating, aspects, such as, properties of precursors, substrate pretreatment and interface engineering are crucial to understand and to consider. These choices can affect, e.g., a phase, conductivity, a grain size, and an interfacial oxide layer that all play an important role in performance of the protective ALD TiO_2 coating.

3.2 Preparation of TiO$_2$/Si photoanodes by atomic layer deposition

In this Thesis [Publications **I**, **II**, **III**, and **IV**], all the ALD TiO_2 thin film depositions were carried out with the same ALD reactor and process using the Picosun Sunale R-200 Advanced ALD system, and tetrakis(dimethylamido)titanium(IV) ($Ti(N(CH_3)_2)_4$, TDMAT, electronic grade 99.999+%, Sigma-Aldrich) and Milli-Q type 1 ultrapure water as precursors. The main ALD process parameters are presented in Table 1. Both, the TDMAT precursor source and the delivery line, were heated to reach the proper vapor pressure and to prevent condensation of TDMAT. The H_2O source, instead, was cooled down by a Peltier element for stability control. Argon (99.9999%, Oy AGA Ab, Finland) was used as a carrier gas flowing through the reactor and the precursor lines. Growth temperatures selected for depositions were 100 °C, 150 °C, 175 °C, and 200 °C. Based on ellipsometer measurements, the required numbers of ALD cycles for 30 nm-thick TiO_2 thin films at the growth temperatures were 480, 636, 733, and 870, respectively.

Table 1.   The main ALD process parameters used for the TiO$_2$ thin film depositions in this work.

	Precursor	
	TDMAT	H$_2$O
Source temperature	76 °C	18 °C
Line temperature	85 °C	–
Carrier gas line flow	100 sccm	100 sccm
Pulse time	1.6 s	0.1 s
Purge time	6.0 s	6.0 s

From the surface chemistry perspective, the TDMAT+H$_2$O ALD process can be expressed as follows

$$Ti(OH)_2{}^* + Ti[N(CH_3)_2]_4 \rightarrow TiO_2 - Ti[N(CH_3)_2]_2{}^* + 2HN(CH_3)_2 \qquad (5)$$

$$TiO_2 - Ti[N(CH_3)_2]_2{}^* + 2H_2O \rightarrow Ti(OH)_2{}^* + 2HN(CH_3)_2 \qquad (6)$$
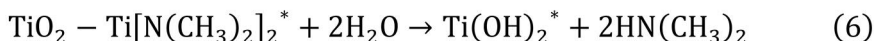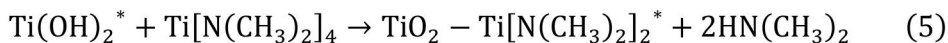
where the asterisks designate the surface species [106]. According to several studies, the process has shown to leave nitrogen traces into TiO$_2$ structure [50,106,153,158,172]. Incorporation of nitrogen into as-grown TiO$_2$ thin film occurs most likely as unreacted Ti–N(CH$_3$)$_2$ bonds due to the incomplete surface reactions or as adsorbed dimethylamine HN(CH$_3$)$_2$ reaction byproducts (Equation 5 and Equation 6) [106,158]. Dimethylamine can also further react with surface OH group leading to protonation of dimethylamine into the alkylammonium cation H$_2$N(CH$_3$)$_2{}^+$ [106,173] as shown in the following Equation 7:

$$-OH^* + HN(CH_3)_2 \rightarrow -(O^-)[H_2N(CH_3)_2]^{+*}. \qquad (7)$$

As in this work and commonly reported in literature, there is a decreasing trend of the GPC value for TDMAT+H$_2$O ALD process in the growth temperature range of 100–200 °C [105,153,158]. Some of the proposed reasons behind the GPC trend are slow molecular H$_2$O desorption at lower growth temperatures, and desorption of hydroxyl groups, or intermediate product (Ti[N(CH$_3$)$_2$]$_2$) reaction with OH group and subsequent desorption at higher growth temperatures [105,174]. At temperatures >250 °C the thermal decomposition of TDMAT molecules takes place

more severely resulting in an increasing GPC as often reported in literature [153,158]. A growth temperature around 300 °C can also increase amount of TDMAT precursor traces and lead to formation of TiN or TiO_xN_y species [153].

For the TiO_2/Si photoanode samples either P-doped or degenerately Sb-doped n-type Si(100) wafers (SIEGERT WAFER GmbH) were used as substrates. Furthermore, Publication **III** examines effect of Si wafer cleaning on deposited ALD TiO_2 thin films and their performance as protective photoelectrode coatings. Prior to ALD of TiO_2 some of the Si substrates were treated with HF, some with HF followed by RCA SC-2 treatment [169] and some of the substrates having a thin native oxide (SiO_2) layer were used as-received from the wafer vendor. In the HF treatment the Si substrate was immersed in 2.5% hydrofluoric acid for 10 seconds, then rinsed in two different Milli-Q type 1 ultrapure water containers, in the first one for 3 seconds and in the second for 10 seconds. After this, the samples were blown dry with nitrogen. In the RCA SC-2 treatment, i.e., chemical oxidation, the Si substrate was soaked in a 6:1:1 H_2O/30% H_2O_2/37% HCl solution at 70–75 °C for 10 min [169]. After the treatment, the wafer was rinsed with H_2O and blown dry with nitrogen. [*Caution*: HF is a highly corrosive and requires the use of Teflon, rather than glassware, and can easily penetrate the skin, bond with Ca^{2+}, and cause nerve damage. As such, even a small exposure (e.g., 2−10% of the body) can be fatal. Proper training is required before handling or working with HF, and appropriate personal protection equipment should always be worn when carrying out these sample preparations.] After the HF/ RCA SC-2 treatment samples were transferred immediately to the ALD system.

3.3   Studying interfacial, molecular, and electronic structure of photoanodes by X-ray photoelectron spectroscopy

X-ray photoelectron spectroscopy, i.e., electron spectroscopy for chemical analysis (ESCA) is a commonly used surface analytical technique to obtain both, qualitative and quantitative information on elements present within a sampling depth around 3–12 nm [175]. Thanks to this highly surface sensitive nature of XPS, it is an exceedingly suitable characterization method for thin films and thin-film/substrate interfaces. In addition to relative concentrations of elements, detailed analysis of XPS spectra can also provide in-depth understanding of atomic-level composition and electronic structure as well as chemistry and morphology of the sample.

Due to the initial state effects the binding energy (BE) of a photoelectron, measured by XPS, depends on chemical bonds between atoms and in more general the charge on an atom and the charge on the surrounding atoms. Consequently, the changes in BE values, i.e., chemical or core-level shifts (CLS) give valuable information on chemistry and atomic-level structure revealing, for instance, oxide defects within TiO_2 structure as shown in Publication **I**. [175] Core-level shifts can be determined theoretically by density functional theory (DFT) calculations. Figure 9 demonstrates the core-level shifts in Ti 2p spectra induced by an oxygen vacancy or an interstitial peroxo species (O_2^{2-}) within anatase TiO_2 structure.
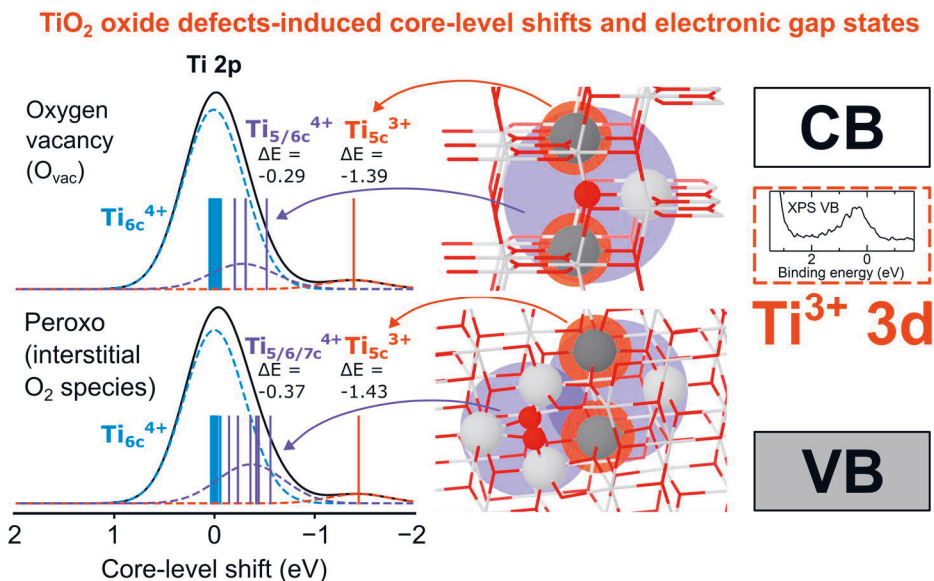
Figure 9. Core-level shifts of Ti 2p spectra determined by DFT calculations in cases when an oxygen vacancy or an interstitial peroxo species are introduced within anatase TiO_2 structure. The excess electrons of Ti^{3+} defects occupy the Ti^{3+} $3d_{xy}$ electronic states within the TiO_2 band gap. These electrons can be observed in an XPS VB spectrum as a peak around 0.2–1.2 eV. The figure was composed based on Publication **I** (complying with the Creative Commons CC BY license).

As mentioned in the subchapter 3.1.1, the formation of oxygen vacancy leads to three pentacoordinated Ti ions (Ti_{5c}) and two unpaired excess electrons delocalized over the entire structure or localized on surrounding Ti_{5c} ions, i.e., Ti^{3+} defects [137,138]. Regarding the CLSs, six-coordinated Ti_{6c} ions that are not directly connected to the introduced oxygen vacancy do not experience any remarkable CLS and the BE remains the same as in pristine anatase TiO_2. However, the Ti_{5c} and Ti_{6c}

ions that are the nearest or next nearest neighbors of oxygen vacancy see a negative CLS of −0.29 eV, and Ti^{3+} defects experience even larger CLS of −1.39 eV. Interestingly, introduction of an interstitial peroxo species together with an oxygen vacancy results in three heptacoordinated Ti_{7c} ions that have also negative shifts compared to the pristine Ti_{6c}^{4+} ions. These Ti_{7c} ions together with the Ti_{5c} and Ti_{6c} ions nearby the oxygen vacancy lead to a CLS of −0.37 eV. These insights into oxide defects of TiO_2 enable better understanding of the formation and controlling of intrinsic Ti^{3+} defects mediating the enhanced charge transport and visible-light absorption of am.-TiO_2 coatings. Besides the Ti 2p transition, the excess electrons of Ti^{3+} defects can be studied by measuring an XPS valence band spectrum where the Ti^{3+} $3d_{xy}$ electronic states within the TiO_2 band gap can be detected as a peak commonly reported to locate around 0.2–1.2 eV below the Fermi level [49,82,84,137,143–145,176]. In the conductivity and absorption measurements UV-grade fused silica, i.e., quartz (Präzisions Glas & Optik GmbH) was used as a substrate.

XPS measurements of this Thesis were conducted using NanoESCA spectromicroscope system (Omicron Nanotechnology GmbH) with focused monochromatized Al Kα ($h\nu$ = 1486.5 eV) as an excitation source and two other XPS systems with non-monochromatized X-ray source (Al Kα). All the XPS systems operate in ultra-high vacuum (UHV) with a base pressure of 1×10^{-8}–1×10^{-10} mbar. The core-level XP spectra were analyzed by the least-squares fitting of Gaussian–Lorentzian lineshapes and using a Shirley type background. Detailed explanations of peak fittings are available in the experimental sections of Publications **I, II, III**, and **IV**. For instance, in Publications **I** and **II** Ti 2p spectra were fitted by using Ti $2p_{3/2}$ reference peak shape measured for crystalline TiO_2, i.e., the six-coordinated Ti^{4+} peak (Ti_{6c}^{4+}), and the amorphous disordered structure was represented by under- and over-coordinated Ti^{4+} ($Ti_{5/7c}^{4+}$) and Ti^{3+} peaks. To the best of our knowledge, there have been no previous efforts to fit am.-TiO_2 Ti 2p spectra in a similar manner. CasaXPS [177] was used as an analysis software and the Scofield photoionization cross-sections as relative sensitivity factors [178].

The quantitative analysis of $TiO_2/SiO_2/Si$ heterostructure morphology demonstrated in Publication **III** is based on the attenuation of a photoelectron signal in a solid material according to the Beer–Lambert law. The analysis method is described in detail in the supporting information of Publication **III**. Figure 10 shows the fundamentals of the electron spectroscopy technique and the Beer–Lambert law determining the measured XPS intensities of Ti 2p, Si^{4+} 2p and Si^0 2p signals from $TiO_2/SiO_2/Si$ heterostructure. The photoemission spectroscopy constant S includes

several factors, such as, the cross-section at a certain photon energy and the number of atoms per unit volume that affect the photoelectron intensity [179]. An inelastic mean free path (IMFP) is a key concept explaining the surface sensitivity of electron spectroscopic techniques. Whereas X-rays can penetrate around 1 µm into a material, electrons can only escape the material from a depth approximately around 10 nm. This leads to fundamental reason why XPS, especially when using a soft X-ray source (Al Kα), can probe only the uppermost surface layers. Furthermore, the characteristic photoemission peaks that are particularly of interest in XPS, originate from photoelectrons undergone no energy losses after absorbing a photon. The IMFP value λ describes the average distance for photoelectrons with a certain kinetic energy to traverse through a certain material without any losses in their kinetic energy. According to the Beer–Lambert law, the IMFP value corresponds to the thickness t where 37% of photoelectrons with no energy losses, i.e., information, originate from. Analogously, three times λ is the depth where 95% of the information comes from, and thus commonly known as the sampling depth. [175]

$$I_{Si} = S_{Si}^{Si\ 2p}\lambda_{Si}^{Si\ 2p}[\exp(-t_{SiO2}\ /\ \lambda_{SiO2}^{Si\ 2p})][\exp(-t_{TiO2}\ /\ \lambda_{TiO2}^{Si\ 2p})]$$

$$I_{SiO2} = S_{SiO2}^{Si\ 2p}\lambda_{SiO2}^{Si\ 2p}[1 - \exp(-t_{SiO2}\ /\ \lambda_{SiO2}^{Si\ 2p})][\exp(-t_{TiO2}\ /\ \lambda_{TiO2}^{Si\ 2p})]$$

$$I_{TiO2} = S_{TiO2}^{Ti\ 2p}\lambda_{TiO2}^{Ti\ 2p}[1 - \exp(-t_{TiO2}\ /\ \lambda_{TiO2}^{Ti\ 2p})]$$

SURFACE SENSITIVE INFORMATION

1–4 nm | Inelastic mean free path λ (IMFP): 37% of photoelectrons with no energy loss

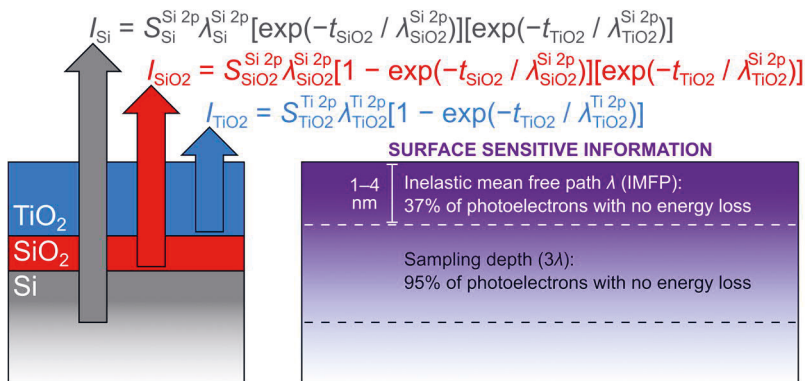Sampling depth (3λ): 95% of photoelectrons with no energy loss

Figure 10. Photoelectron intensities originating from a TiO₂ thin-film overlayer (I_{TiO2}), an interfacial SiO₂ (I_{SiO2}), and a Si substrate (I_{Si}) and attenuated based on the Beer–Lambert law. The equations were derived based on the ref. [179]. The concept of the inelastic mean free path related to surface sensitivity of electron spectroscopy is depicted based on the ref. [175].

In-depth analysis of XPS intensities enables understanding of sample morphology, for instance, a thickness of an interfacial SiO₂ between the Si substrate and the TiO₂ thin-film overlayer [175,179]. With a thin TiO₂ overlayer (<4 nm) the interfacial SiO₂ and the Si substrate can still be probed by XPS. Using the XPS peak intensities I_{SiO2} and I_{Si}, the thickness t_{SiO2} of the interfacial SiO₂ can be derived from the ratio I_{SiO2}/I_{Si} as follows

$$t_{SiO2} = \lambda_{SiO2}^{Si\ 2p} \ln\left[1 + \frac{I_{SiO2}}{I_{Si}} \frac{N_{Si}\lambda_{Si}^{Si\ 2p}}{N_{SiO2}\lambda_{SiO2}^{Si4+\ 2p}} \right], \qquad (8)$$

where the IMFP values of $\lambda_{Si} = 3.09$ nm and $\lambda_{SiO2} = 3.75$ nm, can be calculated by TPP-2M formula [180] and the number of Si atoms per unit volume values $N_{Si} = 49.737$ atoms/nm^3 and $N_{SiO2} = 26.557$ atoms/nm^3 can be derived by basic chemistry equations using literature values for density and a molar mass of a compound. Besides these calculations, there are also other XPS-based morphology analysis methods, for instance, angle-resolved XPS (ARXPS) or comparing experimental results with spectra modelled by a simulation software such as SESSA (Simulation of Electron Spectra for Surface Analysis) [175,181].

3.4   Photoelectrochemical performance measurements

Publications **III** and **IV** consider more closely the stability and the onset potential of TiO_2/Si photoanodes under PEC conditions. The PEC performance of TiO_2/Si photoanode samples were studied in a homemade PEC cell (Figure 11) using three-electrode configuration with an Ag/AgCl reference electrode, Pt counter electrode and TiO_2/Si sample as the working electrode in an aqueous 1 M NaOH electrolyte solution (pH 13.6). The measurement was controlled by Autolab PGSTAT12 potentiostat (Metrohm AG). Simulated solar spectrum was produced with a HAL-C100 solar simulator (Asahi Spectra Co., Ltd., JIS Class A at 400–1100 nm with AM1.5G filter) and the intensity was adjusted to 1.00 Sun using a 1 sun checker (model CS-30, Asahi Spectra Co., Ltd.). The detailed sample preparation and measurement procedure is described in the supporting information of Publication **IV**.
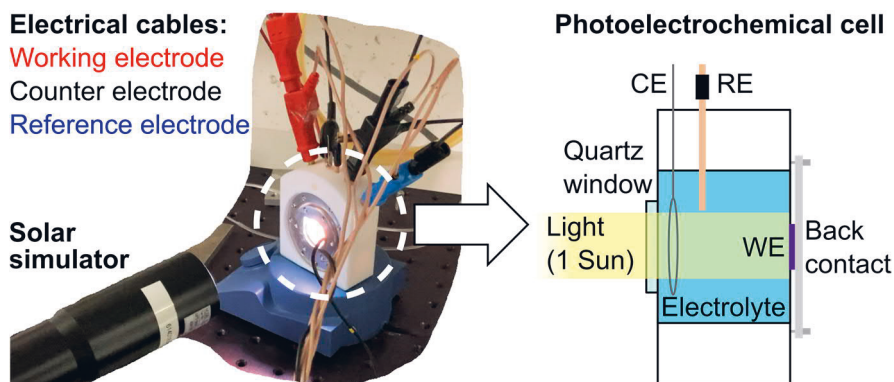
Figure 11. The PEC measurement setup consisting of a solar simulator and a homemade PEC cell using three-electrode configuration with a reference electrode (RE), counter electrode (CE), and a working electrode (WE) connected to a potentiostat with electrical cables.

The stability of photoanodes can be studied by constant potential amperometry at the water oxidation potential of 1.23 V in respect of reversible hydrogen electrode (RHE). As clearly demonstrated in the work by Hannula et al. unstable behaviour of the photocurrent indicates degradation of the protective TiO_2 photoelectrode coating whereas a stable photocurrent implies good protective behaviour under PEC conditions [42]. In this work, the chemical stability of the ALD TiO_2 photoelectrode coatings on silicon were studied during 1 h chopped light test and during continuous 10/24 h illumination test in the PEC cell with bias of 1.23 V *vs*. RHE. The linear sweep voltammetry, i.e., current–voltage (*I–V*) characteristics was utilized to study a photocurrent generated under 1 Sun illumination during a potential sweep providing essential information on photocurrent onset potentials and kinetics. According to the subchapter 2.2, the target in the PEC performance measurements for TiO_2/Si photoanodes was to obtain a low and steep photocurrent onset potential and protection against corrosion, i.e., a long-term stability of the photocurrent and no visible degradation of the film.

4 INSIGHTS INTO CRYSTALLIZATION AND CHARGE TRANSFER PROPERTIES OF PROTECTIVE ALD TiO$_2$ COATINGS ON Si PHOTOELECTRODES

This chapter focuses on describing the key findings of the Thesis research and reflects the importance of the results in the context of the ALD, XPS, TiO$_2$ and PEC research fields. Albeit electronically "leaky" ALD TiO$_2$ thin films as protective photoelectrode coatings have been studied, all-encompassing understanding of the Ti^{3+}-rich am.-TiO$_2$ structure and its controllability has remained unclear. Furthermore, crystalline TiO$_2$ thin films can be used in PEC cells as well, but the stability and the performance of the coating are sensitive to grain boundaries, phase, and the crystallization temperature. All these aspects related to amorphous and crystalline TiO$_2$ are crucial to understand and to consider comprehensively when designing an optimized PEC photoelectrode with the protective ALD TiO$_2$ coating.

The first part of the chapter addresses the question about formation of oxide defects, i.e., oxygen vacancies, interstitial peroxo species, and Ti^{3+} / Ti$_{5/7c}$ ions, and their effect on the curious and tunable charge carrier properties of ALD-grown am.-TiO$_2$ thin films. The second part considers how the ALD growth temperature-mediated oxide defects and TDMAT precursor traces affect crystallization of am.-TiO$_2$ thin films. The third part covers the effects of Si wafer cleaning methods and post deposition annealing on an interfacial SiO$_2$ layer thickness. The fourth part studies the amorphous and crystalline ALD TiO$_2$ thin films as Si photoelectrode coatings in terms of stability and the photocurrent onset potential.

In addition to the results discussed in the original publications, the subchapters 4.3 and 4.4 present previously unpublished research related to the interfacial SiO$_2$ thickness after 500 min PDA at 250 °C (in Figure 16b) and to long-term stability and the photocurrent onset potential of post deposition-annealed ALD TiO$_2$ grown at 200 °C (Figure 19). This data supports the work as supplementary results and offers some prospects to continue the research.

4.1 Effect of ALD growth temperature on oxide defects and charge transfer properties of amorphous TiO$_2$ thin films

As discussed in the subchapters 3.1.1 and 3.3, exceptional charge carrier transport and visible-light absorption properties of amorphous TiO$_2$ have been commonly attributed to oxide defects, i.e., oxygen vacancies, interstitial peroxo species, and Ti^{3+} / Ti$_{5/7c}$ ions within am.-TiO$_2$ structure. Especially, these exceptional properties and intrinsic Ti^{3+} defects are associated with the am.-TiO$_2$ grown by ALD using TDMAT and H$_2$O as precursors. The oxide defects have been studied computationally and experimentally, for instance, by XPS. [32,34,40,49,84,121,122]

In many cases, the Ti^{3+}-mediated conductivity has been reported and studied only with am.-TiO$_2$ thin films grown at 150 °C [40,49,84,91]. However, Publication **I** examines how the ALD growth temperature between 100–200 °C affects the concentration of Ti^{3+} defects and charge carrier dynamics of 30 nm-thick the am.-TiO$_2$ thin film when using the TDMAT+H$_2$O ALD process. Figure 12 shows the most prominent XPS results evidencing the presence of the Ti^{3+} ions, i.e., the oxide defects and how the concentration of the defects can be controlled by changing the ALD growth temperature. In Figure 12a, according to general consensus, the low-BE shoulder peak at 457.3±0.1 eV corresponds to Ti^{3+} ions which clearly appear in all am.-TiO$_2$ thin films [42,182,183]. The main Ti^{4+} peak was fitted by using Ti 2p$_{3/2}$ reference peak shape measured for crystalline TiO$_2$, i.e., the six-coordinated Ti^{4+} peak (Ti$_{6c}$$^{4+}$). This narrow Ti 2p$_{3/2}$ peak at 459.0±0.1 eV was fitted to the am.-TiO$_2$ spectra by keeping a constrained shape and position. This allowed us to fit another component next to the Ti$_{6c}$$^{4+}$ peak with a BE separation of -0.39 eV. According to the computational DFT calculations carried out in Publication **I** and discussed in the subchapter 3.3, presence of oxygen vacancies and interstitial peroxo species can induce such a core-level shift in Ti 2p XPS spectrum (Ti$_{5/6/7c}$$^{4+}$) which also matches well with distinct presence of Ti^{3+} ions within am.-TiO$_2$ thin films.
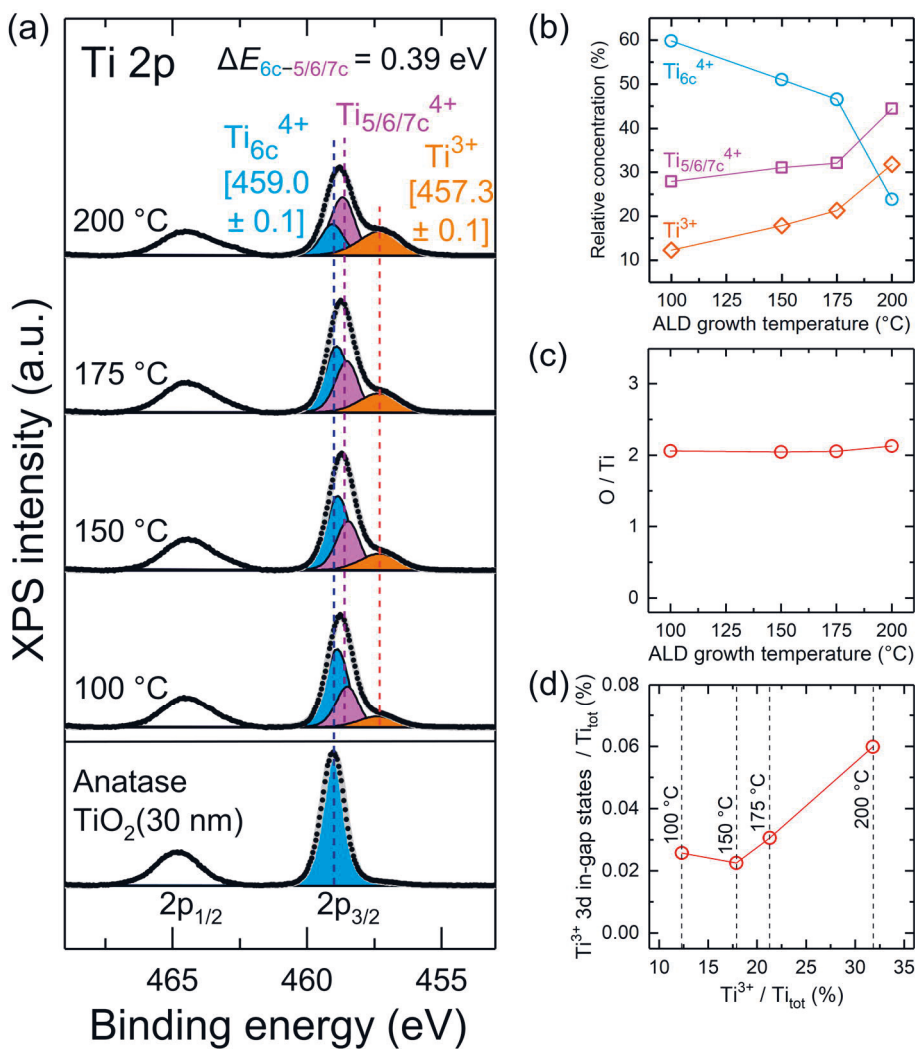
Figure 12. (a) The Ti 2p XP spectra, (b) the relative concentrations of the components, (c) the O/Ti ratio, and (d) the relative concentration of Ti^{3+} 3d in-gap states as a function of Ti^{3+} concentration for the am.-TiO_2 thin films (30 nm) deposited at 100 °C, 150 °C, 175 °C and 200 °C. Crystalline anatase TiO_2(30 nm) serves as a reference peak shape for the six-coordinated Ti_{6c}^{4+} ions in Ti 2p XPS analysis. The figure was composed based on Publication **I** (complying with the Creative Commons CC BY license).

As clearly seen in Figure 12a and Figure 12b, there is an increasing trend in concentrations of Ti^{3+} and $Ti_{5/6/7c}^{4+}$ ions together with the increasing growth temperature between 100–200 °C, and simultaneously as the Ti_{6c}^{4+} peak decreases. However, despite the distinct presence of oxygen vacancies-induced Ti^{3+} ions, am.-TiO_2 thin films seem to exhibit stoichiometric composition (O/Ti = 2) as presented

in Figure 12c. This implies and can be explained by displacement of oxygen ions instead of removal of them upon O vacancy and Ti^{3+} defect formation. Indeed, as shown in Figure 9, introducing the interstitial peroxo species (O_2^{2-}) together with the oxygen vacancy leads to the larger core-level shift (-0.37 eV) of the second Ti^{4+} peak ($Ti_{5/6/7c}^{4+}$) which corresponds exceedingly well with the experimental results. Thus, the results support that the Ti^{3+}-rich structure of ALD-grown am.-TiO_2 (TDMAT+H_2O) originates from simultaneous formation of oxygen vacancies and interstitial peroxo species leading to defective but stoichiometric am.-TiO_2.

However, the fundamental reason for the formation of these oxide defects remained an unresolved question and is beyond this Thesis. In Publication **I**, in addition to oxide defects, distinct ALD growth temperature-induced differences in nitrogen (TDMAT precursor traces) concentrations were also observed. The concentration of TDMAT precursor traces was higher within am.-TiO_2 grown at 100 °C and decreased towards higher ALD growth temperatures (200 °C). According to literature, substitutional nitrogen induces oxygen vacancies and thus the TDMAT precursor traces could relate to the observed oxide defects [29]. However, quite contradictory the concentration of nitrogen species decreased when the density of oxide defects increased, and moreover, no substitutional nitrogen was detected within as-deposited am.-TiO_2. In addition to the TDMAT precursor traces, the oxide defects could also be caused by the decomposition of the TDMAT precursor or by the proposed intermediate product desorption during the ALD process at higher growth temperatures [105].

Previously, Hannula et al. showed that upon UHV annealing am.-TiO_2 grown 200 °C reduces into $Ti^{3+}O^-O^{2-}$ / $Ti^{2+}O_2^-$ suboxides through electron transfer from oxygen to titanium ions without releasing any oxygen [42]. The O^- peak at 531.3 eV in the O 1s spectrum was not detected in as-grown am.-TiO_2 thin film in the work by Hannula et al. or in this Thesis. In Publication **I** the computational DFT calculation revealed a positive CLS of 1.87 eV in the O 1s spectrum induced by interstitial peroxo species. This is rather concordant with the dumbbell di-oxygen surface species proposed to account for a shoulder peak in the O 1s spectrum at 532.5 eV observed in experimental ARXPS measurements [49,184]. In Publication **I**, Ti^{3+}-rich am.-TiO_2 grown at 200 °C exhibited slightly more distinct peak around 532 eV that may attribute to the interstitial peroxo species, but it was not possible to differentiate them indisputably from the experimental data.

Interestingly, several studies have reported that there is no clear Ti^{3+} shoulder peak in the Ti 2p XPS spectrum of am.-TiO_2 grown by TDMAT+H_2O process at 150 °C even though the same articles show distinct evidence of Ti^{3+} defects by XPS

VB spectra and by electron paramagnetic resonance (EPR) spectroscopy [49,50,84]. However, based on our work, in addition to the clear Ti^{3+} peaks in the Ti 2p XP spectra (Figure 12a), the Ti^{3+} 3d peaks were observed in the XPS VB spectra and the intensity of the Ti^{3+} 3d peak increases linearly with the Ti^{3+} concentration between growth temperatures of 150 °C and 200 °C as shown in Figure 12d. A deviation at 100 °C may relate to TDMAT precursor traces.

Regarding charge transfer properties, Figure 13a shows the relation between visible-light absorbance and the concentration of Ti^{3+} defects for the am.-TiO_2 thin films grown at 100 °C, 150 °C, 175 °C, and 200 °C. The low Ti^{3+} concentration ($Ti^{3+}/Ti_{tot} = 12\%$) at 100 °C leads to only minor visible-light absorption but subsequently the absorption increases steadily with the Ti^{3+} concentration resulting in black am.-TiO_2 at 200 °C. As emphasized in Figure 13b, this enhanced visible-light absorption is attributed to a higher density of electrons occupying Ti^{3+} 3d in-gap states corresponding with the results in Figure 12d.
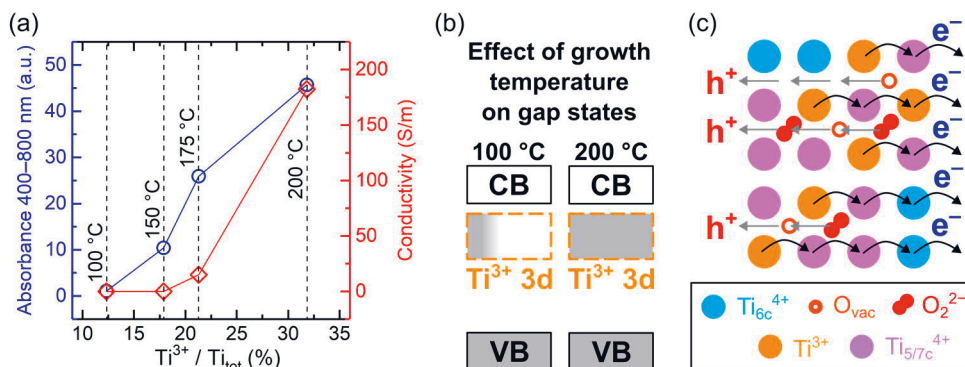

Figure 13. (a) Integrated absorbance in the visible range and electrical conductivity as a function of Ti^{3+} concentration for the am.-TiO_2 thin films (30 nm) deposited at 100 °C, 150 °C, 175 °C, and 200 °C. Schematic illustrations in (b) and (c) to depict the physical phenomena behind visible-light absorption and electrical conductivity of Ti^{3+}-rich TiO_2 thin film. (b) A high density of electrons occupying Ti^{3+} 3d gap states enables visible-light absorption of am.-TiO_2 grown at 200 °C. (c) According to the polaron hopping mechanism, electrons (e^-) can hop from Ti^{3+} sites to adjacent Ti^{4+} sites, and analogously hole (h^+) conduction can be attributed to oxygen vacancies or O–O peroxy linkages. The figures were composed based on Publication **I** (complying with the Creative Commons CC BY license).

The electrical conductivity was determined by measuring a sheet resistance of am.-TiO_2 thin film by using a four-point probe method. The measurement procedure is described in detail in Publication **I**. In contrast to visible-light absorption, an onset of the electrical conductivity takes places at a higher Ti^{3+}/Ti_{tot} concentration (around

20%) in am.-TiO$_2$ thin films grown at 150–175 °C (Figure 13a). Subsequently, the electrical conductivity increases steeply and am.-TiO$_2$ thin film grown at 200 °C exhibits a clearly enhanced conductivity of 180 S/m. Figure 13c illustrates the polaron hopping mechanism, where electrons can hop from Ti^{3+} sites to adjacent Ti^{4+} sites and thus across the am.-TiO$_2$ thin film. Furthermore, analogously, hole conduction may occur via oxygen vacancies or O–O peroxy linkages [32,44,83,136,141,142]. A computational study by Deskins et al. proposes that the hole conduction is strongly related to Ti^{3+}–O–Ti^{3+} linkage probability and Ti^{3+}/Ti^{3+} distances. Comparing the models by Deskins et al. to our experimentally determined Ti^{3+} concentrations (Figure 12b), am.-TiO$_2$ deposited at 200 °C may exhibit the average Ti^{3+}/Ti^{3+} distance around 3 Å which is the minimum for am.-TiO$_2$, and thus accounting for the increased conductivity. [32] Although, the Ti^{3+} defects or oxygen vacancies-induced hole conduction through the am.-TiO$_2$ photoanode protection layer has been studied and reported, an all-encompassing understanding of the relation between Ti^{3+} defects and conductivity has remained unsolved [19,40,49,50,68]. To address this need, Publication **I** evidences the indisputable presence of oxide defects (Ti^{3+} / Ti$_{5/7c}$ ions) in the XP spectra and new atomic-level insights into the formation of the intrinsic oxide defects. Additionally, Publication **I** demonstrates how the electrical conductivity depends on these oxide defects and can be tuned via the ALD growth temperature when using the TDMAT+H$_2$O ALD process at 100–200 °C. This enables more detailed development and optimization of am.-TiO$_2$ coatings for electrocatalyst/am.-TiO$_2$/photoanode structures in future.

4.2   Crystallization kinetics of amorphous TiO$_2$ thin films

As seen in the previous subchapter and in Publication **I**, the composition of am.-TiO$_2$ thin film is highly sensitive to the ALD growth temperature when using the TDMAT and H$_2$O as precursor at 100–200 °C. At these temperatures, though, the process results in amorphous TiO$_2$ thin films [117,153]. Concerning am.-TiO$_2$ as photoelectrode protection layer, there are still doubts about sufficient stability of am.-TiO$_2$ thin films under PEC conditions [42,45,46]. Therefore, crystallization of am.-TiO$_2$ thin films via post deposition annealing may be imperative to achieve desired chemical stability. Crystalline TiO$_2$ can be deposited directly by increasing the growth temperature around 250–300 °C but the thermal decomposition of

TDMAT may complicate the self-limiting ALD process, and hence not studied in the scope of this Thesis [105,117,153,156–158].

Publication **II** examines roles of intrinsic oxide defects (Ti^{3+} ions / O vacancies) and TDMAT precursor traces on the crystallization of ALD grown am.-TiO_2 thin films upon PDA in air. Figure 14 presents SEM images related to the crystallization of 30 nm-thick am.-TiO_2 thin films grown at 100 °C and 200 °C. There is an evident difference in crystallization kinetics of the thin films that can be clearly controlled by the ALD growth temperature. Within the am.-TiO_2 thin film grown at 100 °C, crystal nucleation takes place upon PDA in air at 375 °C and large round grains with diameter over 10 µm start to appear. Based on grazing incidence X-ray diffraction (GIXRD) measurements the grains are anatase [Publication **II**]. A higher PDA temperature of 500 °C leads to full surface coverage with these exceptionally large anatase grains. In contrast to the 100 °C-grown am.-TiO_2, the am.-TiO_2 grown at 200 °C evidences crystal nucleation already at 250 °C when small <1 µm needle and round-like crystals start to form. The GIXRD pattern shows that the crystals are mainly rutile but also brookite peak can be detected indicating mixed-phase TiO_2 thin film with rutile as the primary phase [Publication **II**]. Upon PDA at 500 °C, these small crystals cover the whole surface resulting in higher rutile to brookite ratio. To the best of our knowledge, there are no reports demonstrating as clear and controllable crystallization of ALD TiO_2 into anatase and rutile-rich thin films just via ALD growth temperature-induced effects on the structure of the amorphous TiO_2 thin film. Particularly, the exceptionally low PDA temperature of 250 °C to obtain rutile crystals paves the way to further optimize the rutile TiO_2 thin film fabrication process which has been commonly limited to high temperatures (>400 °C, often even 600–800 °C) [29,115,126].
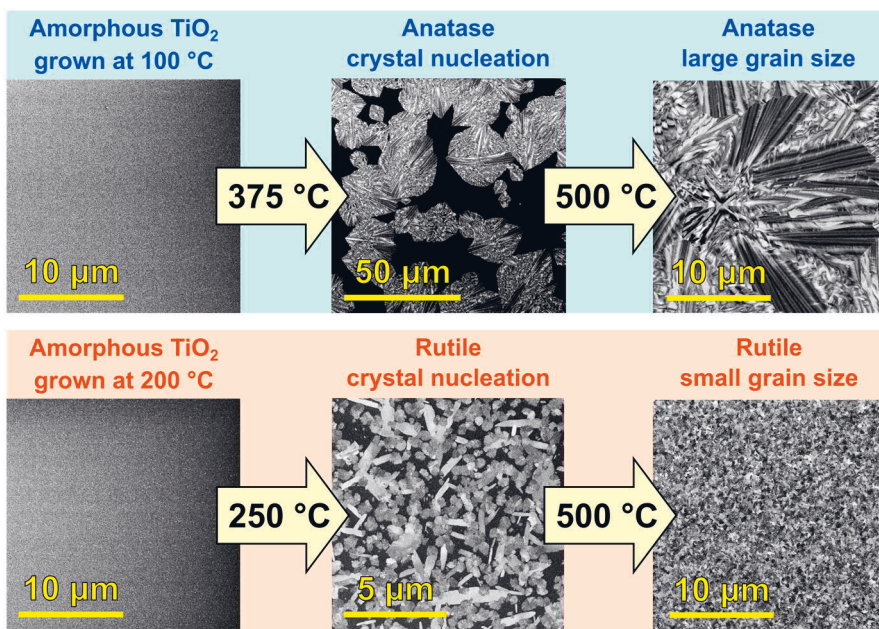
Figure 14. The summary and the SEM images related to crystallization of 30 nm-thick ALD am.-TiO$_2$ thin films grown at 100 °C and 200 °C. Crystal nucleation of 100 °C and 200 °C-grown thin films occur at 375 °C and 250 °C, respectively. The am.-TiO$_2$ thin film grown at 100 °C crystallizes into anatase whereas the am.-TiO$_2$ thin film grown at 200 °C prefers rutile-rich structure with some incorporation of brookite phase. The figure was composed based on Publication **II** (complying with the Creative Commons CC BY license).

Evidently, some characteristics of am.-TiO$_2$ thin films grown at 100 °C and 200 °C predetermine the resulting crystal structure upon the PDA. Based on the XPS measurements there are distinct differences in intrinsic oxide defects (Ti^{3+} ions / O vacancies) and TDMAT precursor traces incorporated within am.-TiO$_2$ thin films. Figure 15 presents the Ti 2p and N 1s XP spectra of as-deposited amorphous and crystallized (PDA 500 °C) ALD TiO$_2$ grown at 100 °C and 200 °C and how the oxide defects evolve upon crystallization. Figure 15a shows that despite the difference in the initial concentrations of oxide defects, i.e., Ti^{3+} and Ti$_{5/7c}^{4+}$ within am.-TiO$_2$ thin films grown at 100 °C and 200 °C, upon PDA at 500 °C the defects are completely removed and only six-coordinated Ti^{4+} ions (Ti$_{6c}^{4+}$) are present in crystalline TiO$_2$, corresponding with the theory [32,134]. Furthermore, according to Figure 15b and Figure 15c, the crystallization of the ALD-grown am.-TiO$_2$ thin films, indeed, occur simultaneously with disappearance of the oxide defects: at 250 °C and 375 °C for TiO$_2$ thin film grown at 200 °C and 100 °C, respectively (cf. Figure 14). The preference of am.-TiO$_2$ thin films grown at 200 °C to crystallize into

rutile could be attributed to the higher concentration of Ti^{3+} ions, i.e., oxygen vacancies, that have been reported as a strategy to promote easier rearrangement of ions to denser and more constrained rutile structure [29,89,130,131]. However, it was shown in Publication **II** that even though more Ti^{3+} defects were introduced in ALD am.-TiO_2 grown at 150 °C, the thin film still favoured the anatase formation similarly as without adding more Ti^{3+} defects [149]. Thus, the Ti^{3+} defects cannot be the only declarative factor steering the crystallization of 200 °C grown am.-TiO_2 towards rutile.
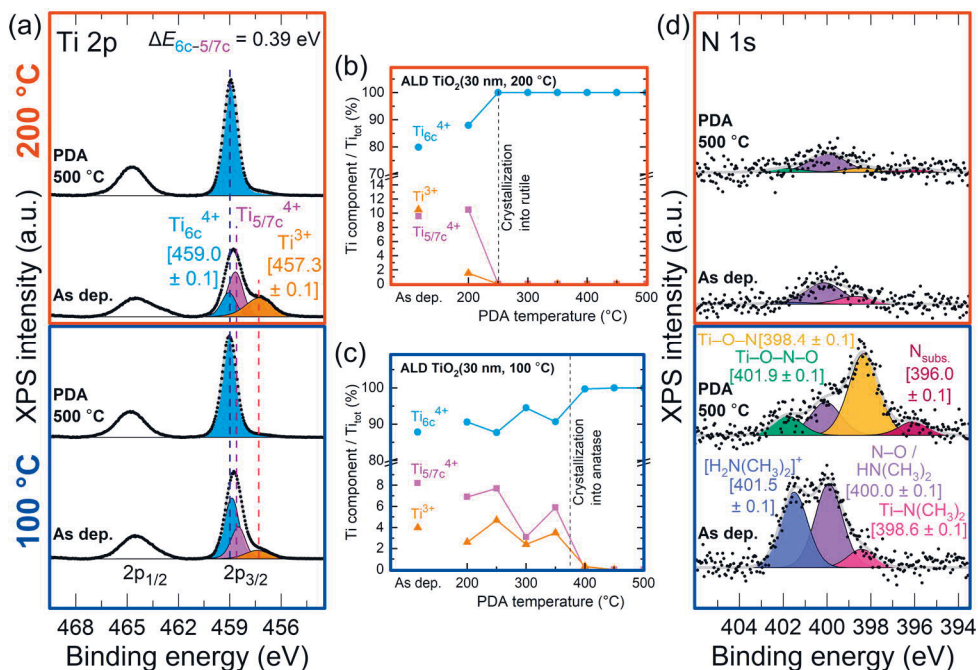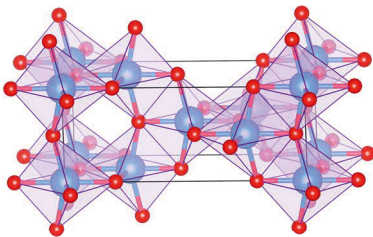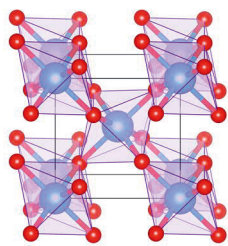

Figure 15. (a) The Ti 2p, and (d) N 1s XP spectra of 30 nm-thick as-deposited and crystallized ALD TiO_2 grown at 100 °C and 200 °C. The evolution of oxide defects upon PDA within ALD TiO_2 grown at (b) 200 °C, and (c) 100 °C. The figure was composed based on Publication **II** (complying with the Creative Commons CC BY license).

In addition to Ti 2p XP spectra, there are also distinct ALD growth temperature and PDA-induced differences in N 1s spectra (Figure 15d). Although, concentrations of TDMAT precursor traces are rather low (0.9 at.% at 100 °C and 0.2 at.% at 200 °C), remarkable differences upon PDA can be observed [Publications **I** and **II**]. Within as-deposited am.-TiO_2 grown at 100 °C, clear peaks assigned to unreacted Ti–$N(CH_3)_2$ bonds (at 398.6±0.1 eV), adsorbed dimethylamine $HN(CH_3)_2$ reaction byproducts (at 400.0±0.1 eV), and protonated dimethylamine $H_2N(CH_3)_2^+$ species

(at 401.5±0.1 eV) can be detected [106,173]. The concentration of TDMAT precursor traces decreases towards higher growth temperatures resulting in rather nitrogen-free thin film at 200 °C [Publication **I**]. As seen in Figure 15d, after the PDA at 500 °C, new peaks have appeared in the N 1s spectrum. Thus, in Publication **II**, it is proposed that the PDA and crystallization lead to decomposition and oxidation of the TDMAT precursor traces resulting in Ti–O–N (at 398.4±0.1 eV) and Ti–O–N–O (at 401.9±0.1 eV) species as well as substitutional nitrogen ($N_{subs.}$), i.e., Ti–N like species at 396.0±0.1 eV [157,172,185–187]. The higher nitrogen incorporation within the film and the somewhat delayed crystallization preferably into anatase (Figure 14) correspond well with literature although it has also been suggested that nitrogen doping can lead to oxygen vacancies facilitating rutile formation [29,172,188–190]. The preference for anatase phase stabilization has been proposed to be on account of a compressive stress induced by substitutional nitrogen ions preventing the crystallization into more dense rutile phase [189]. Furthermore, it has been shown that nitrogen within am.-TiO_2 thin films inhibits crystal nucleation and raise the nucleation temperature [172,190]. Indeed, am.-TiO_2 thin films grown at 150 °C, that contain less nitrogen than ones grown at 100 °C, crystallize into anatase already at 300 °C (cf. am.-TiO_2 grown at 100 °C in Figure 14) [149]. The inhibited crystallization may also account for the exceptionally large anatase grains of TiO_2 thin film grown at 100 °C. The grains are rather similar to the grains of Ti–Nb–O or Ti–Ta–O mixed oxide films reported by Pore et al. who explained the large crystals to be due to a phenomenon known as explosive crystallization [162,191–193].

Besides the chemical composition, mass densities of as-deposited and post deposition-annealed (500 °C) TiO_2 thin films were determined by X-ray reflectivity (XRR) measurements. Interestingly, am.-TiO_2 grown at 200 °C exhibits clearly higher mass density of 3.9 g/cm³ compared to 3.5 g/cm³ of am.-TiO_2 grown at 100 °C which were concordant with the values reported in literature [153]. Moreover, the mass densities did not change during the crystallization into rutile (3.9 g/cm³) and anatase (3.5 g/cm³), respectively. [Publication **II**] Indeed, by literature, rutile has higher mass density than anatase. [29] Because of the distinct difference in mass densities between am.-TiO_2 grown at 100 °C and 200 °C, it is proposed that the growth of denser am.-TiO_2 (at 200 °C) mediates direct crystallization into more dense rutile phase, while the growth of less dense am.-TiO_2 with precursor traces (at 100 °C) favors crystallization into anatase phase. Table 2 summarizes the ALD growth temperature-induced effects on the chemical composition and the structure of am.-TiO_2 thin films and how they affect the crystallization processes.

Table 2. The summary of growth and crystallization of am.-TiO$_2$ thin films grown by ALD using TDMAT and H$_2$O precursors at the growth temperatures of 100 °C and 200 °C. The table was composed based on Publication **II** (complying with the Creative Commons CC BY license).

		ALD growth temperature	
		100 °C	200 °C
As-deposited	**Precursor traces [a]**	+++	+
	Oxide defects [b]	+	+++
	Mass density	3.5 g/cm^3	3.9 g/cm^3
Post deposition annealing	**Crystal nucleation observed at [c]**	375 °C	250 °C
	Primary phase [d]	ANATASE	RUTILE (BROOKITE) [e]

a) Nitrogen species originated from dimethylamide ligands of TDMAT molecules. The plus signs represent the surface concentration determined by the XPS measurement.

b) Oxygen vacancies, interstitial peroxo species (O$_2^{2-}$), and Ti^{3+} / Ti$_{5/7c}^{4+}$ ions formed via displacement of oxygen ions within stoichiometric amorphous TiO$_2$ structure. The plus signs represent the surface concentration determined by the XPS measurement.

c) The results are based on the PDA time of 50 min.

d) The drawings of crystalline TiO$_2$ structures were produced by VESTA software [194] using rutile [195] and anatase [196] crystal structure models provided by The American Mineralogist Crystal Structure Database [197].

e) Rutile is the main phase. The proportion of brookite decreases at higher PDA temperatures.

4.3 Influence of pretreatment and post deposition annealing on interfacial SiO₂ and ALD TiO₂ thin films on Si substrates

An interfacial SiO_2 layer is essential to charge transport in ALD TiO_2/Si photoanode. The resistive SiO_2 layer can be detrimental to the PEC cell performance and therefore its thickness should be minimized [19,50]. The thickness of the interfacial SiO_2 layer should be no more than 2 nm but targeting to <1 nm could improve a photoanode performance even further [65]. Therefore, a substrate pretreatment prior to ALD growth may be desired to remove native oxide layer (<2 nm) or to form a thin oxide layer in a controlled and reproducible manner. However, some studies have preferred to use as-received native oxide Si substrates as well. [41,50,108,151,163,164] Furthermore, the growth of detrimental SiO_2 during post deposition annealing should be taken into account if crystallization of as-deposited am.-TiO_2 coating is needed [50].

In Publication **III**, three standard Si wafer cleaning methods (HF, HF+RCA SC-2, and native oxide) were studied in terms of initial ALD TiO_2 growth and formation of interfacial SiO_2 layer upon the deposition and PDA. Figure 16a presents the thicknesses of the ALD am.-TiO_2 thin films ($TDMAT+H_2O$ at 100 °C) and the interfacial SiO_2 layers calculated based on the XPS analysis described in the subchapter 3.3 and in the supporting information of Publication **III**. The ALD TiO_2 growth shows a clear linear trend, characteristic for the ALD technique. Moreover, the GPC around 0.06 nm/cycle corresponds well with the one determined by ellipsometer [Publication **III**]. As expected, HF treatment resulted in a hydrophobic H-terminated Si surface which hindered the growth during the first ALD cycles (1−10 cycles) after which the GPC stabilized to be the same as on RCA SC-2 -treated and native oxide substrates. Thus, instead of island growth the deposition on HF-treated Si followed the trend of substrate-inhibited layer-by-layer growth of amorphous thin film [108].
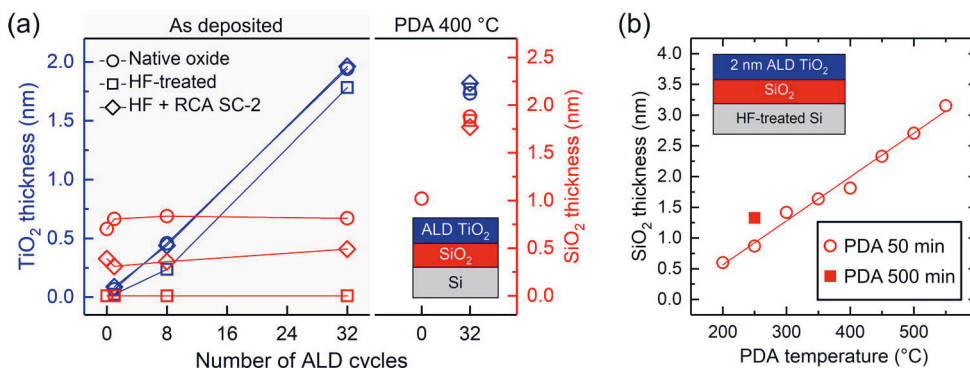
Figure 16. (a) The thickness of the ALD am.-TiO$_2$ thin film (grown at 100 °C) and the interfacial SiO$_2$ layer as a function of ALD TiO$_2$ cycles and after PDA in air at 400 °C (50 min) for different Si surface pretreatments. (b) The thickness of the interfacial SiO$_2$ layer under 2 nm-thick ALD am.-TiO$_2$ thin film (grown at 200 °C) as a function of the PDA temperature. The figures were composed based on Publication **III** (complying with the Creative Commons CC BY license).

The results in Figure 16a evidence that the studied Si pretreatments worked as expected by removing native SiO$_2$ (HF etch) and by forming a thin chemical Si oxide (RCA SC-2). Furthermore, the interfacial Si oxide did not grow during the ALD of TiO$_2$ (TDMAT+H$_2$O at 100 °C). However, upon PDA at 400 °C the SiO$_2$ layer thickness increased to 1.8±0.1 nm despite the initial thickness of the interfacial SiO$_2$ after the deposition. Thus, based on these results, if post deposition crystallization is needed, the PDA is more dominant factor than the Si pretreatment to control the SiO$_2$ layer thickness [Publication **III**].

Figure 16b presents the thickness of the interfacial SiO$_2$ layer under 2 nm-thick ALD am.-TiO$_2$ thin film (grown at 200 °C) as a function of the PDA temperature (200−550 °C). Prior to ALD, Si substrates were HF-treated to remove the native oxide surface. Interestingly, upon 50 min PDA the thickness of the interfacial SiO$_2$ grows rather linearly with the PDA temperature from 0.6 nm (PDA 200 °C) to 3.2 nm (PDA 550 °C). Furthermore, Publication **II** showed that extending the PDA time at 250 °C from 50 min to 500 min leads to complete surface crystallization of am.-TiO$_2$ thin film into rutile–brookite mixed-phase with rutile as the primary polymorph [Publication **II**]. Therefore, the interfacial SiO$_2$ thickness after 500 min PDA at 250 °C was also determined. The thickness of SiO$_2$ after longer PDA treatment was 1.3 nm which was slightly thicker than resulted upon 50 min PDA at 250 °C (0.9 nm) and almost the same as after 50 min PDA at 300 °C (1.4 nm). Thus, the SiO$_2$ thickness depends on the PDA duration as well. When reflecting the results with target SiO$_2$ thicknesses by Scheuermann et al., a limit for less than 2 nm-thick

SiO$_2$ is 50 min PDA at 400 °C and the SiO$_2$ thickness of <1 nm may be achievable at PDA temperatures ≤250 °C [65].

Beside the thicknesses of ALD TiO$_2$ and interfacial SiO$_2$ layers determined in Publication **III**, the effect of Si pretreatment (HF, HF+RCA SC-2, and native oxide) on crystallization of a 30 nm-thick ALD TiO$_2$ thin film (grown at 100 °C) was studied by GIXRD and electron backscatter diffraction (EBSD) measurements. However, despite the different substrate pretreatment, all the TiO$_2$ thin films crystallized into anatase with rather similar crystal morphology [Publication **III**].

4.4 Photoelectrochemical performance of ALD TiO$_2$ coatings on Si photoanodes

All these aspects discussed in the previous subchapters are relevant when improving the photoelectrochemical performance of protective ALD TiO$_2$ coatings for silicon photoelectrodes. According to literature, both amorphous and crystalline TiO$_2$ can serve as a protection layer. However, several factors, such as a phase, conductivity, a grain size, an interfacial oxide layer, use of an electrocatalyst, can play the role in performance of the protective ALD TiO$_2$ coating. [13,40–44,48–50,54] In this subchapter, the results related to stability and the generated photocurrent are linked to the studied properties of ALD TiO$_2$ thin films grown by using the TDMAT+H$_2$O process at 100–200 °C. It should be noted that this work focuses on the properties of ALD TiO$_2$ thin films, and thus electrocatalysts have not been used [Publications **III** and **IV**]. An electrocatalyst may affect the PEC stability of a photoelectrode but studying electrocatalyst materials is beyond the scope of this Thesis.

From the PEC performance point of view, Publication **III** focuses on ALD TiO$_2$(30 nm, 100 °C) photoelectrode coatings. Despite the Si pretreatment (HF, HF+RCA SC-2, and native oxide) prior to ALD of TiO$_2$, the as-deposited am.-TiO$_2$ coatings generated unstable photocurrent during a chopped light constant potential amperometry measurement (1 h) [Publication **III**]. This unstable behaviour of photocurrent has been previously attributed to dissolution of am.-TiO$_2$ thin film [42]. Indeed, as shown in the inset of Figure 17a, the as-deposited am.-TiO$_2$ coating has dissolved completely from the circular area (gray) exposed to the electrolyte during the 10 h stability test. Contrarily, after PDA at 400 °C crystalline anatase TiO$_2$ coatings [Publication **II**] showed stable photocurrent for 10 h and the coatings looked visually intact (Figure 17a). Figure 17b presents the *I–V* characteristics of ALD TiO$_2$(30 nm, 100 °C)/n$^+$-Si photoanodes post deposition-annealed at different

temperatures (200–550 °C). Below the crystallization temperature of 375 °C [Publication **II**] the am.-TiO$_2$ coating is unstable. After crystallization upon PDA at 400 °C, the coating exhibits the highest photocurrent and the lowest onset potential. However, increasing the PDA temperature, the photocurrent decreases and the onset potential increases slightly up to 500 °C followed by a drastic deterioration at 550 °C. This can be attributed to the growth of interfacial SiO$_2$ layer, thickness of which, in fact, may exceed 3 nm upon PDA at 550 °C (cf. Figure 16b). Thus, the PDA at 400 °C is a reasonable choice for Si photoelectrodes with 30 nm-thick ALD TiO$_2$ grown at 100 °C.
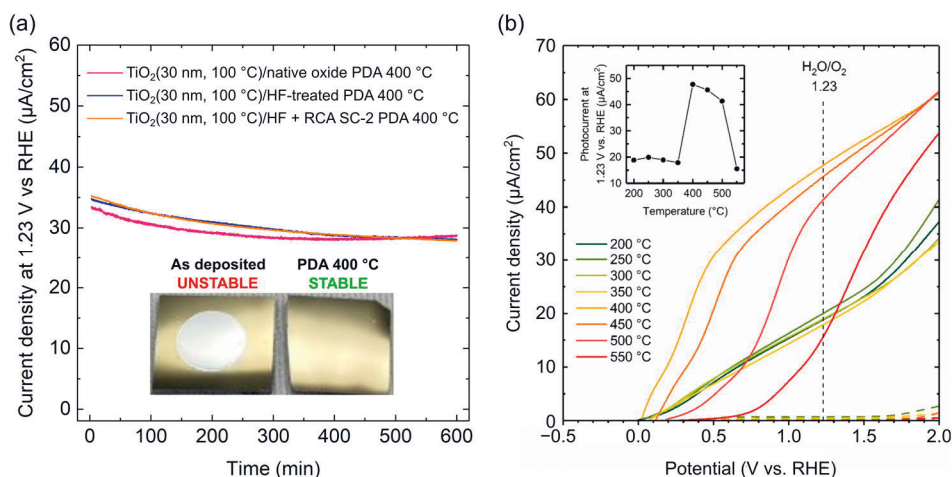

Figure 17. (a) A stability test with continuous 10 h illumination in the PEC cell for the ALD TiO$_2$(30 nm, 100 °C)/n$^+$-Si photoanodes post deposition-annealed at 400 °C. The test was performed in 1 M NaOH at bias of 1.23 V *vs.* RHE. Si wafers with three different pretreatments (HF, HF+RCA SC-2, and native oxide) were used as substrates. The inset shows photos of as-deposited (unstable) and PDA 400 °C (stable) samples after the PEC stability test. (b) The *I–V* characteristics in dark (dashed lines) and under 1 Sun illumination (solid lines) measured in 1 M NaOH by linear sweep voltammetry for ALD TiO$_2$(30 nm, 100 °C)/n$^+$-Si photoanodes post deposition-annealed at different temperatures. The inset highlights that the maximum photocurrent for H$_2$O oxidation was obtained with the PDA 400 °C sample. The figures were composed based on Publication **III** (complying with the Creative Commons CC BY license).

To decrease the thickness of an interfacial SiO$_2$ layer and to improve the photocurrent onset potential even further, the ALD am.-TiO$_2$ photoelectrode coating should be crystallized at a lower crystallization temperature. In fact, ALD am.-TiO$_2$ grown at 150 °C can be crystallized into anatase at the PDA temperature of 300 °C [149]. Figure 18 demonstrates the improvement achieved by using ALD

TiO$_2$(30 nm, 150 °C) post deposition-annealed at 300 °C compared to ALD TiO$_2$(30 nm, 100 °C) after PDA at 400 °C. Both are crystalline and exhibit stable behaviour in PEC cell. However, thanks to the lower PDA temperature (300 °C) for crystallization and a thinner interfacial SiO$_2$ layer, the 150 °C-grown TiO$_2$ enables an improved onset potential (−0.07 V) and a higher generated photocurrent. The higher PDA temperature of 400 °C results in the same higher onset potential for TiO$_2$ coatings grown at 100 °C and 150 °C. However, the photocurrent curve of TiO$_2$ grown at 100 °C has a small drop around 0.2 V and a lower photocurrent at 1.23 V which can be attributed to TDMAT precursor traces in the anatase structure [Publications **II** and **III**].
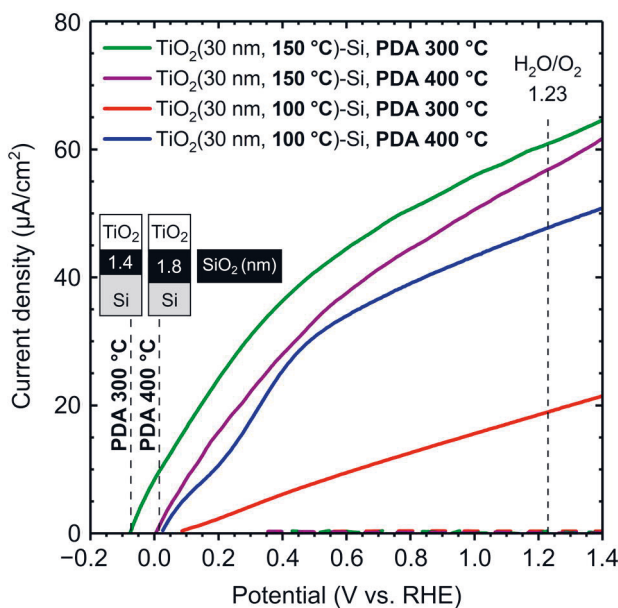
Figure 18. The *I–V* characteristics in dark (dashed lines) and under 1 Sun illumination (solid lines) measured in 1 M NaOH by linear sweep voltammetry for ALD TiO$_2$(30 nm, 100 °C)/n$^+$-Si photoanodes post deposition-annealed at 300 °C and 400 °C. The insets illustrate the SiO$_2$ layer morphologies after the PDA at 300 °C and 400 °C. The figure was composed based on Publication **III** (complying with the Creative Commons CC BY license).

Publication **IV** focuses on the PEC performance of ALD TiO$_2$(30 nm, 200 °C)/n-Si photoanodes in 1 M NaOH. As discussed in the subchapter 4.1, ALD TiO$_2$ grown at 200 °C can be crystallized into rutile already at the PDA temperature of 300 °C or even at 250 °C if an extended PDA time is used. The inset of Figure 19a summarizes the effect of PDA (50 min) on stability and a produced photocurrent during 1 h

chopped light test. The as-deposited 200 °C-grown am.-TiO_2 showed a low and unstable photocurrent leading to complete dissolution of the coating. A fully crystalline surface is obtained upon PDA at 300 °C which leads to good stability but a lower photocurrent than after the PDA at ≥400 °C. This can be explained by gradual crystallization of the thin film into rutile and the higher degree of crystallization [Publication **IV**]. Interestingly, overall, the produced photocurrent values (~100–300 µA) are higher compared to 30 nm-thick anatase TiO_2 films (~30–60 µA, cf. Figure 17 and Figure 18). This may relate to the reported higher photocatalytic activity of rutile toward oxidative reactions, the smaller band gap of rutile, or observed differences in grain size (Figure 14) [29,146,149,198].
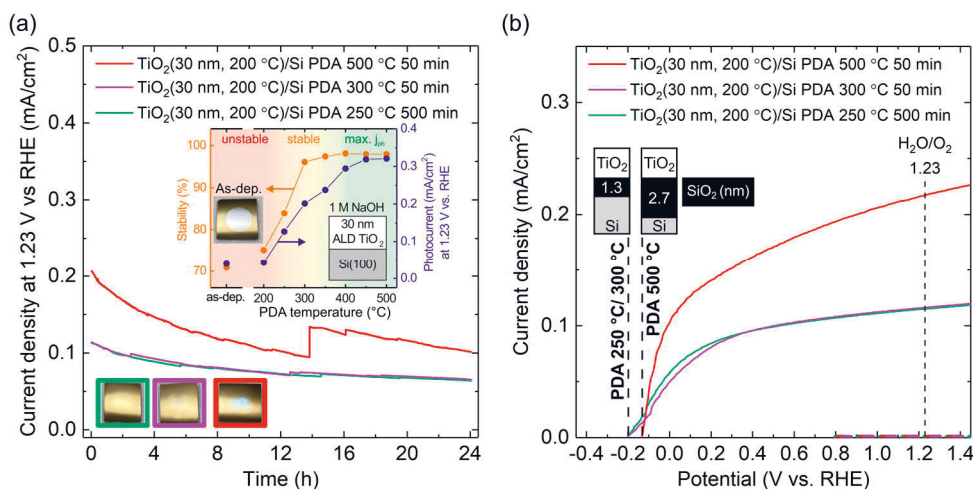

Figure 19. (a) A stability test with continuous 24 h illumination in the PEC cell for the ALD TiO_2(30 nm, 200 °C)/n-Si photoanodes post deposition-annealed for 50 min at 300 °C and 500 °C, and for 500 min at 250 °C. The photos of the crystallized samples after the test do not show clear degradation (cf. as-deposited am.-TiO_2). The test was performed in 1 M NaOH at bias of 1.23 V *vs.* RHE. The inset demonstrates the effect of PDA (50 min) on stability and a generated photocurrent during 1 h chopped light test. (b) The *I–V* characteristics of the same samples. The insets illustrate the SiO_2 layer morphologies after the PDA at 250 °C, 300 °C, and 500 °C. The figure as an inset in (a) was composed based on Publication **IV** (complying with the Creative Commons CC BY license).

Furthermore, stability test with continuous 24 h illumination was carried out for the ALD TiO_2(30 nm, 200 °C)/n-Si photoanodes post deposition-annealed for 50 min at 300 °C and 500 °C, and for 500 min at 250 °C (Figure 19a). As shown in Publication **II**, the PDA at 250 °C for 500 min results in complete surface crystallization of am.-TiO_2 thin film into rutile–brookite mixed-phase which, based

on Figure 19a, exhibits excellent stability under PEC conditions. PDA 250 °C (500 min) showed similar behaviour as the sample post deposition-annealed at 300 °C for 50 min: both produced rather stable photocurrent for 24 h and clear degradation of the coatings was not observed. The sample post deposition-annealed at 500 °C for 50 min, instead, exhibited initially a higher photocurrent which surprisingly started to decrease during the test. This decrease may be attributed to oxygen gas bubble formation on the photoanode surface. If the bubbles cannot leave the photoanode surface they will disturb the performance of the photoanode. Moreover, the abrupt increase in the photocurrent after 14 h test may be due to the gas bubble leaving the photoanode surface. Albeit, some visual changes were observed on the surface, the sample looked intact and did not show any clear evidence of degradation or instability. These differences seen by eye were not studied further in this work.

The I–V curves of the ALD TiO$_2$(30 nm, 200 °C)/n-Si photoanodes post deposition-annealed for 50 min at 300 °C and 500 °C, and for 500 min at 250 °C are presented in Figure 19b. As expected, based on the SiO$_2$ thickness analysis (Figure 16b), the photoanodes post deposition-annealed at lower temperatures (250 °C and 300 °C) exhibit lower onset potential (−0.20 V) but more slowly increasing photocurrent than the PDA 500 °C sample. Interestingly, in all cases, the rutile TiO$_2$ coatings exhibited a lower photocurrent onset potential than the anatase TiO$_2$ coatings. This may be due to the differences in photocatalytic activity and the band gap of anatase and rutile TiO$_2$ [146], but was not comprehensively investigated in the scope of this Thesis.

Hereby, regardless of the ALD growth temperature, to achieve chemical stability under alkaline PEC conditions, post deposition annealing for ALD am.-TiO$_2$ (TDMAT+H$_2$O) is imperative. In terms of the interfacial SiO$_2$ layer and the photocurrent onset potential, the lower PDA temperature was observed to be preferable. For instance, ALD am.-TiO$_2$ thin films grown at 150 °C and 200 °C can be crystallized upon PDA in air at relatively low temperature of 300 °C leading to chemically stable anatase and rutile-rich thin films, respectively. However, regarding the generated photocurrent, the ALD TiO$_2$(30 nm, 200 °C) thin film post deposition-annealed and crystallized at 500 °C into rutile exhibited the highest value.

Despite the extensive research conducted, some questions related to ALD TiO$_2$ coatings on Si photoanodes remained still unresolved. The stability of am.-TiO$_2$ as a protective photoelectrode coating may be highly reliant on electrocatalysts since literature supports both, good stability of electrocatalyst/am.-TiO$_2$/photoanode structures as well as instability of plain am.-TiO$_2$ coatings grown by using TDMAT+H$_2$O ALD process [24,40–42,45,46,54]. Furthermore, it was shown that

the grain size resulting upon a PDA depends remarkably on the ALD growth temperature [Publication **II**]. In literature, a larger grain size has been proposed to improve stability because of smaller number of grain boundaries compared to TiO_2 with smaller grains [48]. In contrast, nanocrystalline rutile TiO_2 has also been reported to exhibit good chemical stability and resistance to the dissolution at the grain boundaries [47]. Although the effect of grain size on the stability was not studied in detail in this Thesis, SEM results in Publication **III** may imply some pinhole formation or degradation of ALD TiO_2 grown at 100 °C during a long PEC stability test which is, in fact, concordant with literature. Instead, ALD TiO_2 (TDMAT+H_2O) coatings grown at 150 °C and 200 °C, and subsequently post-annealed have evidenced indisputable corrosion protection. [47,48]

5 CONCLUSIONS AND OUTLOOK

This Thesis concentrated on ALD-grown amorphous TiO_2 thin films at the atomic level and examined how oxide defect-mediated phenomena can be tuned by the ALD growth temperature. In addition to as-deposited TiO_2 thin films, large part of the work focused on post deposition annealing-induced crystallization of amorphous TiO_2 since ALD growth temperature was shown to determine the crystallization process, and consequently the performance in photocatalytic applications. The insights into charge transfer properties and crystallization kinetics of ALD TiO_2 were also discussed in context of the results. Besides the in-depth understanding of ALD-grown TiO_2 coatings and their performance as TiO_2/Si photoanodes, the Thesis aimed at introducing solar fuel production as a technology in general and its significance for sustainable future. Although, there has been a positive trend in use of solar power, there is a crucial need for solar energy storage technologies due to challenges caused by diurnal cycle and intermittency of sunlight. This Thesis focused on photoelectrochemical technology that aims at storing solar energy into solar fuels by splitting water molecules to hydrogen and oxygen or driving reaction of water and carbon dioxide to methanol, methane or other hydrocarbons and their derivatives.

The results show that oxide defects of am.-TiO_2, i.e., oxygen vacancies and Ti^{3+} defects, can be tuned via the ALD growth temperature when using the TDMAT and H_2O as precursors in the ALD process at 100–200 °C. These Ti^{3+} defects have been proposed to account for hole conduction through the am.-TiO_2 photoanode protection layer. In fact, this Thesis demonstrated that the high ALD growth temperature of 200 °C leads to Ti^{3+}-rich am.-TiO_2 exhibiting clearly higher electrical conductivity than am.-TiO_2 thin films grown at lower temperatures. Furthermore, computational and experimental atomic-level insights support simultaneous Ti^{3+} defects, oxygen vacancies, and peroxo species formation via displacement of oxygen ions without releasing oxygen, leading to stoichiometric but disordered amorphous TiO_2 structure. This in-depth understanding enables more detailed development and optimization of am.-TiO_2 coatings for electrocatalyst/am.-TiO_2/photoanode structures.

The ALD growth temperature was also shown to affect crystallization of as-deposited am.-TiO$_2$ upon post deposition annealing in air. Am.-TiO$_2$ grown at 100 °C incorporates TDMAT precursor traces and exhibits low mass density which was deduced to inhibit crystal nucleation up to 375 °C and to steer crystallization towards anatase phase. Increasing the growth temperature to 150 C resulted in decreased concentration of the TDMAT traces and crystallization into anatase at lower temperature of 300 C. Ti^{3+}-rich am.-TiO$_2$ grown at 200 °C, instead, is almost free of precursor traces and has distinctly higher mass density promoting direct amorphous to rutile crystallization at an exceptionally low PDA temperature of 250 °C. The mixed-phase rutile–brookite with rutile as a primary polymorph forms at lower temperatures and the proportion of rutile increases at higher PDA temperatures.

An interfacial resistive SiO$_2$ layer can be detrimental to charge transport in ALD TiO$_2$/Si-based photoelectrode, and consequently, the PEC cell performance. Based on the morphology analysis of TiO$_2$/SiO$_2$/Si heterostructures, it was concluded that if the post deposition crystallization is needed, the PDA temperature is more dominant factor than the Si pretreatment to control the SiO$_2$ layer thickness. Less than 2 nm-thick SiO$_2$ can be obtained at 400 °C and the SiO$_2$ thickness of <1 nm may be achievable at PDA temperatures ≤250 °C. Therefore, the crystallization kinetics plays an important role in lowering the needed PDA temperature, decreasing the thickness of the interfacial SiO$_2$ layer, and enhancing the PEC performance of ALD TiO$_2$/Si-based photoelectrode.

The PEC stability and photocurrent onset potential results revealed that regardless of the ALD growth temperature, amorphous TiO$_2$ thin films dissolve under alkaline PEC conditions and PDA-induced crystallization is imperative achieving desired chemical stability. Regarding the anatase TiO$_2$ photoelectrode coatings, it is better to choose the growth temperature of 150 °C instead of 100 °C since this enables crystallization into anatase at 300 °C leading to the lower onset potential and higher photocurrent. Am.-TiO$_2$ grown at 200 °C can provide good protective performance already after low-temperature PDA at 250 °C for 500 min resulting in complete surface crystallization into rutile–brookite mixed-phase thin film. However, due to observed gradual crystallization of the thin film into rutile and the higher degree of crystallization, the higher PDA temperature (≥400 °C) leads to an enhanced photocurrent. Although the interfacial SiO$_2$ is thicker after the PDA at ≥400 °C, the higher degree of TiO$_2$ crystallization improves the photocatalytic activity towards the oxygen evolution reaction.

The insights into crystallization of the am.-TiO$_2$ thin films upon PDA, may pave the way to fabrication of new TiO$_2$ structures combining different TiO$_2$ phases:

amorphous, anatase, rutile, and brookite. For instance, fabrication of anatase–rutile phase junction structures by using two different growth temperatures to deposit am.-TiO$_2$ bilayer structure would be interesting approach to develop more efficient TiO$_2$-based photocatalysts. Furthermore, controlling the phases via the ALD growth temperature and the PDA treatment can also enable N-doped rutile, Ti^{3+}-doped anatase, and spatially controlled TiO$_2$ phase patterning at least to some extent.

The results regarding visible-light absorption of am.-TiO$_2$ and fabrication of crystalline rutile TiO$_2$ at exceptionally low temperatures may also be beneficial in wide range of applications related to photocatalysis, optics, and dielectric materials. However, the fundamental mechanism behind the formation of oxide defects within am.-TiO$_2$ remained unresolved. In light of the Thesis, investigating this mechanism, for instance, by in situ and operando XPS methods would be an attractive experiment in future.

From the solar fuel reactor application perspective, one of the most important directions to proceed with the research would be adding an electrocatalyst on protective ALD TiO$_2$ photoelectrode coating and to study long-term stability of protective TiO$_2$ coatings in solar fuel reactors approaching industrially relevant durability of 10 years. Albeit in this work am.-TiO$_2$ was shown to be unstable in alkaline electrolyte, it would be interesting to see if an electrocatalyst affects the chemical stability since it can steer the holes and the electrons to be consumed for OER and HER instead of self-oxidation or self-reduction reactions, resulting in enhanced stability of electrocatalyst/am.-TiO$_2$/photoanode structures. Furthermore, focusing on electrocatalyst research is important, and for instance, improving the selectivity towards desired products in CO$_2$ reduction reactions is still an unresolved challenge. In general, integrated photoelectrochemical solar fuel reactors still lack efficiency, product selectivity, stability, and understanding related to large-scale systems. Therefore, regarding economic viability, a lifetime >10 years, selective solar-to-chemical efficiency >10% (22% for H$_2$ production), and low manufacturing costs (<300 \$/m^2) are general milestones to target in future [10,13,199].

REFERENCES

[1]   R. Lindsey, Climate Change: Atmospheric Carbon Dioxide. National Oceanic and Atmospheric Administration, https://www.climate.gov/print/8431 (accessed 19.09.2022).

[2]   N.S. Lewis, D.G. Nocera, Powering the Planet: Chemical Challenges in Solar Energy Utilization, *Proc. Natl. Acad. Sci. U. S. A.* 103 (2006) 15729–15735.

[3]   E. Kalamaras, M.M. Maroto-Valer, M. Shao, J. Xuan, H. Wang, Solar Carbon Fuel via Photoelectrochemistry, *Catal. Today* 317 (2018) 56–75.

[4]   BP Statistical Review of World Energy 2021, 70th edition. Data compilation: Centre for Energy Economics Research and Policy, Heriot-Watt University, https://www.bp.com/en/global/corporate/energy-economics/statistical-review-of-world-energy.html (accessed 06.08.2021).

[5]   N.S. Lewis, G. Crabtree, A.J. Nozik, M.R. Wasielewski, P. Alivisatos, H. Kung, J. Tsao, E. Chandler, W. Walukiewicz, M. Spitler, R. Ellingson, R. Overend, J. Mazer, M. Gress, J. Horwitz, C. Ashton, B. Herndon, L. Shapard, R.M. Nault, Basic Research Needs for Solar Energy Utilization, Report of the Basic Energy Sciences Workshop on Solar Energy Utilization, United States, April 18-21, (2005).

[6]   R. van de Krol, M. Grätzel, Eds., *Photoelectrochemical Hydrogen Production*, Electronic Materials: Science & Technology; Springer US, (2012).

[7]   H. Dau, E. Fujita, L. Sun, Artificial Photosynthesis: Beyond Mimicking Nature, *ChemSusChem* 10 (2017) 4228–4235.

[8]   J. Su, L. Vayssieres, A Place in the Sun for Artificial Photosynthesis?, *ACS Energy Lett.* 1 (2016) 121–135.

[9]   G. Li, Y. Liu, Q. Zhang, Q. Hu, W. Guo, X. Cao, Y. Dou, L. Cheng, Y. Song, J. Su, L. Huang, R. Ye, Development of Catalysts and Electrolyzers Toward Industrial-Scale CO_2 Electroreduction, *J. Mater. Chem. A* (2022).

[10] G. Segev, J. Kibsgaard, C. Hahn, Z.J. Xu, W.-H. (Sophia) Cheng, T.G. Deutsch, C. Xiang, J.Z. Zhang, L. Hammarström, D.G. Nocera, A.Z. Weber, P. Agbo, T. Hisatomi, F.E. Osterloh, K. Domen, F.F. Abdi, S. Haussener, D.J. Miller, S. Ardo, P.C. McIntyre, T. Hannappel, S. Hu, H. Atwater, J.M. Gregoire, M.Z. Ertem, I.D. Sharp, K.-S. Choi, J.S. Lee, O. Ishitani, J.W. Ager, R.R. Prabhakar, A.T. Bell, S.W. Boettcher, K. Vincent, K. Takanabe, V. Artero, R. Napier, B.R. Cuenya, M.T.M. Koper, R. Van De Krol, F. Houle, The 2022 Solar Fuels Roadmap, *J. Phys. D: Appl. Phys.* 55 (2022) 323003.

[11] T.A. Kistler, M.Y. Um, J.K. Cooper, I.D. Sharp, P. Agbo, Monolithic Photoelectrochemical CO_2 Reduction Producing Syngas at 10% Efficiency, *Adv. Energy Mater.* 11 (2021) 2100070.

[12] A.Y. Khodakov, W. Chu, P. Fongarland, Advances in the Development of Novel Cobalt Fischer−Tropsch Catalysts for Synthesis of Long-Chain Hydrocarbons and Clean Fuels, *Chem. Rev.* 107 (2007) 1692–1744.

[13] W.-H. Cheng, M.H. Richter, M.M. May, J. Ohlmann, D. Lackner, F. Dimroth, T. Hannappel, H.A. Atwater, H.-J. Lewerenz, Monolithic Photoelectrochemical Device for Direct Water Splitting with 19% Efficiency, *ACS Energy Lett.* 3 (2018) 1795–1800.

[14] J. Tournet, Y. Lee, S.K. Karuturi, H.H. Tan, C. Jagadish, III–V Semiconductor Materials for Solar Hydrogen Production: Status and Prospects, *ACS Energy Lett.* 5 (2020) 611–622.

[15] S. Hu, C. Xiang, S. Haussener, A.D. Berger, N.S. Lewis, An Analysis of the Optimal Band Gaps of Light Absorbers in Integrated Tandem Photoelectrochemical Water-Splitting Systems, *Energy Environ. Sci.* 6 (2013) 2984–2993.

[16] J. Jia, L.C. Seitz, J.D. Benck, Y. Huo, Y. Chen, J.W.D. Ng, T. Bilir, J.S. Harris, T.F. Jaramillo, Solar Water Splitting by Photovoltaic-Electrolysis with a Solar-to-Hydrogen Efficiency over 30%, *Nat. Commun.* 7 (2016) 13237.

[17] M. Reuß, J. Reul, T. Grube, M. Langemann, S. Calnan, M. Robinius, R. Schlatmann, U. Rau, D. Stolten, Solar Hydrogen Production: a Bottom-up Analysis of Different Photovoltaic–Electrolysis Pathways, *Sustainable Energy Fuels* 3 (2019) 801–813.

[18] S. Ardo, D. Fernandez Rivas, M.A. Modestino, V. Schulze Greiving, F.F. Abdi, E. Alarcon Llado, V. Artero, K. Ayers, C. Battaglia, J.-P. Becker, D.

Bederak, A. Berger, F. Buda, E. Chinello, B. Dam, V. Di Palma, T. Edvinsson, K. Fujii, H. Gardeniers, H. Geerlings, S.M. H. Hashemi, S. Haussener, F. Houle, J. Huskens, B.D. James, K. Konrad, A. Kudo, P.P. Kunturu, D. Lohse, B. Mei, E.L. Miller, G.F. Moore, J. Muller, K.L. Orchard, T.E. Rosser, F.H. Saadi, J.-W. Schüttauf, B. Seger, S.W. Sheehan, W.A. Smith, J. Spurgeon, M.H. Tang, R. van de Krol, P.C.K. Vesborg, P. Westerik, Pathways to Electrochemical Solar-Hydrogen Technologies, *Energy Environ. Sci.* 11 (2018) 2768–2783.

[19]   C. Ros, T. Andreu, J.R. Morante, Photoelectrochemical Water Splitting: a Road from Stable Metal Oxides to Protected Thin Film Solar Cells, *J. Mater. Chem. A* 8 (2020) 10625–10669.

[20]   L. Santinacci, ALD for Photoelectrochemical Water Splitting, In *Atomic Layer Deposition in Energy Conversion Applications*; J. Bachmann, Ed., John Wiley & Sons, Ltd., (2017), pp. 225–257.

[21]   Z. Chen, H.N. Dinh, E. Miller, Eds., *Photoelectrochemical Water Splitting*, SpringerBriefs in Energy; Springer New York, New York, NY, (2013).

[22]   Y.-H. Chiu, T.-H. Lai, M.-Y. Kuo, P.-Y. Hsieh, Y.-J. Hsu, Photoelectrochemical Cells for Solar Hydrogen Production: Challenges and Opportunities, *APL Mater.* 7 (2019) 080901.

[23]   T.J. Jacobsson, V. Fjällström, M. Edoff, T. Edvinsson, Sustainable Solar Hydrogen Production: from Photoelectrochemical Cells to PV-Electrolyzers and Back Again, *Energy Environ. Sci.* 7 (2014) 2056–2070.

[24]   D. Bae, B. Seger, P.C.K. Vesborg, O. Hansen, I. Chorkendorff, Strategies for Stable Water Splitting via Protected Photoelectrodes, *Chem. Soc. Rev.* 46 (2017) 1933–1954.

[25]   A. Fujishima, K. Honda, Electrochemical Photolysis of Water at a Semiconductor Electrode, *Nature* 238 (1972) 37–38.

[26]   W. Septina, S.D. Tilley, Emerging Earth-Abundant Materials for Scalable Solar Water Splitting, *Curr. Opin. Electrochem.* 2 (2017) 120–127.

[27]   M. Pelaez, N.T. Nolan, S.C. Pillai, M.K. Seery, P. Falaras, A.G. Kontos, P.S.M. Dunlop, J.W.J. Hamilton, J.A. Byrne, K. O'Shea, M.H. Entezari, D.D. Dionysiou, A Review on the Visible Light Active Titanium Dioxide

Photocatalysts for Environmental Applications, *Appl. Catal., B* 125 (2012) 331–349.

[28] H. Park, Y. Park, W. Kim, W. Choi, Surface Modification of TiO_2 Photocatalyst for Environmental Applications, *J. Photochem. Photobiol., C* 15 (2013) 1–20.

[29] D.A.H. Hanaor, C.C. Sorrell, Review of the Anatase to Rutile Phase Transformation, *J. Mater. Sci.* 46 (2011) 855–874.

[30] D.O. Scanlon, C.W. Dunnill, J. Buckeridge, S.A. Shevlin, A.J. Logsdail, S.M. Woodley, C.R.A. Catlow, M.J. Powell, R.G. Palgrave, I.P. Parkin, G.W. Watson, T.W. Keal, P. Sherwood, A. Walsh, A.A. Sokol, Band Alignment of Rutile and Anatase TiO_2, *Nat. Mater.* 12 (2013) 798–801.

[31] J. Aarik, A. Aidla, A.-A. Kiisler, T. Uustare, V. Sammelselg, Effect of Crystal Structure on Optical Properties of TiO_2 Films Grown by Atomic Layer Deposition, *Thin Solid Films* 305 (1997) 270–273.

[32] N.A. Deskins, J. Du, P. Rao, The Structural and Electronic Properties of Reduced Amorphous Titania, *Phys. Chem. Chem. Phys.* 19 (2017) 18671–18684.

[33] G.G. Lenzi, C.V.B. Fávero, L.M.S. Colpini, H. Bernabe, M.L. Baesso, S. Specchia, O.A.A. Santos, Photocatalytic Reduction of Hg(II) on TiO_2 and Ag/TiO_2 Prepared by the Sol–Gel and Impregnation Methods, *Desalination* 270 (2011) 241–247.

[34] V.-A. Glezakou, R. Rousseau, Shedding Light on Black Titania, *Nat. Mater.* 17 (2018) 856–857.

[35] X. Liu, G. Zhu, X. Wang, X. Yuan, T. Lin, F. Huang, Progress in Black Titania: A New Material for Advanced Photocatalysis, *Adv. Energy Mater.* 6 (2016) 1600452.

[36] X. Chen, L. Liu, Z. Liu, M.A. Marcus, W.-C. Wang, N.A. Oyler, M.E. Grass, B. Mao, P.-A. Glans, P.Y. Yu, J. Guo, S.S. Mao, Properties of Disorder-Engineered Black Titanium Dioxide Nanoparticles through Hydrogenation, *Sci. Rep.* 3 (2013) 1510.

[37] X. Chen, L. Liu, F. Huang, Black Titanium Dioxide (TiO_2) Nanomaterials, *Chem. Soc. Rev.* 44 (2015) 1861–1885.

[38] J. Dendooven, C. Detavernier, Basics of Atomic Layer Deposition: Growth Characteristics and Conformality, In *Atomic Layer Deposition in Energy Conversion Applications*; J. Bachmann, Ed., John Wiley & Sons, Ltd., (2017), pp. 1–40.

[39] S. Zhuiykov, M.K. Akbari, Z. Hai, C. Xue, H. Xu, L. Hyde, Wafer-Scale Fabrication of Conformal Atomic-Layered TiO_2 by Atomic Layer Deposition Using Tetrakis (Dimethylamino) Titanium and H_2O precursors, *Mater. Des.* 120 (2017) 99–108.

[40] S. Hu, M.R. Shaner, J.A. Beardslee, M. Lichterman, B.S. Brunschwig, N.S. Lewis, Amorphous TiO_2 Coatings Stabilize Si, GaAs, and GaP Photoanodes for Efficient Water Oxidation, *Science* 344 (2014) 1005–1009.

[41] Y.W. Chen, J.D. Prange, S. Dühnen, Y. Park, M. Gunji, C.E.D. Chidsey, P.C. McIntyre, Atomic Layer-Deposited Tunnel Oxide Stabilizes Silicon Photoanodes for Water Oxidation, *Nat. Mater.* 10 (2011) 539–544.

[42] M. Hannula, H. Ali-Löytty, K. Lahtonen, E. Sarlin, J. Saari, M. Valden, Improved Stability of Atomic Layer Deposited Amorphous TiO_2 Photoelectrode Coatings by Thermally Induced Oxygen Defects, *Chem. Mater.* 30 (2018) 1199–1208.

[43] B. Mei, T. Pedersen, P. Malacrida, D. Bae, R. Frydendal, O. Hansen, P.C.K. Vesborg, B. Seger, I. Chorkendorff, Crystalline TiO_2: A Generic and Effective Electron-Conducting Protection Layer for Photoanodes and -Cathodes, *J. Phys. Chem. C* 119 (2015) 15019–15027.

[44] B. Wang, G. M. Biesold, M. Zhang, Z. Lin, Amorphous Inorganic Semiconductors for the Development of Solar Cell, Photoelectrocatalytic and Photocatalytic Applications, *Chem. Soc. Rev.* 50 (2021) 6914–6949.

[45] G.C. Correa, B. Bao, N.C. Strandwitz, Chemical Stability of Titania and Alumina Thin Films Formed by Atomic Layer Deposition, *ACS Appl. Mater. Interfaces* 7 (2015) 14816–14821.

[46] H. Kriegel, J. Kollmann, R. Raudsepp, T. Klassen, M. Schieda, Chemical and Photoelectrochemical Instability of Amorphous TiO_2 Layers Quantified by Spectroscopic Ellipsometry, *J. Mater. Chem. A* 8 (2020) 18173–18179.

[47]   L. Palmolahti, H. Ali-Löytty, M. Hannula, J. Saari, W. Wang, A. Tukiainen, K. Lahtonen, M. Valden, Pinhole-Resistant Nanocrystalline Rutile TiO_2 Photoelectrode Coatings, *Acta Mater.* 239 (2022) 118257.

[48]   M.E. Dufond, J.-N. Chazalviel, L. Santinacci, Electrochemical Stability of n-Si Photoanodes Protected by TiO_2 Thin Layers Grown by Atomic Layer Deposition, *J. Electrochem. Soc.* 168 (2021) 031509.

[49]   P. Nunez, M.H. Richter, B.D. Piercy, C.W. Roske, M. Cabán-Acevedo, M.D. Losego, S.J. Konezny, D.J. Fermin, S. Hu, B.S. Brunschwig, N.S. Lewis, Characterization of Electronic Transport through Amorphous TiO_2 Produced by Atomic Layer Deposition, *J. Phys. Chem. C* 123 (2019) 20116–20129.

[50]   M.T. McDowell, M.F. Lichterman, A.I. Carim, R. Liu, S. Hu, B.S. Brunschwig, N.S. Lewis, The Influence of Structure and Processing on the Behavior of TiO_2 Protective Layers for Stabilization of n-Si/TiO_2/Ni Photoanodes for Water Oxidation, *ACS Appl. Mater. Interfaces* 7 (2015) 15189–15199.

[51]   B. Zhang, L. Sun, Artificial Photosynthesis: Opportunities and Challenges of Molecular Catalysts, *Chem. Soc. Rev.* 48 (2019) 2216–2264.

[52]   X.-G. Zhu, S.P. Long, D.R. Ort, Improving Photosynthetic Efficiency for Greater Yield, *Annu. Rev. Plant Biol.* 61 (2010) 235–261.

[53]   R.E. Blankenship, D.M. Tiede, J. Barber, G.W. Brudvig, G. Fleming, M. Ghirardi, M.R. Gunner, W. Junge, D.M. Kramer, A. Melis, T.A. Moore, C.C. Moser, D.G. Nocera, A.J. Nozik, D.R. Ort, W.W. Parson, R.C. Prince, R.T. Sayre, Comparing Photosynthetic and Photovoltaic Efficiencies and Recognizing the Potential for Improvement, *Science* 332 (2011) 805–809.

[54]   S. Zhu, D. Wang, Photocatalysis: Basic Principles, Diverse Forms of Implementations and Emerging Scientific Opportunities, *Adv. Energy Mater.* 7 (2017) 1700841.

[55]   Standard Tables for Reference Solar Spectral Irradiances: Direct Normal and Hemispherical on 37° Tilted Surface, https://www.astm.org/g0173-03r20.html (accessed 13.09.2022).

[56]   Reference Air Mass 1.5 Spectra, https://www.nrel.gov/grid/solar-resource/spectra-am1.5.html (accessed 23.03.2022).

[57]   V. Polojärvi, Novel III-V Heterostructures for High Efficiency Solar Cells, D.Sc. (Technology) Dissertation, (Tampere University of Technology. Publication; Vol. 1383), Tampere University of Technology, (2016).

[58]   J.F. Geisz, R.M. France, K.L. Schulte, M.A. Steiner, A.G. Norman, H.L. Guthrey, M.R. Young, T. Song, T. Moriarty, Six-Junction III–V Solar Cells with 47.1% Conversion Efficiency under 143 Suns Concentration, *Nat. Energy* 5 (2020) 326–335.

[59]   S. Chen, L.-W. Wang, Thermodynamic Oxidation and Reduction Potentials of Photocatalytic Semiconductors in Aqueous Solution, *Chem. Mater.* 24 (2012) 3659–3666.

[60]   J. Zhao, S. Xue, J. Barber, Y. Zhou, J. Meng, X. Ke, An Overview of Cu-Based Heterogeneous Electrocatalysts for CO_2 Reduction, *J. Mater. Chem. A* 8 (2020) 4700–4734.

[61]   M.G. Walter, E.L. Warren, J.R. McKone, S.W. Boettcher, Q. Mi, E.A. Santori, N.S. Lewis, Solar Water Splitting Cells, *Chem. Rev.* 110 (2010) 6446–6473.

[62]   M. Hannula, H. Ali-Löytty, K. Lahtonen, J. Saari, A. Tukiainen, M. Valden, Highly Efficient Charge Separation in Model Z-Scheme $TiO_2/TiSi_2/Si$ Photoanode by Micropatterned Titanium Silicide Interlayer, *Acta Mater.* 174 (2019) 237–245.

[63]   A.G. Scheuermann, J.P. Lawrence, K.W. Kemp, T. Ito, A. Walsh, C.E.D. Chidsey, P.K. Hurley, P.C. McIntyre, Design Principles for Maximizing Photovoltage in Metal-Oxide-Protected Water-Splitting Photoanodes, *Nat. Mater.* 15 (2016) 99–105.

[64]   A.G. Scheuermann, J.D. Prange, M. Gunji, C.E.D. Chidsey, P.C. McIntyre, Effects of Catalyst Material and Atomic Layer Deposited TiO_2 Oxide Thickness on the Water Oxidation Performance of Metal–Insulator–Silicon Anodes, *Energy Environ. Sci.* 6 (2013) 2487–2496.

[65]   A.G. Scheuermann, K.W. Kemp, K. Tang, D.Q. Lu, P.F. Satterthwaite, T. Ito, C.E.D. Chidsey, P.C. McIntyre, Conductance and Capacitance of Bilayer Protective Oxides for Silicon Water Splitting Anodes, *Energy Environ. Sci.* 9 (2016) 504–516.

[66] M. Pourbaix, *Atlas of Electrochemical Equilibria in Aqueous Solutions*, 2nd ed., National Association of Corrosion Engineers, Houston, TX, (1974).

[67] P. Acevedo-Peña, J. Vazquez-Arenas, R. Cabrera-Sierra, L. Lartundo-Rojas, I. González, Ti Anodization in Alkaline Electrolyte: The Relationship between Transport of Defects, Film Hydration and Composition, *J. Electrochem. Soc.* 160 (2013) C277.

[68] D. Bae, S. Shayestehaminzadeh, E.B. Thorsteinsson, T. Pedersen, O. Hansen, B. Seger, P.C.K. Vesborg, S. Ólafsson, I. Chorkendorff, Protection of Si Photocathode using TiO_2 Deposited by High Power Impulse Magnetron Sputtering for H_2 Evolution in Alkaline Media, *Sol. Energy Mater. Sol. Cells* 144 (2016) 758–765.

[69] H. Seidel, L. Csepregi, A. Heuberger, H. Baumgärtel, Anisotropic Etching of Crystalline Silicon in Alkaline Solutions: I . Orientation Dependence and Behavior of Passivation Layers, *J. Electrochem. Soc.* 137 (1990) 3612.

[70] R.H. Coridan, A.C. Nielander, S.A. Francis, M.T. McDowell, V. Dix, S.M. Chatman, N.S. Lewis, Methods for Comparing the Performance of Energy-Conversion Systems for Use in Solar Fuels and Solar Electricity Generation, *Energy Environ. Sci.* 8 (2015) 2886–2901.

[71] S.Z. Oener, S. Ardo, S.W. Boettcher, Ionic Processes in Water Electrolysis: The Role of Ion-Selective Membranes, *ACS Energy Lett.* 2 (2017) 2625–2634.

[72] J. Luo, D.A. Vermaas, D. Bi, A. Hagfeldt, W.A. Smith, M. Grätzel, Bipolar Membrane-Assisted Solar Water Splitting in Optimal pH, *Adv. Energy Mater.* 6 (2016) 1600100.

[73] R. Pärnamäe, S. Mareev, V. Nikonenko, S. Melnikov, N. Sheldeshov, V. Zabolotskii, H.V.M. Hamelers, M. Tedesco, Bipolar Membranes: A Review on Principles, Latest Developments, and Applications, *J. Membr. Sci.* 617 (2021) 118538.

[74] A.B. Murphy, P.R.F. Barnes, L.K. Randeniya, I.C. Plumb, I.E. Grey, M.D. Horne, J.A. Glasscock, Efficiency of Solar Water Splitting using Semiconductor Electrodes, *Int. J. Hydrogen Energy* 31 (2006) 1999–2017.

[75] M.A. Lukowski, A.S. Daniel, F. Meng, A. Forticaux, L. Li, S. Jin, Enhanced Hydrogen Evolution Catalysis from Chemically Exfoliated Metallic MoS_2 Nanosheets, *J. Am. Chem. Soc.* 135 (2013) 10274–10277.

[76]   X. Yang, R. Liu, Y. He, J. Thorne, Z. Zheng, D. Wang, Enabling Practical Electrocatalyst-Assisted Photoelectron-Chemical Water Splitting with Earth Abundant Materials, *Nano Res.* 8 (2015) 56–81.

[77]   C.C.L. McCrory, S. Jung, I.M. Ferrer, S.M. Chatman, J.C. Peters, T.F. Jaramillo, Benchmarking Hydrogen Evolving Reaction and Oxygen Evolving Reaction Electrocatalysts for Solar Water Splitting Devices, *J. Am. Chem. Soc.* 137 (2015) 4347–4357.

[78]   S.-H. Hsu, J. Miao, L. Zhang, J. Gao, H. Wang, H. Tao, S.-F. Hung, A. Vasileff, S.Z. Qiao, B. Liu, An Earth-Abundant Catalyst-Based Seawater Photoelectrolysis System with 17.9% Solar-to-Hydrogen Efficiency, *Adv. Mater.* 30 (2018) 1707261.

[79]   H. Ali-Löytty, M.W. Louie, M.R. Singh, L. Li, H.G. Sanchez Casalongue, H. Ogasawara, E.J. Crumlin, Z. Liu, A.T. Bell, A. Nilsson, D. Friebel, Ambient-Pressure XPS Study of a Ni–Fe Electrocatalyst for the Oxygen Evolution Reaction, *J. Phys. Chem. C* 120 (2016) 2247–2253.

[80]   K.P. Kuhl, T. Hatsukade, E.R. Cave, D.N. Abram, J. Kibsgaard, T.F. Jaramillo, Electrocatalytic Conversion of Carbon Dioxide to Methane and Methanol on Transition Metal Surfaces, *J. Am. Chem. Soc.* 136 (2014) 14107–14113.

[81]   A. Eilert, F. Cavalca, F.S. Roberts, J. Osterwalder, C. Liu, M. Favaro, E.J. Crumlin, H. Ogasawara, D. Friebel, L.G.M. Pettersson, A. Nilsson, Subsurface Oxygen in Oxide-Derived Copper Electrocatalysts for Carbon Dioxide Reduction, *J. Phys. Chem. Lett.* 8 (2017) 285–290.

[82]   C. Franchini, M. Reticcioli, M. Setvin, U. Diebold, Polarons in Materials, *Nat. Rev. Mater.* 6 (2021) 560–586.

[83]   Z. Guo, F. Ambrosio, A. Pasquarello, Hole Diffusion across Leaky Amorphous TiO_2 Coating Layers for Catalytic Water Splitting at Photoanodes, *J. Mater. Chem. A* 6 (2018) 11804–11810.

[84]   M.H. Richter, W.-H. Cheng, E.J. Crumlin, W.S. Drisdell, H.A. Atwater, D. Schmeißer, N.S. Lewis, B.S. Brunschwig, X-ray Photoelectron Spectroscopy and Resonant X-ray Spectroscopy Investigations of Interactions between Thin Metal Catalyst Films and Amorphous Titanium Dioxide Photoelectrode Protection Layers, *Chem. Mater.* 33 (2021) 1265–1275.

[85]   S. Hu, M.H. Richter, M.F. Lichterman, J. Beardslee, T. Mayer, B.S. Brunschwig, N.S. Lewis, Electrical, Photoelectrochemical, and Photoelectron Spectroscopic Investigation of the Interfacial Transport and Energetics of Amorphous TiO_2/Si Heterojunctions, *J. Phys. Chem. C* 120 (2016) 3117–3129.

[86]   W. Cui, T. Moehl, S. Siol, S. David Tilley, *Operando* Electrochemical Study of Charge Carrier Processes in Water Splitting Photoanodes Protected by Atomic Layer Deposited TiO_2, *Sustainable Energy Fuels* 3 (2019) 3085–3092.

[87]   B. Seger, T. Pedersen, A.B. Laursen, P.C.K. Vesborg, O. Hansen, I. Chorkendorff, Using TiO_2 as a Conductive Protective Layer for Photocathodic H_2 Evolution, *J. Am. Chem. Soc.* 135 (2013) 1057–1064.

[88]   C. Ros, T. Andreu, M.D. Hernández-Alonso, G. Penelas-Pérez, J. Arbiol, J.R. Morante, Charge Transfer Characterization of ALD-Grown TiO_2 Protective Layers in Silicon Photocathodes, *ACS Appl. Mater. Interfaces* 9 (2017) 17932–17941.

[89]   A. Li, Z. Wang, H. Yin, S. Wang, P. Yan, B. Huang, X. Wang, R. Li, X. Zong, H. Han, C. Li, Understanding the Anatase–Rutile Phase Junction in Charge Separation and Transfer in a TiO_2 Electrode for Photoelectrochemical Water Splitting, *Chem. Sci.* 7 (2016) 6076–6082.

[90]   W. Yang, R. Ramanujam Prabhakar, J. Tan, S. David Tilley, J. Moon, Strategies for Enhancing the Photocurrent, Photovoltage, and Stability of Photoelectrodes for Photoelectrochemical Water Splitting, *Chem. Soc. Rev.* 48 (2019) 4979–5015.

[91]   E. Verlage, S. Hu, R. Liu, R.J.R. Jones, K. Sun, C. Xiang, N.S. Lewis, H.A. Atwater, A Monolithically Integrated, Intrinsically Safe, 10% Efficient, Solar-Driven Water-Splitting System Based on Active, Stable Earth-Abundant Electrocatalysts in Conjunction with Tandem III–V Light Absorbers Protected by Amorphous TiO_2 Films, *Energy Environ. Sci.* 8 (2015) 3166–3172.

[92]   R.W. Johnson, A. Hultqvist, S.F. Bent, A Brief Review of Atomic Layer Deposition: from Fundamentals to Applications, *Mater. Today* 17 (2014) 236–246.

[93]   R.L. Puurunen, A Short History of Atomic Layer Deposition: Tuomo Suntola's Atomic Layer Epitaxy, *Chem. Vap. Deposition* 20 (2014) 332–344.

[94]   V.B. Aleskovskii, S.I. Kolt'sov, Some Characteristics of Molecular Layering Reactions, Abstract of Scientific and Technical Conference, Goskhimizdat, Leningrad, USSR, (1965), p. 67.

[95]   J. Aarik, A.R. Akbashev, M. Bechelany, M. Berdova, D. Cameron, N. Chekurov, V.E. Drozd, S.D. Elliott, G. Gottardi, K. Grigoras, M. Junige, T. Kallio, J. Kanervo, M.-L. Kääriäinen, T. Kääriäinen, L. Lamagna, A. Malkov, A. Malygin, J. Molarius, C. Ozgit-Akgun, H. Pedersen, R.L. Puurunen, A.P. Perros, R.H.A. Ras, F. Roozeboom, T. Sajavaara, H. Savin, T.E. Seidel, P. Sundberg, J. Sundqvist, M. Tallarida, J.R. van Ommen, T. Wächtler, C. Wiemer, O.M.E. Ylivaara, On the Early History of ALD: Molecular Layering,   https://vph-ald.com/VPHApublications/VPHA_Kyoto2014_ML-poster_v15_FINAL.pdf (accessed 19.09.2022).

[96]   G.V. Sveshnikova, S.I. Kolt'sov, V.B. Aleskovskii, Interaction of Titanium Tetrachloride with Hydroxylated Silicon Surfaces, *Zh. Prikl. Khim.* 43 (1970) 430.

[97]   S.I. Kolt'sov, Preparation and Investigation of the Products of Interaction between Titanium Tetrachloride and Silica Gel, *Zh. Prikl. Khim.* 42 (1969) 1023.

[98]   A.M. Shevjakov, G.N. Kuznetsova, V.B. Aleskovskii, Interaction of Titanium and Germanium Tetrachlorides with Hydroxylated Silicon Dioxide, Chemistry of High Temperature Materials, 2nd USSR Conference on High Temperature Chemistry of Oxides, Leningrad, USSR, (1965), pp. 149–155.

[99]   E. Ahvenniemi, A.R. Akbashev, S. Ali, M. Bechelany, M. Berdova, S. Boyadjiev, D.C. Cameron, R. Chen, M. Chubarov, V. Cremers, A. Devi, V. Drozd, L. Elnikova, G. Gottardi, K. Grigoras, D.M. Hausmann, C.S. Hwang, S.-H. Jen, T. Kallio, J. Kanervo, I. Khmelnitskiy, D.H. Kim, L. Klibanov, Y. Koshtyal, A.O.I. Krause, J. Kuhs, I. Kärkkänen, M.-L. Kääriäinen, T. Kääriäinen, L. Lamagna, A.A. Łapicki, M. Leskelä, H. Lipsanen, J. Lyytinen, A. Malkov, A. Malygin, A. Mennad, C. Militzer, J. Molarius, M. Norek, Ç. Özgit-Akgün, M. Panov, H. Pedersen, F. Piallat, G. Popov, R.L. Puurunen, G. Rampelberg, R.H.A. Ras, E. Rauwel, F. Roozeboom, T. Sajavaara, H. Salami, H. Savin, N. Schneider, T.E. Seidel, J. Sundqvist, D.B. Suyatin, T. Törndahl, J.R. van Ommen, C. Wiemer, O.M.E. Ylivaara, O. Yurkevich, Review Article: Recommended Reading List of Early Publications on Atomic Layer Deposition—Outcome of the "Virtual Project on the History of ALD," *J. Vac. Sci. Technol., A* 35 (2017) 010801.

[100] T. Suntola, J. Antson, Method for Producing Compound Thin Films, US4058430A, (1977). https://patents.google.com/patent/US4058430A/en (accessed 19.09.2022).

[101] T. Kääriäinen, D. Cameron, M.-L. Kääriäinen, A. Sherman, Atomic layer deposition: principles, characteristics, and nanotechnology applications, 2nd Edition, Scrivener Publishing, Beverly, MA, (2013).

[102] Enabling Smart Technology, Millennium Technology Prize. https://millenniumprize.org/winners/enabling-smart-technology/ (accessed 19.09.2022).

[103] S.M. George, Atomic Layer Deposition: An Overview, *Chem. Rev.* 110 (2010) 111–131.

[104] H.C.M. Knoops, S.E. Potts, A.A. Bol, W.M.M. Kessels, Atomic Layer Deposition, In *Handbook of Crystal Growth*, T. Kuech, Ed., Elsevier, (2015), pp. 1101–1134.

[105] Q. Xie, Y.-L. Jiang, C. Detavernier, D. Deduytsche, R.L. Van Meirhaeghe, G.-P. Ru, B.-Z. Li, X.-P. Qu, Atomic Layer Deposition of TiO_2 from Tetrakis-Dimethyl-Amido Titanium or Ti Isopropoxide Precursors and H_2O, *J. Appl. Phys.* 102 (2007) 083521.

[106] A.R. Head, S. Chaudhary, G. Olivieri, F. Bournel, J.N. Andersen, F. Rochet, J.-J. Gallet, J. Schnadt, Near Ambient Pressure X-ray Photoelectron Spectroscopy Study of the Atomic Layer Deposition of TiO_2 on RuO_2(110), *J. Phys. Chem. C* 120 (2016) 243–251.

[107] R.L. Puurunen, Surface Chemistry of Atomic Layer Deposition: A Case Study for the Trimethylaluminum/Water Process, *J. Appl. Phys.* 97 (2005) 121301.

[108] K. Devloo-Casier, J. Dendooven, K.F. Ludwig, G. Lekens, J. D'Haen, C. Detavernier, *In Situ* Synchrotron Based X-ray Fluorescence and Scattering Measurements during Atomic Layer Deposition: Initial Growth of HfO_2 on Si and Ge Substrates, *Appl. Phys. Lett.* 98 (2011) 231905.

[109] R.L. Puurunen, W. Vandervorst, Island Growth as a Growth Mode in Atomic Layer Deposition: A Phenomenological Model, *J. Appl. Phys.* 96 (2004) 7686–7695.

[110] T. Iivonen, M.J. Heikkilä, G. Popov, H.-E. Nieminen, M. Kaipio, M. Kemell, M. Mattinen, K. Meinander, K. Mizohata, J. Räisänen, M. Ritala, M. Leskelä, Atomic Layer Deposition of Photoconductive Cu_2O Thin Films, *ACS Omega* 4 (2019) 11205–11214.

[111] T. Arroval, L. Aarik, R. Rammula, V. Kruusla, J. Aarik, Effect of Substrate-Enhanced and Inhibited Growth on Atomic Layer Deposition and Properties of Aluminum–Titanium Oxide Films, *Thin Solid Films* 600 (2016) 119–125.

[112] V. Miikkulainen, M. Leskelä, M. Ritala, R.L. Puurunen, Crystallinity of Inorganic Films Grown by Atomic Layer Deposition: Overview and General Trends, *J. Appl. Phys.* 113 (2013) 021301.

[113] N.E. Richey, C. de Paula, S.F. Bent, Understanding Chemical and Physical Mechanisms in Atomic Layer Deposition, *J. Chem. Phys.* 152 (2020) 040902.

[114] G.E. Jellison, L.A. Boatner, J.D. Budai, B.-S. Jeong, D.P. Norton, Spectroscopic Ellipsometry of Thin Film and Bulk Anatase (TiO_2), *J. Appl. Phys.* 93 (2003) 9537–9541.

[115] L. Cui, W. Wang, Optical Properties of Anatase and Rutile TiO_2 Films Deposited by using a Pulsed Laser, *Appl. Opt.* 60 (2021) 8453–8457.

[116] U. Diebold, The Surface Science of Titanium Dioxide, *Surf. Sci. Rep.* 48 (2003) 53–229.

[117] J.-P. Niemelä, G. Marin, M. Karppinen, Titanium Dioxide Thin Films by Atomic Layer Deposition: A Review, *Semicond. Sci. Technol.* 32 (2017) 093005.

[118] S.K. Kim, K.M. Kim, D.S. Jeong, W. Jeon, K.J. Yoon, C.S. Hwang, Titanium Dioxide Thin Films for Next-Generation Memory Devices, *J. Mater. Res.* 28 (2013) 313–325.

[119] A. Di Paola, M. Bellardita, L. Palmisano, Brookite, the Least Known TiO_2 Photocatalyst, *Catalysts* 3 (2013) 36–73.

[120] D. Dambournet, I. Belharouak, K. Amine, Tailored Preparation Methods of TiO_2 Anatase, Rutile, Brookite: Mechanism of Formation and Electrochemical Properties, *Chem. Mater.* 22 (2010) 1173–1179.

[121]   K. Sivula, Defects Give New Life to an Old Material: Electronically Leaky Titania as a Photoanode Protection Layer, *ChemCatChem* 6 (2014) 2796–2797.

[122]   T.S. Rajaraman, S.P. Parikh, V.G. Gandhi, Black TiO_2: A Review of Its Properties and Conflicting Trends, *Chem. Eng. J.* 389 (2020) 123918.

[123]   J. Aarik, A. Aidla, V. Sammelselg, T. Uustare, Effect of Growth Conditions on Formation of TiO_2-II Thin Films in Atomic Layer Deposition Process, *J. Cryst. Growth* 181 (1997) 259–264.

[124]   K. Möls, L. Aarik, H. Mändar, A. Kasikov, A. Niilisk, R. Rammula, J. Aarik, Influence of Phase Composition on Optical Properties of TiO_2: Dependence of Refractive Index and Band Gap on Formation of TiO_2-II Phase in Thin Films, *Opt. Mater.* 96 (2019) 109335.

[125]   J. Zhang, P. Sun, P. Jiang, Z. Guo, W. Liu, Q. Lu, W. Cao, The Formation Mechanism of TiO_2 Polymorphs under Hydrothermal Conditions Based on The Structural Evolution of $[Ti(OH)_h(H_2O)_{6-h}]^{4-h}$ Monomers, *J. Mater. Chem. C* 7 (2019) 5764–5771.

[126]   B. Kim, Y. Choi, D. Lee, S. Cheon, Y. Byun, H. Jeon, Atomic Layer Deposition for Rutile Structure TiO_2 Thin Films using a SnO_2 Seed Layer and Low Temperature Heat Treatment, *Nanotechnology* 33 (2021) 115701.

[127]   Y. Li, J. Liu, Z. Jia, Morphological Control and Photodegradation Behavior of Rutile TiO_2 Prepared by a Low-Temperature Process, *Mater. Lett.* 60 (2006) 1753–1757.

[128]   K. Yang, J. Zhu, J. Zhu, S. Huang, X. Zhu, G. Ma, Sonochemical Synthesis and Microstructure Investigation of Rod-Like Nanocrystalline Rutile Titania, *Mater. Lett.* 57 (2003) 4639–4642.

[129]   M. Zhang, T. Chen, Y. Wang, Insights into TiO_2 Polymorphs: Highly Selective Synthesis, Phase Transition, and Their Polymorph-Dependent Properties, *RSC Adv.* 7 (2017) 52755–52761.

[130]   D. Rafieian, W. Ogieglo, T. Savenije, R.G.H. Lammertink, Controlled Formation of Anatase and Rutile TiO_2 Thin Films by Reactive Magnetron Sputtering, *AIP Adv.* 5 (2015) 097168.

[131] D.-K. Lee, S.-H. Kwon, J.-H. Ahn, Growth of Rutile-TiO_2 Thin Films via Sn Doping and Insertion of Ultra-Thin SnO_2 Interlayer by Atomic Layer Deposition, *Mater. Lett.* 246 (2019) 1–4.

[132] S.K. Kim, S. Han, J.H. Han, W. Lee, C.S. Hwang, Atomic Layer Deposition of TiO_2 and Al-Doped TiO_2 Films on Ir Substrates for Ultralow Leakage Currents, *Phys. Status Solidi RRL* 5 (2011) 262–264.

[133] W. Jeon, S. Yoo, H.K. Kim, W. Lee, C.H. An, M.J. Chung, C.J. Cho, S.K. Kim, C.S. Hwang, Evaluating the Top Electrode Material for Achieving an Equivalent Oxide Thickness Smaller than 0.4 nm from an Al-Doped TiO_2 Film, *ACS Appl. Mater. Interfaces* 6 (2014) 21632–21637.

[134] B. Prasai, B. Cai, M.K. Underwood, J.P. Lewis, D.A. Drabold, Properties of Amorphous and Crystalline Titanium Dioxide from First Principles, *J. Mater. Sci.* 47 (2012) 7515–7521.

[135] D. Mora-Fonz, M. Kaviani, A.L. Shluger, Disorder-Induced Electron and Hole Trapping in Amorphous TiO_2, *Phys. Rev. B.* 102 (2020) 054205.

[136] B. Wang, M. Zhang, X. Cui, Z. Wang, M. Rager, Y. Yang, Z. Zou, Z.L. Wang, Z. Lin, Unconventional Route to Oxygen-Vacancy-Enabled Highly Efficient Electron Extraction and Transport in Perovskite Solar Cells, *Angew. Chem.* 132 (2020) 1628–1635.

[137] C. Di Valentin, G. Pacchioni, A. Selloni, Reduced and n-Type Doped TiO_2: Nature of Ti^{3+} Species, *J. Phys. Chem. C* 113 (2009) 20543–20552.

[138] F.G. Santomauro, A. Lübcke, J. Rittmann, E. Baldini, A. Ferrer, M. Silatani, P. Zimmermann, S. Grübel, J.A. Johnson, S.O. Mariager, P. Beaud, D. Grolimund, C. Borca, G. Ingold, S.L. Johnson, M. Chergui, Femtosecond X-ray Absorption Study of Electron Localization in Photoexcited Anatase TiO_2, *Sci. Rep.* 5 (2015) 14834.

[139] Y. Natanzon, A. Azulay, Y. Amouyal, Evaluation of Polaron Transport in Solids from First-principles, *Isr. J. Chem.* 60 (2020) 768–786.

[140] N.A. Deskins, M. Dupuis, Electron Transport via Polaron Hopping in Bulk TiO_2: A Density Functional Theory Characterization, *Phys. Rev. B.* 75 (2007) 195212.

[141] H.H. Pham, L.-W. Wang, Oxygen Vacancy and Hole Conduction in Amorphous TiO$_2$, *Phys. Chem. Chem. Phys.* 17 (2014) 541–550.

[142] N.A. Deskins, M. Dupuis, Intrinsic Hole Migration Rates in TiO$_2$ from Density Functional Theory, *J. Phys. Chem. C* 113 (2009) 346–358.

[143] Z. Wang, B. Wen, Q. Hao, L.-M. Liu, C. Zhou, X. Mao, X. Lang, W.-J. Yin, D. Dai, A. Selloni, X. Yang, Localized Excitation of Ti^{3+} Ions in the Photoabsorption and Photocatalytic Activity of Reduced Rutile TiO$_2$, *J. Am. Chem. Soc.* 137 (2015) 9146–9152.

[144] C. Di Valentin, G. Pacchioni, A. Selloni, Electronic Structure of Defect States in Hydroxylated and Reduced Rutile TiO$_2$(110) Surfaces, *Phys. Rev. Lett.* 97 (2006) 166803.

[145] B. Liu, X. Zhao, J. Yu, I.P. Parkin, A. Fujishima, K. Nakata, Intrinsic Intermediate Gap States of TiO$_2$ Materials and Their Roles in Charge Carrier Kinetics, *J. Photochem. Photobiol., C* 39 (2019) 1–57.

[146] A. Yamakata, J.J.M. Vequizo, Curious Behaviors of Photogenerated Electrons and Holes at the Defects on Anatase, Rutile, and Brookite TiO$_2$ Powders: A Review, *J. Photochem. Photobiol., C* 40 (2019) 234–243.

[147] X. Chen, L. Liu, P.Y. Yu, S.S. Mao, Increasing Solar Absorption for Photocatalysis with Black Hydrogenated Titanium Dioxide Nanocrystals, *Science* 331 (2011) 746–750.

[148] N. Martin, C. Rousselot, D. Rondot, F. Palmino, R. Mercier, Microstructure Modification of Amorphous Titanium Oxide Thin Films during Annealing Treatment, *Thin Solid Films* 300 (1997) 113–121.

[149] R. Khan, H. Ali-Löytty, J. Saari, M. Valden, A. Tukiainen, K. Lahtonen, N.V. Tkachenko, Optimization of Photogenerated Charge Carrier Lifetimes in ALD Grown TiO$_2$ for Photonic Applications, *Nanomaterials* 10 (2020) 1567.

[150] T.T. Hatanpää, Precursor Chemistry for Atomic Layer Deposition. Ph.D. Dissertation, University of Helsinki, (2019).

[151] C. Ros, N.M. Carretero, J. David, J. Arbiol, T. Andreu, J.R. Morante, Insight into the Degradation Mechanisms of Atomic Layer Deposited TiO$_2$ as Photoanode Protective Layer, *ACS Appl. Mater. Interfaces* 11 (2019) 29725–29735.

[152] M.E. Dufond, M.W. Diouf, C. Badie, C. Laffon, P. Parent, D. Ferry, D. Grosso, J.C.S. Kools, S.D. Elliott, L. Santinacci, Quantifying the Extent of Ligand Incorporation and the Effect on Properties of TiO_2 Thin Films Grown by Atomic Layer Deposition Using an Alkoxide or an Alkylamide, *Chem. Mater.* 32 (2020) 1393–1407.

[153] B. Abendroth, T. Moebus, S. Rentrop, R. Strohmeyer, M. Vinnichenko, T. Weling, H. Stöcker, D.C. Meyer, Atomic Layer Deposition of TiO_2 from Tetrakis(dimethylamino)titanium and H_2O, *Thin Solid Films* 545 (2013) 176–182.

[154] M. Ritala, M. Leskelä, E. Nykänen, P. Soininen, L. Niinistö, Growth of Titanium Dioxide Thin Films by Atomic Layer Epitaxy, *Thin Solid Films* 225 (1993) 288–295.

[155] G.T. Lim, D.-H. Kim, Characteristics of TiO_x films Prepared by Chemical Vapor Deposition Using Tetrakis-Dimethyl-Amido-Titanium and Water, *Thin Solid Films* 498 (2006) 254–258.

[156] J.W. Elam, M. Schuisky, J.D. Ferguson, S.M. George, Surface Chemistry and Film Growth during TiN Atomic Layer Deposition using TDMAT and NH_3, *Thin Solid Films* 436 (2003) 145–156.

[157] J.P.A.M. Driessen, J. Schoonman, K.F. Jensen, Infrared Spectroscopic Study of Decomposition of $Ti(N(CH_3)_2)_4$, *J. Electrochem. Soc.* 148 (2001) G178.

[158] M. Reiners, K. Xu, N. Aslam, A. Devi, R. Waser, S. Hoffmann-Eifert, Growth and Crystallization of TiO_2 Thin Films by Atomic Layer Deposition Using a Novel Amido Guanidinate Titanium Source and Tetrakis-dimethylamido-titanium, *Chem. Mater.* 25 (2013) 2934–2943.

[159] A.T. Iancu, M. Logar, J. Park, F.B. Prinz, Atomic Layer Deposition of Undoped TiO_2 Exhibiting p-Type Conductivity, *ACS Appl. Mater. Interfaces* 7 (2015) 5134–5140.

[160] K.S. Finnie, G. Triani, K.T. Short, D.R.G. Mitchell, D.J. Attard, J.R. Bartlett, C.J. Barbé, Influence of Si(100) Surface Pretreatment on the Morphology of TiO_2 Films Grown by Atomic Layer Deposition, *Thin Solid Films* 440 (2003) 109–116.

[161] D.R.G. Mitchell, D.J. Attard, G. Triani, Transmission Electron Microscopy Studies of Atomic Layer Deposition TiO$_2$ Films Grown on Silicon, *Thin Solid Films* 441 (2003) 85–95.

[162] C.J. Cho, J.-Y. Kang, W.C. Lee, S.-H. Baek, J.-S. Kim, C.S. Hwang, S.K. Kim, Interface Engineering for Extremely Large Grains in Explosively Crystallized TiO$_2$ Films Grown by Low-Temperature Atomic Layer Deposition, *Chem. Mater.* 29 (2017) 2046–2054.

[163] R. Methaapanon, S.F. Bent, Comparative Study of Titanium Dioxide Atomic Layer Deposition on Silicon Dioxide and Hydrogen-Terminated Silicon, *J. Phys. Chem. C* 114 (2010) 10498–10504.

[164] S. McDonnell, R.C. Longo, O. Seitz, J.B. Ballard, G. Mordi, D. Dick, J.H.G. Owen, J.N. Randall, J. Kim, Y.J. Chabal, K. Cho, R.M. Wallace, Controlling the Atomic Layer Deposition of Titanium Dioxide on Silicon: Dependence on Surface Termination, *J. Phys. Chem. C* 117 (2013) 20250–20259.

[165] Y.B. Kim, M. Tuominen, I. Raaijmakers, R. de Blank, R. Wilhelm, S. Haukka, Initial Stage of the Ultrathin Oxide Growth in Water Vapor on Si(100) Surface, *Electrochem. Solid-State Lett.* 3 (2000) 346.

[166] M. Morita, T. Ohmi, E. Hasegawa, M. Kawakami, M. Ohwada, Growth of Native Oxide on a Silicon Surface, *J. Appl. Phys.* 68 (1990) 1272–1281.

[167] D. Gräf, M. Grundner, R. Schulz, Reaction of Water with Hydrofluoric Acid Treated Silicon(111) and (100) Surfaces, *J. Vac. Sci. Technol., A* 7 (1989) 808–813.

[168] K. Hermansson, U. Lindberg, B. Hok, G. Palmskog, Wetting Properties of Silicon Surfaces, TRANSDUCERS '91: 1991 International Conference on Solid-State Sensors and Actuators. Digest of Technical Papers, (1991), pp 193−196.

[169] W. Kern, The Evolution of Silicon Wafer Cleaning Technology, *J. Electrochem. Soc.* 137 (1990) 1887.

[170] P. Dixit, X. Chen, J. Miao, S. Divakaran, R. Preisser, Study of Surface Treatment Processes for Improvement in the Wettability of Silicon-Based Materials Used in High Aspect Ratio Through-Via Copper Electroplating, *Appl. Surf. Sci.* 253 (2007) 8637–8646.

[171]   R.L. Puurunen, T. Sajavaara, E. Santala, V. Miikkulainen, T. Saukkonen, M. Laitinen, M. Leskelä, Controlling the Crystallinity and Roughness of Atomic Layer Deposited Titanium Dioxide Films, *J. Nanosci. Nanotechnol.* 11 (2011) 8101–8107.

[172]   S. Deng, S.W. Verbruggen, S. Lenaerts, J.A. Martens, S. Van den Berghe, K. Devloo-Casier, W. Devulder, J. Dendooven, D. Deduytsche, C. Detavernier, Controllable Nitrogen Doping in As Deposited TiO_2 Film and Its Effect on Post Deposition Annealing, *J. Vac. Sci. Technol., A* 32 (2013) 01A123.

[173]   B.A. Sperling, W.A. Kimes, J.E. Maslar, Reflection Absorption Infrared Spectroscopy during Atomic Layer Deposition of HfO_2 Films from Tetrakis(ethylmethylamido)hafnium and Water, *Appl. Surf. Sci.* 256 (2010) 5035–5041.

[174]   B.A. Sperling, J. Hoang, W.A. Kimes, J.E. Maslar, K.L. Steffens, N.V. Nguyen, Time-Resolved Surface Infrared Spectroscopy during Atomic Layer Deposition of TiO_2 using Tetrakis(dimethylamido)titanium and Water, *J. Vac. Sci. Technol., A* 32 (2014) 031513.

[175]   J.C. Vickerman, I.S. Gilmore, Eds., *Surface analysis the principal techniques*, 2nd Edition, Wiley, Hoboken, NJ, (2009).

[176]   P. Reckers, M. Dimamay, J. Klett, S. Trost, K. Zilberberg, T. Riedl, B.A. Parkinson, J. Brötz, W. Jaegermann, T. Mayer, Deep and Shallow TiO_2 Gap States on Cleaved Anatase Single Crystal (101) Surfaces, Nanocrystalline Anatase Films, and ALD Titania Ante and Post Annealing, *J. Phys. Chem. C* 119 (2015) 9890–9898.

[177]   N. Fairley, V. Fernandez, M. Richard-Plouet, C. Guillot-Deudon, J. Walton, E. Smith, D. Flahaut, M. Greiner, M. Biesinger, S. Tougaard, D. Morgan, J. Baltrusaitis, Systematic and Collaborative Approach to Problem Solving Using X-ray Photoelectron Spectroscopy, *Appl. Surf. Sci. Adv.* 5 (2021) 100112.

[178]   J.H. Scofield, Hartree-Slater Subshell Photoionization Cross-Sections at 1254 and 1487 eV, *J. Electron Spectrosc. Relat. Phenom.* 8 (1976) 129–137.

[179]   J.T. Newberg, D.E. Starr, S. Yamamoto, S. Kaya, T. Kendelewicz, E.R. Mysak, S. Porsgaard, M.B. Salmeron, G.E. Brown, A. Nilsson, H. Bluhm, Formation of Hydroxyl and Water Layers on MgO Films Studied with Ambient Pressure XPS, *Surf. Sci.* 605 (2011) 89–94.

[180] QUASES-IMFP-TPP2M - QUASES, http://www.quases.com/products/quases-imfp-tpp2m/ (accessed 19.09.2022).

[181] C.J. Powell, NIST Database for the Simulation of Electron Spectra for Surface Analysis (SESSA), Version 2.1.1, (2018). https://www.nist.gov/publications/nist-database-simulation-electron-spectra-surface-analysis-sessa-version-211 (accessed 19.09.2022).

[182] K. Henkel, C. Das, M. Kot, D. Schmeißer, F. Naumann, I. Kärkkänen, H. Gargouri, In-Gap States in Titanium Dioxide and Oxynitride Atomic Layer Deposited Films, *J. Vac. Sci. Technol., A* 35 (2016) 01B135.

[183] C. Das, M. Richter, M. Tallarida, D. Schmeisser, Electronic Properties of Atomic Layer Deposition Films, Anatase and Rutile TiO_2 Studied by Resonant Photoemission Spectroscopy, *J. Phys. D: Appl. Phys.* 49 (2016) 275304.

[184] M.F. Lichterman, S. Hu, M.H. Richter, E.J. Crumlin, S. Axnanda, M. Favaro, W. Drisdell, Z. Hussain, T. Mayer, B.S. Brunschwig, N.S. Lewis, Z. Liu, H.-J. Lewerenz, Direct Observation of the Energetics at a Semiconductor/Liquid Junction by Operando X-ray Photoelectron Spectroscopy, *Energy Environ. Sci.* 8 (2015) 2409–2416.

[185] J.-C. Hsu, Y.-H. Lin, P.W. Wang, X-ray Photoelectron Spectroscopy Analysis of Nitrogen-Doped TiO_2 Films Prepared by Reactive-Ion-Beam Sputtering with Various NH_3/O_2 Gas Mixture Ratios, *Coatings* 10 (2020) 47.

[186] E. Martínez-Ferrero, Y. Sakatani, C. Boissière, D. Grosso, A. Fuertes, J. Fraxedas, C. Sanchez, Nanostructured Titanium Oxynitride Porous Thin Films as Efficient Visible-Active Photocatalysts, *Adv. Funct. Mater.* 17 (2007) 3348–3354.

[187] R. Asahi, T. Morikawa, T. Ohwaki, K. Aoki, Y. Taga, Visible-Light Photocatalysis in Nitrogen-Doped Titanium Oxides, *Science* 293 (2001) 269–271.

[188] V. Pore, M. Heikkilä, M. Ritala, M. Leskelä, S. Areva, Atomic Layer Deposition of $TiO_{2-x}N_x$ Thin Films for Photocatalytic Applications, *J. Photochem. Photobiol., A* 177 (2006) 68–75.

[189] H.-E. Cheng, Y.-R. Chen, W.-T. Wu, C.-M. Hsu, Effect of Nitrogen Doping Concentration on the Properties of TiO_2 Films Grown by Atomic Layer Deposition, *Mater. Sci. Eng., B* 176 (2011) 596–599.

[190] K. Hukari, R. Dannenberg, E.A. Stach, Nitrogen Effects on Crystallization Kinetics of Amorphous TiO_xN_y Thin Films, *J. Mater. Res.* 17 (2002) 550–555.

[191] V. Pore, M. Ritala, M. Leskelä, T. Saukkonen, M. Järn, Explosive Crystallization in Atomic Layer Deposited Mixed Titanium Oxides, *Cryst. Growth Des.* 9 (2009) 2974–2978.

[192] E.J. Albenze, M.O. Thompson, P. Clancy, Molecular Dynamics Study of Explosive Crystallization of SiGe and Boron-Doped SiGe Alloys, *Ind. Eng. Chem. Res.* 45 (2006) 5628–5639.

[193] C. Buchner, W. Schneider, Explosive Crystallization in Thin Amorphous Layers on Heat Conducting Substrates, *J. Appl. Phys.* 117 (2015) 245301.

[194] K. Momma, F. Izumi, VESTA 3 for Three-Dimensional Visualization of Crystal, Volumetric and Morphology Data, *J. Appl. Crystallogr.* 44 (2011) 1272–1276.

[195] W.H. Baur, Über die Verfeinerung der Kristallstrukturbestimmung einiger Vertreter des Rutiltyps: TiO_2, SnO_2, GeO_2 und MgF_2, *Acta Cryst.* 9 (1956) 515–520.

[196] C.J. Howard, T.M. Sabine, F. Dickson, Structural and Thermal Parameters for Rutile and Anatase, *Acta Cryst. B* 47 (1991) 462–468.

[197] R.T. Downs, M. Hall-Wallace, The *American Mineralogist* Crystal Structure Database, *Am. Mineral.* 88 (2003) 247–250.

[198] I. Jelovica Badovinac, R. Peter, A. Omerzu, K. Salamon, I. Šarić, A. Samaržija, M. Perčić, I. Kavre Piltaver, G. Ambrožić, M. Petravić, Grain Size Effect on Photocatalytic Activity of TiO_2 Thin Films Grown by Atomic Layer Deposition, *Thin Solid Films* 709 (2020) 138215.

[199] M.R. Shaner, H.A. Atwater, N.S. Lewis, E.W. McFarland, A Comparative Technoeconomic Analysis of Renewable Hydrogen Production using Solar Energy, *Energy Environ. Sci.* 9 (2016) 2354–2371.

ORIGINAL PUBLICATIONS

Publication **I**   **Saari, J.**, Ali-Löytty, H., Kauppinen, M.M., Hannula, M., Khan, R., Lahtonen, K., Palmolahti, L., Tukiainen, A., Grönbeck, H., Tkachenko, N.V., Valden, M. Tunable Ti^{3+}-Mediated Charge Carrier Dynamics of Atomic Layer Deposition-Grown Amorphous TiO_2. *J. Phys. Chem. C* 126 (2022) 4542–4554.

Publication **II**   **Saari, J.**, Ali-Löytty, H., Lahtonen, K., Hannula, M., Palmolahti, L., Tukiainen, A., Valden, M. Low-Temperature Route to Direct Amorphous to Rutile Crystallization of TiO_2 Thin Films Grown by Atomic Layer Deposition. *J. Phys. Chem. C* 126 (2022) 15357–15366.

Publication **III** **Saari, J.**, Ali-Löytty, H., Honkanen, M., Tukiainen, A., Lahtonen, K., Valden, M. Interface Engineering of TiO_2 Photoelectrode Coatings Grown by Atomic Layer Deposition on Silicon. *ACS Omega* 6 (2021) 27501–27509.

Publication **IV** Ali-Löytty, H., Hannula, M., **Saari, J.**, Palmolahti, L., Bhuskute, B.D., Ulkuniemi, R., Nyyssönen, T., Lahtonen, K., Valden, M. Diversity of TiO_2: Controlling the Molecular and Electronic Structure of Atomic-Layer-Deposited Black TiO_2. *ACS Appl. Mater. Interfaces* 11 (2019) 2758–2762.

PUBLICATION
I

Tunable Ti³⁺-Mediated Charge Carrier Dynamics of
Atomic Layer Deposition-Grown Amorphous TiO₂

Jesse Saari, Harri Ali-Löytty, Minttu Maria Kauppinen, Markku Hannula,
Ramsha Khan, Kimmo Lahtonen, Lauri Palmolahti, Antti Tukiainen,
Henrik Grönbeck, Nikolai V. Tkachenko, and Mika Valden

Article

Tunable Ti³⁺-Mediated Charge Carrier Dynamics of Atomic Layer Deposition-Grown Amorphous TiO₂

Jesse Saari, Harri Ali-Löytty,* Minttu Maria Kauppinen, Markku Hannula, Ramsha Khan, Kimmo Lahtonen, Lauri Palmolahti, Antti Tukiainen, Henrik Grönbeck, Nikolai V. Tkachenko, and Mika Valden*

Read Online

ACCESS | 📊 Metrics & More | 📑 Article Recommendations | 🆂🅸 Supporting Information

ABSTRACT: Amorphous titania (am.-TiO₂) has gained wide interest in the field of photocatalysis, thanks to exceptional disorder-mediated optical and electrical properties compared to crystalline TiO₂. Here, we study the effects of intrinsic Ti³⁺ and nitrogen defects in am.-TiO₂ thin films via the atomic layer deposition (ALD) chemistry of tetrakis(dimethylamido)titanium-(IV) (TDMAT) and H₂O precursors at growth temperatures of 100−200 °C. X-ray photoelectron spectroscopy (XPS) and computational analysis allow us to identify structural disorder-induced penta- and heptacoordinated Ti^{4+} ions ($Ti_{5/7c}^{4+}$), which are related to the formation of Ti³⁺ defects in am.-TiO₂. The Ti³⁺-rich ALD-grown am.-TiO₂ has stoichiometric composition, which is explained by the formation of interstitial peroxo species with oxygen vacancies. The occupation of Ti³⁺ 3d in-gap states increases with the ALD growth temperature, inducing both visible-light absorption and electrical conductivity via the polaron hopping mechanism. At 200 °C, the in-gap states become fully occupied extending the lifetime of photoexcited charge carriers from the picosecond to the nanosecond time domain. Nitrogen traces from the TDMAT precursor had no effect on optical properties and only little on charge transfer properties. These results provide insights into the charge transfer properties of ALD-grown am.-TiO₂ that are essential to the performance of protective photoelectrode coatings in photoelectrochemical solar fuel reactors.
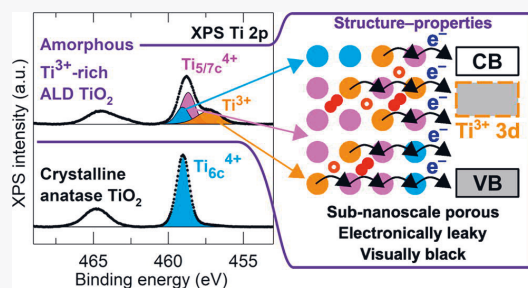
INTRODUCTION

Since the discovery of photoelectrochemical (PEC) water splitting introduced first by Fujishima and Honda in 1972 using n-type rutile titanium dioxide (TiO₂), photocatalysts based on crystalline TiO₂ have been widely studied materials.[1] Doping crystalline TiO₂ with substitutional nitrogen is an efficient means to extend the light absorption from UV to visible range and enable visible-light active TiO₂.[2] Recently, immense interest in amorphous TiO₂ (am.-TiO₂) has emerged for its exceptional charge transfer properties in photocatalytic applications. Based on computational studies, the am.-TiO₂ structure consists of mainly Ti–O₆ octahedra and also under- (e.g., Ti_{5c}) and overcoordinated (e.g., Ti_{7c}) titanium ions, whereas in crystalline TiO₂ only six-coordinated (Ti_{6c}) ions are present.[3,4] For example, in computational models of am.-TiO₂, pentacoordinated Ti ions (Ti_{5c}) are reported to be rather abundant (>20%).[3,5] However, experimental methods for the analysis of the amorphous structure considering coordination numbers of Ti ions are rarely reported. The disordered structure of am.-TiO₂ can induce exceptional optical and electrical properties that have been demonstrated to improve photocatalytic activity and protect photoelectrodes in photo-

electrochemical cells.[6−8] Particularly, amorphous "black" titania is regarded as a significant potential material for photocatalytic applications.[7,9,10]

Atomic layer deposition (ALD) is known for providing thin films with excellent controllability, uniformity, and conformality, and provides a potential method to modify the TiO₂ defect composition in a controlled manner via surface chemical reactions.[11−14] Particularly, the ALD growth temperature is an essential factor affecting surface reaction pathways during the growth process.[15,16] For example, an alkylamido organometallic ALD precursor, tetrakis(dimethylamido)titanium (TDMAT), has been shown to leave nitrogen residues into as-grown TiO₂ thin films, especially at lower growth temperatures.[13,17,18] Use of a higher growth temperature (200 °C) has been found to decrease the amount of nitrogen but
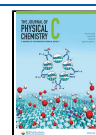
simultaneously result in the formation of Ti^{3+} species.[12,13,19] These Ti^{3+} defects can increase electrical conductivity and induce visible-light absorption in am.-TiO_2.[12] The mechanism is different from the visible absorption induced by substitutional nitrogen doping of crystalline TiO_2 but similar to the hydrogenated "black" TiO_2 that can be also categorized as reduced TiO_2 with a disordered structure.[7,12,19−22] The commonly accepted view is that an oxygen vacancy within TiO_2 is surrounded by three pentacoordinated Ti_{5c} ions and initially two of them are Ti^{3+} ions.[20,23] These Ti^{3+} defects carry unpaired excess electrons that can couple with phonons from vibrations of surrounding ions and form quasiparticles called electron polarons.[7,24] These polarons can hop from Ti^{3+} ion to an adjacent Ti^{4+} ion converting it to a Ti^{3+} ion, which is known as polaron hopping.[24,25] Based on molecular dynamics simulations, Deskins et al. proposed that electron transport in amorphous TiO_2 depends on the distances between adjacent Ti^{4+} ions, whereas hole transport is related to the distances between Ti^{3+} ions.[4] Consequently, these computational results imply that the polaron hopping mechanism is responsible for the conductivity of TiO_2 and strongly related to the concentration of Ti^{3+} defects.[4,7,20,25] This charge transport mechanism and its relation to the Ti^{3+} defects is also supported by experimental studies.[21,26] Furthermore, Ti^{3+} defects form energy states within the band gap enabling light absorption in the visible range.[7,12,27,28]

Regarding charge carrier dynamics and kinetics, careful investigation of in-gap states, especially electron and hole traps, in am.-TiO_2 is needed.[28] According to the current understanding, the disordered structure, undercoordinated ions, and elongated metal−oxygen bonds in amorphous metal oxides may induce electron and hole traps in the band gap.[5,29] Additionally, Ti^{3+} defects have been reported to generate in-gap trap states with intrinsic self-trapped electrons.[20,28,30] However, the nature and relationship of these trap states and the structure of am.-TiO_2 are still under debate. Experimentally, in-gap trap states have been studied by various methods, such as photoelectron spectroscopy (PES) and transient absorption spectroscopy (TAS).[28,31−33] Based on the reported PES valence band (VB) spectra, electron trap states of TiO_2 are commonly located around 0.2−1.2 eV below the Fermi level.[21,24,26,28,31] Transient absorption spectroscopy, instead, provides a method to study the dynamics of charge carriers, and thus determine, e.g., carrier lifetime that is a critical factor to determine the photocatalytic activity of a material.[32−35]

This work utilizes X-ray photoelectron spectroscopy (XPS) analysis and density functional theory (DFT) calculations to identify structural disorder-induced penta- and heptacoordinated Ti ions ($Ti_{5/7c}^{4+}$), and examines how titanium and nitrogen defects of amorphous TiO_2 can be controlled by the ALD growth temperature while using TDMAT and H_2O as precursors. The lower deposition temperature causes trapping and adsorption of nitrogen-containing reaction byproducts, whereas the higher growth temperature leads to enhanced byproduct desorption as well as increased concentration of Ti^{3+} and penta-/heptacoordinated $Ti_{5/7c}^{4+}$ species. The structural disorder of am.-TiO_2 involving under- and over-coordinated Ti ions is found to provide trap states for charge carriers, which recombine in the picosecond time domain. Ti^{3+} defects with intrinsic self-trapped electrons in the band gap states allow visible-light absorption, extend charge carrier lifetime to the nanosecond (ns) time domain, and induce electrical conductivity. The structural disorder alone induces

only broadening of core-level peaks, whereas the formation of Ti^{3+} defects mediates a chemical shift also in the 2p binding energy of neighboring Ti^{4+} ions. Controlling the optical and electrical properties of amorphous TiO_2 by modifying the defects is a promising approach to tailor optimized am.-TiO_2 thin films for many fields of applications including photocatalysis and protective photoelectrode coatings in photoelectrochemical solar fuel reactors.

■ EXPERIMENTAL SECTION

Substrates. The P-doped (resistivity: 1−10 Ω cm) n-Si(100) wafers from SIEGERT WAFER GmbH (Germany) cleaved into 10 mm × 10 mm × 0.525 mm pieces were used as substrates in photoelectron spectroscopy (PES), grazing incidence X-ray diffraction (GIXRD), and ellipsometry experiments. For UV−vis spectroscopy, transient absorption spectroscopy (TAS), and electrical conductivity measurements, UV-grade fused silica (quartz) (10 mm × 10 mm × 1 mm) from Präzisions Glas & Optik GmbH (Germany) was used as a substrate.

Atomic Layer Deposition. The ALD of TiO_2 was carried out using a Picosun Sunale ALD R-200 Advanced reactor and tetrakis(dimethylamido)titanium(IV) ($Ti(N(CH_3)_2)_4$, TDMAT, electronic grade 99.999+%, Sigma-Aldrich) and Milli-Q type 1 ultrapure water as precursors. To reach the proper TDMAT precursor vapor pressure, the bubbler was heated to 76 °C, and to prevent condensation of the precursor gas the delivery line was heated to 85 °C. The water bubbler was maintained at 18 °C using a Peltier element for stability control. Argon (99.9999%, Oy AGA Ab, Finland) was used as a carrier gas. During the deposition, the continuous Ar flow in the TDMAT and H_2O lines was 100 sccm. The ALD cycle consisted of the 1.6 s TDMAT pulse followed by the 0.1 s H_2O pulse. Between each pulse, the excess precursor was pumped during the 6.0 s purge period. TiO_2 films were deposited at the growth temperatures of 100, 150, 175, and 200 °C. The thicknesses of TiO_2 films were verified by ellipsometer (Rudolph Auto EL III Ellipsometer, Rudolph Research Analytical) using the helium−neon laser (λ = 632.8 nm) as a light source. The required number of ALD cycles for 30 nm thick TiO_2 at growth temperatures of 100, 150, 175, and 200 °C were 480, 636, 733, and 870, respectively. Based on the GIXRD measurements shown in Figure S1, the as-deposited 30 nm thick thin films grown at temperatures between 100 and 200 °C were amorphous.

Anatase TiO_2(30 nm) Reference. The anatase TiO_2(30 nm) samples were prepared from ALD TiO_2 (30 nm, 100 °C) grown on Si(100) substrates by a heat treatment in air at 500 °C for 45 min.

Photoelectron Spectroscopy (XPS, Ultraviolet Photoelectron Spectroscopy (UPS)). Photoelectron spectroscopy (PES) measurements consisting of X-ray photoelectron spectroscopy (XPS) and ultraviolet photoelectron spectroscopy (UPS) were conducted in a NanoESCA spectromicroscope (Omicron Nanotechnology GmbH) in ultra-high vacuum (UHV) with a base pressure below 1 × 10^{-10} mbar. For core-level XPS, focused monochromatized Al Kα ($h\nu$ = 1486.5 eV) was used as excitation radiation, whereas in UPS measurements focused non-monochromatized He Iα radiation ($h\nu$ = 21.22 eV) from HIS 13 VUV Source (Focus GmbH) was utilized to study the valence band structure. The angle-resolved XPS (ARXPS) measurements were carried out using non-monochromatized DAR400 X-ray source (Al Kα) and

Argus hemispherical electron spectrometer (Omicron Nanotechnology GmbH). The core-level XP spectra were analyzed by least-squares fitting of Gaussian−Lorentzian lineshapes and using a Shirley-type background. UPS valence band spectra were analyzed by fitting a Tougaard-type background. The Ti 2p spectra were fitted using the anatase TiO_2 Ti $2p_{3/2}$ reference peak shape for the six-coordinated Ti^{4+} peak (Ti_{6c}^{4+}), and the amorphous disordered structure was represented by the pentacoordinated Ti^{4+} (Ti_{5c}^{4+}) and Ti^{3+} peaks. The binding energy (BE) scale of the spectra was calibrated by fixing the O^{2-} peak of TiO_2 to 530.20 eV. CasaXPS version 2.3.22 PR1.0[36] was used as analysis software, and the Scofield photoionization cross-sections were used as relative sensitivity factors.[37]

Computational Analysis of Core-Level Shifts. Modeling the amorphous phase of titania (am.-TiO_2) is challenging due to its lack of long-range order and a defined crystal structure. Previous computational studies have employed molecular dynamics to generate structural models for am.-TiO_2 using the melt-and-quench method.[5,38] As the structural models for am.-TiO_2 necessarily have large unit cells containing >200 atoms, sampling the core-level shifts (CLSs) of all atoms for many structures becomes infeasible. Moreover, it is not clear how representative the melt-and-quench structures are for the experimental am.-TiO_2 structures. Because of structural ambiguity, we performed calculations for both the crystalline anatase phase and a model of am.-TiO_2.

Spin-polarized calculations were performed using the Vienna Ab initio Simulation Package (VASP; version 5.4.4).[39−42] The GGA + U approach was employed using the Perdew−Burke−Ernzerhof (PBE) functional[43,44] with a Hubbard correction[45] of U = 4.2 eV applied to the 3d orbitals of Ti atoms. This value for the correction has been used previously in calculations involving amorphous TiO_2[38] and anatase;[46] see the Supporting Information for more details concerning the choice and impact of the U value. The valence−core interactions were treated with the projector augmented-wave (PAW) method,[47,48] and the valence configurations were $2s^2 2p^4$ (O) and $3s^2 3p^6 4s^2 3d^2$ (Ti). A plane-wave basis set with a cutoff energy of 500 eV was used for geometry optimizations and core-level shift calculations. The pristine anatase bulk was optimized using a 12 × 12 × 4 Γ-centered k-point mesh until residual forces were less than 0.01 eV/Å. The optimized lattice parameters are a = 3.86 and c = 9.74 Å, which are in fair agreement with experimental values (a = 3.78 Å, c = 9.51 Å).[49,50] The band gap was found to be 2.64 eV, which is close to the previously reported value of 2.87 eV using the PBE functional with a Hubbard-U value of 4.0 eV.[51] A 144 atom 4 × 3 × 1 supercell of the optimized bulk was used for subsequent calculations to reduce the interaction of the oxygen vacancy with its periodic image. Model structures for am.-TiO_2 (15 in total) were obtained from the work of Mora-Fonz et al.[5] The unit cells and atomic positions of the model structures[5] were re-optimized using the present computational setups. The lowest energy structure (see Figure S2a) was used in the core-level shift calculations. Due to the large size of the amorphous TiO_2 unit cell and the large supercell for anatase, the sampling of the Brillouin zone was restricted to the Γ-point.

The oxygen vacancy formation energy E_f^{vac} was calculated as

$$E_f^{vac} = E_{tot}^{vac} + \frac{1}{2} E_{O_2} + E_{tot} \tag{1}$$

where E_{tot} is the total energy of the pristine structure, E_{tot}^{vac} is the total energy of the same structure containing a single oxygen vacancy, and E_{O_2} is the energy of an oxygen molecule in the gas phase. Bader charge analyses were performed using the code developed by the Henkelman group.[52−55]

CLSs were calculated with respect to a reference atom in the final state picture, i.e., complete screening of the core hole by valence electrons was assumed. The core-level shifts were computed systematically for all atoms in the supercells. The structures with a core hole in Ti 2p or O 1s were obtained using a PAW potential with an electron−hole in the 2p and 1s shell of Ti and O, respectively. As the studied systems have band gaps, the charge neutrality in the presence of a core hole was maintained by employing a homogeneous jellium background. To facilitate the comparison with experiments, a Gaussian fit was applied to the CLS peaks, with a standard deviation of 0.43. The parameters are chosen such that they reproduce a qualitatively similar width at half-maximum as the peaks in the experimental spectra. All CLS values were shifted so that the maximum of the largest fitted Gaussian peak was centered at zero.

Grazing Incidence X-ray Diffraction (GIXRD). The phase structure of the ALD TiO_2 samples was defined via grazing incidence X-ray diffraction (GIXRD, PANalytical X'Pert³ MRD diffractometer) with Cu Kα radiation (λ = 1.5406 Å, $h\nu$ = 8.05 keV) and 45 kV and 40 mA cathode voltage and current, respectively. The samples were scanned in 2θ between 20 and 52° using grazing-incidence angle Ω = 0.3°. The background was removed from each of the scans to allow easier comparison of the measured GIXRD patterns.

Electrical Conductivity Measurement. Electrical conductivity was determined by measuring the sheet resistance of the am.-TiO_2 thin film grown on quartz substrates using the four-probe method. In the measurement, four nickel-plated tungsten probe tips (Picoprobe ST-20-5-NP, GGB Industries Inc.) were positioned on the sample surface (size 10 mm × 10 mm) in line with equal 2 mm spacing, and a linear scan voltammetry measurement was performed at 100 mV/s with an Autolab PGSTAT101 potentiostat (Metrohm AG). The sheet resistance, R_s, for the given configuration was calculated by

$$R_s = 0.7744 \cdot \frac{\pi}{\ln(2)} \frac{\Delta V}{I} \tag{2}$$

where ΔV is the voltage difference over the two inner probe tips, I is the current through the outer two probe tips, and the constant 0.7744 is the geometric correction factor.[56] Conductivity was then calculated as follows

$$\text{conductivity} = \frac{1}{\rho} = \frac{1}{R_s \cdot t} \tag{3}$$

where ρ is the film resistivity and t is the am.-TiO_2 film thickness.

Steady-State UV−Vis Spectroscopy. The optical properties were measured on 30 nm thick am.-TiO_2 films deposited on quartz substrates. Measurements were conducted by measuring both the transmission, T, and reflectance, R, of the am.-TiO_2 film with an integrating sphere module of a spectrophotometer (PerkinElmer 1050). A reflection-corrected formula was used for calculating the absorption $A = -\log[T/(1 - R)]$.[57]

Sub-Nanoscale Porosity Modeling. The sub-nanoscale porosity of ALD am.-TiO$_2$ thin films was determined based on the refractive index results measured by ellipsometer (Rudolph Auto EL III Ellipsometer, Rudolph Research Analytical) using the helium−neon laser (λ = 632.8 nm) as a light source and the Lorentz−Lorenz effective medium approximation (EMA).[58] The sub-nanoscale porosity was calculated using the EMA equation

$$\frac{n^2 - 1}{n^2 + 2} = (1 - p)\frac{n_{\text{anatase}}^2 - 1}{n_{\text{anatase}}^2 + 2} + p\frac{n_{\text{air}}^2 - 1}{n_{\text{air}}^2 + 2} \qquad (4)$$

where p is the sub-nanoscale porosity and n, n_{anatase}, and n_{air} are the refractive indices of am.-TiO$_2$, anatase TiO$_2$ reference (n = 2.396), and air (n = 1.000), respectively.

Transient Absorption Spectroscopy (TAS). Transient absorption spectra of all the samples were measured using a femtosecond pump−probe setup. The samples were excited with a wavelength of 320 nm in a transmittance mode in both UV−vis and near-infrared (NIR) regions. The fundamental laser pulses were generated using the Ti:sapphire laser, Libra F (Coherent Inc., 800 nm) with a repetition rate of 1 kHz. The fundamental beam was split into two, and the main part of the beam was directed onto the optical amplifier (Topas C, Light Conversion Ltd.) to produce the desired wavelength of 320 nm in our study. The rest of the fundamental beam was delivered to a white continuum generator (sapphire crystal) for sample probing. The probe light was further split into reference and signal beams, which were focused on the samples. The lifetime decay of the samples was measured up to 5 ns for all the samples.

■ RESULTS AND DISCUSSION

To investigate the effect of the ALD growth temperature on the chemical and electronic structures of am.-TiO$_2$, the 30 nm thick ALD am.-TiO$_2$ grown at 100, 150, 175, and 200 °C was measured by XPS and UPS. Figure 1 shows Ti 2p and O 1s XP spectra of the 30 nm thick ALD am.-TiO$_2$ deposited at different growth temperatures. Annealing the sample grown at 100 °C in air at 500 °C resulted in anatase TiO$_2$ (Figure S1), which served as a reference for the six-coordinated Ti^{4+} (Ti$_{6c}^{4+}$).[3,4] Anatase TiO$_2$ showed a narrow Ti 2p$_{3/2}$ peak at 459.0 ± 0.1 eV that was fitted with a constrained peak width and position to the spectra recorded for ALD am.-TiO$_2$ samples. All of the Ti 2p spectra of ALD am.-TiO$_2$ thin films in Figure 1a show clear evidence of Ti^{3+} defects as a shoulder at 457.3 ± 0.1 eV.[12,19] The middle component is assigned to structural disorder-induced Ti^{4+} ions (Ti$_{5/6/7c}^{4+}$), which are related to the nearest or next-nearest neighbors of oxygen vacancies or interstitial peroxo species that are responsible for the formation of Ti^{3+} defects in am.-TiO$_2$. The peak separation in the binding energy (BE) between Ti$_{6c}^{4+}$ and Ti$_{5/6/7c}^{4+}$ peaks was 0.39 eV. Figure 1b shows that the O 1s peak consists mainly of the O−Ti component (O^{2-}) at 530.2 eV and a minor peak at 532.0 ± 0.2 eV, regardless of the ALD growth temperature. The component at higher BE is assigned to either −OH/O−C or interstitial peroxo (O$_2^{2-}$) species. Additionally, Figure S4 highlights the differences between Ti 2p spectra and the similarity of O 1s spectra shown in Figure 1. Interestingly, despite the distinct presence of oxygen vacancies-induced Ti^{3+} ions, the O/Ti atomic ratios of all am.-TiO$_2$ thin films are close to 2 (Figure S5), implying the displacement of oxygen ions within the films instead of removal of them upon vacancy
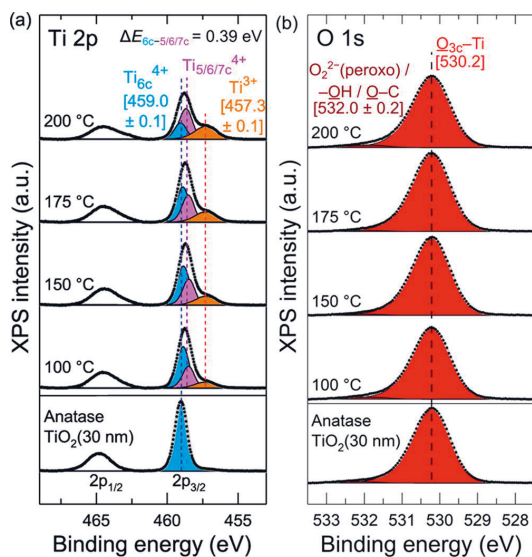

Figure 1. (a) Ti 2p and (b) O 1s XP spectra of the 30 nm thick ALD am.-TiO$_2$ grown at 100, 150, 175, and 200 °C. Anatase TiO$_2$ (30 nm) is used as a reference sample for the six-coordinated Ti$_{6c}^{4+}$ peak.

formation. The result can be rationalized by the presence of local oxygen-rich centers such as interstitial peroxo species.

As a comparison with the proposed experimental XPS Ti 2p peak fitting (Figure 1), Figure S6 presents the more traditional peak fitting and analysis of the Ti^{4+} component and analysis of the full width at half-maximum (FWHM). The FWHM is clearly larger for am.-TiO$_2$ compared to crystalline anatase; moreover, the peak width increases as the ALD growth temperature is increased (details on the fitting parameters are presented in Table S2). The fitting results suggest that it is not sufficient to fit the Ti^{4+} 2p of am.-TiO$_2$ with only one component. Using a second component results in an adequate fit. A slight shift in the binding energy of Ti$_{6c}^{4+}$ and Ti$_{5/6/7c}^{4+}$ peak positions can originate from differences in the amount of more rare over- and undercoordinated Ti ions (Ti$_{8c}^{4+}$, Ti$_{7c}^{4+}$, Ti$_{4c}^{4+}$) and wide distributions of bond lengths and angles, which are also partly attributed to local effects of polarons.[3−5,24]

To the best of our knowledge, there are no previously reported efforts to identify Ti^{4+} ions (Ti$_{5/6/7c}^{4+}$), which are related to the nearest or next-nearest neighbors of oxygen vacancies, experimentally by photoelectron spectroscopy as proposed in this work. Therefore, we performed density functional theory calculations of CLSs mediated by an oxygen vacancy or interstitial peroxo species in anatase TiO$_2$ and an am.-TiO$_2$ structure. Figure 2 presents the results from the computational analysis of oxygen defect-induced CLSs in anatase TiO$_2$. In the case of pristine anatase, there were no CLSs in either Ti 2p or O 1s since all of the Ti/O sites have identical environments.

In the second case, the oxygen vacancy was formed by removing one of the lattice oxygens from the 144-atom bulk anatase supercell and re-relaxing the atomic positions of the resulting structure (see Figure 2c). Upon vacancy creation, the two excess electrons can either localize fully on nearby pentacoordinated Ti$_{5c}$ cations or partially, with one electron on a Ti$_{5c}$ ion and the other one delocalized over the entire
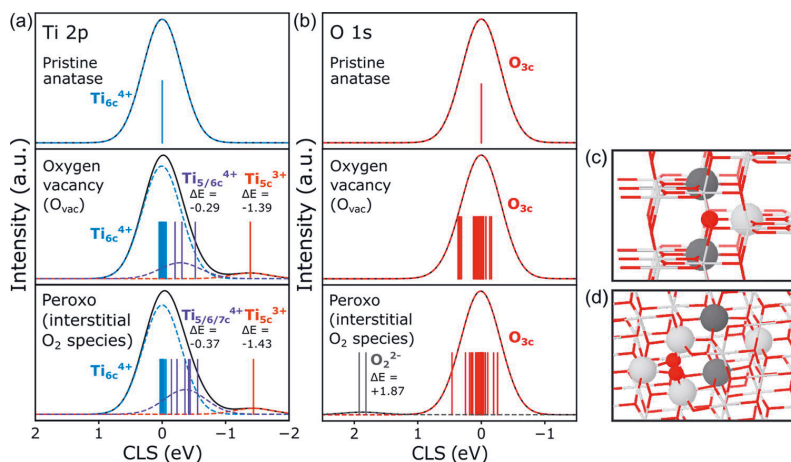
Figure 2. (a) Ti 2p and (b) O 1s core-level shifts of anatase TiO$_2$. The top row corresponds to pristine TiO$_2$, the middle row corresponds to TiO$_2$ with one oxygen vacancy, and the bottom row corresponds to an interstitial peroxo species containing TiO$_2$. The vertical lines indicate the CLS of individual atoms. (c) Pristine anatase bulk shows the oxygen atom that is removed to create the oxygen vacancy (red sphere) and the titanium atoms (gray spheres) coordinated to it. (d) Structure of the anatase bulk with interstitial peroxo species (red spheres) showing the Ti atoms (Ti$_{7c}^{4+}$) directly coordinated to the peroxo species and the three Ti atoms (Ti$_{5c}^{4+/3+}$) that surround the oxygen vacancy. Ti^{3+} ions are indicated by a darker shade of gray.

structure.[20,23] For the oxygen vacancy containing anatase, three groupings of peaks in the Ti 2p spectrum can be identified. Most Ti atoms in the bulk have CLS values within 0.11 eV of each other (blue peak labeled as Ti$_{6c}^{4+}$). These atoms are not directly connected to the created vacancy and are six-coordinated and have the same Bader charges as in the pristine bulk. The next group of shifts with lower binding energy are within 0.32 eV of each other, i.e., more spread out than the Ti$_{6c}^{4+}$ peak. The maximum of the fitted Gaussian peak (violet peak labeled as Ti$_{5/6c}^{4+}$) is shifted by −0.29 eV from the Ti$_{6c}^{4+}$ peak. There are six shifts in total, three at −0.12 eV, two at −0.22 eV, and one at −0.43 eV. The most negatively shifted value in the group comes from the pentacoordinated Ti$_{5c}$ next to the oxygen vacancy, which accepts the least excess charge from the vacancy. The five others are Ti$_{6c}$ atoms that are the next-nearest neighbors to the vacancy. The most negative shifts in the Ti 2p spectrum come from the two pentacoordinated Ti$_{5c}^{3+}$ cations, where the excess electrons from the vacancy are localized. The peak (orange peak labeled as Ti$_{5c}^{3+}$) maximum is shifted by −1.39 eV compared to the Ti$_{6c}^{4+}$ peak. The O 1s CLS of the oxygen vacancy containing anatase has two groups of values. Most oxygen atoms in the bulk have values within a range of 0.28 eV. Five oxygen anions give more positive values with the peak maximum (note: the fitted peak is not shown in Figure 2b) shifted by 0.36 eV compared to the main peak. These are oxygen anions that are the next-nearest neighbors to the vacancy and are in the same atomic layer as the vacancy.

In the third case, since the experimental XPS data show that amorphous titania retains a constant oxygen/titania ratio for increasing the ALD growth temperature (Figure S5), the possibility of having interstitial peroxo species in the anatase bulk was also investigated (see Figure 2d). The structure was generated by displacing one oxygen from its lattice position and placing it close to another oxygen. This creates an interstitial O$_2$ species (O$_2^{2-}$) connected to three heptacoordinated Ti$_{7c}$ cations. The displaced oxygen leaves behind an

oxygen vacancy with three pentacoordinated Ti$_{5c}$ cations. The anatase structure with interstitial peroxo species has very similar Ti 2p shifts compared to anatase with an oxygen vacancy. The most negative Ti$_{5c}^{3+}$ shift differs only by 0.04 eV, meaning that the oxygen vacancy created by the displacement of the lattice oxygen gives the same CLS signature as one created by the removal of oxygen. The main difference between the two spectra is the Ti$_{5/6/7c}^{4+}$ peak. The maximum of the fitted peak is shifted slightly more to the negative CLS for the peroxo structure (−0.37 eV). This is due to the fact that the three Ti$_{7c}^{4+}$ cations that are coordinated to the peroxo species also have negative shifts compared to the ideal Ti$_{6c}^{4+}$ further away from the defect sites. The O 1s spectrum of the peroxo anatase shows that the shifts of the oxygen anions are slightly more spread out than in the case of anatase with oxygen vacancy. In addition, the peroxo species gives a positive shift with a fitted peak maximum at +1.87 eV.

These computational results provide strong support for the proposed experimental XPS peak fitting (Figure 1), and especially, for identifying oxygen displacement-induced Ti^{4+} ions (Ti$_{5/6/7c}^{4+}$) from the spectra. In addition to the more negative shift of the Ti$_{5/6/7c}^{4+}$ peak (−0.37 eV) due to the interstitial peroxo species, oxygen vacancy formation via displacement of oxygen ions corresponds well with the experimentally determined rather stoichiometric and constant O/Ti ratio of 2. Albeit there are no remarkable differences between measured XPS O 1s spectra (Figure 1b), the slightly more distinct peak around 532 eV may imply more peroxo species in Ti^{3+}-rich am.-TiO$_2$ grown at 200 °C.

Besides anatase TiO$_2$, oxygen vacancy-induced core-level shifts in am.-TiO$_2$ were also computed. The calculated Ti 2p and O 1s core-level shifts for pristine and oxygen vacancy containing am.-TiO$_2$ (Figure S7) and the details of the analysis are presented in the Supporting Information. The Ti 2p shifts of pristine am.-TiO$_2$ are spread out but no obvious peak assignment correlating to the five-, six-, or seven-coordinated

Ti atoms can be made, i.e., the shifts do not correlate with the coordination number of the Ti atoms. Experimentally, this pristine amorphous phase should, in principle, give a broader peak than the anatase bulk due to the large spread of CLS. This is indeed observed in the experimental XPS Ti 2p data in Figure S6. Similarly, the O 1s shifts also span a broad range, with negative shifts showing slightly more separation between the shifts. For the oxygen vacancy containing am.-TiO$_2$, the shifts coming from five-, six-, and seven-coordinated Ti^{4+} cations are somewhat bunched together compared to the pristine bulk. The two Ti^{3+} cations have significant negative shifts, with the maximum of the fitted peak sitting at −1.37 eV. This is in quite good agreement with the assigned experimental Ti^{3+} peak, which is shifted by −1.7 eV compared to the anatase reference peak. Furthermore, despite the wide distribution of assorted Ti$_{5/6/7c}^{4+}$ core-level shifts that are not clearly correlating with any specific Ti ion bonding environment in am.-TiO$_2$, the computational peak fitting function was able to deconvolute two distinct Ti$_{5/6/7c}^{4+}$ peaks with CLS of −0.35 eV for oxygen vacancy containing am.-TiO$_2$ but not for pristine am.-TiO$_2$ (Figure S7). However, it should be noted that compared to computational results from anatase TiO$_2$, am.-TiO$_2$ is more challenging and the in-depth understanding of how a position of individual Ti$_{5/6/7c}^{4+}$ ion correlates with the observed CLS remains unclear.

Figure 3 presents the N 1s XP spectra of 30 nm thick ALD am.-TiO$_2$ deposited at different growth temperatures. Three
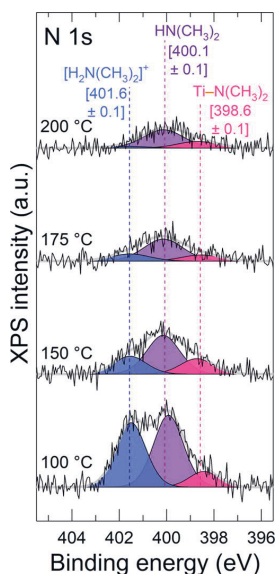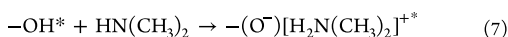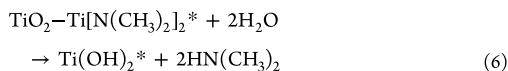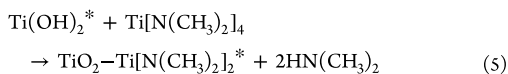

Figure 3. N 1s XP spectra of 30 nm thick ALD am.-TiO$_2$ grown at 100, 150, 175, and 200 °C.

nitrogen components were identified based on the surface reactions related to the TDMAT + H$_2$O process shown in eqs 5−7.[14,59]

$$Ti(OH)_2{}^* + Ti[N(CH_3)_2]_4$$
$$\rightarrow TiO_2-Ti[N(CH_3)_2]_2{}^* + 2HN(CH_3)_2 \qquad (5)$$

$$TiO_2-Ti[N(CH_3)_2]_2{}^* + 2H_2O$$
$$\rightarrow Ti(OH)_2{}^* + 2HN(CH_3)_2 \qquad (6)$$

$$-OH^* + HN(CH_3)_2 \rightarrow -(O^-)[H_2N(CH_3)_2]^{+*} \qquad (7)$$

The component at low binding energy (398.6 ± 0.1 eV) was assigned to unreacted Ti−N(CH$_3$)$_2$ bonds due to the incomplete TDMAT dissociation (eq 5).[14,60] Regarding ALD from TDMAT and H$_2$O, dissociation of TDMAT through the scission of the N−Ti bond is energetically more favorable than breaking of N−C bonds of the TDMAT molecule.[61] Moreover, dimethylamine (N(CH$_3$)$_2$) formation is preferred at growth temperatures <200 °C, whereas at higher temperatures decomposition of TDMAT and dimethylamine molecules leads to the increase of methane and carbon-containing species, i.e., carbon contamination in the coating.[62] Consequently, the middle component most likely originates from trapped or re-adsorbed HN(CH$_3$)$_2$ reaction byproducts (eq 6), which can also react with surface −OH groups and form protonated H$_2$N(CH$_3$)$_2^+$ species (eq 7) causing the high binding energy peak in N 1s spectra.[14,59] Figure S8, showing the angle-resolved XPS (ARXPS) analysis of the N 1s spectrum for 30 nm thick as-deposited ALD am.-TiO$_2$ grown at 100 °C, confirms that the component at 400.1 eV has higher intensity with 60° photoelectron take-off angle, indicating the corresponding species to locate closer to the surface compared to the high binding energy (401.7 eV) N species. This further supports assigning the component at 400.1 eV to the HN(CH$_3$)$_2$ reaction byproducts instead of interstitial nitrogen, which is also known to appear around 400 eV.[63] The oxidized nitrogen species (Ti−N−O) can also have N 1s around 400 eV.[64,65] Although the Ti−N−O species cannot be completely excluded based on the N 1s binding energy alone, their presence is considered unlikely. The formation of oxidized nitrogen species would require the decomposition of the HN(CH$_3$)$_2$ product, which is stable up to 227 °C.[62]

The relative concentrations of titanium and nitrogen species as a function of the ALD growth temperature, presented in Figure 4, were obtained by a quantitative analysis of the XP spectra. Figure 4a shows that as the growth temperature is increased, the concentrations of Ti^{3+} and oxygen displacement-induced Ti^{4+} ions (Ti$_{5/6/7c}^{4+}$) steadily increase, simultaneously with the decreasing number of Ti$_{6c}^{4+}$ ions, and when the growth temperature of 150 °C is exceeded, >50% concentration of O ions displacement-mediated titanium defects (Ti^{3+} + Ti$_{5/6/7c}^{4+}$) starts to dominate the amorphous titania structure. At the growth temperature of 200 °C, the amount of Ti^{3+} defects is more than double compared to am.-TiO$_2$ grown at 100 °C. The results are also concordant with the theory that the concentration of Ti$_{5/6/7c}^{4+}$ ions increases together with the Ti^{3+} defects since they both arise due to the displacement of oxygen ions in the am.-TiO$_2$ structure.[20,23]

Deskins et al. used classical molecular dynamics to study amorphous TiO$_x$ with different stoichiometries and calculated the probabilities of Ti^{4+}−O−Ti^{4+} and Ti^{3+}−O−Ti^{3+} linkages and average Ti^{4+}/Ti^{4+} and Ti^{3+}/Ti^{3+} distances.[4] There are always two Ti^{3+} ions involved in the Ti^{3+}−O−Ti^{3+} bond structure but because Ti^{4+}−O−Ti^{3+} connections also exist, the concentration of Ti^{3+} defects cannot be directly calculated by multiplying the probability by 2. Consequently, concerning the experimental results shown in Figure 4a, the am.-TiO$_2$ deposited at 100 °C (Ti^{3+}/Ti$_{tot}$ = 12%) may have Ti^{3+}−O−
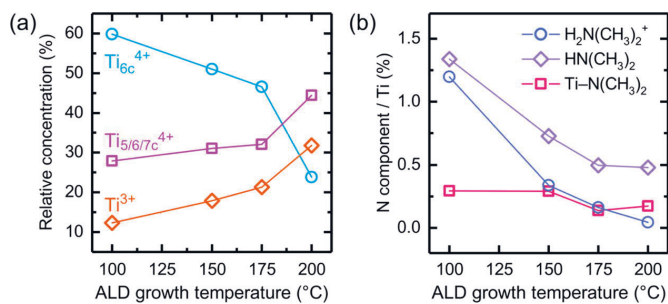
Figure 4. XPS analysis of (a) Ti and (b) N components for 30 nm thick ALD am.-TiO$_2$ grown at 100, 150, 175, and 200 °C.
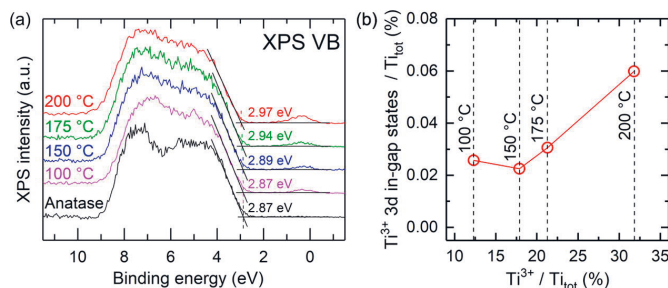

Figure 5. (a) VB XP spectra of 30 nm thick ALD am.-TiO$_2$ grown at 100, 150, 175, and 200 °C. Anatase TiO$_2$(30 nm) is shown as a reference for defect-free crystalline TiO$_2$. (b) The relative in-gap state concentration as a function of Ti^{3+} concentration for 30 nm thick ALD am.-TiO$_2$ grown at 100, 150, 175, and 200 °C.

Ti^{3+} linkage probability even less than 0.05, which, based on the work by Deskins et al., corresponds with am.-TiO$_{1.90-2.00}$ and average Ti^{3+}/Ti^{3+} distance of 3−7 Å. By contrast, am.-TiO$_2$ deposited at 200 °C (Ti^{3+}/Ti$_{tot}$ = 32%) exhibits most likely higher Ti^{3+}−O−Ti^{3+} linkage probability and thus average Ti^{3+}/Ti^{3+} distance around 3 Å, which is the minimum distance within am.-TiO$_2$.[4] These differences in the hopping distance were suggested to explain enhanced hole conduction in am.-TiO$_2$ with a higher Ti^{3+} defect concentration.[4] Despite the fact that in this work, the O/Ti ratio of am.-TiO$_2$ thin films is close to 2 (Figure S5), and Deskins et al. studied amorphous titania with different stoichiometries, both studies involve similar phenomena and Ti^{3+} defects within am.-TiO$_2$.[4]

Regarding nitrogen impurities as a function of ALD growth temperature shown in Figure 4b, the concentrations of TDMAT fragments, i.e., HN(CH$_3$)$_2$ and H$_2$N(CH$_3$)$_2$$^+$ species, are clearly higher in am.-TiO$_2$ grown at 100 °C than at 150−200 °C, whereas the amount of unreacted Ti−N(CH$_3$)$_2$ remains rather constant. This is probably due to the slower desorption or re-adsorption of the reaction byproducts during the ALD growth at lower growth temperatures, albeit there are still some trapped HN(CH$_3$)$_2$ in am.-TiO$_2$ deposited at 200 °C. Based on the relative concentrations of elements of the am.-TiO$_2$ samples shown in Table S3, all of the samples contain also some carbon impurities (3−5 atom %). It is, however, not feasible to differentiate these species from adventitious carbon that results from the sample transfer between the ALD chamber and the XPS system.

To acquire a deeper understanding of how titanium and nitrogen defects influence the in-gap states, the XPS valence band (VB) spectra of am.-TiO$_2$ grown at 100, 150, 175, and 200 °C were measured. The analysis of XPS valence band

spectra in Figure 5a reveals an in-gap state in the binding energy range of 0.3−0.4 eV, which can be assigned to the Ti^{3+} 3d electronic state.[28,31] Similar defect state is also seen in the computational density of state analysis when oxygen vacancy is introduced in the anatase TiO$_2$ lattice (Figure S9). Accordingly, the intensity of the in-gap state increases linearly with the Ti^{3+} concentration determined from the Ti 2p transition between growth temperatures of 150 and 200 °C. At 100 °C, some deviation from the trend is observed (Figure 5b). This deviation is likely due to the high amount of nitrogen species within the 100 °C grown am.-TiO$_2$, which may also introduce the density of states within the band gap.[66] Nevertheless, the observed in-gap state peak is clearly mainly induced by the Ti^{3+} defects and not by the N species. The anatase TiO$_2$ reference does not have any Ti^{3+} and shows no in-gap state. An attempt was made to measure in-gap states with ultraviolet photoelectron spectroscopy (UPS) but the peak was not clearly resolved (Figure S10). The UPS VB measurement is more surface sensitive than the XPS VB measurement due to much lower photoelectron energies (15 vs 1480 eV).[67] Thus, the apparent discrepancy is likely due to the surface effects, either impurities or difference in surface vs bulk composition. Previously, we observed the onset of the Ti$^{3+/2+}$ 3d peak at 0.72−0.50 eV in the UPS data only after annealing at 400 °C in a vacuum despite the presence of Ti$^{3+/2+}$ species in the as-deposited ALD am.-TiO$_2$ thin film, and the onset coincided with the removal of adventitious contamination.[19]

To understand how the Ti^{3+}-mediated defect states influence the properties of am.-TiO$_2$, steady-state absorbance, transient absorption spectroscopy, and electrical conductivity measurements were carried out. Steady-state absorbance
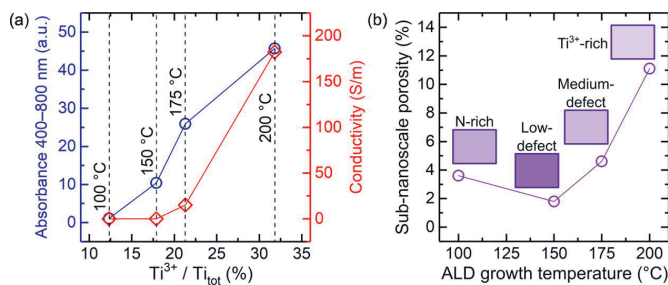
Figure 6. (a) Integrated absorbance in the visible range and electrical conductivity and (b) sub-nanoscale porosity of 30 nm thick ALD am.-TiO$_2$ grown at 100, 150, 175, and 200 °C.

spectra in the UV−vis range are presented in Figure S11a, and further analysis of the optical band gap is shown in Figure S11b. The results in Figure S11a show increasing visible-light absorption with increasing ALD TiO$_2$ growth temperature. Here, visible-light absorption is caused by the Ti^{3+} defects that have energy states within the band gap. The broader UV−NIR range absorption measurement presented in Figure S12 revealed that the 200 °C grown ALD am.-TiO$_2$ has a broad Ti^{3+} 3d defect-mediated absorption band within the band gap with a maximum at 937 nm (1.32 eV) and the defect band edge at 0.24 eV (5200 nm). The small amount of Ti^{3+} 3d defect states in the 100 °C grown ALD am.-TiO$_2$ is not sufficient to form a defect band-like absorption. The main absorption edge of amorphous TiO$_2$ is less steep compared to crystalline TiO$_2$,[68] due to the tailing of electronic states into the band gap.[3,12,69,70] Although the visible-light absorption was strongly affected by the growth temperature, only a subtle increase from 3.53 to 3.61 eV was observed in the optical band gap (Figure S11b) and concurrent shift (0.1 eV) toward higher binding energies was observed in the XPS VB edge position (Figure 5a), suggesting a slight widening of the band gap. Interestingly, the band gap values were large compared to those of the bulk anatase TiO$_2$ (3.2 eV) and 30 nm thick anatase TiO$_2$ thin film (3.4 eV).[35] Such a blue-shift could have been caused by the quantum confinement effects,[71] while the band gap broadening with ALD growth temperature could be induced by the high concentration of Ti^{3+} states giving rise to the Moss−Burstein effect.[12,72] It has been proposed that due to the shallow nature of Ti^{3+} defect states, the electrons could be excited thermally to the conduction band (CB) and induce free carrier absorption and electronic conductivity.[20,73] However, the observed defect band edge at 0.24 eV shows that the band does not reach the conduction band and thermal excitation is unlikely.

In contrast to the growth temperatures of 150−200 °C, am.-TiO$_2$ grown at 100 °C showed only little absorption for the wavelengths above 350 nm. Especially, features at 400−500 nm associated with substitutional N-doping[65,74] were not observed (Figure S11a, inset). This suggests that the nitrogen precursor traces, mainly present in the 100 °C grown ALD am.-TiO$_2$, do not induce absorption in the visible range, and furthermore, with only a low concentration of Ti^{3+}, the thin film can be considered transparent to the visible light.

Figure 6a emphasizes the relation between visible range absorbance and Ti^{3+} defects by presenting the integrated absorbance in the wavelength range of 400−800 nm as a function of relative Ti^{3+} ion concentration. We note that the absorption band has the maximum outside the visible range at

937 nm but the integrated area is proportional to the absorption band area. Am.-TiO$_2$ grown at 100 °C shows only minor visible-light absorption and has the lowest Ti^{3+} concentration (Ti^{3+}/Ti$_{tot}$ = 12%). Then, the visible range absorption increases with the concentration of Ti^{3+} defects. Compared to the visible range absorbance, electrical conductivity starts to increase steeply after 20% Ti^{3+}/Ti$_{tot}$ concentration is reached (Figure 6a). The observed electrical conductivity corresponds to the computationally studied polaron hopping mechanism, which is strongly related to the unpaired electrons of Ti^{3+} defects and distances between adjacent Ti^{3+} ions, as discussed also earlier in this work.[4,7,20,25] Furthermore, this is supported by Nunez et al., who found a correlation between the concentration of Ti^{3+} and conductivity by comparing ALD TiO$_2$ grown using either TDMAT or TiCl$_4$ precursors.[21] They stated that the conductivity of TiO$_2$ thin films is consistent with the hopping mechanism, instead of conduction via the conduction or valence bands.[21] The hopping mechanism also explains the differences in the onsets of visible-light absorption and conductivity. Thus, around 20% Ti^{3+}/Ti$_{tot}$ concentration is needed for a sufficient amount of unpaired electrons and proximity of Ti^{3+} ions for continuous electron flow through defect pathways to induce electrical conductivity, whereas visible-light absorption occurs with lower Ti^{3+}/Ti$_{tot}$ concentration since it depends only on the concentration of occupied Ti^{3+} 3d in-gap states and is not affected by the average distances of Ti^{3+} ions. With a high enough Ti^{3+} concentration, as in the case of the 200 °C grown am.-TiO$_2$, the Ti^{3+} 3d states overlap sufficiently for delocalization and form a defect band responsible for the increased electrical conductivity. This defect band does not however reach the conduction band, and therefore, the conduction mechanism via free (delocalized) electrons in the conduction band is not supported.

Ellipsometer measurements (Figure S13) revealed a significant change in the refractive index of am.-TiO$_2$ as the ALD growth temperature was changed. In general, a higher refractive index can be interpreted as a higher density material and, for example, the refractive index is reported to vary between 2.1 and 2.9 depending on the phase and the density of TiO$_2$: am.-TiO$_2$ (2.1−2.4), anatase TiO$_2$ (2.4−2.5) and rutile TiO$_2$ (2.8−2.9).[58,75,76] Thus, we propose that the observed differences in the refractive indices are due to the sub-nanoscale porosity within the am.-TiO$_2$ structure being the highest for am.-TiO$_2$ grown at 200 °C. The sub-nanoscale porosity of ALD am.-TiO$_2$ modeled by the Lorentz−Lorenz effective medium approximation (EMA) is presented in Figure 6b. The same model was also used earlier by Dufond et al. to

study the effect of ligands within ALD am.-TiO$_2$ grown using titanium isopropoxide (TTIP) and H$_2$O as ALD precursors.[58] Based on the modeling and the results in Figure 6b, the am.-TiO$_2$ grown at 150 °C is the most dense (n = 2.35, p = 2%), likely due to the rather low concentration of both nitrogen and titanium defects. The Am.-TiO$_2$ grown at 100 °C, instead, includes N-bearing TDMAT fragments that decrease the packing density of am.-TiO$_2$ leading to a slightly higher sub-nanoscale porosity of around 4%. Increasing the ALD growth temperature to >150 °C results in more oxygen displacement-induced Ti^{4+} ions (Ti$_{5/6/7c}^{4+}$) and Ti^{3+} defects that imply the formation of oxygen vacancies, i.e., local sub-nanoscale porosity within am.-TiO$_2$. Therefore, the Ti^{3+}-rich am.-TiO$_2$ grown at 200 °C exhibits the lowest refractive index of 2.14, corresponding to the sub-nanoscale porosity of 11%.

In addition to the refractive index, Figure S13 shows the ALD growth per cycle (GPC) calculated by dividing the thin film thickness by the number of ALD cycles. There is a distinct decrease in the GPC, as the ALD growth temperature is increased from 100 to 200 °C. Some reasons for lower GPC are proposed to be attributed to slower adsorption of TDMAT or intermediate product desorption.[16,60] It should be also noticed that the thermal decomposition of TDMAT may affect the self-limiting ALD process at 200 °C.[16] We consider that, possibly, the intermediate product desorption and nonideal ALD process at 200 °C are the reasons for the observed unprecedented Ti^{3+}-rich nature and sub-nanoscale porosity of our ALD am.-TiO$_2$ grown at 200 °C.[16]

Transient absorption spectroscopy (TAS) was carried out to study the charge carrier dynamics in am.-TiO$_2$ thin films. am.-TiO$_2$ samples were excited at 320 nm and monitored at 410–1250 nm (3.0–1.0 eV). The excitation (pump) energy used was 60 μJ/cm^2. The excitation wavelength was chosen to match the band gap absorption (Figure S11a), i.e., to excite electrons from the valence band to the conduction band, but it also excites electrons from any band gap state to the conduction band.

Two types of responses were observed depending on the am.-TiO$_2$ deposition temperature. The positive broad absorbance band with a maximum in the 600–800 nm range was recorded for am.-TiO$_2$ deposited at 100 °C (Figure S14) and 150 °C (Figure S15). This response can be assigned to the carriers in the CB or to the carriers, either holes or electrons, trapped to the in-gap states 1.5–2.5 eV above the valence band.[68] The carrier lifetimes for 100–150 °C grown am.-TiO$_2$ were extremely short, less than 10 ps, as presented in Figure 7. Quite surprisingly, this broadband response is similar to
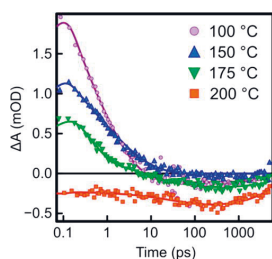
crystalline TiO$_2$ thin films with the exception that in crystalline TiO$_2$ the carrier lifetimes are in the nanosecond range.[68] The short carrier lifetime indicates fast recombination of trapped charge carriers in am.-TiO$_2$ and is assigned to its defective nature.[35] Indeed, the XPS VB spectra (Figure 5a) show an increased amount of band gap states for all of the am.-TiO$_2$ compared to the crystalline TiO$_2$ reference. On the contrary, for 200 °C grown am.-TiO$_2$, the response is negative (Figure S17) and arises from bleaching of the ground state absorption in the visible and NIR range.[77] Yet, the response (ΔA) was still of broad band nature in the 600–800 nm range. Since the origin of the ground-state absorption is the transition from the VB and in-gap states to the CB, the explanation for the observation is the excitation of the electrons of in-gap states by the pump pulse. This transition gives rather a long lifetime of the charge carriers, extended to the ns time scale. The am.-TiO$_2$ deposited at 175 °C (Figure S16) presents an intermediate case when both types of responses were observed simultaneously, a fast decay of the positive response (fast recombination of the carriers in the CB) characteristic for am.-TiO$_2$ and slow relaxation of the ground-state absorption bleaching (relaxation of the electrons back to the in-gap states) exhibited by Ti^{3+}-rich "black" am.-TiO$_2$.

The carrier lifetime of the 200 °C grown am.-TiO$_2$ is similar to the crystalline TiO$_2$.[68] This is at first surprising since the carrier lifetime is known to increase with amorphous to crystalline transition due to the decrease in the amount of oxide defects and trap states. The "black" am.-TiO$_2$ grown at 200 °C is loaded with oxide defects, and one would expect carrier lifetimes to become even shorter due to the fast recombination at the oxide defects and trap states. We have to bear in mind that the 200 °C grown "black" am.-TiO$_2$ thin film has an exceptionally high concentration of Ti^{3+} defects that seem to correlate with the extended carrier lifetime. The long carrier lifetime indicates slow recombination of charge carriers, which indicates a decrease in the amount of trap states. Thus, it seems plausible that Ti^{3+} defects fill trap states responsible for the carrier recombination. In the case of 200 °C grown am.-TiO$_2$, these trap states are fully occupied resulting in an increased carrier lifetime. In a broader context, carrier lifetimes can be increased either by removing defects and trap states, i.e., crystalline TiO$_2$ or by saturating the material with defects, as was shown here for "black" am.-TiO$_2$ grown at 200 °C.

Vequizo et al. presented a photodynamic mechanism of photogenerated electrons in nonreduced and reduced SrTiO$_3$ photocatalysts.[33] In nonreduced SrTiO$_3$ with a minor amount of oxygen vacancies and Ti^{3+} defects, electrons can be deeply trapped at the intrinsic in-gap states after the pump pulse and then subsequently be excited to the conduction band by absorbing vis–NIR light. However, in reduced and Ti^{3+}-rich SrTiO$_3$, in-gap states are already occupied by electrons leading to an extended lifetime of charge carriers photoexcited by the pump pulse and absorption of lower energy IR photons by electrons at shallow trap states.[33] Our proposed mechanism for the extended carrier lifetime of 200 °C grown am.-TiO$_2$ with an also high degree of Ti^{3+} defects is in accordance with this model, albeit our probe range was limited to >1 eV transitions.

To assess the contribution of TDMAT fragments to the carrier dynamics, a comparison was made with amorphous TiO$_2$ grown by the ion-beam sputtering (IBS) method. The IBS am.-TiO$_2$ does not contain any nitrogen impurities but Ti 2p is similar to ALD am.-TiO$_2$ grown at 100 °C (Figure S18), indicating low Ti^{3+} concentration and lattice disorder-mediated

Figure 7. TAS decay spectra at 750 nm (1.65 eV) in the picosecond time domain of 30 nm thick amorphous ALD am.-TiO$_2$ grown at 100, 150, 175, and 200 °C.

broadening of the Ti^{4+} peak compared to the crystalline TiO_2. The TA spectra of IBS am.-TiO_2 were found to be similar to the ALD am.-TiO_2 grown at 100 °C (Figure S19) but the carriers had more than ten times longer lifetimes (>100 ps). This suggests that even though the TA spectra are not affected by the N-bearing TDMAT fragments in the am.-TiO_2 thin film, they may still contribute to carrier trapping. The similarity of Ti 2p spectra recorded for the amorphous IBS TiO_2 and ALD TiO_2 thin films in Figure S18a also indicates generality of the proposed component analysis, where in addition to hexacoordinated (Ti_{6c}^{4+}) ions, penta- and heptacoordinated ($Ti_{5/7c}^{4+}$) ions are also required to fit the Ti 2p spectrum of amorphous IBS TiO_2.

As reported by Khan et al., conversion from the am.-TiO_2 to polycrystalline anatase phase leads to a strong increase in carrier lifetimes, from ps to ns range,[35] which can be now experimentally rationalized by the absence of penta- and heptacoordinated ($Ti_{5/7c}^{4+}$) ions in crystalline TiO_2 that are, on the contrary, rather common in am.-TiO_2.[3−5] The Ti^{3+} 3d in-gap state is also removed upon oxidation but is not responsible for the short carrier lifetimes. Conversely, the introduction of high Ti^{3+} concentration to the am.-TiO_2 was followed by carrier lifetimes similar to the polycrystalline TiO_2. On the other hand, our results suggest that N-bearing TDMAT fragments in the am.-TiO_2 thin film could contribute to the short carrier lifetimes acting as carrier traps.

The schematic illustration in Figure 8 summarizes the ALD growth temperature-induced controllability of Ti^{3+} defects
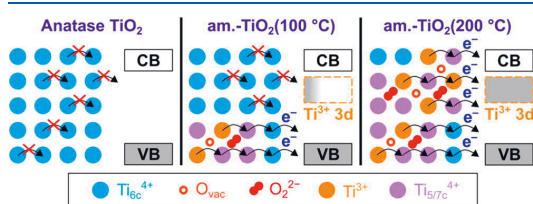

Figure 8. Schematic illustration of electrical conduction in am.-TiO_2 by the polaron hopping mechanism. Ti^{3+} defects in am.-TiO_2 populate the Ti 3d state within the band gap with an excess charge carrier polaron that can "hop" from a Ti^{3+} site to a Ti^{4+} site, i.e., Ti^{3+}−Ti^{4+} ↔ Ti^{4+}−Ti^{3+}. Pure anatase TiO_2 does not have any electronic state within the band gap and no Ti^{3+} defects to initiate electron hopping. Conductivity scales with the Ti^{3+} concentration can be controlled with ALD growth temperature. With increasing Ti^{3+} concentration, the Ti^{3+} 3d states within the band gap become close enough and form a defect band. By common theory, an oxygen vacancy, O_{vac}, generates two Ti^{3+} sites and decreases the coordination of neighboring Ti^{4+} cations. Furthermore, the O ion that formed O_{vac} can bond with another oxygen creating an interstitial O_2 species (O_2^{2-}) connected to three heptacoordinated Ti_{7c} cations. Amorphous TiO_2 is rich in under- and overcoordinated $Ti_{5/7c}$ cations, whereas crystalline TiO_2 consists of only six-coordinated (Ti_{6c}) cations.

within am.-TiO_2 and their effect on the electrical conduction mechanism. From the PEC application point of view, comprehensive research regarding tunable charge carrier dynamics, absorption, and electrical "leakiness" of ALD am.-TiO_2 presented in this work provides a better understanding of possible tailoring of properties related to protective ALD am.-TiO_2 photoelectrode coatings made of nonconductive or degenerated/intrinsically "leaky" amorphous ALD am.-TiO_2 grown using TDMAT and H_2O precursors.[6,78−80] Further-

more, the controllable and direct synthesis of "black" am.-TiO_2 via atomic layer deposition is of wide interest in photocatalyst applications,[7,9,10] whereas low conductivity of low-temperature grown am.-TiO_2 may be applied as a high-κ dielectric.[81,82] Such a diversity in the properties of amorphous titania could also provide an interesting approach to area-selective ALD, e.g., by possible differences in adsorption of self-assembled monolayers (SAMs) or preferential growth of metallic or oxide materials on conductive (high density of donor defects) and nonconductive (low density of donor defects) substrates.[83,84]

■ CONCLUSIONS

In summary, a comprehensive electron and optical absorption spectroscopy study were conducted for atomic layer deposited am.-TiO_2 to provide insights into the amorphous structure of titania and its charge carrier dynamics. The correlation between our electron spectroscopy results and a first-principles core-level shift analysis allowed us to differentiate penta- and heptacoordinated ($Ti_{5/7c}^{4+}$) ions, induced by oxygen vacancies and interstitial peroxo species within the amorphous TiO_2 structure. The formation of Ti^{3+} defects was found to induce a chemical shift to the Ti^{4+} 2p core-level spectrum of am.-TiO_2, which could not be explained by the structural disorder alone. Furthermore, we showed that Ti^{3+} and nitrogen defects in am.-TiO_2 can be tailored in a controlled and elegant manner via tuning the ALD growth temperature between 100 and 200 °C when using TDMAT and H_2O as the precursors. The lower deposition temperature results in nitrogen-bearing precursor traces within the am.-TiO_2, whereas the higher growth temperature leads to increased concentration of Ti^{3+} and oxygen displacement-induced Ti^{4+} ions ($Ti_{5/6/7c}^{4+}$).

The am.-TiO_2 grown at 100 °C shows no visible-light absorption but after the Ti^{3+} concentration (Ti^{3+}/Ti_{tot}) exceeds ∼12%, the visible light absorption increases with the amount of Ti^{3+} defects resulting in "black" am.-TiO_2 at ALD growth temperature of 200 °C. The onset of electrical conductivity requires >20% Ti^{3+}/Ti_{tot}, and the conductivity mechanism was identified as polaron hopping-induced conductivity. The transient absorption (TA) response of am.-TiO_2 grown at 100 °C was similar to crystalline TiO_2 in terms of the TA spectrum but the carrier lifetime was only <10 ps (vs few ns for crystalline TiO_2) due to the amorphous structure. In contrast, the high concentration of Ti^{3+} defects in "black" am.-TiO_2 was shown to decrease the recombination rate and thereby increase the carrier lifetime to the nanosecond time domain, which is comparable to the crystalline low-defect TiO_2. Nitrogen traces from the TDMAT precursor, on the other hand, had no remarkable effect on either the optical or the charge transfer properties.

These results provide new atomic-level insights into the formation and controlling of intrinsic Ti^{3+} defects in ALD grown am.-TiO_2. The ALD grown am.-TiO_2 has stoichiometric composition despite the high (up to 33%) Ti^{3+} concentration, which is explained by the formation of interstitial peroxo species with oxygen vacancies. The Ti^{3+} defects mediate the enhanced charge transfer of am.-TiO_2 that is a critical parameter in the optimization of ALD TiO_2-based protective photoelectrode coatings in photoelectrochemical solar fuel reactors.

■ ASSOCIATED CONTENT

⑤Ⓘ Supporting Information

The Supporting Information is available free of charge at https://pubs.acs.org/doi/10.1021/acs.jpcc.1c10919.

Details of the computational method; the effect of applied U-value; details on the formation of oxygen vacancies and peroxo species; results for am.-TiO$_2$; GIXRD measurements; and XPS, UPS, steady-state UV−vis−NIR spectroscopy, ellipsometry, and transient absorption spectroscopy (PDF)

■ AUTHOR INFORMATION

Corresponding Authors

Harri Ali-Löytty − *Surface Science Group, Faculty of Engineering and Natural Sciences, Tampere University, FI-33014 Tampere, Finland;* ⓞ orcid.org/0000-0001-8746-7268; Email: harri.ali-loytty@tuni.fi

Mika Valden − *Surface Science Group, Faculty of Engineering and Natural Sciences, Tampere University, FI-33014 Tampere, Finland;* Email: mika.valden@tuni.fi

Authors

Jesse Saari − *Surface Science Group, Faculty of Engineering and Natural Sciences, Tampere University, FI-33014 Tampere, Finland;* ⓞ orcid.org/0000-0001-6741-0838

Minttu Maria Kauppinen − *Competence Centre for Catalysis and Department of Physics, Chalmers University of Technology, SE-412 96 Göteborg, Sweden*

Markku Hannula − *Surface Science Group, Faculty of Engineering and Natural Sciences, Tampere University, FI-33014 Tampere, Finland;* ⓞ orcid.org/0000-0003-1110-7439

Ramsha Khan − *Photonic Compounds and Nanomaterials Group, Faculty of Engineering and Natural Sciences, Tampere University, FI-33014 Tampere, Finland*

Kimmo Lahtonen − *Faculty of Engineering and Natural Sciences, Tampere University, FI-33014 Tampere, Finland;* ⓞ orcid.org/0000-0002-8138-7918

Lauri Palmolahti − *Surface Science Group, Faculty of Engineering and Natural Sciences, Tampere University, FI-33014 Tampere, Finland;* ⓞ orcid.org/0000-0001-9992-6628

Antti Tukiainen − *Faculty of Engineering and Natural Sciences, Tampere University, FI-33014 Tampere, Finland*

Henrik Grönbeck − *Competence Centre for Catalysis and Department of Physics, Chalmers University of Technology, SE-412 96 Göteborg, Sweden*

Nikolai V. Tkachenko − *Photonic Compounds and Nanomaterials Group, Faculty of Engineering and Natural Sciences, Tampere University, FI-33014 Tampere, Finland;* ⓞ orcid.org/0000-0002-8504-2335

Complete contact information is available at:
https://pubs.acs.org/10.1021/acs.jpcc.1c10919

Notes

The authors declare no competing financial interest.

■ ACKNOWLEDGMENTS

■ REFERENCES

(1) Fujishima, A.; Honda, K. Electrochemical Photolysis of Water at a Semiconductor Electrode. *Nature* **1972**, *238*, 37−38.

(2) Pelaez, M.; Nolan, N. T.; Pillai, S. C.; Seery, M. K.; Falaras, P.; Kontos, A. G.; Dunlop, P. S. M.; Hamilton, J. W. J.; Byrne, J. A.; O'Shea, K.; et al. Review on the Visible Light Active Titanium Dioxide Photocatalysts for Environmental Applications. *Appl. Catal., B* **2012**, *125*, 331−349.

(3) Prasai, B.; Cai, B.; Underwood, M. K.; Lewis, J. P.; Drabold, D. A. Properties of Amorphous and Crystalline Titanium Dioxide from First Principles. *J. Mater. Sci.* **2012**, *47*, 7515−7521.

(4) Deskins, N. A.; Du, J.; Rao, P. The Structural and Electronic Properties of Reduced Amorphous Titania. *Phys. Chem. Chem. Phys.* **2017**, *19*, 18671−18684.

(5) Mora-Fonz, D.; Kaviani, M.; Shluger, A. L. Disorder-Induced Electron and Hole Trapping in Amorphous TiO$_2$. *Phys. Rev. B* **2020**, *102*, No. 054205.

(6) Hu, S.; Shaner, M. R.; Beardslee, J. A.; Lichterman, M.; Brunschwig, B. S.; Lewis, N. S. Amorphous TiO$_2$ Coatings Stabilize Si, GaAs, and GaP Photoanodes for Efficient Water Oxidation. *Science* **2014**, *344*, 1005−1009.

(7) Glezakou, V.-A.; Rousseau, R. Shedding Light on Black Titania. *Nat. Mater.* **2018**, *17*, 856−857.

(8) Sivula, K. Defects Give New Life to an Old Material: Electronically Leaky Titania as a Photoanode Protection Layer. *ChemCatChem* **2014**, *6*, 2796−2797.

(9) Liu, X.; Zhu, G.; Wang, X.; Yuan, X.; Lin, T.; Huang, F. Progress in Black Titania: A New Material for Advanced Photocatalysis. *Adv. Energy Mater.* **2016**, *6*, No. 1600452.

(10) Chen, X.; Liu, L.; Huang, F. Black Titanium Dioxide (TiO$_2$) Nanomaterials. *Chem. Soc. Rev.* **2015**, *44*, 1861−1885.

(11) Dendooven, J.; Detavernier, C. In *Atomic Layer Deposition in Energy Conversion Applications*; Bachmann, J., Ed.; John Wiley & Sons, Ltd., 2017; pp 1−40.

(12) Ali-Löytty, H.; Hannula, M.; Saari, J.; Palmolahti, L.; Bhuskute, B. D.; Ulkuniemi, R.; Nyyssönen, T.; Lahtonen, K.; Valden, M. Diversity of TiO$_2$: Controlling the Molecular and Electronic Structure of Atomic-Layer-Deposited Black TiO$_2$. *ACS Appl. Mater. Interfaces* **2019**, *11*, 2758−2762.

(13) Reiners, M.; Xu, K.; Aslam, N.; Devi, A.; Waser, R.; Hoffmann-Eifert, S. Growth and Crystallization of TiO$_2$ Thin Films by Atomic Layer Deposition Using a Novel Amido Guanidinate Titanium Source and Tetrakis-Dimethylamido-Titanium. *Chem. Mater.* **2013**, *25*, 2934−2943.

(14) Head, A. R.; Chaudhary, S.; Olivieri, G.; Bournel, F.; Andersen, J. N.; Rochet, F.; Gallet, J.-J.; Schnadt, J. Near Ambient Pressure X-Ray Photoelectron Spectroscopy Study of the Atomic Layer Deposition of TiO$_2$ on RuO$_2$(110). *J. Phys. Chem. C* **2016**, *120*, 243−251.

(15) Kääriäinen, T.; Cameron, D.; Kääriäinen, M.-L.; Sherman, A. *Atomic Layer Deposition: Principles, Characteristics, and Nanotechnology Applications*, 2nd ed.; Scrivener Publishing: Beverly, MA, 2013.

(16) Xie, Q.; Jiang, Y.-L.; Detavernier, C.; Deduytsche, D.; Van Meirhaeghe, R. L.; Ru, G.-P.; Li, B.-Z.; Qu, X.-P. Atomic Layer Deposition of TiO_2 from Tetrakis-Dimethyl-Amido Titanium or Ti Isopropoxide Precursors and H_2O. *J. Appl. Phys.* **2007**, *102*, No. 083521.

(17) McDowell, M. T.; Lichterman, M. F.; Carim, A. I.; Liu, R.; Hu, S.; Brunschwig, B. S.; Lewis, N. S. The Influence of Structure and Processing on the Behavior of TiO_2 Protective Layers for Stabilization of n-Si/TiO_2/Ni Photoanodes for Water Oxidation. *ACS Appl. Mater. Interfaces* **2015**, *7*, 15189−15199.

(18) Deng, S.; Verbruggen, S. W.; Lenaerts, S.; Martens, J. A.; Van den Berghe, S.; Devloo-Casier, K.; Devulder, W.; Dendooven, J.; Deduytsche, D.; Detavernier, C. Controllable Nitrogen Doping in as Deposited TiO_2 Film and Its Effect on Post Deposition Annealing. *J. Vac. Sci. Technol., A* **2013**, *32*, No. 01A123.

(19) Hannula, M.; Ali-Löytty, H.; Lahtonen, K.; Sarlin, E.; Saari, J.; Valden, M. Improved Stability of Atomic Layer Deposited Amorphous TiO_2 Photoelectrode Coatings by Thermally Induced Oxygen Defects. *Chem. Mater.* **2018**, *30*, 1199−1208.

(20) Di Valentin, C.; Pacchioni, G.; Selloni, A. Reduced and n-Type Doped TiO_2: Nature of Ti^{3+} Species. *J. Phys. Chem. C* **2009**, *113*, 20543−20552.

(21) Nunez, P.; Richter, M. H.; Piercy, B. D.; Roske, C. W.; Cabán-Acevedo, M.; Losego, M. D.; Konezny, S. J.; Fermin, D. J.; Hu, S.; Brunschwig, B. S.; et al. Characterization of Electronic Transport through Amorphous TiO_2 Produced by Atomic Layer Deposition. *J. Phys. Chem. C* **2019**, *123*, 20116−20129.

(22) Chen, X.; Liu, L.; Liu, Z.; Marcus, M. A.; Wang, W.-C.; Oyler, N. A.; Grass, M. E.; Mao, B.; Glans, P.-A.; Yu, P. Y.; et al. Properties of Disorder-Engineered Black Titanium Dioxide Nanoparticles through Hydrogenation. *Sci. Rep.* **2013**, *3*, No. 1510.

(23) Santomauro, F. G.; Lübcke, A.; Rittmann, J.; Baldini, E.; Ferrer, A.; Silatani, M.; Zimmermann, P.; Grübel, S.; Johnson, J. A.; Mariager, S. O.; et al. Femtosecond X-ray Absorption Study of Electron Localization in Photoexcited Anatase TiO_2. *Sci. Rep.* **2015**, *5*, No. 14834.

(24) Franchini, C.; Reticcioli, M.; Setvin, M.; Diebold, U. Polarons in Materials. *Nat. Rev. Mater.* **2021**, *6*, 560−586.

(25) Deskins, N. A.; Dupuis, M. Electron Transport via Polaron Hopping in Bulk TiO_2: A Density Functional Theory Characterization. *Phys. Rev. B* **2007**, *75*, No. 195212.

(26) Richter, M. H.; Cheng, W.-H.; Crumlin, E. J.; Drisdell, W. S.; Atwater, H. A.; Schmeißer, D.; Lewis, N. S.; Brunschwig, B. S. X-ray Photoelectron Spectroscopy and Resonant X-ray Spectroscopy Investigations of Interactions between Thin Metal Catalyst Films and Amorphous Titanium Dioxide Photoelectrode Protection Layers. *Chem. Mater* **2021**, *33*, 1265−1275.

(27) Wang, Z.; Wen, B.; Hao, Q.; Liu, L.-M.; Zhou, C.; Mao, X.; Lang, X.; Yin, W.-J.; Dai, D.; Selloni, A.; et al. Localized Excitation of Ti^{3+} Ions in the Photoabsorption and Photocatalytic Activity of Reduced Rutile TiO_2. *J. Am. Chem. Soc.* **2015**, *137*, 9146−9152.

(28) Liu, B.; Zhao, X.; Yu, J.; Parkin, I. P.; Fujishima, A.; Nakata, K. Intrinsic Intermediate Gap States of TiO_2 Materials and Their Roles in Charge Carrier Kinetics. *J. Photochem. Photobiol., C* **2019**, *39*, 1−57.

(29) Strand, J.; Kaviani, M.; Gao, D.; El-Sayed, A.-M.; Afanas'ev, V. V.; Shluger, A. L. Intrinsic Charge Trapping in Amorphous Oxide Films: Status and Challenges. *J. Phys.: Condens. Matter* **2018**, *30*, No. 233001.

(30) Yang, S.; Brant, A. T.; Giles, N. C.; Halliburton, L. E. Intrinsic Small Polarons in Rutile TiO_2. *Phys. Rev. B* **2013**, *87*, No. 125201.

(31) Reckers, P.; Dimamay, M.; Klett, J.; Trost, S.; Zilberberg, K.; Riedl, T.; Parkinson, B. A.; Brötz, J.; Jaegermann, W.; Mayer, T. Deep and Shallow TiO_2 Gap States on Cleaved Anatase Single Crystal (101) Surfaces, Nanocrystalline Anatase Films, and ALD Titania Ante and Post Annealing. *J. Phys. Chem. C* **2015**, *119*, 9890−9898.

(32) Qian, R.; Zong, H.; Schneider, J.; Zhou, G.; Zhao, T.; Li, Y.; Yang, J.; Bahnemann, D. W.; Pan, J. H. Charge Carrier Trapping, Recombination and Transfer during TiO_2 Photocatalysis: An Overview. *Catal. Today* **2019**, *335*, 78−90.

(33) Vequizo, J. J. M.; Nishioka, S.; Hyodo, J.; Yamazaki, Y.; Maeda, K.; Yamakata, A. Crucial Impact of Reduction on the Photocarrier Dynamics of $SrTiO_3$ Powders Studied by Transient Absorption Spectroscopy. *J. Mater. Chem. A* **2019**, *7*, 26139−26146.

(34) Yamakata, A.; Vequizo, J. J. M. Curious Behaviors of Photogenerated Electrons and Holes at the Defects on Anatase, Rutile, and Brookite TiO_2 Powders: A Review. *J. Photochem. Photobiol., C* **2019**, *40*, 234−243.

(35) Khan, R.; Ali-Löytty, H.; Saari, J.; Valden, M.; Tukiainen, A.; Lahtonen, K.; Tkachenko, N. V. Optimization of Photogenerated Charge Carrier Lifetimes in ALD Grown TiO_2 for Photonic Applications. *Nanomaterials* **2020**, *10*, No. 1567.

(36) CasaXPS: Processing Software for XPS, AES, SIMS and More. http://www.casaxps.com/ (accessed July 2, 2020).

(37) Scofield, J. H. Hartree-Slater Subshell Photoionization Cross-Sections at 1254 and 1487 eV. *J. Electron Spectrosc. Relat. Phenom.* **1976**, *8*, 129−137.

(38) Pham, H. H.; Wang, L.-W. Oxygen Vacancy and Hole Conduction in Amorphous TiO_2. *Phys. Chem. Chem. Phys.* **2015**, *17*, 541−550.

(39) Kresse, G.; Hafner, J. Ab Initio Molecular Dynamics for Liquid Metals. *Phys. Rev. B* **1993**, *47*, 558−561.

(40) Kresse, G.; Hafner, J. Ab Initio Molecular-Dynamics Simulation of the Liquid-Metal–Amorphous-Semiconductor Transition in Germanium. *Phys. Rev. B* **1994**, *49*, 14251−14269.

(41) Kresse, G.; Furthmüller, J. Efficiency of Ab-Initio Total Energy Calculations for Metals and Semiconductors Using a Plane-Wave Basis Set. *Comput. Mater. Sci.* **1996**, *6*, 15−50.

(42) Kresse, G.; Furthmüller, J. Efficient Iterative Schemes for Ab Initio Total-Energy Calculations Using a Plane-Wave Basis Set. *Phys. Rev. B* **1996**, *54*, 11169−11186.

(43) Perdew, J. P.; Burke, K.; Ernzerhof, M. Generalized Gradient Approximation Made Simple. *Phys. Rev. Lett.* **1996**, *77*, 3865−3868.

(44) Perdew, J. P.; Burke, K.; Ernzerhof, M. Generalized Gradient Approximation Made Simple [Phys. Rev. Lett. 77, 3865 (1996)]. *Phys. Rev. Lett.* **1997**, *78*, 1396.

(45) Dudarev, S. L.; Botton, G. A.; Savrasov, S. Y.; Humphreys, C. J.; Sutton, A. P. Electron-Energy-Loss Spectra and the Structural Stability of Nickel Oxide: An LSDA+U Study. *Phys. Rev. B* **1998**, *57*, 1505−1509.

(46) Morgan, B. J.; Watson, G. W. GGA+*U* Description of Lithium Intercalation into Anatase TiO_2. *Phys. Rev. B* **2010**, *82*, No. 144119.

(47) Blöchl, P. E. Projector Augmented-Wave Method. *Phys. Rev. B* **1994**, *50*, 17953−17979.

(48) Kresse, G.; Joubert, D. From Ultrasoft Pseudopotentials to the Projector Augmented-Wave Method. *Phys. Rev. B* **1999**, *59*, 1758−1775.

(49) Cromer, D. T.; Herrington, K. The Structures of Anatase and Rutile. *J. Am. Chem. Soc.* **1955**, *77*, 4708−4709.

(50) Rao, K. V. K.; Naidu, S. V. N.; Iyengar, L. Thermal Expansion of Rutile and Anatase. *J. Am. Ceram. Soc.* **1970**, *53*, 124−126.

(51) Finazzi, E.; Di Valentin, C.; Pacchioni, G.; Selloni, A. Excess Electron States in Reduced Bulk Anatase TiO_2: Comparison of Standard GGA, GGA+*U*, and Hybrid DFT Calculations. *J. Chem. Phys.* **2008**, *129*, No. 154113.

(52) Tang, W.; Sanville, E.; Henkelman, G. A Grid-Based Bader Analysis Algorithm without Lattice Bias. *J. Phys.: Condens. Matter* **2009**, *21*, No. 084204.

(53) Henkelman, G.; Arnaldsson, A.; Jónsson, H. A Fast and Robust Algorithm for Bader Decomposition of Charge Density. *Comput. Mater. Sci.* **2006**, *36*, 354−360.

(54) Yu, M.; Trinkle, D. R. Accurate and Efficient Algorithm for Bader Charge Integration. *J. Chem. Phys.* **2011**, *134*, No. 064111.

(55) Sanville, E.; Kenny, S. D.; Smith, R.; Henkelman, G. Improved Grid-Based Algorithm for Bader Charge Allocation. *J. Comput. Chem.* **2007**, *28*, 899−908.

(56) Sheet Resistance Equations and Theory|Complete Guide. https://www.ossila.com/pages/sheet-resistance-theory (accessed July 2, 2020).

(57) van de Krol, R.; Grätzel, M., Eds. *Photoelectrochemical Hydrogen Production*; Electronic Materials: Science & Technology; Springer US, 2012.

(58) Dufond, M. E.; Diouf, M. W.; Badie, C.; Laffon, C.; Parent, P.; Ferry, D.; Grosso, D.; Kools, J. C. S.; Elliott, S. D.; Santinacci, L. Quantifying the Extent of Ligand Incorporation and the Effect on Properties of TiO₂ Thin Films Grown by Atomic Layer Deposition Using an Alkoxide or an Alkylamide. *Chem. Mater.* **2020**, *32*, 1393−1407.

(59) Sperling, B. A.; Kimes, W. A.; Maslar, J. E. Reflection Absorption Infrared Spectroscopy during Atomic Layer Deposition of HfO₂ Films from Tetrakis(Ethylmethylamido)Hafnium and Water. *Appl. Surf. Sci.* **2010**, *256*, 5035−5041.

(60) Abendroth, B.; Moebus, T.; Rentrop, S.; Strohmeyer, R.; Vinnichenko, M.; Weling, T.; Stöcker, H.; Meyer, D. C. Atomic Layer Deposition of TiO₂ from Tetrakis(Dimethylamino)Titanium and H₂O. *Thin Solid Films* **2013**, *545*, 176−182.

(61) Rodríguez-Reyes, J. C. F.; Teplyakov, A. V. Chemistry of Diffusion Barrier Film Formation: Adsorption and Dissociation of Tetrakis(Dimethylamino)Titanium on Si(100)-2 × 1. *J. Phys. Chem. C* **2007**, *111*, 4800−4808.

(62) Driessen, J. P. A. M.; Schoonman, J.; Jensen, K. F. Infrared Spectroscopic Study of Decomposition of Ti(N(CH₃)₂)₄. *J. Electrochem. Soc.* **2001**, *148*, G178.

(63) Choi, W. H.; Lee, C. H.; Kim, H.; Lee, S. U.; Bang, J. H. Designing a High-Performance Nitrogen-Doped Titanium Dioxide Anode Material for Lithium-Ion Batteries by Unravelling the Nitrogen Doping Effect. *Nano Energy* **2020**, *74*, No. 104829.

(64) Braun, A.; Akurati, K. K.; Fortunato, G.; Reifler, F. A.; Ritter, A.; Harvey, A. S.; Vital, A.; Graule, T. Nitrogen Doping of TiO₂ Photocatalyst Forms a Second e_g State in the Oxygen 1s NEXAFS Pre-edge. *J. Phys. Chem. C* **2010**, *114*, 516−519.

(65) Romero-Gómez, P.; Rico, V.; Borrás, A.; Barranco, A.; Espinós, J. P.; Cotrino, J.; González-Elipe, A. R. Chemical State of Nitrogen and Visible Surface and Schottky Barrier Driven Photoactivities of n-Doped TiO₂ Thin Films. *J. Phys. Chem. C* **2009**, *113*, 13341−13351.

(66) Henkel, K.; Das, C.; Kot, M.; Schmeißer, D.; Naumann, F.; Kärkkänen, I.; Gargouri, H. In-Gap States in Titanium Dioxide and Oxynitride Atomic Layer Deposited Films. *J. Vac. Sci. Technol., A* **2016**, *35*, No. 01B135.

(67) Sherwood, P. M. A. In *Surface Analysis by Auger and X-ray Photoelectron Spectroscopy*; Briggs, D.; Grant, J. T., Eds.; IM Publications: Trowbridge, 2003; pp 531−555.

(68) Khan, R.; Ali-Löytty, H.; Tukiainen, A.; Tkachenko, N. V. Comparison of the Heat-Treatment Effect on Carrier Dynamics in TiO₂ Thin Films Deposited by Different Methods. *Phys. Chem. Chem. Phys.* **2021**, *23*, 17672−17682.

(69) Dow, J. D.; Redfield, D. Toward a Unified Theory of Urbach's Rule and Exponential Absorption Edges. *Phys. Rev. B* **1972**, *5*, 594−610.

(70) Al-Dhhan, Z. T.; Hogarth, C. A.; Riddleston, N. The Optical Absorption Edge in Thin Amorphous Oxide Films Based on Cerium Dioxide. *Phys. Status Solidi B* **1988**, *145*, 145−149.

(71) King, D. M.; Du, X.; Cavanagh, A. S.; Weimer, A. W. Quantum Confinement in Amorphous TiO₂ films Studied via Atomic Layer Deposition. *Nanotechnology* **2008**, *19*, No. 445401.

(72) Burstein, E. Anomalous Optical Absorption Limit in InSb. *Phys. Rev.* **1954**, *93*, 632−633.

(73) Panayotov, D. A.; Yates, J. T. n-Type Doping of TiO₂ with Atomic Hydrogen-Observation of the Production of Conduction Band Electrons by Infrared Spectroscopy. *Chem. Phys. Lett.* **2007**, *436*, 204−208.

(74) Asahi, R.; Morikawa, T.; Ohwaki, T.; Aoki, K.; Taga, Y. Visible-Light Photocatalysis in Nitrogen-Doped Titanium Oxides. *Science* **2001**, *293*, 269−271.

(75) Martin, N.; Rousselot, C.; Rondot, D.; Palmino, F.; Mercier, R. Microstructure Modification of Amorphous Titanium Oxide Thin Films during Annealing Treatment. *Thin Solid Films* **1997**, *300*, 113−121.

(76) Hanaor, D. A. H.; Sorrell, C. C. Review of the Anatase to Rutile Phase Transformation. *J. Mater. Sci.* **2011**, *46*, 855−874.

(77) Berera, R.; van Grondelle, R.; Kennis, J. T. M. Ultrafast Transient Absorption Spectroscopy: Principles and Application to Photosynthetic Systems. *Photosynth. Res.* **2009**, *101*, 105−118.

(78) Chen, Y. W.; Prange, J. D.; Dühnen, S.; Park, Y.; Gunji, M.; Chidsey, C. E. D.; McIntyre, P. C. Atomic Layer-Deposited Tunnel Oxide Stabilizes Silicon Photoanodes for Water Oxidation. *Nat. Mater.* **2011**, *10*, 539−544.

(79) Scheuermann, A. G.; Prange, J. D.; Gunji, M.; Chidsey, C. E. D.; McIntyre, P. C. Effects of Catalyst Material and Atomic Layer Deposited TiO₂ Oxide Thickness on the Water Oxidation Performance of Metal−Insulator−Silicon Anodes. *Energy Environ. Sci.* **2013**, *6*, 2487−2496.

(80) Scheuermann, A. G.; Lawrence, J. P.; Kemp, K. W.; Ito, T.; Walsh, A.; Chidsey, C. E. D.; Hurley, P. K.; McIntyre, P. C. Design Principles for Maximizing Photovoltage in Metal-Oxide-Protected Water-Splitting Photoanodes. *Nat. Mater.* **2016**, *15*, 99−105.

(81) Swaminathan, S.; McIntyre, P. C. Titania/Alumina Bilayer Gate Dielectrics for Ge MOS Devices: Frequency- and Temperature-Dependent Electrical Characteristics. *Electrochem. Solid-State Lett.* **2010**, *13*, G79.

(82) Scott, E. A.; Gaskins, J. T.; King, S. W.; Hopkins, P. E. Thermal Conductivity and Thermal Boundary Resistance of Atomic Layer Deposited High-k Dielectric Aluminum Oxide, Hafnium Oxide, and Titanium Oxide Thin Films on Silicon. *APL Mater.* **2018**, *6*, No. 058302.

(83) de Melo, C.; Jullien, M.; Ghanbaja, J.; Montaigne, F.; Pierson, J.-F.; Soldera, F.; Rigoni, F.; Almqvist, N.; Vomiero, A.; Mücklich, F.; et al. Local Structure and Point-Defect-Dependent Area-Selective Atomic Layer Deposition Approach for Facile Synthesis of p-Cu₂O/n-ZnO Segmented Nanojunctions. *ACS Appl. Mater. Interfaces* **2018**, *10*, 37671−37678.

(84) Liu, T.-L.; Bent, S. F. Area-Selective Atomic Layer Deposition on Chemically Similar Materials: Achieving Selectivity on Oxide/Oxide Patterns. *Chem. Mater.* **2021**, *33*, 513−523.

PUBLICATION
II

Low-Temperature Route to Direct Amorphous to Rutile Crystallization of TiO₂ Thin Films Grown by Atomic Layer Deposition

Jesse Saari, Harri Ali-Löytty, Kimmo Lahtonen, Markku Hannula,
Lauri Palmolahti, Antti Tukiainen, and Mika Valden

Article

Low-Temperature Route to Direct Amorphous to Rutile Crystallization of TiO₂ Thin Films Grown by Atomic Layer Deposition

Jesse Saari, Harri Ali-Löytty,* Kimmo Lahtonen, Markku Hannula, Lauri Palmolahti, Antti Tukiainen, and Mika Valden*

Read Online

ACCESS | Metrics & More | Article Recommendations | Supporting Information

ABSTRACT: The physicochemical properties of titanium dioxide (TiO₂) depend strongly on the crystal structure. Compared to anatase, rutile TiO₂ has a smaller bandgap, a higher dielectric constant, and a higher refractive index, which are desired properties for TiO₂ thin films in many photonic applications. Unfortunately, the fabrication of rutile thin films usually requires temperatures that are too high (>400 °C, often even 600−800 °C) for applications involving, e.g., temperature-sensitive substrate materials. Here, we demonstrate atomic layer deposition (ALD)-based fabrication of anatase and rutile TiO₂ thin films mediated by precursor traces and oxide defects, which are controlled by the ALD growth temperature when using tetrakis(dimethylamido)titanium(IV) (TDMAT) and water as precursors. Nitrogen traces within amorphous titania grown at 100 °C inhibit the crystal nucleation until 375 °C and stabilize the anatase phase. In contrast, a higher growth temperature (200 °C) leads to a low nitrogen concentration, a high degree of oxide defects, and high mass density facilitating direct amorphous to rutile crystal nucleation at an exceptionally low post deposition annealing (PDA) temperature of 250 °C. The mixed-phase (rutile−brookite) TiO₂ thin film with rutile as the primary phase forms upon the PDA at 250−500 °C that allows utilization in broad range of TiO₂ thin film applications.
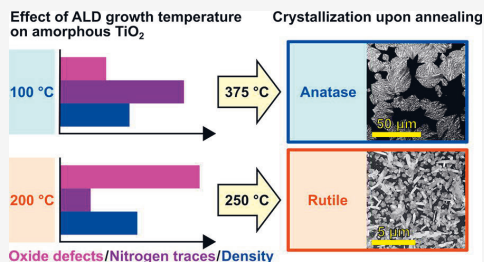
INTRODUCTION

Titanium dioxide (TiO₂) is one of the most widely applied and studied photocatalyst materials, being earth-abundant, non-toxic, and stable in various environments.[1−3] Generally, TiO₂ appears in four phases: amorphous, anatase, rutile, and brookite. The first three are the most commonly used having their own advantages, whereas brookite has remained mainly inapplicable due to the challenges in fabrication of its pure form.[4,5] Amorphous titania (am.-TiO₂) thin films, typically grown at low temperatures, can provide exceptional optical properties and charge carrier dynamics due to the disordered structure and intrinsic Ti³⁺ defects.[6−10] However, concerning photocatalytic applications, defect-induced gap states may increase the possibility to detrimental electron−hole recombi-nation, and the chemical instability of am.-TiO₂ without additional electrocatalysts limits the operating conditions.[11−16] Crystalline defect-free TiO₂, instead, is chemically stable and exhibits reduced charge carrier recombination.[12,17,18]

When comparing the two main crystalline TiO₂ phases, anatase and rutile, the metastable anatase TiO₂ is often regarded as a better photocatalyst than the thermodynamically stable rutile.[3] In fact, based on recent research, rutile is photocatalytically more active in some reactions, especially, oxidative ones, whereas anatase promotes reduction reac-tions.[19] Another interesting approach to enhance charge carrier

separation and photocatalytic activity is a controllable fabrication of anatase−rutile phase junction structures that are reported to outperform pristine single-phase anatase and rutile, e.g., in photoelectrochemical water splitting applica-tions.[20,21]

Unfortunately, the major challenge with rutile thin films in many applications is the need of high processing temperatures (>400 °C, often even 600−800 °C).[22] Some aqueous-phase processes enable growth of rutile nanocrystals at low temperatures (<200 °C), and atomic layer deposition of the anatase−rutile mixed phase is reported around 300 °C, but particularly, methods for obtaining pure rutile thin films at low temperatures are exceedingly limited.[23−27] Epitaxial ALD of rutile TiO₂ thin films on substrates with the rutile-structured SnO₂, RuO₂, or IrO₂ seed layer has been demonstrated around 250 °C.[28] Another potential way to promote rutile formation involves dopant ion-induced oxygen vacancies or oxygen-deficient growth conditions to obtain disordered oxygen

ACS Publications
© 2022 The Authors. Published by
American Chemical Society
15357
https://doi.org/10.1021/acs.jpcc.2c04905
J. Phys. Chem. C 2022, 126, 15357−15366

sublattice enhancing the rearrangement of ions to form easier the constrained and dense rutile phase.[21,22,29]

One possible approach to modify the defect structure of titania is atomic layer deposition, known for its controllable, uniform, and conformal thin film growth via self-limiting surface reactions.[12,24,30,31] Previously, we have shown that intrinsic precursor traces and oxide defects are highly sensitive to ALD growth temperature when using tetrakis-(dimethylamido)titanium(IV) and water as precursors.[10] Interestingly, the growth temperature is also shown to steer the crystallization process toward anatase or rutile TiO$_2$ phases, but understanding of this phenomenon in more detail has remained without comprehensive investigation.[12,18]

This work shows the role of ALD growth temperature-controlled (100−200 °C) intrinsic precursor traces and oxide defects on TiO$_2$ thin film crystallization upon post deposition annealing (PDA, 50 min at 200−500 °C and 500 min at 250 °C). X-ray photoelectron spectroscopy (XPS) is used to investigate the evolution of intrinsic titanium (i.e., Ti^{3+} and under- and over-coordinated Ti^{4+}) and nitrogen (TDMAT fragments or reaction byproducts) defects within the amorphous titania upon PDA in air. Surface chemical analysis together with grazing incidence X-ray diffraction (GIXRD) measurements, X-ray reflectivity (XRR), and scanning electron microscopy (SEM) offers insights into the defect-mediated crystallization of ALD TiO$_2$ and fabrication of the rutile−brookite TiO$_2$ thin film at an exceptionally low PDA temperature of 250 °C.

■ EXPERIMENTAL SECTION

Substrates. The P-doped (resistivity 1−10 Ω·cm) n-type Si(100) wafers from SIEGERT WAFER GmbH (Germany) cleaved in 10 mm × 10 mm × 0.525 mm pieces were used as substrates in all of the experiments.

Atomic Layer Deposition. The ALD of TiO$_2$ was carried out using a Picosun Sunale ALD R-200 Advanced reactor and tetrakis(dimethylamido)titanium(IV) (Ti(N(CH$_3$)$_2$)$_4$, TDMAT, electronic grade 99.999+%, Sigma-Aldrich) and Milli-Q type 1 ultrapure water as precursors. To reach the proper TDMAT precursor vapor pressure, the bubbler was heated to 76 °C, and to prevent condensation of the precursor gas, the delivery line was heated to 85 °C. The water bubbler was sustained at 18 °C by a Peltier element for stability control. Argon (99.9999%, Oy AGA Ab, Finland) was used as a carrier gas. During the deposition, the continuous Ar flow in the TDMAT and H$_2$O lines was 100 sccm. One ALD cycle consisted of a 1.6 s TDMAT pulse followed by a 0.1 s H$_2$O pulse. The excess precursor was pumped away from the reaction chamber during the 6.0 s purge period between each pulse. TiO$_2$ films were deposited at growth temperatures of 100 and 200 °C. The required numbers of ALD cycles for 30 nm-thick TiO$_2$ at growth temperatures of 100 and 200 °C were 480 and 870, respectively.

Post Deposition Annealing. The post deposition annealing for the samples was performed in atmospheric air by placing the samples into a pre-heated tube furnace for 50 min. After the heat treatment, the samples were removed from the tube furnace and let to cool down freely.

X-ray Photoelectron Spectroscopy. Majority of the X-ray photoelectron spectroscopy measurements were conducted using a NanoESCA spectromicroscope system (Omicron Nanotechnology GmbH) in ultrahigh vacuum (UHV) with a base pressure below 1 × 10^{-10} mbar. In NanoESCA, focused

monochromatized Al Kα ($h\nu$ = 1486.5 eV) was used as an excitation radiation for XPS. The investigation of evolution of intrinsic Ti and N defects as a function of oxidation temperature was carried out by using a non-monochromatized DAR400 X-ray source (Al Kα) and Argus hemispherical electron spectrometer (Omicron Nanotechnology GmbH). The core level XP spectra were analyzed by the least-squares fitting of Gaussian−Lorentzian lineshapes and using a Shirley-type background. Ti 2p spectra were fitted as in our previous work[10] by using the Ti 2p$_{3/2}$ reference peak shape measured for crystalline TiO$_2$, i.e., the six-coordinated Ti^{4+} peak (Ti$_{6c}^{4+}$), and the amorphous disordered structure was represented by under- and over-coordinated Ti^{4+} (Ti$_{5/7c}^{4+}$) and Ti^{3+} peaks. The binding energy scale of the spectra was calibrated by fixing the O^{2-} peak of TiO$_2$ to 530.20 eV. CasaXPS version 2.3.22 PR1.0[32] was used as an analysis software and the Scofield photoionization cross-sections as relative sensitivity factors.[33]

Ultraviolet (UV) Light Treatment/Ar$^+$ Ion Bombardment. Ti^{3+} defects were generated within am.-TiO$_2$ thin films via UV treatment and Ar$^+$ ion bombardment. The treatments were carried out using a NanoESCA system (Omicron Nanotechnology GmbH) equipped with an Hg arc UV source (HBO 103 W/2 type lamp, 4.9 eV, 3 h) and an Ar$^+$ ion gun (30 s with 5 kV acceleration voltage; P_{Ar} = 2.5 × 10^{-5} mbar).

Grazing Incidence X-ray Diffraction and X-ray Reflectivity. Structural properties of TiO$_2$ thin films were analyzed by GIXRD and XRR using two diffractometers (PANalytical Empyrean multipurpose and X'Pert^3 MRD diffractometers) equipped with a Cu Kα X-ray source (λ = 1.5406 Å, $h\nu$ = 8.05 keV). In GIXRD measurement, samples were scanned in the 2θ ranges of 24−34 and 20−52° at the grazing incidence angle of ω = 0.3°. The background was removed from each scan to allow easier comparison of the XRD patterns. In XRR measurement, samples were scanned in the coupled ω-2θ range of 0.5−4°. XRR data was modeled by the GenX program (version 3.5.5.) to extract TiO$_2$ film thickness, mass density, and surface roughness using a single-layer model of TiO$_2$ on a Si substrate.[34]

Scanning Electron Microscopy. The surface morphology of TiO$_2$ thin films was studied by scanning electron microscopy (Zeiss Ultra 55, Carl Zeiss Microscopy GmbH). The SEM images were measured by using in-lens mode with a working distance of 2.3−2.4 mm, electron high tension (EHT) of 1.00 kV, and aperture size of 30.00 μm.

■ RESULTS AND DISCUSSION

The amount of intrinsic oxide defects and nitrogen traces in am.-TiO$_2$ depends on the ALD growth temperature when using TDMAT and H$_2$O as precursors.[10] The ALD process at 100 °C leaves nitrogen containing TDMAT fragments or reaction byproducts within the am.-TiO$_2$ film, whereas the growth at 200 °C leads to a low nitrogen content but an increased amount of Ti^{3+}. The amount of under- and over-coordinated Ti$_{5/7c}^{4+}$ ions scales with the amount of Ti^{3+} defects. Furthermore, we have shown that am.-TiO$_2$ grown at 100 °C prefers crystallization into the anatase structure whereas 200 °C growth temperature induces direct crystallization into rutile at the same oxidative annealing temperature (400−500 °C).[12,18] To understand how the intrinsic defects contribute to the crystallization upon post deposition annealing in air, 30 nm-thick ALD TiO$_2$ films grown at 100 and 200 °C were first investigated by X-ray photoelectron spectroscopy before and after PDA at 500 °C.
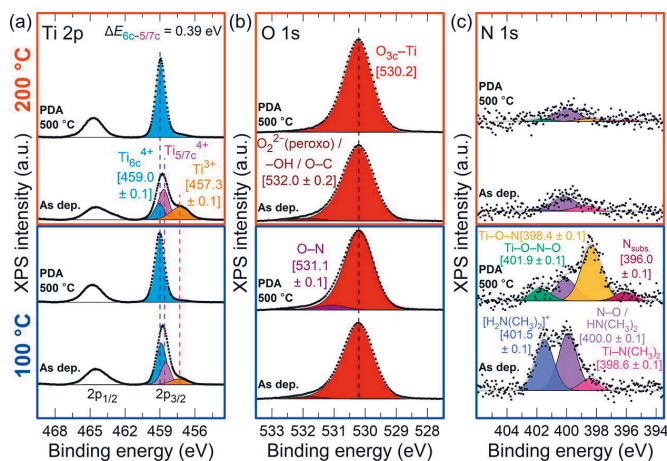
Figure 1. (a) Ti 2p, (b) O 1s, and (c) N 1s XP spectra of 30 nm-thick as-deposited and post deposition-annealed ALD TiO_2 grown at 100 and 200 °C.

Figure 1 shows Ti 2p, O 1s, and N 1s XP spectra of as-deposited amorphous and crystallized (PDA 500 °C) ALD TiO_2 grown at 100 and 200 °C (surface concentrations of elements are presented in Table S1). Figure 1a shows that oxide defects, i.e., Ti^{3+} and $Ti_{5/7c}^{4+}$ defects, were completely removed from both samples upon PDA at 500 °C despite the difference in the initial amounts. Only six-coordinated Ti^{4+} ions (Ti_{6c}^{4+}) were present in PDA 500 °C samples supporting the crystallized structure, i.e., $Ti-O_6$ octahedra are the building blocks of crystalline TiO_2.[35,36] Few subtle changes were observed in the O 1s transition (Figure 1b) consisting of the O–Ti component (O^{2-}) at 530.2 eV and minor O_2^{2-}/–OH/ O–C and O–N peaks at 532.0 ± 0.2 and 531.1 ± 0.1 eV, respectively. The 532.0 eV component of as-deposited samples corresponds to the interstitial peroxo (O_2^{2-}) species as discussed in our previous work.[10] The O 1s O–N peak was detected only in the TiO_2 (100 °C) PDA 500 °C sample. In addition, a difference was observed in the O 1s linewidths that decreased upon the PDA from 1.16 to 1.14 and 1.07 eV for 100 and 200 °C grown samples, respectively (Figure S1). The narrower O 1s linewidth is attributed to the lower nitrogen concentration and higher degree of crystalline order for the 200 °C grown sample after the PDA. It should be noted that the broader peak and a high binding energy tail of the O 1s spectra could be attributed to hydroxyl groups.[13,37] However, the concentration of possible hydroxyl groups was too low to be reliably differentiated from the O 1s spectra, and no difference was observed between the growth temperatures.

The removal of Ti^{3+} defects upon the PDA was accompanied by the disappearance of the Ti^{3+} gap state peak at 0.3–0.4 eV from the XPS valence band spectra (Figure S2). Again, a subtle difference was observed between the growth temperatures. Upon the PDA, the valence band edge position shifted 0.20 eV toward lower binding energy for the 200 °C grown sample but no change was observed for the 100 °C grown sample. This may relate to the band gap difference between rutile TiO_2 (E_g = 3.0 eV) and anatase TiO_2 (E_g = 3.2 eV).[22] N 1s spectra in Figure 1c reveal strong difference between the samples. Nitrogen containing reaction byproducts and

TDMAT fragments within am.-TiO_2 were clearly detected for the 100 °C grown sample as represented by the three components at 401.5 ± 0.1, at 400.0 ± 0.1, and at 398.6 ± 0.1 eV.[10,31,38] After the PDA at 500 °C, an additional component at lower binding energy (396.0 ± 0.1 eV) emerged in the ALD TiO_2 grown at 100 °C. The component at 396 eV is typically reported to relate to substitutional nitrogen located at O^{2-} sites, i.e., Ti–N-like species within the TiO_2 lattice.[39–42] Due to dimethylamine decomposition at >275 °C,[43] unreacted TDMAT ligands ($Ti-N(CH_3)_2$) and protonated dimethylamine ($H_2N(CH_3)_2^+$) species are proposed to decompose during the PDA leading to the formation of TiO_2 with Ti–O–N and Ti–O–N–O species at 398.4 ± 0.1 and 401.9 ± 0.1 eV, respectively. These species contribute to the O–N component in O 1s (Figure 1b).[44] The formation mechanism of these nitrogen species within the TiO_2 lattice is discussed in more detail in Figure 4. The N 1s signal detected at 400.0 ± 0.1 eV was assigned to dimethylamine ALD process byproducts ($HN(CH_3)_2$) and their decomposed and oxidized N–O species locating primarily at the surface from where these species may have partially desorbed during the PDA. Indeed, in our previous study, these species (N 1s at 400.0 ± 0.1 eV) showed strong surface enrichment (1.8 at.% vs initial 0.2 at.%) after similar PDA at 350 °C that resulted in partial crystallization.[12] Therefore, it is suggested that the desorption of dimethylamine species is followed by crystallization and the remaining nitrogen species at higher temperatures are oxidized to N–O species that have similar N 1s binding energy with dimethylamine. Surface decomposition of pure dimethylamine takes place at >275 °C, and therefore, it is unlikely to have these species at the surface after PDA at 500 °C.[43] Compared to the am.-TiO_2 thin film grown at 100 °C, only a minor amount of nitrogen was observed in ALD TiO_2 grown at 200 °C.

Despite the strong chemical changes in Ti and N species upon the PDA, only subtle changes were observed in the elemental surface concentrations (Table S1). The O^{2-}/Ti ratio was close to 2 for all the samples suggesting stoichiometric TiO_2, although ionic coordination of titanium differs between as-deposited amorphous and crystallized (PDA 500 °C)

TiO_2.[10,35,36] The nitrogen concentrations were 0.9 and 0.2 at.% for the samples grown at 100 and 200 °C, respectively. In addition, all the surfaces had 2−5 at.% of carbon. Detailed analysis of carbon species in the film was compromised due to the build-up of adventitious carbon during the sample transfer via air. TiO_2 films also contain hydrogen that cannot be directly probed with XPS, but hydrogen bonded to nitrogen species was indirectly analyzed from N 1s spectra. Indeed, Xia et al. recently studied the same TDMAT + H_2O ALD process and, by using elastic recoil detection analysis (ERDA), observed elevated hydrogen concentration in ALD TiO_2 grown at 100 °C (H/Ti = 0.5) compared to the film grown at 225 °C (H/Ti = 0.1).[37] The difference in the hydrogen content was found to follow the same growth temperature trend with N-bearing TDMAT fragments.

Grazing incidence X-ray diffraction measurements were conducted to study the crystallization of 30 nm-thick ALD TiO_2 grown at 100 and 200 °C upon PDA at 300, 400, and 500 °C. Figure 2a reveals that am.-TiO_2 grown at 100 °C
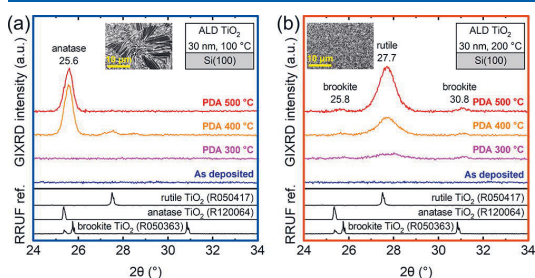

Figure 2. GIXRD patterns of 30 nm-thick ALD TiO_2 grown at (a) 100 °C and (b) 200 °C upon post deposition annealing. The XRD references are from the RRUF database.[45] The insets show the SEM images after PDA at 500 °C.

retains the amorphous phase during the PDA at 300 °C but shows similarly strong anatase peaks at 400 and at 500 °C, suggesting abrupt crystallization. Previously, we have observed that the abrupt am.-TiO_2 to anatase TiO_2 transition depends on the ALD growth temperature and takes place already at 300 °C for a growth temperature of 150 °C.[18] In contrast, am.-TiO_2 grown at 200 °C shows gradual crystallization to mainly rutile TiO_2 already at 300 °C. In addition to the rutile phase, some brookite phase characterized by the peaks at 30.8 and 25.8° is also present after the PDA in TiO_2 grown at 200 °C. For both growth temperatures, complete crystallization was reached upon the PDA at 500 °C.[12,18] Broader XRD peaks reflect in average smaller grain size for the rutile TiO_2 films compared to the anatase TiO_2, as supported by the SEM images in the insets of Figure 2.

As-deposited and PDA 500 °C samples were analyzed by XRR, and TiO_2 film thickness, mass density, and roughness were extracted via modeling (Figure S3 and Table 1). The thickness of the sample grown at 100 °C decreased by 3.3% during the PDA, while only a marginal change was observed in the 200 °C grown sample. The densities of TiO_2 films grown at 100 and 200 °C were 3.5 and 3.9 g/cm³, respectively. The PDA induced a small decrease in film roughness but had only little if any effect on the film density. The difference in film densities after the PDA can be understood by the higher bulk density of rutile vs anatase TiO_2 (4.2 vs 3.9 g/cm³). Quite

Table 1. XRR Modeling Results for 30 nm-Thick ALD TiO_2 Grown at 100 and 200 °C on Si after Deposition and after Post Deposition Annealing at 500 °C

	TiO_2 density (g/cm³)	TiO_2 thickness (nm)	TiO_2 roughness (nm)
100 °C, as-deposited	3.52	30.4	0.83
100 °C, PDA 500 °C	3.50	29.4	0.73
200 °C, as-deposited	3.94	33.5	1.06
200 °C, PDA 500 °C	3.93	33.6	0.91

surprisingly, the apparent mass densities did not change upon crystallization. The decrease in film thickness in the case of the 100 °C grown sample is likely due to the desorption of excess precursor traces and re-structuring of the film.

These density results are concordant with the values reported by Abendroth et al. for am.-TiO_2 grown by using the TDMAT + H_2O ALD process at growth temperatures of 120−200 °C.[27] The density increased from 3.65 g/cm³ (120 °C) to 3.95 g/cm³ (200 °C) and reached the highest value of 4.1 g/cm³ at growth temperatures of 320−330 °C, resulting in an anatase−rutile mixed phase with a relatively high N concentration of around 6 at.%. Furthermore, Busani and Devine reported similar densities for anatase (3.62 g/cm³) and mixed anatase−rutile (3.85 g/cm³) TiO_2 thin films deposited by PECVD, but before the PDA at 600 °C, the density of their am.-TiO_2 was smaller (3.2 g/cm³).[46] Piercy et al. observed ALD TiO_2 film density to increase with growth temperature from 3.3 g/cm³ (38 °C) to 3.8 g/cm³ (150 °C) when using $TiCl_4$ and H_2O as precursors.[47] Also, the concentration of trace Cl⁻ within the TiO_2 films decreased with the growth temperature and was reported to significantly decrease with TiO_2 crystallization above 160 °C. Go et al. fabricated ALD TiO_2 at 80 °C with TDMAT and O_3 using a process where crystallization was induced by the duration of oxygen plasma exposure during the ALD growth cycle.[48] Short (3 s) plasma exposure resulted in less dense (3.73 g/cm³) am.-TiO_2, while 30 s plasma exposure was sufficient to grow anatase TiO_2 with a density of 4.15 g/cm³. The duration of O_3 plasma exposure affected also to the amount of N traces within the TiO_2 film and was <2 at.% for the two samples.

Concerning rutile formation, Rafieian et al. reported that tuning of the oxygen concentration during reactive magnetron sputtering can be utilized to fabricate sub-stoichiometric and stoichiometric am.-TiO_2, which crystallize into rutile and anatase upon annealing in air at 500 °C, respectively.[29] Furthermore, according to Li et al., oxygen deficiency prefers rutile formation upon rapid thermal annealing (RTA) at 800 °C for 4 min.[21] However, even though the am.-TiO_2 grown at 200 °C showed a considerable concentration of Ti^{3+}, the film was not oxygen-deficient as the O^{2-}/Ti ratio was close to 2, and still, the film crystallized as rutile.

The difference in ALD TiO_2 crystallization was mediated by the ALD growth temperature that affected essentially the concentration of oxide defects and nitrogen traces. Thus, we tested if the crystallization could be steered toward rutile by the introduction of Ti^{3+} defects, i.e., oxygen vacancies, to the as-deposited TiO_2 using UV light treatment and Ar⁺ ion bombardment (Figures S4 and S5). The test was performed using ALD TiO_2 grown at 150 °C that contains less nitrogen traces compared to TiO_2 grown at 100 °C but still favors crystallization to anatase TiO_2.[10,18] Neither the UV light treatment nor the Ar⁺ ion bombardment changed the

crystallization from anatase upon the PDA at 500 °C, even though the concentration of Ti^{3+} defects, within XPS information depth, exceeded that of the 200 °C grown sample. Thus, the result suggests that Ti^{3+} defects were not the declarative factor determining the crystallization.

Crystallization to anatase TiO_2 is more common for PDA temperatures <500 °C. McDowell et al. reported that am.-TiO_2 grown from TDMAT and H_2O at 150 °C, containing nitrogen impurities but no Ti^{3+}, crystallized into the anatase phase upon 1 h of annealing in air at 500 °C.[49] Furthermore, Pore et al. found that nitrogen and particularly Ti−N bonds prefer formation of pure anatase instead of the anatase−rutile mixed phase.[50] Similar results were also reported by Cheng et al. who considered the anatase phase stabilization to occur due to the compressive stress induced by substitutional nitrogen ions preventing the formation of more dense rutile TiO_2.[51] Regarding the anatase to rutile phase transition due to the ionic size effect, nitrogen presumably inhibits the phase transformation, but on the other hand, oxygen vacancies induced by N doping should promote rutile formation.[22] Our results suggest that intrinsic nitrogen defects in am.-TiO_2 delay and steer the crystallization toward anatase TiO_2, and without nitrogen traces, a more dense am.-TiO_2 favors crystallization to also more dense rutile TiO_2.

The scanning electron microscopy images in the insets of Figure 2a,b highlight the prominent difference in the morphology and grain size of anatase and rutile TiO_2 (PDA 500 °C). The same SEM images in a larger image size are presented in Figure 3. ALD TiO_2 grown at 100 °C exhibits
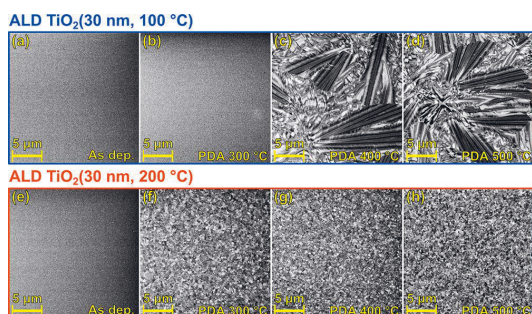
exceptionally large anatase grains with a lateral size of >10 μm, which is over 300 times larger than the film thickness. Based on literature, anatase grains with similar magnitude of size have been fabricated by post deposition annealing of ALD grown amorphous Ti−Nb−O or Ti−Ta−O mixed oxide films.[52] Crystallization of undoped ALD grown am.-TiO_2 into anatase is reported to result in micron-wide grains, instead.[49,53] The rutile thin film (PDA-treated TiO_2 grown at 200 °C), by contrast, consists of much smaller grains (<1 μm).

As implied by GIXRD results (Figure 2) and sizes of the anatase and rutile grains, the crystallization kinetics of ALD am.-TiO_2 grown at 100 and 200 °C are totally different. Figure 3 shows that full crystalline coverage on TiO_2 grown at 200 °C is obtained already during PDA at 300 °C (Figure 3f), whereas TiO_2 grown at 100 °C shows no crystal nucleation after the same PDA treatment (Figure 3b). However, during PDA at 400 °C (Figure 3c), large grains appear in a 100 °C grown film. To find the nucleation temperature of ALD TiO_2 grown at 100 °C, the PDA temperature range of 300−400 °C was studied in more detail. Figure S6 reveals that, upon PDA 350 °C treatment, some tiny crystal nuclei appear probably due to random impurities or defects but PDA at 375 °C leads to partial surface crystallization with large round grains with a diameter over 10 μm.

To understand how the oxide defects and nitrogen precursor traces evolve upon crystallization of ALD TiO_2, the Ti and N species at the surface were analyzed as a function of PDA temperature. Figure 4 shows the Ti and N species (cf., Figure 1) for the N-rich ALD TiO_2 grown at 100 °C (Figure S8 shows the XPS spectra). The concentration of Ti defects (Ti^{3+} and $Ti_{5/7c}^{4+}$ species) was shown to decrease gradually with increasing PDA temperature until they disappeared completely at 400 °C that coincided with the crystallization. In the case of ALD TiO_2 grown at 200 °C, the Ti defects disappeared already at 250 °C (Figures S7 and S9) in line with the lower crystallization temperature. The evolution of N species in the case of the 200 °C grown sample was included in our previous work; besides 350 °C PDA temperature where surface enrichment of 1.8 at.% N (N 1s at 400.0 ± 0.1 eV) was detected, the amount of N at the surface was too low (0.2 at.%) for the analysis.[12] In contrast, N species in ALD TiO_2 grown at 100 °C showed a clear evolution with PDA temperature while there was only a slight decrease in the total amount of surface N (from 0.86 to 0.78 at.% N and from 2.8 to 1.8 at.% N/Ti). As the temperature increased from 200 to 400 °C, the amount of protonated dimethylamine ($H_2N(CH_3)_2^+$) reaction byproducts (i.e., $HN(CH_3)_2$ reacted with the −OH group at 401.5 eV) decreased with a rather
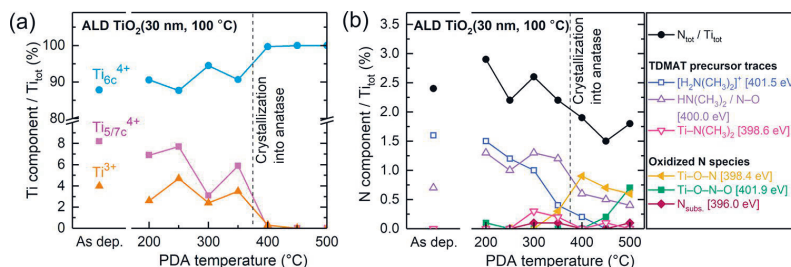

Figure 3. SEM images of 30 nm-thick ALD TiO_2 grown at (a−d) 100 °C and (e−h) 200 °C: (a, e) as-deposited and after post deposition annealing (50 min) at (b, f) 300 °C, (c, g) 400 °C, and (d, h) 500 °C. All the images were taken with the same magnification.

Figure 4. Evolution of (a) Ti and (b) N species as a function of the PDA temperature for 30 nm-thick ALD TiO_2 grown at 100 °C. The binding energy values of N 1s components in panel (b) are depicted in brackets.

concomitant increase in Ti—O—N species (at 398.4 eV). Thus, it is suggested that, during the PDA, N—C bonds break and CH_4 desorbs as follows

$$Ti - (O^-)[H_2N(CH_3)_2]^+ \ (s)$$
$$\rightarrow Ti - O - N \ (s) + 2CH_4(g) \tag{1}$$
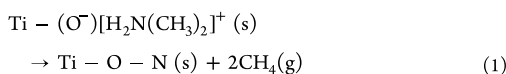
For the PDA temperature above crystallization, a high binding energy component appears in N 1s at 401.9 eV, slightly above the $H_2N(CH_3)_2^+$ component observed for lower temperatures at 401.5 eV. The binding energy corresponds to strongly oxidized nitrogen species,[54] and it is suggested that, for temperatures >400 °C, Ti—O—N species oxidize to Ti—O—N—O. Substitutional nitrogen (N 1s at 396.0 eV) appeared for temperatures above the crystallization temperature (400 °C). Such substitutional N species induce visible-light absorption that is desirable in photocatalysis.[39] However, in our case, the amount of substitutional nitrogen was too small to induce visible-light absorption (cf., Figure S1c in ref 18). In addition, at 300 °C, a minor increase in the N 1s peak component at 400.0 eV was observed for the ALD TiO_2 grown at 100 °C, which suggests surface segregation and subsequent desorption of $HN(CH_3)_2$ that were observed to take place at 350 °C for the ALD TiO_2 grown at 200 °C.[12] Furthermore, these dimethylamine reaction byproducts and unreacted TDMAT ligands (at 398.6 eV) will likely react or oxidize to N—O-like species during the annealing.

Nitrogen is known to inhibit the TiO_2 crystal nucleation and raise the nucleation temperature.[55] Nitrogen also stabilizes the anatase phase.[22,51] According to Hukari et al., the nucleation onset temperature of stoichiometric am.-TiO_2 is in the range of 250—300 °C, whereas an additional nitrogen content can raise the nucleation temperature up to 400 °C.[55] Our results show that the excess of N-bearing TDMAT fragments or reaction byproducts within am.-TiO_2 can cause the aforementioned N-mediated effects. Nitrogen defects can also contribute to the exceptionally large anatase crystal size detected for ALD TiO_2 grown at 100 °C. Similarly large crystals have been observed to result from explosive crystallization of Ti—Nb—O or Ti—Ta—O mixed oxide films prepared by Pore et al.[52] In the explosive crystallization process, the amorphous material crystallizes rapidly in a self-sustaining manner due to the latent heat released during the crystallization and consequently inducing further amorphous material to convert into crystalline form.[52,56,57] Although the explosive crystallization is an autocatalytic phenomenon, the speed of the process depends still on the temperature and orientation of the crystal growth.[56] However, as shown in Figure S6c and in the work by Pore et al., crystallization fronts proceed until collision with an adjacent grain and therefore inhibited nucleation and low distribution density of crystal nuclei is a desired feature when targeting formation of exceptionally large grains.[52,58] By increasing temperature, further energy barriers for nucleation are overcome and complete crystallization is obtained (Figure S6d).[52]

In contrast to the ALD TiO_2 grown at 100 °C, the ALD TiO_2 grown at 200 °C containing only little N traces evidences strictly different crystallization properties. As shown in Figure 5a, the ALD TiO_2 grown at 200 °C shows partial surface crystallization already at 250 °C. Furthermore, Figure 5 depicts that extending the PDA duration at 250 °C from 50 min (Figure 5a) to 500 min (Figure 5b) resulted in complete surface crystallization with crystal size <1 μm. The GIXRD
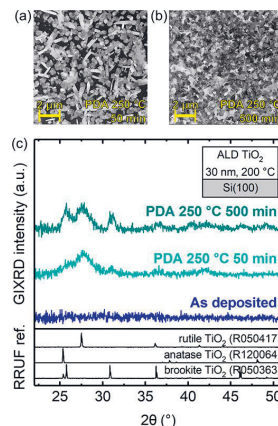

Figure 5. SEM images of 30 nm-thick ALD TiO_2 grown at 200 °C after PDA at 250 °C (a) for 50 min and (b) for 500 min. (c) GIXRD patterns of the samples. The XRD references are from the RRUF database.[45]
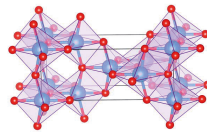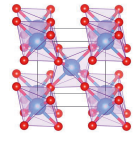
patterns (Figure 5c) show both rutile and brookite TiO_2 peaks indicating the mixed-phase TiO_2 thin film with rutile as the primary phase. The rutile to brookite ratio was found to increase with increasing PDA temperature (cf. Figure 2).

Two distinct crystal morphologies were observed after crystal nucleation of am.-TiO_2: needle- and round-like crystals (Figure 5a). Li et al. stated that the preferential growth of different rutile crystal morphologies in the aqueous-phase process is attributed to the concentration of $TiOH^{3+}$ ions around the TiO_2 nucleus.[25] A low $TiOH^{3+}$ concentration around the nucleus induces needle-like morphology, whereas a high concentration prefers radial growth of crystalline material. Comparing this crystallization mechanism to our observations, we propose that the different crystal morphologies may be analogously induced by local variations in oxide defect density within the am.-TiO_2 structure.

In general, the crystallization of am.-TiO_2 can be considered a random process that is affected by many factors. Nucleation, i.e., how TiO_6 octahedra join each other, determines whether am.-TiO_2 crystallizes as anatase or rutile.[59] Growth of metastable anatase is statistically more likely since there are more possibilities for octahedra to join at right angles compared to joining linearly sharing two edges required for the rutile phase.[22] Apparently, the chemical composition and structure of the am.-TiO_2 thin film predetermined the resulting phase structure upon the PDA. We note that the crystallization can be affected by, for example, film thickness, substrate, and PDA process parameters that should be studied separately. Also, it is worth pointing out that crystallization can proceed at even lower temperatures if the duration of the PDA treatment is extended.

The effects of intrinsic defects on crystallization of ALD am.-TiO_2 upon PDA are summarized in Table 2. Lower growth temperature (100 °C) prefers trapping of TDMAT-based nitrogen species that leads to delayed crystal nucleation (at 375 °C) and exceptionally large anatase grains (>10 μm). Higher ALD growth temperature (200 °C) results in higher mass density and higher concentration of intrinsic oxide defects but less nitrogen traces. Interestingly, this am.-TiO_2 favors direct crystallization into mixed rutile-brookite phase TiO_2 with rutile

Table 2. Summary of Growth and Crystallization of am.-TiO$_2$ Thin Films Grown by ALD Using TDMAT and H$_2$O Precursors at the Growth Temperatures of 100 and 200 °C

		ALD growth temperature	
		100 °C	200 °C
As–deposited	Precursor traces[a]	+++	+
	Oxide defects[b]	+	+++
	Mass density	3.5 g/cm^3	3.9 g/cm^3
Post deposition annealing	Crystal nucleation observed at[c]	375 °C	250 °C
	Primary phase[d]	ANATASE	RUTILE (BROOKITE)[e]

[a]Nitrogen species originated from dimethylamide ligands of TDMAT molecules. The plus signs represent the surface concentration determined by the XPS measurement. [b]Oxygen vacancies, interstitial peroxo species (O$_2^{2-}$), and Ti^{3+}/Ti$_{5/7c}^{4+}$ ions formed via displacement of oxygen ions within the stoichiometric amorphous TiO$_2$ structure. The plus signs represent the surface concentration determined by the XPS measurement. [c]The results are based on a PDA time of 50 min. [d]The drawings of crystalline TiO$_2$ structures were produced by VESTA software[63] using rutile[64] and anatase[65] crystal structure models provided by the American Mineralogist Crystal Structure Database.[66] [e]Rutile is the main phase. The proportion of brookite decreases at higher PDA temperatures.

as the primary phase already at 250 °C, which is exceptionally low for TiO$_2$ thin films. ALD of the anatase−rutile mixed phase thin film has been reported at 300 °C.[23,24,27] Fabrication of rutile-rich thin films at relatively low temperature is of interest in optical and photocatalytic applications since rutile exhibits optically anisotropic nature, a high refractive index, and desirable catalytic activity in oxidation reactions.[3,19,60] Lowering the fabrication temperature of photocatalytically active TiO$_2$ thin films enables applications involving temperature-sensitive materials such as polymers. Furthermore, enabling low processing temperatures (250−400 °C) to form rutile-rich TiO$_2$ thin films without an additional seed layer is of interest for high-κ applications, such as dynamic random-access memory (DRAM) capacitors.[61,62] Our work demonstrated that tuning the ALD TiO$_2$ process parameters enabled lowering the fabrication temperature of the rutile-rich TiO$_2$ thin film to 250 °C. Controlling the thin film defects was essential to lowering the crystallization temperature, and we believe that the provided mechanistic understanding paves the way to further optimize the process for even higher rutile purity at even lower temperatures.

CONCLUSIONS

The role of intrinsic defects on crystallization of am.-TiO$_2$ thin films grown by ALD using TDMAT and H$_2$O precursors upon PDA treatment in air was studied as a function of ALD growth temperature (100−200 °C). The am.-TiO$_2$ film grown at 100 °C contained 0.9 at.% of nitrogen-bearing traces of the TDMAT precursor that inhibited crystal nucleation up to 375 °C and led to explosive crystallization of large anatase grains (>10 μm). In contrast, the am.-TiO$_2$ grown at 200 °C contained less precursor traces (0.2 at.% N) and crystallized into the mixed-phase (rutile−brookite) TiO$_2$ thin film with rutile as the primary phase at 250 °C. The concentration of

Ti^{3+} defects increased with ALD growth temperature, and upon crystallization, these oxide defects were completely removed. Increasing the amount of Ti^{3+} defects within am.-TiO$_2$ either by UV treatment or Ar$^+$-ion sputtering did not affect the crystallization. The mass densities of ALD TiO$_2$ thin films were 3.5 g/cm^3 for the film grown at 100 °C and 3.9 g/cm^3 for the film grown at 200 °C. The mass densities did not change during the crystallization. Therefore, it is suggested that the growth of denser am.-TiO$_2$ mediates direct crystallization into a more dense and stable rutile phase, while the growth of less dense am.-TiO$_2$ with precursor traces favors crystallization into a metastable anatase phase. Often, am.-TiO$_2$ thin films crystallize first into anatase and subsequently transform from an anatase to rutile phase requiring typically PDA temperatures >500 °C. By controlling the ALD growth temperature, we were able to demonstrate direct amorphous to rutile-rich TiO$_2$ thin film fabrication at 250−500 °C that has potential applications in the fields requiring high-κ thin films such as DRAM capacitors. Moreover, the fabrication of crystalline TiO$_2$ thin films at an exceptionally low temperature of 250 °C enables applications involving temperature-sensitive materials such as polymers.

ASSOCIATED CONTENT

Supporting Information

The Supporting Information is available free of charge at https://pubs.acs.org/doi/10.1021/acs.jpcc.2c04905.

Data and analysis from XPS, SEM, XRR, and GIXRD measurements (PDF)

AUTHOR INFORMATION

Corresponding Authors

Harri Ali-Löytty − *Surface Science Group, Faculty of Engineering and Natural Sciences, Tampere University, Tampere FI-33014, Finland;* orcid.org/0000-0001-8746-7268; Email: harri.ali-loytty@tuni.fi

Mika Valden − *Surface Science Group, Faculty of Engineering and Natural Sciences, Tampere University, Tampere FI-33014, Finland;* Email: mika.valden@tuni.fi

Authors

Jesse Saari − *Surface Science Group, Faculty of Engineering and Natural Sciences, Tampere University, Tampere FI-33014, Finland;* orcid.org/0000-0001-6741-0838

Kimmo Lahtonen − *Faculty of Engineering and Natural Sciences, Tampere University, Tampere FI-33014, Finland;* orcid.org/0000-0002-8138-7918

Markku Hannula − *Surface Science Group, Faculty of Engineering and Natural Sciences, Tampere University, Tampere FI-33014, Finland;* orcid.org/0000-0003-1110-7439

Lauri Palmolahti − *Surface Science Group, Faculty of Engineering and Natural Sciences, Tampere University, Tampere FI-33014, Finland;* orcid.org/0000-0001-9992-6628

Antti Tukiainen − *Faculty of Engineering and Natural Sciences, Tampere University, Tampere FI-33014, Finland*

Complete contact information is available at:
https://pubs.acs.org/10.1021/acs.jpcc.2c04905

Notes

The authors declare no competing financial interest.

ACKNOWLEDGMENTS

REFERENCES

(1) Septina, W.; Tilley, S. D. Emerging Earth-Abundant Materials for Scalable Solar Water Splitting. *Curr. Opin. Electrochem.* 2017, 2, 120−127.

(2) Pelaez, M.; Nolan, N. T.; Pillai, S. C.; Seery, M. K.; Falaras, P.; Kontos, A. G.; Dunlop, P. S. M.; Hamilton, J. W. J.; Byrne, J. A.; O'Shea, K.; et al. Review on the Visible Light Active Titanium Dioxide Photocatalysts for Environmental Applications. *Appl. Catal., B* 2012, 125, 331−349.

(3) Park, H.; Park, Y.; Kim, W.; Choi, W. Surface Modification of TiO_2 Photocatalyst for Environmental Applications. *J. Photochem. Photobiol., C* 2013, 15, 1−20.

(4) Di Paola, A.; Bellardita, M.; Palmisano, L. Brookite, the Least Known TiO_2 Photocatalyst. *Catalysts* 2013, 3, 36−73.

(5) Dambournet, D.; Belharouak, I.; Amine, K. Tailored Preparation Methods of TiO_2 Anatase, Rutile, Brookite: Mechanism of Formation and Electrochemical Properties. *Chem. Mater.* 2010, 22, 1173−1179.

(6) Hu, S.; Shaner, M. R.; Beardslee, J. A.; Lichterman, M.; Brunschwig, B. S.; Lewis, N. S. Amorphous TiO_2 Coatings Stabilize Si, GaAs, and GaP Photoanodes for Efficient Water Oxidation. *Science* 2014, 344, 1005−1009.

(7) Glezakou, V.-A.; Rousseau, R. Shedding Light on Black Titania. *Nat. Mater.* 2018, 17, 856−857.

(8) Sivula, K. Defects Give New Life to an Old Material: Electronically Leaky Titania as a Photoanode Protection Layer. *ChemCatChem* 2014, 6, 2796−2797.

(9) Nunez, P.; Richter, M. H.; Piercy, B. D.; Roske, C. W.; Cabán-Acevedo, M.; Losego, M. D.; Konezny, S. J.; Fermin, D. J.; Hu, S.; Brunschwig, B. S.; Lewis, N. S. Characterization of Electronic Transport through Amorphous TiO_2 Produced by Atomic Layer Deposition. *J. Phys. Chem. C* 2019, 123, 20116−20129.

(10) Saari, J.; Ali-Löytty, H.; Kauppinen, M. M.; Hannula, M.; Khan, R.; Lahtonen, K.; Palmolahti, L.; Tukiainen, A.; Grönbeck, H.; Tkachenko, N. V.; et al. Tunable Ti^{3+}-Mediated Charge Carrier Dynamics of Atomic Layer Deposition-Grown Amorphous TiO_2. *J. Phys. Chem. C* 2022, 126, 4542−4554.

(11) Ros, C.; Andreu, T.; Morante, J. R. Photoelectrochemical Water Splitting: A Road from Stable Metal Oxides to Protected Thin Film Solar Cells. *J. Mater. Chem. A* 2020, 8, 10625−10669.

(12) Ali-Löytty, H.; Hannula, M.; Saari, J.; Palmolahti, L.; Bhuskute, B. D.; Ulkuniemi, R.; Nyyssönen, T.; Lahtonen, K.; Valden, M. Diversity of TiO_2: Controlling the Molecular and Electronic Structure of Atomic-Layer-Deposited Black TiO_2. *ACS Appl. Mater. Interfaces* 2019, 11, 2758−2762.

(13) Hannula, M.; Ali-Löytty, H.; Lahtonen, K.; Sarlin, E.; Saari, J.; Valden, M. Improved Stability of Atomic Layer Deposited Amorphous TiO_2 Photoelectrode Coatings by Thermally Induced Oxygen Defects. *Chem. Mater.* 2018, 30, 1199−1208.

(14) Correa, G. C.; Bao, B.; Strandwitz, N. C. Chemical Stability of Titania and Alumina Thin Films Formed by Atomic Layer Deposition. *ACS Appl. Mater. Interfaces* 2015, 7, 14816−14821.

(15) Kriegel, H.; Kollmann, J.; Raudsepp, R.; Klassen, T.; Schieda, M. Chemical and Photoelectrochemical Instability of Amorphous TiO_2 Layers Quantified by Spectroscopic Ellipsometry. *J. Mater. Chem. A* 2020, 8, 18173−18179.

(16) Saari, J.; Ali-Löytty, H.; Honkanen, M.; Tukiainen, A.; Lahtonen, K.; Valden, M. Interface Engineering of TiO_2 Photoelectrode Coatings Grown by Atomic Layer Deposition on Silicon. *ACS Omega* 2021, 6, 27501−27509.

(17) Cheng, W.-H.; Richter, M. H.; May, M. M.; Ohlmann, J.; Lackner, D.; Dimroth, F.; Hannappel, T.; Atwater, H. A.; Lewerenz, H.-J. Monolithic Photoelectrochemical Device for Direct Water Splitting with 19% Efficiency. *ACS Energy Lett.* 2018, 3, 1795−1800.

(18) Khan, R.; Ali-Löytty, H.; Saari, J.; Valden, M.; Tukiainen, A.; Lahtonen, K.; Tkachenko, N. V. Optimization of Photogenerated Charge Carrier Lifetimes in ALD Grown TiO_2 for Photonic Applications. *Nanomaterials* 2020, 10, 1567.

(19) Yamakata, A.; Vequizo, J. J. M. Curious Behaviors of Photogenerated Electrons and Holes at the Defects on Anatase, Rutile, and Brookite TiO_2 Powders: A Review. *J. Photochem. Photobiol., C* 2019, 40, 234−243.

(20) Scanlon, D. O.; Dunnill, C. W.; Buckeridge, J.; Shevlin, S. A.; Logsdail, A. J.; Woodley, S. M.; Catlow, C. R. A.; Powell, M. J.; Palgrave, R. G.; Parkin, I. P.; et al. Band Alignment of Rutile and Anatase TiO_2. *Nat. Mater.* 2013, 12, 798−801.

(21) Li, A.; Wang, Z.; Yin, H.; Wang, S.; Yan, P.; Huang, B.; Wang, X.; Li, R.; Zong, X.; Han, H.; Li, C. Understanding the Anatase−Rutile Phase Junction in Charge Separation and Transfer in a TiO_2 Electrode for Photoelectrochemical Water Splitting. *Chem. Sci.* 2016, 7, 6076−6082.

(22) Hanaor, D. A. H.; Sorrell, C. C. Review of the Anatase to Rutile Phase Transformation. *J. Mater. Sci.* **2011**, *46*, 855−874.

(23) Aarik, J.; Aidla, A.; Kiisler, A.-A.; Uustare, T.; Sammelselg, V. Effect of Crystal Structure on Optical Properties of TiO₂ Films Grown by Atomic Layer Deposition. *Thin Solid Films* **1997**, *305*, 270−273.

(24) Reiners, M.; Xu, K.; Aslam, N.; Devi, A.; Waser, R.; Hoffmann-Eifert, S. Growth and Crystallization of TiO₂ Thin Films by Atomic Layer Deposition Using a Novel Amido Guanidinate Titanium Source and Tetrakis-Dimethylamido-Titanium. *Chem. Mater.* **2013**, *25*, 2934−2943.

(25) Li, Y.; Liu, J.; Jia, Z. Morphological Control and Photo-degradation Behavior of Rutile TiO₂ Prepared by a Low-Temperature Process. *Mater. Lett.* **2006**, *60*, 1753−1757.

(26) Yang, K.; Zhu, J.; Zhu, J.; Huang, S.; Zhu, X.; Ma, G. Sonochemical Synthesis and Microstructure Investigation of Rod-like Nanocrystalline Rutile Titania. *Mater. Lett.* **2003**, *57*, 4639−4642.

(27) Abendroth, B.; Moebus, T.; Rentrop, S.; Strohmeyer, R.; Vinnichenko, M.; Weling, T.; Stöcker, H.; Meyer, D. C. Atomic Layer Deposition of TiO₂ from Tetrakis(Dimethylamino)Titanium and H₂O. *Thin Solid Films* **2013**, *545*, 176−182.

(28) Niemelä, J.-P.; Marin, G.; Karppinen, M. Titanium Dioxide Thin Films by Atomic Layer Deposition: A Review. *Semicond. Sci. Technol.* **2017**, *32*, No. 093005.

(29) Rafieian, D.; Ogieglo, W.; Savenije, T.; Lammertink, R. G. H. Controlled Formation of Anatase and Rutile TiO₂ Thin Films by Reactive Magnetron Sputtering. *AIP Adv.* **2015**, *5*, No. 097168.

(30) Dendooven, J.; Detavernier, C. *Atomic Layer Deposition in Energy Conversion Applications*; Bachmann, J., Ed.; John Wiley & Sons, Ltd., 2017; pp. 1−40.

(31) Head, A. R.; Chaudhary, S.; Olivieri, G.; Bournel, F.; Andersen, J. N.; Rochet, F.; Gallet, J.-J.; Schnadt, J. Near Ambient Pressure X-ray Photoelectron Spectroscopy Study of the Atomic Layer Deposition of TiO₂ on RuO₂(110). *J. Phys. Chem. C* **2016**, *120*, 243−251.

(32) Fairley, N.; Fernandez, V.; Richard-Plouet, M.; Guillot-Deudon, C.; Walton, J.; Smith, E.; Flahaut, D.; Greiner, M.; Biesinger, M.; Tougaard, S.; et al. Systematic and Collaborative Approach to Problem Solving using X-ray Photoelectron Spectroscopy. *Appl. Surf. Sci. Adv.* **2021**, *5*, No. 100112.

(33) Scofield, J. H. Hartree-Slater Subshell Photoionization Cross-Sections at 1254 and 1487 eV. *J. Electron Spectrosc. Relat. Phenom.* **1976**, *8*, 129−137.

(34) Björck, M.; Andersson, G. GenX: An Extensible X-ray Reflectivity Refinement Program Utilizing Differential Evolution. *J. Appl. Crystallogr.* **2007**, *40*, 1174−1178.

(35) Prasai, B.; Cai, B.; Underwood, M. K.; Lewis, J. P.; Drabold, D. A. Properties of Amorphous and Crystalline Titanium Dioxide from First Principles. *J. Mater. Sci.* **2012**, *47*, 7515−7521.

(36) Deskins, N. A.; Du, J.; Rao, P. The Structural and Electronic Properties of Reduced Amorphous Titania. *Phys. Chem. Chem. Phys.* **2017**, *19*, 18671−18684.

(37) Xia, B.; Ganem, J.-J.; Vickridge, I.; Briand, E.; Steydli, S.; Benbalagh, R.; Rochet, F. Water-Rich Conditions during Titania Atomic Layer Deposition in the 100 °C-300 °C Temperature Window Produce Films with TiᴵⱽOxidation State but Large H and O Content Variations. *Appl. Surf. Sci.* **2022**, *601*, No. 154233.

(38) Sperling, B. A.; Kimes, W. A.; Maslar, J. E. Reflection Absorption Infrared Spectroscopy during Atomic Layer Deposition of HfO₂ Films from Tetrakis(Ethylmethylamido)Hafnium and Water. *Appl. Surf. Sci.* **2010**, *256*, 5035−5041.

(39) Asahi, R.; Morikawa, T.; Ohwaki, T.; Aoki, K.; Taga, Y. Visible-Light Photocatalysis in Nitrogen-Doped Titanium Oxides. *Science* **2001**, *293*, 269−271.

(40) Hashimoto, K.; Irie, H.; Fujishima, A. TiO₂ Photocatalysis: A Historical Overview and Future Prospects. *Jpn. J. Appl. Phys.* **2005**, *44*, 8269.

(41) Deng, S.; Verbruggen, S. W.; Lenaerts, S.; Martens, J. A.; Van den Berghe, S.; Devloo-Casier, K.; Devulder, W.; Dendooven, J.; Deduytsche, D.; Detavernier, C. Controllable Nitrogen Doping in as

Deposited TiO₂ Film and Its Effect on Post Deposition Annealing. *J. Vac. Sci. Technol., A* **2014**, *32*, No. 01A123.

(42) Martínez-Ferrero, E.; Sakatani, Y.; Boissière, C.; Grosso, D.; Fuertes, A.; Fraxedas, J.; Sanchez, C. Nanostructured Titanium Oxynitride Porous Thin Films as Efficient Visible-Active Photo-catalysts. *Adv. Funct. Mater.* **2007**, *17*, 3348−3354.

(43) Driessen, J. P. A. M.; Schoonman, J.; Jensen, K. F. Infrared Spectroscopic Study of Decomposition of Ti(N(CH₃)₂)₄. *J. Electro-chem. Soc.* **2001**, *148*, G178.

(44) Hsu, J.-C.; Lin, Y.-H.; Wang, P. W. X-ray Photoelectron Spectroscopy Analysis of Nitrogen-Doped TiO₂ Films Prepared by Reactive-Ion-Beam Sputtering with Various NH₃/O₂ Gas Mixture Ratios. *Coatings* **2020**, *10*, 47.

(45) Lafuente, B.; Downs, R. T.; Yang, H.; Stone, N. The Power of Databases: The RRUFF Project. In *Highlights in Mineralogical Crystallography*; Armbruster, T.; Danisi, R. M., Eds.; Walter de Gruyter GmbH & Co KG, 2015; pp. 1−30 DOI: 10.1515/9783110417104-003.

(46) Busani, T.; Devine, R. A. B. Dielectric and Infrared Properties of TiO₂ Films Containing Anatase and Rutile. *Semicond. Sci. Technol.* **2005**, *20*, 870−875.

(47) Piercy, B. D.; Leng, C. Z.; Losego, M. D. Variation in the Density, Optical Polarizabilities, and Crystallinity of TiO₂ Thin Films Deposited via Atomic Layer Deposition from 38 to 150 °C Using the Titanium Tetrachloride-Water Reaction. *J. Vac. Sci. Technol., A* **2017**, *35*, No. 03E107.

(48) Go, D.; Lee, J.; Shin, J. W.; Lee, S.; Kang, W.; Han, J. H.; An, J. Phase-Gradient Atomic Layer Deposition of TiO₂ Thin Films by Plasma-Induced Local Crystallization. *Ceram. Int.* **2021**, *47*, 28770−28777.

(49) McDowell, M. T.; Lichterman, M. F.; Carim, A. I.; Liu, R.; Hu, S.; Brunschwig, B. S.; Lewis, N. S. The Influence of Structure and Processing on the Behavior of TiO₂ Protective Layers for Stabilization of n-Si/TiO₂/Ni Photoanodes for Water Oxidation. *ACS Appl. Mater. Interfaces* **2015**, *7*, 15189−15199.

(50) Pore, V.; Heikkilä, M.; Ritala, M.; Leskelä, M.; Areva, S. Atomic Layer Deposition of TiO₂₋ₓNₓ Thin Films for Photocatalytic Applications. *J. Photochem. Photobiol., A* **2006**, *177*, 68−75.

(51) Cheng, H.-E.; Chen, Y.-R.; Wu, W.-T.; Hsu, C.-M. Effect of Nitrogen Doping Concentration on the Properties of TiO₂ Films Grown by Atomic Layer Deposition. *Mater. Sci. Eng., B* **2011**, *176*, 596−599.

(52) Pore, V.; Ritala, M.; Leskelä, M.; Saukkonen, T.; Järn, M. Explosive Crystallization in Atomic Layer Deposited Mixed Titanium Oxides. *Cryst. Growth Des.* **2009**, *9*, 2974−2978.

(53) Dufond, M. E.; Chazalviel, J.-N.; Santinacci, L. Electrochemical Stability of n-Si Photoanodes Protected by TiO₂ Thin Layers Grown by Atomic Layer Deposition. *J. Electrochem. Soc.* **2021**, *168*, No. 031509.

(54) Viswanathan, B.; Krishanmurthy, K. R. Nitrogen Incorporation in TiO₂: Does It Make a Visible Light Photo-Active Material? *Int. J. Photoenergy* **2012**, *2012*, 1−10.

(55) Hukari, K.; Dannenberg, R.; Stach, E. A. Nitrogen Effects on Crystallization Kinetics of Amorphous TiOₓNᵧ Thin Films. *J. Mater. Res.* **2002**, *17*, 550−555.

(56) Albenze, E. J.; Thompson, M. O.; Clancy, P. Molecular Dynamics Study of Explosive Crystallization of SiGe and Boron-Doped SiGe Alloys. *Ind. Eng. Chem. Res.* **2006**, *45*, 5628−5639.

(57) Buchner, C.; Schneider, W. Explosive Crystallization in Thin Amorphous Layers on Heat Conducting Substrates. *J. Appl. Phys.* **2015**, *117*, 245301.

(58) Cho, C. J.; Kang, J.-Y.; Lee, W. C.; Baek, S.-H.; Kim, J.-S.; Hwang, C. S.; Kim, S. K. Interface Engineering for Extremely Large Grains in Explosively Crystallized TiO₂ Films Grown by Low-Temperature Atomic Layer Deposition. *Chem. Mater.* **2017**, *29*, 2046−2054.

(59) Petkov, V.; Holzhu, G. Atomic-Scale Structure of Amorphous TiO₂ by Electron, X-ray Diffraction and Reverse Monte Carlo Simulations. *J. Non-Cryst. Solids* **1998**, *231*, 17−30.

(60) Jellison, G. E., Jr.; Boatner, L. A.; Budai, J. D.; Jeong, B.-S.; Norton, D. P. Spectroscopic Ellipsometry of Thin Film and Bulk Anatase (TiO$_2$). *J. Appl. Phys.* **2003**, *93*, 9537−9541.

(61) Lee, D.-K.; Kwon, S.-H.; Ahn, J.-H. Growth of Rutile-TiO$_2$ Thin Films via Sn Doping and Insertion of Ultra-Thin SnO$_2$ Interlayer by Atomic Layer Deposition. *Mater. Lett.* **2019**, *246*, 1−4.

(62) Kim, B.; Choi, Y.; Lee, D.; Cheon, S.; Byun, Y.; Jeon, H. Atomic Layer Deposition for Rutile Structure TiO$_2$ Thin Films Using a SnO$_2$ Seed Layer and Low Temperature Heat Treatment. *Nanotechnology* **2021**, *33*, 115701.

(63) Momma, K.; Izumi, F. VESTA 3 for Three-Dimensional Visualization of Crystal, Volumetric and Morphology Data. *J. Appl. Crystallogr.* **2011**, *44*, 1272−1276.

(64) Baur, W. H. Über die Verfeinerung der Kristallstrukturbestimmung einiger Vertreter des Rutiltyps: TiO$_2$, SnO$_2$, GeO$_2$ und MgF$_2$. *Acta Cryst.* **1956**, *9*, 515−520.

(65) Howard, C. J.; Sabine, T. M.; Dickson, F. Structural and Thermal Parameters for Rutile and Anatase. *Acta Cryst. B* **1991**, *47*, 462−468.

(66) Downs, R. T.; Hall-Wallace, M. The *American Mineralogist* Crystal Structure Database. *Am. Mineral.* **2003**, *88*, 247−250.

📖 Recommended by ACS

Nucleation Effects in the Atomic Layer Deposition of Nickel–Aluminum Oxide Thin Films

Jon G. Baker, Stacey F. Bent, *et al.*
FEBRUARY 10, 2020
CHEMISTRY OF MATERIALS   READ 🔗

Selective Hydroxylation of In$_2$O$_3$ as A Route to Site-Selective Atomic Layer Deposition

Nannan Shan, Lei Cheng, *et al.*
JUNE 14, 2022
THE JOURNAL OF PHYSICAL CHEMISTRY C   READ 🔗

Film Conformality and Extracted Recombination Probabilities of O Atoms during Plasma-Assisted Atomic Layer Deposition of SiO$_2$, TiO$_2$, Al$_2$O$_3$, and HfO$_2$

Karsten Arts, Harm C. M. Knoops, *et al.*
OCTOBER 16, 2019
THE JOURNAL OF PHYSICAL CHEMISTRY C   READ 🔗

Impact of Ions on Film Conformality and Crystallinity during Plasma-Assisted Atomic Layer Deposition of TiO$_2$

Karsten Arts, Harm C. M. Knoops, *et al.*
APRIL 29, 2021
CHEMISTRY OF MATERIALS   READ 🔗

Get More Suggestions >

PUBLICATION
III

Interface Engineering of TiO₂ Photoelectrode Coatings Grown by Atomic Layer Deposition on Silicon

Jesse Saari, Harri Ali-Löytty, Mari Honkanen, Antti Tukiainen, Kimmo Lahtonen, and Mika Valden

Interface Engineering of TiO$_2$ Photoelectrode Coatings Grown by Atomic Layer Deposition on Silicon

Jesse Saari,* Harri Ali-Löytty,* Mari Honkanen, Antti Tukiainen, Kimmo Lahtonen, and Mika Valden*

Read Online

ACCESS | Metrics & More | Article Recommendations | Supporting Information

ABSTRACT: Titanium dioxide (TiO$_2$) can protect photoelectrochemical (PEC) devices from corrosion, but the fabrication of high-quality TiO$_2$ coatings providing long-term stability has remained challenging. Here, we compare the influence of Si wafer cleaning and postdeposition annealing temperature on the performance of TiO$_2$/n$^+$-Si photoanodes grown by atomic layer deposition (ALD) using tetrakis(dimethylamido)titanium (TDMAT) and H$_2$O as precursors at a growth temperature of 100 °C. We show that removal of native Si oxide before ALD does not improve the TiO$_2$ coating performance under alkaline PEC water splitting conditions if excessive postdeposition annealing is needed to induce crystallization. The as-deposited TiO$_2$ coatings were amorphous and subject to photocorrosion. However, the TiO$_2$ coatings were found to be stable over a time period of 10 h after heat treatment at 400 °C that induced crystallization of amorphous TiO$_2$ into anatase TiO$_2$. No interfacial Si oxide formed during the ALD growth, but during the heat treatment, the thickness of interfacial Si oxide increased to 1.8 nm for all of the samples. Increasing the ALD growth temperature to 150 °C enabled crystallization at 300 °C, which resulted in reduced growth of interfacial Si oxide followed by a 70 mV improvement in the photocurrent onset potential.
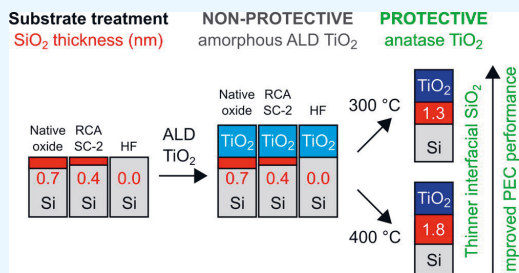
INTRODUCTION

Photoelectrochemical (PEC) solar fuel production from H$_2$O and CO$_2$ is one of the potential methods for storing solar energy in chemical form as hydrogen and hydrocarbons.[1] Solar fuel production at a large scale using a PEC reactor requires photoelectrodes that are efficient, chemically stable, and cost-effective. Titanium dioxide (TiO$_2$) is a common photocatalyst for solar fuel production but lacks efficiency due to the band gap in the UV range. One viable approach to increase the efficiency is to use semiconductor materials of high-efficiency solar cells, such as Si, GaAs, and GaP, as photoelectrode materials, but because of their intrinsic chemical instability under PEC conditions, a protective coating is required.[2] Recently, the stability of semiconductor photoelectrodes has been successfully increased by TiO$_2$ thin film coatings grown by atomic layer deposition (ALD) using either amorphous[3,4] or crystalline[5] TiO$_2$. However, the fabrication of high-quality TiO$_2$ thin films providing long-term stability to the photoelectrodes has remained challenging and the stability of amorphous TiO$_2$ (am.-TiO$_2$) has shown to be controversial.[6]

In addition to corrosion protection, the TiO$_2$ photoelectrode coating serves as a charge transfer layer between the semiconductor and the catalyst surface of the photoelectrode. Therefore, TiO$_2$ photoelectrode protection layers need to be either electrically "leaky" and thick (4−143 nm) am.-TiO$_2$,[3] dielectric, and ultrathin (∼2 nm) to allow the tunneling of charge carriers[4] or a semiconductor with a favorable band

alignment with respect to the substrate semiconductor and the energy level of a chemical reaction.[5] The electrically "leaky" TiO$_2$ has the ability to conduct holes due to midgap defect states in the electronic structure of am.-TiO$_2$.[3,7] However, the stability of am.-TiO$_2$ without additional co-catalyst has remained controversial.[8] In contrast to am.-TiO$_2$, crystalline TiO$_2$ is thermodynamically stable under alkaline water splitting conditions.[6] Furthermore, with sufficient contact to catalyst material, the crystalline n-type TiO$_2$ coating can also behave as a charge transfer layer and conduct electrons from the catalyst−electrolyte interface to the semiconductor substrate in a photoanode and vice versa in a photocathode.[9,10] In our recent studies, we have reported means to thermally modify the defect structure of ALD-grown am.-TiO$_2$ thin film under oxidative[6] and reductive[11] conditions. Based on our research, annealing in air at 500 °C results in stable and photocatalytically active crystalline TiO$_2$.[6] However, compared to the oxidation a heat treatment in reductive ultrahigh vacuum (UHV) at 500 °C can retain the amorphous phase for TiO$_2$

and enhance the stability due to the formation of O^- species via electron transfer from O to Ti.[11]

Atomic layer deposition providing good controllability, uniformity, and conformality can be used to fabricate high-quality and pinhole-free TiO_2 photoelectrode protection layers.[4,12,13] The choices of precursors and process conditions affect the TiO_2 phase structure. ALD of crystalline TiO_2 has been reported using $TiCl_4$ (at 200 °C) or TTIP (at 250 °C) as titanium precursors and H_2O or O_3 as oxygen sources, respectively.[14,15] The growth of TiO_2 using more volatile TDMAT and H_2O allows ALD at growth temperatures as low as 50 °C, which enables growth on sensitive materials.[16] However, based on our knowledge, there are no reports on thermal ALD from TDMAT and H_2O between 100 and 200 °C that results in a fully crystalline TiO_2 film without additional heat treatment.[6,17] Growth at higher temperatures could result in crystalline TiO_2, but the thermal decomposition of TDMAT challenges the self-limiting ALD process.[18−20]

Substrate pretreatment, interface engineering of a TiO_2/semiconductor heterojunction, and the morphology of TiO_2 are the key factors affecting charge carrier transport of the heterojunction and thus the performance of photoelectrodes.[7,14,21,22] For example, on Si-based electrodes, the growth of a resistive interfacial silicon oxide layer at the TiO_2/Si interface can prevent the charge transfer.[7,23] According to Scheuermann et al., less than 2 nm thick SiO_2 has no substantial effect on conductivity, but the performance of the photoanode could be remarkably improved by preparing a TiO_2/Si heterojunction with a less than 1 nm thick interfacial silicon oxide.[23] Cho et al. reported the effect of the substrate surface energy on the grain size of as-deposited ALD TiO_2 films grown from TTIP and O_3 on SiO_2, Al_2O_3, HfO_2, and Pt substrates.[14] The deposition on a high-surface-energy substrate can lead to large anatase grains (2−3 μm) due to the higher interfacial energy between TiO_2 and the substrate, which decreases the number of crystal nuclei on the surface.[14] Furthermore, Pore et al. were able to prepare much larger explosively crystallized anatase TiO_2 grains with a width of several tens of microns by postannealing amorphous Ti−Nb−O or Ti−Ta−O mixed oxide films.[24] The large anatase grain size accompanied with small grain boundary volume is reported to improve the thermal stability and photocatalytic activity of TiO_2 thin films,[24,25] which are also desired features for protective photoelectrode coatings since corrosion reactions are often initiated at grain boundaries.

The surface termination of the Si substrate depends on the surface treatment and can strongly influence the ALD growth that is essentially a surface-mediated process.[21,22,26−28] Prior to ALD, native SiO_2 can be removed from the surface by HF treatment, which terminates the Si surface by Si−H bonds.[26] The hydrogen-terminated Si surface is hydrophobic, lowering the initial ALD growth rate of TiO_2 due to the slower adsorption of ALD precursor molecules on the Si surface.[22,26] For example, McDonnell et al. reported 185 times greater TiO_2 deposition rate on an oxide-terminated Si compared to a H-terminated surface using $TiCl_4$ and H_2O.[28] Devloo-Casier et al. reported that HF treatment of Si changed the growth mode from layer by layer to island growth for HfO_2 using tetrakis(ethylmethylamino)hafnium and H_2O.[27] In contrast to the HF treatment, boiling in $HCl−H_2O_2−H_2O$ (RCA SC-2 treatment[29]) leads to a hydrophilic surface due to the high density of surface hydroxyl groups,[30,31] which are reported to influence the crystallization and grain size of ALD TiO_2 grown

from $TiCl_4$ and H_2O precursors.[21,22] Therefore, the substrate pretreatment is of primary importance especially to the fabrication of ultrathin pinhole-free tunnel oxides and 2D materials for the semiconductor technology[13] but can be also utilized in area-selective growth.[28]

This work examines the influence of silicon wafer pretreatment (1) on the initial ALD TiO_2 (0−2 nm) growth; (2) on the TiO_2/Si interface composition; and (3) on the performance of TiO_2 (30 nm) protective coating on Si under photoelectrochemical (PEC) water splitting conditions. ALD TiO_2 thin films were grown from TDMAT and H_2O precursors at 100 °C (1) on native Si oxide; (2) on oxide-free Si surface after exposing the Si wafer to dilute HF solution; and (3) on chemical Si oxide that forms on an HF-dipped Si wafer surface during boiling in $HCl−H_2O_2−H_2O$. The as-deposited TiO_2 thin films were amorphous and dissolved under alkaline PEC conditions. The stability of the TiO_2 thin film over a time period of >10 h under PEC conditions was obtained after heat treatment in air at 400 °C that induced crystallization of am.-TiO_2 into anatase TiO_2. Nondestructive X-ray photoelectron spectroscopy analysis was applied to quantitatively analyze the morphology of TiO_2 (2 nm)/SiO_2/Si heterostructures and revealed that no interfacial Si oxide formed during the ALD growth, but during the heat treatment, the thickness of interfacial Si oxide increased to 1.8 ± 0.1 nm for all of the samples. By increasing the growth temperature from 100 to 150 °C, the crystallization temperature can be decreased from ~400 to 300 °C,[17] which limits the growth of interfacial Si oxide and is shown to result in more significant improvement in the PEC performance compared to the wafer pretreatments.

It is evident from the results shown here that growing a high-quality ALD TiO_2 thin film on Si wafer depends on how the Si surface is cleaned, albeit the choice of the cleaning method affected only little the final structure and properties of the 30 nm thick TiO_2 thin film as a photoelectrode coating on Si. Further improvement in the quality of the TiO_2/Si photoelectrode would require either the development of the ALD growth process itself or the postgrowth heat treatment of the as-deposited TiO_2 thin film to result in a crystalline low-defect TiO_2 structure at a lower temperature and thereby avoiding the formation of interfacial Si oxide that is detrimental to the charge transfer. These properties are not sensitive to the doping of Si substrate, and therefore, our results obtained using degenerately doped n⁺-Si as the substrate are applicable to Si-based photoelectrodes in general.

■ MATERIALS AND METHODS

Substrates. In the experiments, the degenerately Sb-doped (resistivity 0.008−0.02 Ω cm) n⁺-Si(100) wafers from SIEGERT WAFER GmbH (Germany) were used as substrates. The use of degenerately doped Si substrates allowed the investigation of photogenerated charge carriers within TiO_2 coating only, while Si substrate served as a conductor. Prior to atomic layer deposition of TiO_2, some of the substrates were treated with hydrofluoric acid (HF), some with HF followed by RCA SC-2 treatment (Radio Corporation of America standard clean 2),[29] and some of the substrates having a thin native oxide (SiO_2) layer were used as received from the wafer vendor. In the HF treatment, the Si wafer was immersed in 2.5% hydrofluoric acid (HF) for 10 s, then rinsed in two different deionized water (DI-H_2O) containers, in the first one for 3 s and in the second for 10 s. After this, the

samples were blown dry with nitrogen. The HF treatment etches the native oxide layer, resulting in a H-terminated hydrophobic Si surface.[21,31] In the RCA SC-2 treatment, i.e., chemical oxidation, the Si wafer was soaked in a 6:1:1 H_2O/ 30% H_2O_2/37% HCl solution at 70−75 °C for 10 min.[29] After the treatment, the wafer was rinsed with DI-H_2O and blown dry with nitrogen. This treatment produces a silicon wafer with a thin silicon oxide layer that is hydrophilic due to the high density of hydroxyl groups (−OH) on the surface.[30,31] [Caution: HF is highly corrosive and requires the use of Teflon, rather than glassware, and can easily penetrate the skin, bond with Ca^{2+}, and cause nerve damage. As such, even a small exposure (e.g., 2−10% of the body) can be fatal. Proper training is required before handling or working with HF, and appropriate personal protection equipment should be worn at all times when carrying out these sample preparations.]

Water Contact Angle (CA) Measurements. The water contact angle measurements were performed using an Attension Theta contact angle meter equipped with an Automatic Single Liquid Dispenser. The DI-H_2O drop size used for the experiments was 5.0 ± 0.5 μL. The drop was stroked on the surface and given to stabilize for 2−3 s. The right and left contact angles were recorded for 10 s (15 frames per second), and the contact angle was determined as an average of the right and left contact angles.

Atomic Layer Deposition (ALD). ALD of TiO_2 was carried out using a Picosun Sunale ALD R-200 Advanced reactor and tetrakis(dimethylamido)titanium(IV) (Ti(N-(CH_3)$_2$)$_4$, TDMAT, electronic grade >99.999%, Sigma-Aldrich) and deionized water as precursors. To reach the proper TDMAT precursor vapor pressure, the bubbler was heated to 76 °C, and to prevent condensation of the precursor gas, the delivery line was heated to 85 °C. The water bubbler was sustained at 18 °C by a Peltier element for stability control. Argon (99.9999%, Oy AGA Ab, Finland) was used as a carrier gas. During the ALD, the Si substrates were held at 100 °C. A lower deposition temperature was chosen to get more stoichiometric TiO_2 and to hinder the growth of the resistive interfacial silicon oxide layer. The thickness of the TiO_2 (480 ALD cycles) film was measured by ellipsometry and was 30 nm (Rudolph Auto EL III Ellipsometer, Rudolph Research Analytical). Based on the calculated growth rate, the number of ALD cycles for studying the initial growth was selected to be 1, 8 (5 Å), and 32 (2 nm). At a 150 °C growth temperature, 636 ALD cycles were required for a 30 nm thick TiO_2 thin film.[17]

Heat Treatment. The post-treatment for the TiO_2/Si samples was performed in air by placing the samples directly into a preheated tube furnace for 45 min. After the heat treatment, the samples were removed from the tube furnace and let to cool down freely. The heat treatment temperature for TiO_2 grown at 100 °C was optimized to yield the maximum photocurrent for H_2O oxidation (Figure S4). The heat treatment for the TiO_2 grown at 150 °C was decided based on the crystallization temperature.[17]

X-ray Photoelectron Spectroscopy (XPS). The chemical composition and thin film morphology of sample surfaces were analyzed with X-ray photoelectron spectroscopy (XPS). Nonmonochromatic Al Kα ($h\nu$ = 1486.5 eV) X-ray was used as an excitation source. The core-level XP spectra were analyzed by the least-squares fitting of Gaussian−Lorentzian lineshapes and using a Shirley-type background. The binding energy scale of the XP spectra was calibrated by fixing the Si^0

2p$_{3/2}$ peak to 99.3 eV. CasaXPS version 2.3.22 PR1.0. was used as the analysis software, and the Scofield photoionization cross sections were used as relative sensitivity factors. The quantitative analysis of the TiO_2/SiO_2/Si heterostructure morphology was based on the attenuation of photoelectron signal in solid material according to the Beer−Lambert law and is described in detail in the Supporting Information.

Scanning Electron Microscopy (SEM). The surface morphology of Si substrates after different pretreatments was studied by scanning electron microscopy (SEM, Zeiss Ultra 55, Carl Zeiss Microscopy GmbH). The SEM images were measured using in-lens mode with a working distance of 2.3 mm, an electron high tension (EHT) of 1.00 kV, and an aperture size of 30.00 μm.

Electron Backscatter Diffraction (EBSD). The electron backscatter diffraction (EBSD) analysis was carried out using SEM (Zeiss Ultra Plus, Carl Zeiss Microscopy GmbH) equipped with an EBSD system (Symmetry, Oxford Instruments). The EBSD maps were collected using a 70° sample tilt, an EHT of 10 kV, an aperture size of 120 μm, and a step size of 0.1 μm. Here, pattern quality, i.e., band contrast (BC), maps were presented. The BC map represents the quality of the Kikuchi pattern for each measurement pixel; bright signifies good pattern quality and black poor quality such as in grain boundaries.

Grazing-Incidence X-ray Diffraction (GIXRD). The phase structures of the samples were obtained via grazing-incidence X-ray diffraction (GIXRD, PANalytical X'Pert^3 MRD diffractometer) with Cu Kα radiation (λ = 1.5406 Å, $h\nu$ = 8.05 keV) and 45 kV and 40 mA cathode voltage and current, respectively. The samples were scanned in 2θ between 20 and 52° using a grazing-incidence angle Ω = 0.3°. Background was removed from each of the scans to allow easier comparison of the measured curves.

Photoelectrochemical (PEC) Analysis. The photoelectrochemical performance was studied in a homemade PEC cell using three-electrode configuration with an Ag/AgCl reference electrode, Pt counter electrode, and TiO_2/Si sample as the working electrode following the procedure described in detail in our previous work.[6] The measurement was controlled by an Autolab PGSTAT12 potentiostat (Metrohm AG). An aqueous solution of 1 M NaOH (pH 13.6) was used as an electrolyte. Simulated solar spectrum was produced with a HAL-C100 solar simulator (Asahi Spectra Co., Ltd., JIS Class A at 400−1100 nm with AM1.5G filter), and the intensity was adjusted to 1.00 Sun using a 1 sun checker (model CS-30, Asahi Spectra Co., Ltd.).

■ RESULTS AND DISCUSSION

Figure 1 shows Si 2p XP spectra and SEM images together with water contact angle measurements for the Si(100) surfaces after different surface treatments, i.e., the surface condition prior to the atomic layer deposition of TiO_2. The XP spectra of Si 2p transition show a strong doublet peak with Si 2p$_{3/2}$ at 99.3 eV corresponding to elemental Si from the Si substrate. Other peaks are observed at 103.3 eV for the native oxide and at 103.1 eV for the chemical oxide that are both assigned to oxidized Si, mainly Si^{4+} oxide, with a slight deviation in the chemical environment between the two oxides. In contrast, Si oxide was not detected on the HF-treated sample, which confirms the temporal passivation of Si surface against oxidation. The doublet separation of 0.60 eV was applied in peak fitting for all of the chemical states in Si 2p.
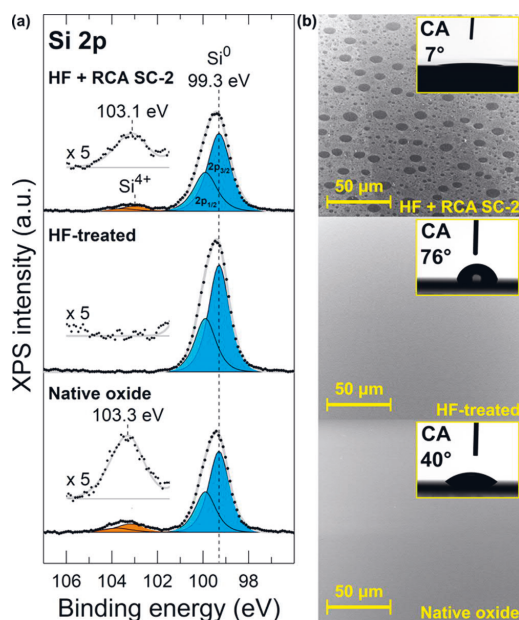
Figure 1. (a) XP Si 2p spectra and (b) SEM images and CA measurements for the native oxide, HF-treated, and HF + RCA SC-2-treated Si(100) substrates.

SEM images and water contact angles presented in Figure 1b reveal the disparity in surface morphology and hydrophilicity between different surface treatments. The surface with native oxide is flat, and the water contact angle is rather low (40°) in accordance with the literature.[31,32] HF treatment results in flat surface morphology and a large CA (76°), indicating the hydrophobic behavior caused by the H-terminated Si surface.[31-33] Thus, both the native oxide and HF-treated Si(100) surfaces were flat and homogeneous albeit chemically different. In contrast, the RCA SC-2 process results in a distinct nonhomogeneous surface morphology that is strongly hydrophilic with CA of 7°. The surface is covered with round voids that have the size of up to 10 μm in diameter. Such a nonhomogeneous surface morphology can be linked to the H_2 bubble formation that takes place vigorously in the freshly prepared SC-2 solution upon the decomposition of H_2O_2. Gas bubbles may have adhered to the surface limiting the surface reactions and thus led to void formation. Similar void formation has been reported to result from cleaning in Fe-contaminated alkaline SC-1 solution ($NH_4OH/H_2O_2/H_2O$), where Fe catalyzes H_2O_2 decomposition[34] but rarely upon cleaning in acidic SC-2. Bubble-induced void formation can be effectively mitigated by the implementation of sonication to the RCA cleaning procedure.[35] Despite the nonhomogeneous surface morphology, the treatment was found reproducible and served as an interesting substrate for the ALD TiO2 thin films. The hydrophilicity is attributed to the high density of hydroxyl groups on the surface.[30,31] Compared to the native oxide, the Si^{4+} 2p peak in the RCA SC-2-treated Si appeared to be 0.2 eV closer to the Si^0 peak that is now supported with the difference in the surface termination and with the nonhomogeneous oxide layer. The lower binding energy can also indicate the

presence of some Si suboxides ($Si^{3+}-Si^{1+}$) reported to exist in a chemically grown Si oxide.[36] The amount of adventitious carbon was similar (4-6 at. %) for all of the surface treatments (Table S1), and no metal impurities were detected.

To study the influence of surface treatment on the initial ALD TiO2 growth and on the formation of interfacial Si oxide, surface analysis by XPS was performed as a function of ALD TiO2 cycles and after oxidation in air at 400 °C as shown in Figure 2. The growth rate of ALD TiO2 as determined by
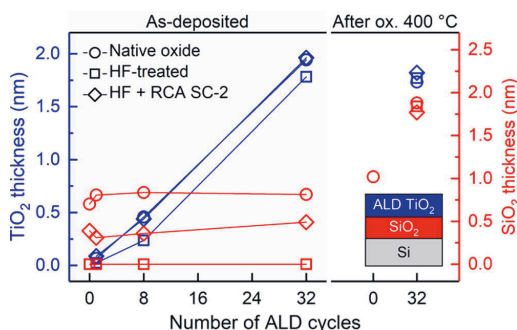

Figure 2. Thicknesses of TiO2 surface layer and interfacial SiO2 as a function of ALD TiO2 cycles and after oxidation in air at 400 °C for different surface treatments.

electron spectroscopy was found to follow a linear trend (0.06 ± 0.01 nm/cycle) on oxidized surfaces, i.e., the native oxide and HF + RCA SC-2 surfaces, in good agreement with the average growth per cycle (GPC = 0.063 ± 0.003 nm/cycle) determined for a 30 nm thick ALD TiO2 layer using ellipsometry. In contrast, the initial growth on oxide-free Si substrate (HF-treated) was strongly hindered up to eight ALD cycles after which the growth rate continued at the same rate as with the other Si surfaces. Thus, the HF treatment did not change the growth from layer-by-layer to island mode,[27] which would have resulted in an increase in the apparent growth rate. This inhibition period on the oxide-free surface resulted effectively in a 0.2 nm smaller TiO2 film thicknesses compared to oxide surfaces when total TiO2 thickness exceeded 0.2 nm (~1 monolayer of TiO2). The initial growth rate is lower on H-terminated Si and higher on SiO2 surfaces due to the enhanced precursor adsorption and surface reactions with hydroxyl groups on the surface.[26]

The thickness of the interfacial Si oxide layer did not change during the ALD process. Most significantly, the TiO2/Si interface for the HF-treated surface remained free from Si oxides, which is largely due to the low growth temperature of 100 °C. A similar result was observed by Methaapanon et al.[26] The thicknesses of interfacial Si oxide in the native oxide and HF + RCA SC-2 -treated samples were 0.8 ± 0.1 and 0.4 ± 0.1 nm, respectively. The chemical oxide that forms in the rapid HF + RCA SC-2 treatment was not fully developed and is expected to reach the thickness of native oxide with time when exposed to air. The Si^{4+} 2p binding energy for the interfacial Si oxide was shifted by −0.4 eV compared to the Si^{4+} 2p at the surface (Figure S1). The formation of an interfacial compound might induce such a binding energy shift. However, based on our nondestructive angle-resolved XPS analysis, the Ti−O−Si interface width was only 0.4 nm (~1 monolayer of SiO2 or

TiO_2), which does not support substantial mixing of TiO_2 and Si oxide (Figure S2).[37] More specifically, only Ti^{4+} and no suboxides of Ti, i.e., Ti^{1-3+}, were present since the normalized Ti 2p spectra (Figure S2a) recorded at different electron emission angles were identical. The Si^{4+} 2p binding energy shift was therefore assigned to the TiO_2 overlayer-induced change in the chemical environment.[26] This contradicts the work by Dwivedi et al. who reported mixed oxide (SiO_x + TiO_x) interfacial layer formation with Ti^{2+} for ALD TiO_2 grown on HF-treated Si at 100 °C from $TiCl_4$ and H_2O.[38]

The heat treatment in air at 400 °C did not affect the thickness of TiO_2 overlayer. However, the thickness of the interfacial Si oxide layer was increased to 1.8 ± 0.1 nm for all of the samples despite the difference before the heat treatment. No substantial mixing of TiO_2 with Si oxide was observed, but the width of the Ti—O—Si interface evidenced a slight increase from 0.4 nm (as-deposited) to 0.6 nm (400 °C) as analyzed in more detail in the case of HF + RCA SC-2-treated substrate (Figure S2). In addition, the thickness of the interfacial Si oxide was observed to increase linearly with heat treatment temperature from 200 to 550 °C (Figure S3). Interestingly, the same heat treatment induced only minor oxide growth on the bare Si substrate, i.e., 0 ALD cycles in Figure 2. We suggest that this apparent discrepancy is due to the higher catalytic activity of the TiO_2 surface to dissociate O_2, i.e., the initial step of oxidation, compared to SiO_2 surface.[39,40] This so-called catalytic effect on the interfacial SiO_2 formation has been observed also for other high-κ metal oxide materials on silicon.[41] The heat treatment at 400 °C did not affect the Si^{4+} 2p binding energy, and the morphology analysis did not support intermixing of SiO_2 with TiO_2 (Figure S2).

The heat treatment temperature was optimized in terms of the performance of the 30 nm thick ALD TiO_2 thin film grown at 100 °C on n^+-Si to act as a photocatalyst for water oxidation. We note that in the experiment, only TiO_2 contributes to the photocurrent, while the degenerately doped n^+-Si substrate serves as a conductor. The maximum photocurrent was measured after heat treatment at 400 °C (Figure S4). For higher heat treatment temperatures, the photocurrent decreased slightly up to 500 °C followed by a drastic drop at 550 °C. The decrease in photocurrent is attributed to the increase of the resistive interfacial Si oxide layer thickness above the tunneling limit, which was estimated to be ∼3 nm based on an experiment performed using ALD TiO_2 (2 nm)/Si model system (Figure S3). For temperatures below 400 °C, the TiO_2 thin film was not stable under PEC conditions. Previously, we have shown that a high temperature is required to convert chemically unstable amorphous ALD TiO_2 into stable crystalline TiO_2.[6] Therefore, it can be concluded that further improvement in the performance of ALD TiO_2/Si photoelectrode would require the development of ALD growth parameters that enables fabrication of crystalline TiO_2 at a lower temperature where resistive interfacial SiO_2 does not form. To constrain the thickness of the interfacial Si oxide below 1 nm limit for improved charge transfer as was suggested by Scheuermann et al.,[23] the oxidation temperature should not exceed 250 °C in the case of studied 45 min heat treatment time (Figure S3).

Figure 3 shows GIXRD patterns and BC maps for 30 nm thick ALD TiO_2 films after oxidation at 400 °C for different surface treatments. The GIXRD patterns for oxidized ALD TiO_2 thin films corresponded to anatase TiO_2 for all of the surface treatments and showed no features of other phases of
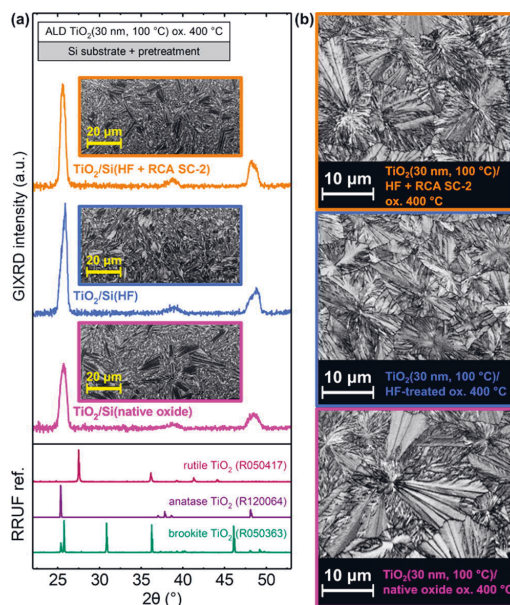

Figure 3. (a) GIXRD patterns and SEM images (insets) and (b) BC maps of 30 nm thick ALD TiO_2 films after oxidation at 400 °C for as-deposited am.-TiO_2 grown on native oxide, HF-treated, and HF + RCA SC-2-treated Si(100) substrates. The XRD references are from RRUF database.[42]

TiO_2 such as rutile or brookite. Small differences in the anatase XRD peak shapes were observed, suggesting differences in anatase crystal morphology, crystal anisotropy, or thin film stress. The BC maps in Figure 3b show fern leaf-like grains for all anatase TiO_2 thin films. Similar grain morphology has been reported to be typical for explosively crystallized thin films.[14,24] The determination of crystallographic orientation and local misorientation maps from the EBSD data was very challenging due to stretched and distorted Kikuchi patterns. However, the anatase thin film on native oxide had the largest crystals with the lateral size of nearly 20 μm. Thus, the largest crystals were over 500 times larger than the film thickness. Moreover, the anatase crystals on HF and HF + RCA SC-2-treated Si appeared to be exceptionally large (about 10 μm) but still smaller than the largest grains on the native oxide substrate.

In addition to the precursor adsorption and the initial ALD growth rate, the differences in the water contact angle are related to differences in the substrate surface energy, which was reported to affect crystallization and the grain size of TiO_2 during the ALD growth.[14,22] Larger grains are observed on substrates with higher surface energy that corresponds with a lower contact angle.[14] Our results suggest that a high substrate surface energy could also mediate the growth of large grains upon postgrowth heat treatment. However, based on the substrate surface energy, HF + RCA SC-2-treated Si should have the largest grains, but the nonhomogeneous and morphologically uneven surface can provide increased number of nucleation sites for crystallization compared to the flat native oxide SiO_2.

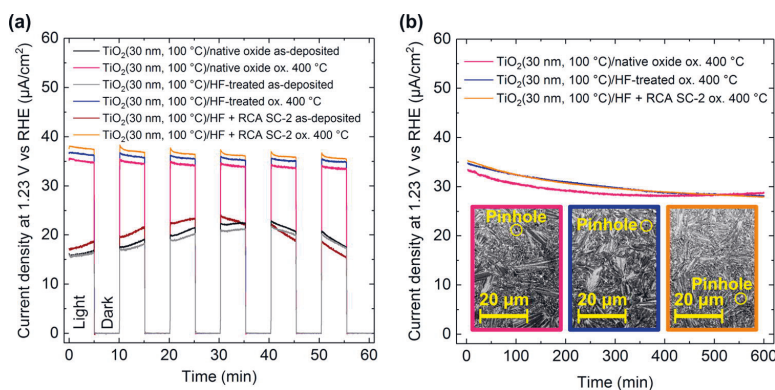The XPS results presented in Table S2 show similar elemental concentrations for all of the as-deposited am.-TiO_2

Figure 4. (a) Chopped light (1 Sun) constant potential amperometry measurement in 1 M NaOH for as-deposited (amorphous) TiO_2 and at 400 °C oxidized (anatase) TiO_2 thin films on n^+-Si substrates with different surface treatments; (b) 10 h stability tests for the ox. 400 °C samples under 1 Sun. The insets in (b) are SEM images of the surfaces after the 10 h stability test.

films and also some nitrogen traces (1.0−1.3 at. %) that are most likely dimethylamino fragments from the dissociative adsorption of TDMAT or dimethylamine readsorbing on certain sites of the growing film.[43] The surface concentration of N was found to decrease to 0.3−0.5 at. % upon heat treatment at 400 °C. This implies that nitrogen traces in am.-TiO_2 drive the phase stabilization toward anatase instead of rutile, as discussed in our previous article.[6] TiO_2 films grown at 200 °C were amorphous, contained less nitrogen traces, and crystallized into rutile in a similar heat treatment. This raises a question if the nitrogen traces mediate the explosive crystallization serving nucleation sites for the large anatase crystals. According to Hukari et al., nitrogen in am.-TiO_2 inhibits the crystallization and raises the nucleation temperature.[44] Indeed, we have observed crystallization temperature to depend on the ALD growth temperature,[17] which in return affects the amount of TDMAT traces in the thin film.[18] Based on this, we conclude that the explosive crystallization and the large grain size are likely caused by the nitrogen-containing fragments of the TDMAT precursor.

Figure 4a shows chopped light constant potential amperometry measurement results for TiO_2/n^+-Si photoelectrodes before and after oxidation at 400 °C for different surface treatments. The measurement reveals photoelectrochemical performance of TiO_2/n^+-Si photoelectrodes in terms of stability and photocatalytic activity for solar water oxidation. Regardless of the Si surface treatment, the as-deposited amorphous TiO_2 films evidenced highly unstable photocurrent: first, the photocurrent increases until after 30−40 min, it starts to decline steadily. For similar TiO_2/Si samples, we have shown that this photocurrent trend leads to complete dissolution of TiO_2 coating in <10 h.[11] Indeed, after the stability test, the dissolution of amorphous TiO_2 coatings was verified for all of the surface treatment by visual inspection of photoelectrodes showing a color change from yellowish intact coating to gray as the electrolyte had reached the Si substrate (Figure S5). Better understanding of degradation mechanism calls for more detailed studies and is beyond the scope of this work. In contrast, anatase TiO_2 films for all Si surface treatments show a stable photocurrent of ~30 $\mu A/cm^2$ for 10 h (Figure 4b). SEM analysis of anatase TiO_2 samples after the stability test revealed only a few pinholes in the films as shown

in the insets in Figures 4b and S6. Thus, despite the minor differences in 30 nm thick anatase TiO_2 thin film morphologies, they all serve as protection layers for Si substrate that would otherwise dissolve in NaOH.[35] Therefore, it can be concluded that Si surface treatment had little effect on the PEC performance of TiO_2/n^+-Si photoelectrodes. However, we note that this result is not generic to all ALD processes. For example, surface treatment-induced change in the growth mode from layer-by-layer to island growth results more probably in nonprotective ALD coating. Therefore, optimization of surface treatment is required for each photoelectrode system.

The current−voltage (I−V) characteristics measured under simulated solar light after crystallization under oxidative conditions (anatase TiO_2) showed a sluggish increase in photocurrent and a low photocurrent at 1.23 V (Figure S7) compared to rutile TiO_2 fabricated using similar synthesis but at a higher ALD growth temperature of 200 °C.[6] The sluggish increase in photocurrent is an indication of slow kinetics and high degree of recombination, which we assign to the N traces in the anatase TiO_2 thin films. The difference in the photocurrent at 1.23 V, on the other hand, is also affected by the difference in band gap energies between anatase and rutile TiO_2, and by the difference in grain size.[45] Rutile TiO_2 has a smaller band gap and therefore absorbs a larger fraction of solar spectrum, which makes it a better photocatalyst. Anatase TiO_2 with a larger band gap is more transparent to solar light and is therefore better suited as a protective window material for solar cells.[5]

Recently, we showed that amorphous-to-anatase phase-transition temperature for the TDMAT and H_2O ALD TiO_2 process can be decreased from ~400 to 300 °C by increasing the growth temperature from 100 to 150 °C.[17] Next, we leverage this finding to improve the performance of the ALD TiO_2/n^+-Si photoelectrode.

Figure 5 shows the characteristics for ALD TiO_2 (30 nm) thin films grown at 100 and 150 °C and subsequently oxidized at 300 and 400 °C. For the amorphous TiO_2 (growth temperature of 100 °C, oxidation at 300 °C), the photocurrent generation is strongly limited due to the high degree of defect states and fast recombination of photogenerated charge carriers. The ALD TiO_2 thin films grown at 150 °C depict
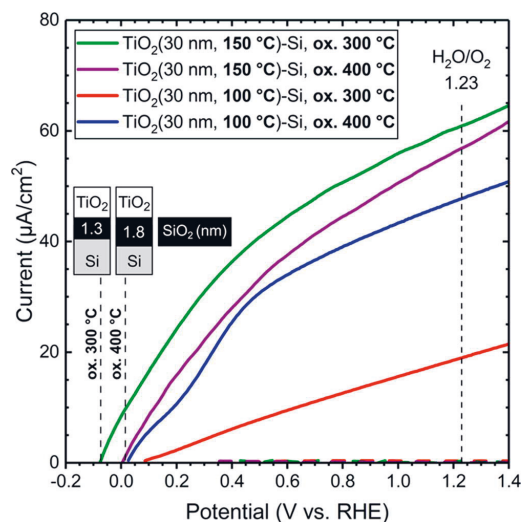
Figure 5. Current−voltage characteristics in the dark (dashed lines) and under simulated solar illumination (solid lines) measured in 1 M NaOH by linear sweep voltammetry for ALD TiO_2 (30 nm) thin films grown at 100 and 150 °C on n^+-Si with native oxide and subsequently oxidized at 300 and 400 °C. SiO_2 layer morphologies after oxidation at 300 and 400 °C are illustrated as insets.

steeper photocurrent onsets after both oxidation temperatures compared to the TiO_2 thin film grown at 100 °C and oxidized at 400 °C. Interestingly, the photocurrent slope decreases temporarily at 0.14 V for the TiO_2 thin film grown at 100 °C but not for the thin films grown at 150 °C. We suggest that this feature is due to the difference in the degree of nitrogen-bearing TDMAT traces in the anatase TiO_2 that affect photocurrent kinetics. Most strikingly, the photocurrent onset potentials (+0.02 ± 0.02 V) were found similar for the TiO_2 thin films oxidize at 400 °C, whereas the photocurrent onset potential was decreased to −0.07 V for the TiO_2 thin film grown at 150 °C and oxidized at 300 °C. The decrease in photocurrent onset potential followed an increase in the photocurrent at the water redox potential of 1.23 V. The improved performance can be assigned to the thinner interfacial Si oxide layer that forms at a lower oxidation temperature (i.e., 1.3 nm; cf. Figure S3).

The thickness of the interfacial Si oxide layer is directly associated with the photovoltage loss in oxide-protected water splitting anodes and should be minimized for improved efficiency.[46,47] Here, we have demonstrated that compared to the postdeposition annealing (PDA) temperature, the silicon wafer cleaning had only little effect on the ALD TiO_2/n^+-Si photoelectrode performance. Currently, the performance is not limited by the native oxide on Si wafers but by the excessive PDA temperature that is required to form crystalline low defect protective TiO_2 coating. We have found earlier that the required minimum PDA temperature can be sensitive to the ALD growth temperature. Here, we have shown the implication on photoelectrode performance using TiO_2/n^+-Si as a model system, but we suggest that the performance of any Si-based photoelectrode can be improved by decreasing the PDA temperature that can be enabled by careful optimization of the ALD process.

CONCLUSIONS

In summary, we have studied the effect of standard cleaning treatments of Si wafers on the fabrication of the ALD TiO_2 photoelectrode coating for photoelectrochemical applications. The TiO_2/Si thin film morphology was quantitatively analyzed using nondestructive XPS measurement. Wet chemical cleaning of Si wafer either by exposing the wafer to dilute HF solution or by boiling an HF-dipped wafer in $HCl-H_2O_2-H_2O$ did not improve the performance of the 30 nm thick TiO_2 thin film under PEC conditions for water splitting reaction compared to the TiO_2 film grown on native Si oxide (thickness, t = 0.7 nm). Instead, the HF dip cleaning resulted in a hydrophobic oxide-free Si surface (t = 0.0 nm) that hindered the initial TiO_2 growth and the chemical Si oxide (t = 0.4 nm) that formed in $HCl-H_2O_2-H_2O$ was nonuniform. The as-deposited TiO_2 thin films were amorphous and subject to photocorrosion. However, the TiO_2 thin film was found to be stable over a time period of 10 h at 1.23 V in 1 M NaOH after heat treatment at 400 °C that induced crystallization of amorphous TiO_2 into anatase TiO_2. Substrate cleaning prior to the ALD growth did not significantly affect the anatase grain size that was the largest (>10 μm) for the films grown on the native Si oxide. No interfacial Si oxide was formed during the ALD growth, but during the heat treatment, the thickness of interfacial Si oxide increased to 1.8 nm for all of the samples. By increasing the growth temperature from 100 to 150 °C, we were able to reduce the required postdeposition annealing temperature to 300 °C that reduced the formation of interfacial Si oxide and resulted in improved PEC performance.

These results clearly indicate that even though the interfacial Si oxide and the initial ALD process were sensitive to the Si substrate cleaning, the choice of cleaning method had only little effect on the structure and performance of the 30 nm thick TiO_2 thin film as a photoelectrode protection layer. Further improvement in the performance of ALD TiO_2/Si photoelectrode would require the development of new precursor chemistry for low-temperature ALD, adjusting the ALD growth parameters, or developing a postgrowth heat treatment of the as-deposited TiO_2 thin film to result in a crystalline low-defect TiO_2 structure at a lower temperature, preferably <250 °C, where the formation of interfacial Si oxide that is detrimental to the charge transfer can be limited to an oxide thickness of <1 nm.

ASSOCIATED CONTENT

ⓢ Supporting Information

The Supporting Information is available free of charge at https://pubs.acs.org/doi/10.1021/acsomega.1c04478.

XPS and SEM analyses and data from photoelectro-chemical measurements (PDF)

AUTHOR INFORMATION

Corresponding Authors

Jesse Saari − *Surface Science Group, Faculty of Engineering and Natural Sciences, Tampere University, FI 33014 Tampere, Finland;* ⓘ orcid.org/0000-0001-6741-0838; Email: jesse.saari@tuni.fi

Harri Ali-Löytty − *Surface Science Group, Faculty of Engineering and Natural Sciences, Tampere University, FI 33014 Tampere, Finland;* ⓘ orcid.org/0000-0001-8746-7268; Email: harri.ali-loytty@tuni.fi

Mika Valden − *Surface Science Group, Faculty of Engineering and Natural Sciences, Tampere University, FI 33014 Tampere, Finland*; Email: mika.valden@tuni.fi

Authors

Mari Honkanen − *Tampere Microscopy Center, Faculty of Engineering and Natural Sciences, Tampere University, FI 33014 Tampere, Finland*

Antti Tukiainen − *Faculty of Engineering and Natural Sciences, Tampere University, FI 33014 Tampere, Finland*

Kimmo Lahtonen − *Faculty of Engineering and Natural Sciences, Tampere University, FI 33014 Tampere, Finland*

Complete contact information is available at:
https://pubs.acs.org/10.1021/acsomega.1c04478

Notes

The authors declare no competing financial interest.

■ REFERENCES

(1) *Photoelectrochemical Hydrogen Production*; van de Krol, R.; Grätzel, M., Eds.; Electronic Materials: Science & Technology; Springer, 2012.

(2) Bae, D.; Seger, B.; Vesborg, P. C. K.; Hansen, O.; Chorkendorff, I. Strategies for Stable Water Splitting via Protected Photoelectrodes. *Chem. Soc. Rev.* **2017**, 46, 1933−1954.

(3) Hu, S.; Shaner, M. R.; Beardslee, J. A.; Lichterman, M.; Brunschwig, B. S.; Lewis, N. S. Amorphous TiO_2 Coatings Stabilize Si, GaAs, and GaP Photoanodes for Efficient Water Oxidation. *Science* **2014**, 344, 1005−1009.

(4) Chen, Y. W.; Prange, J. D.; Dühnen, S.; Park, Y.; Gunji, M.; Chidsey, C. E. D.; McIntyre, P. C. Atomic Layer-Deposited Tunnel Oxide Stabilizes Silicon Photoanodes for Water Oxidation. *Nat. Mater.* **2011**, 10, 539−544.

(5) Cheng, W.-H.; Richter, M. H.; May, M. M.; Ohlmann, J.; Lackner, D.; Dimroth, F.; Hannappel, T.; Atwater, H. A.; Lewerenz, H.-J. Monolithic Photoelectrochemical Device for Direct Water Splitting with 19% Efficiency. *ACS Energy Lett.* **2018**, 3, 1795−1800.

(6) Ali-Löytty, H.; Hannula, M.; Saari, J.; Palmolahti, L.; Bhuskute, B. D.; Ulkuniemi, R.; Nyyssönen, T.; Lahtonen, K.; Valden, M. Diversity of TiO_2: Controlling the Molecular and Electronic Structure of Atomic-Layer-Deposited Black TiO_2. *ACS Appl. Mater. Interfaces* **2019**, 11, 2758−2762.

(7) McDowell, M. T.; Lichterman, M. F.; Carim, A. I.; Liu, R.; Hu, S.; Brunschwig, B. S.; Lewis, N. S. The Influence of Structure and Processing on the Behavior of TiO_2 Protective Layers for Stabilization of n-Si/TiO_2/Ni Photoanodes for Water Oxidation. *ACS Appl. Mater. Interfaces* **2015**, 7, 15189−15199.

(8) Sivula, K. Defects Give New Life to an Old Material: Electronically Leaky Titania as a Photoanode Protection Layer. *ChemCatChem* **2014**, 6, 2796−2797.

(9) Mei, B.; Pedersen, T.; Malacrida, P.; Bae, D.; Frydendal, R.; Hansen, O.; Vesborg, P. C. K.; Seger, B.; Chorkendorff, I. Crystalline TiO_2: A Generic and Effective Electron-Conducting Protection Layer for Photoanodes and -Cathodes. *J. Phys. Chem. C* **2015**, 119, 15019−15027.

(10) Seger, B.; Castelli, I. E.; Vesborg, P. C. K.; Jacobsen, K. W.; Hansen, O.; Chorkendorff, I. 2-Photon Tandem Device for Water Splitting: Comparing Photocathode First versus Photoanode First Designs. *Energy Environ. Sci.* **2014**, 7, 2397−2413.

(11) Hannula, M.; Ali-Löytty, H.; Lahtonen, K.; Sarlin, E.; Saari, J.; Valden, M. Improved Stability of Atomic Layer Deposited Amorphous TiO_2 Photoelectrode Coatings by Thermally Induced Oxygen Defects. *Chem. Mater.* **2018**, 30, 1199−1208.

(12) Dendooven, J.; Detavernier, C. Basics of Atomic Layer Deposition: Growth Characteristics and Conformality. In *Atomic Layer Deposition in Energy Conversion Applications*; John Wiley & Sons, Ltd.: 2017; pp 1−40.

(13) Zhuiykov, S.; Akbari, M. K.; Hai, Z.; Xue, C.; Xu, H.; Hyde, L. Wafer-Scale Fabrication of Conformal Atomic-Layered TiO_2 by Atomic Layer Deposition Using Tetrakis (Dimethylamino) Titanium and H_2O Precursors. *Mater. Des.* **2017**, 120, 99−108.

(14) Cho, C. J.; Kang, J.-Y.; Lee, W. C.; Baek, S.-H.; Kim, J.-S.; Hwang, C. S.; Kim, S. K. Interface Engineering for Extremely Large Grains in Explosively Crystallized TiO_2 Films Grown by Low-Temperature Atomic Layer Deposition. *Chem. Mater.* **2017**, 29, 2046−2054.

(15) Ros, C.; Andreu, T.; Hernández-Alonso, M. D.; Penelas-Pérez, G.; Arbiol, J.; Morante, J. R. Charge Transfer Characterization of ALD-Grown TiO_2 Protective Layers in Silicon Photocathodes. *ACS Appl. Mater. Interfaces* **2017**, 9, 17932−17941.

(16) Xie, Q.; Jiang, Y.-L.; Detavernier, C.; Deduytsche, D.; Van Meirhaeghe, R. L.; Ru, G.-P.; Li, B.-Z.; Qu, X.-P. Atomic Layer Deposition of TiO_2 from Tetrakis-Dimethyl-Amido Titanium or Ti Isopropoxide Precursors and H2O. *J. Appl. Phys.* **2007**, 102, No. 083521.

(17) Khan, R.; Ali-Löytty, H.; Saari, J.; Valden, M.; Tukiainen, A.; Lahtonen, K.; Tkachenko, N. V. Optimization of Photogenerated Charge Carrier Lifetimes in ALD Grown TiO_2 for Photonic Applications. *Nanomaterials* **2020**, 10, No. 1567.

(18) Reiners, M.; Xu, K.; Aslam, N.; Devi, A.; Waser, R.; Hoffmann-Eifert, S. Growth and Crystallization of TiO_2 Thin Films by Atomic Layer Deposition Using a Novel Amido Guanidinate Titanium Source and Tetrakis-Dimethylamido-Titanium. *Chem. Mater.* **2013**, 25, 2934−2943.

(19) Elam, J. W.; Schuisky, M.; Ferguson, J. D.; George, S. M. Surface Chemistry and Film Growth during TiN Atomic Layer Deposition Using TDMAT and NH3. *Thin Solid Films* **2003**, 436, 145−156.

(20) Driessen, J. P. A. M.; Schoonman, J.; Jensen, K. F. Infrared Spectroscopic Study of Decomposition of $Ti(N(CH_3)_2)_4$. *J. Electrochem. Soc.* **2001**, 148, No. G178.

(21) Mitchell, D. R. G.; Attard, D. J.; Triani, G. Transmission Electron Microscopy Studies of Atomic Layer Deposition TiO_2 Films Grown on Silicon. *Thin Solid Films* **2003**, 441, 85−95.

(22) Finnie, K. S.; Triani, G.; Short, K. T.; Mitchell, D. R. G.; Attard, D. J.; Bartlett, J. R.; Barbé, C. J. Influence of Si(100) Surface Pretreatment on the Morphology of TiO_2 Films Grown by Atomic Layer Deposition. *Thin Solid Films* **2003**, 440, 109−116.

(23) Scheuermann, A. G.; Kemp, K. W.; Tang, K.; Lu, D. Q.; Satterthwaite, P. F.; Ito, T.; Chidsey, C. E. D.; McIntyre, P. C. Conductance and Capacitance of Bilayer Protective Oxides for Silicon Water Splitting Anodes. *Energy Environ. Sci.* **2016**, 9, 504−516.

(24) Pore, V.; Ritala, M.; Leskelä, M.; Saukkonen, T.; Järn, M. Explosive Crystallization in Atomic Layer Deposited Mixed Titanium Oxides. *Cryst. Growth Des.* **2009**, 9, 2974−2978.

(25) Lee, J.; Lee, S. J.; Han, W. B.; Jeon, H.; Park, J.; Kim, H.; Yoon, C. S.; Jeon, H. Effect of Crystal Structure and Grain Size on Photo-Catalytic Activities of Remote-Plasma Atomic Layer Deposited

Titanium Oxide Thin Film. *ECS J. Solid State Sci. Technol.* **2012**, *1*, Q63.

(26) Methaapanon, R.; Bent, S. F. Comparative Study of Titanium Dioxide Atomic Layer Deposition on Silicon Dioxide and Hydrogen-Terminated Silicon. *J. Phys. Chem. C* **2010**, *114*, 10498−10504.

(27) Devloo-Casier, K.; Dendooven, J.; Ludwig, K. F.; Lekens, G.; D'Haen, J.; Detavernier, C. In Situ Synchrotron Based X-Ray Fluorescence and Scattering Measurements during Atomic Layer Deposition: Initial Growth of HfO$_2$ on Si and Ge Substrates. *Appl. Phys. Lett.* **2011**, *98*, No. 231905.

(28) McDonnell, S.; Longo, R. C.; Seitz, O.; Ballard, J. B.; Mordi, G.; Dick, D.; Owen, J. H. G.; Randall, J. N.; Kim, J.; Chabal, Y. J.; Cho, K.; Wallace, R. M. Controlling the Atomic Layer Deposition of Titanium Dioxide on Silicon: Dependence on Surface Termination. *J. Phys. Chem. C* **2013**, *117*, 20250−20259.

(29) Kern, W. The Evolution of Silicon Wafer Cleaning Technology. *J. Electrochem. Soc.* **1990**, *137*, 1887.

(30) Dixit, P.; Chen, X.; Miao, J.; Divakaran, S.; Preisser, R. Study of Surface Treatment Processes for Improvement in the Wettability of Silicon-Based Materials Used in High Aspect Ratio through-via Copper Electroplating. *Appl. Surf. Sci.* **2007**, *253*, 8637−8646.

(31) Hermansson, K.; Lindberg, U.; Hok, B.; Palmskog, G. In *Wetting Properties of Silicon Surfaces*, TRANSDUCERS '91: 1991 International Conference on Solid-State Sensors and Actuators. Digest of Technical Papers, 1991; pp 193−196.

(32) Morita, M.; Ohmi, T.; Hasegawa, E.; Kawakami, M.; Ohwada, M. Growth of Native Oxide on a Silicon Surface. *J. Appl. Phys.* **1990**, *68*, 1272−1281.

(33) Gräf, D.; Grundner, M.; Schulz, R. Reaction of Water with Hydrofluoric Acid Treated Silicon(111) and (100) Surfaces. *J. Vac. Sci. Technol., A* **1989**, *7*, 808−813.

(34) De Gendt, S.; Knotter, D. M.; Kenis, K.; Mertens, P. W.; Heyns, M. M. Impact of Iron Contamination and Roughness Generated in Ammonia Hydrogen Peroxide Mixtures (SC1) on 5 nm Gate Oxides. *J. Electrochem. Soc.* **1998**, *145*, 2589.

(35) Reinhardt, K. *Handbook of Silicon Wafer Cleaning Technology*, 3rd ed.; Elsevier: Waltham, MA, 2018.

(36) Hibino, H.; Uematsu, M.; Watanabe, Y. Void Growth during Thermal Decomposition of Silicon Oxide Layers Studied by Low-Energy Electron Microscopy. *J. Appl. Phys.* **2006**, *100*, No. 113519.

(37) Gallas, B.; Brunet-Bruneau, A.; Fisson, S.; Vuye, G.; Rivory, J. SiO$_2$−TiO$_2$ Interfaces Studied by Ellipsometry and X-Ray Photoemission Spectroscopy. *J. Appl. Phys.* **2002**, *92*, 1922−1928.

(38) Dwivedi, N.; Yeo, R. J.; Tan, H. R.; Stangl, R.; Aberle, A. G.; Bhatia, C. S.; Danner, A.; Liao, B. Evidence for Chemicals Intermingling at Silicon/Titanium Oxide (TiO$_x$) Interface and Existence of Multiple Bonding States in Monolithic TiO$_x$. *Adv. Funct. Mater.* **2018**, *28*, No. 1707018.

(39) Liu, L.; Liu, Q.; Xiao, W.; Pan, C.; Wang, Z. O$_2$ Adsorption and Dissociation on an Anatase (101) Surface with a Subsurface Ti Interstitial. *Phys. Chem. Chem. Phys.* **2016**, *18*, 4569−4576.

(40) Kulkarni, A. D.; Truhlar, D. G.; Goverapet Srinivasan, S.; van Duin, A. C. T.; Norman, P.; Schwartzentruber, T. E. Oxygen Interactions with Silica Surfaces: Coupled Cluster and Density Functional Investigation and the Development of a New ReaxFF Potential. *J. Phys. Chem. C* **2013**, *117*, 258−269.

(41) Schlom, D. G.; Guha, S.; Datta, S. Gate Oxides Beyond SiO$_2$. *MRS Bull.* **2008**, *33*, 1017−1025.

(42) Lafuente, B.; Downs, R. T.; Yang, H.; Stone, N. The Power of Databases: The RRUFF Project. In *Highlights in Mineralogical Crystallography*; Walter de Gruyter GmbH & Co KG, 2015; pp 1−30.

(43) Rodríguez-Reyes, J. C. F.; Teplyakov, A. V. Chemistry of Diffusion Barrier Film Formation: Adsorption and Dissociation of Tetrakis(Dimethylamino)Titanium on Si(100)-2 × 1. *J. Phys. Chem. C* **2007**, *111*, 4800−4808.

(44) Hukari, K.; Dannenberg, R.; Stach, E. A. Nitrogen Effects on Crystallization Kinetics of Amorphous TiO$_x$N$_y$ Thin Films. *J. Mater. Res.* **2002**, *17*, 550−555.

(45) Jelovica Badovinac, I.; Peter, R.; Omerzu, A.; Salamon, K.; Šarić, I.; Samaržija, A.; Perčić, M.; Kavre Piltaver, I.; Ambrožić, G.; Petravić, M. Grain Size Effect on Photocatalytic Activity of TiO$_2$ Thin Films Grown by Atomic Layer Deposition. *Thin Solid Films* **2020**, *709*, No. 138215.

(46) Scheuermann, A. G.; Lawrence, J. P.; Kemp, K. W.; Ito, T.; Walsh, A.; Chidsey, C. E. D.; Hurley, P. K.; McIntyre, P. C. Design Principles for Maximizing Photovoltage in Metal-Oxide-Protected Water-Splitting Photoanodes. *Nat. Mater.* **2016**, *15*, 99−105.

(47) Ros, C.; Andreu, T.; Morante, J. R. Photoelectrochemical Water Splitting: A Road from Stable Metal Oxides to Protected Thin Film Solar Cells. *J. Mater. Chem. A* **2020**, *8*, 10625−10669.

PUBLICATION
IV

Diversity of TiO$_2$: Controlling the Molecular and Electronic Structure of Atomic-Layer-Deposited Black TiO$_2$

Harri Ali-Löytty, Markku Hannula, Jesse Saari, Lauri Palmolahti, Bela D. Bhuskute, Riina Ulkuniemi, Tuomo Nyyssönen, Kimmo Lahtonen, and Mika Valden

Diversity of TiO2: Controlling the Molecular and Electronic Structure of Atomic-Layer-Deposited Black TiO2

Harri Ali-Löytty,*,[†] Markku Hannula,[†] Jesse Saari,[†] Lauri Palmolahti,[†] Bela D. Bhuskute,[†] Riina Ulkuniemi,[†] Tuomo Nyyssönen,[‡] Kimmo Lahtonen,[†] and Mika Valden[†]

[†]Surface Science Group, Laboratory of Photonics, and [‡]Metals Technology Group, Laboratory of Materials Science, Tampere University of Technology, Tampere FI-33101, Finland

S Supporting Information

ABSTRACT: Visually black, electrically leaky, amorphous titania (am-TiO2) thin films were grown by atomic layer deposition (ALD) for photocatalytic applications. Broad spectral absorbance in the visible range and exceptional conductivity are attributed to trapped Ti^{3+} in the film. Oxidation of Ti^{3+} upon heat treatment leads to a drop in conductivity, a color change from black to white, and crystallization of am-TiO2. ALD-grown black TiO2, without any heat treatment, is subject to dissolution in alkaline photoelectrochemical conditions. The best photocatalytic activity for solar water splitting is obtained for completely crystalline white TiO2.

KEYWORDS: atomic layer deposition, titanium dioxide, oxide defects, crystallization, protecting overlayers, photocatalysis, water splitting
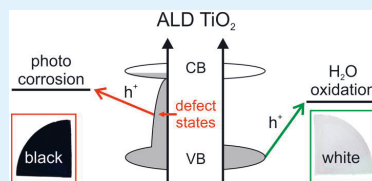
Black titania (TiO2) is a promising material for providing increased photocatalytic efficiency due to its pronounced solar absorption compared to conventional white or transparent, nonconductive TiO2 with large bandgap (3.0−3.2 eV) which is capable of absorbing light only in the UV range.[1] Black TiO2 is often synthesized from white TiO2 via treatment in a reductive H2 atmosphere that introduces disorder via oxide defects or H dopants into the TiO2 structure.[1−4] On the other hand, transparent amorphous TiO2 (am-TiO2) thin film grown by atomic layer deposition (ALD) has shown exceptional charge transfer properties and is therefore utilized as a protection layer for unstable semiconductor materials in photoelectrochemical (PEC) applications.[5] However, the stability of ALD grown am-TiO2 under PEC conditions has remained controversial, since most studies have involved an additional catalyst overlayer on am-TiO2.[6] Recent work by Yu et al.[7] revealed a metastable intermediate within an ALD grown am-TiO2 thin film on Si photoanode that induced corrosion, despite the additional Ni overlayer. We have shown that bare ALD grown am-TiO2 is subject to rapid photo-corrosion under PEC conditions.[8] Even crystalline TiO2 that is believed to be extremely stable, has been shown to suffer from photohole induced corrosion under PEC conditions.[9] There is an urgent need for better understanding of the TiO2 corrosion mechanism to be able to develop TiO2-based materials for photocatalytic energy conversion devices. Here we report a direct synthesis of black TiO2 by ALD and address the question of inherent stability of ALD-grown electrically leaky titania.

ALD of TiO2 was carried out at 200 °C in a commercial ALD reactor using tetrakis(dimethylamido)titanium(IV) (TDMAT) and water as precursors and Ar as carrier/purge/

venting gas.[8] N-type Si(100) wafer was used as a substrate with the exceptions of optical and electrical measurements for which a transparent quartz (SiO2) glass was used as a substrate. The TiO2 film thickness of 30 nm was optimized in terms of PEC efficiency for water oxidation, and thus chosen for detailed analysis.

Figure 1 shows the UV−vis absorption results of ALD TiO2 after deposition and after annealing in oxidizing (air) and reducing (UHV) conditions. The oxidized sample depicts characteristic absorption behavior of rutile TiO2 with absorption edge at 387 nm (3.2 eV) and no absorption in the visible range. In contrast, the absorption edge for the as-deposited TiO2 was observed at 344 nm (3.6 eV), which is strongly blue-shifted from the absorption edge of rutile TiO2 and the absorption edge is followed by a broad absorption that gives rise to the black color of the TiO2 film.

The increased absorption below the band gap energy is characteristic to free charge carrier absorption or absorption due to intraband gap states. The broad absorption of the as-deposited sample following approximately a logarithmic trend from 350 to 800 nm suggests trapped charge carriers within the band gap, which are assigned later to Ti^{3+}.[10] This is supported by the blue-shift in absorption edge compared to rutile TiO2 which we interpret as the Moss−Burstein effect[11] due to the excess population of the conduction band. Interestingly, annealing under reductive conditions induced a clear decrease in the absorption at 528 nm that corresponds to the absorption of trapped holes in TiO2.[12] Recently, we showed that the same
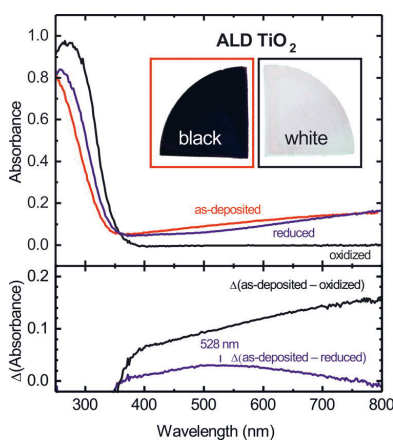
Figure 1. Absorbance of a 30 nm thick black TiO_2 film measured after ALD growth (as-deposited), after annealing in air at 500 °C (oxidized) and after annealing in ultrahigh vacuum (UHV) at 600 °C (reduced). The inset shows pictures of 200 nm thick TiO_2 films after deposition (black) and after annealing in air at 500 °C (white). The difference spectra in the bottom presents the change in absorbance induced by the heat treatments.

reductive heat treatment improved the stability of black am-TiO_2 under PEC conditions, which was attributed to the formation of O^- species via electron transfer from O to Ti.[8] The clear change in optical absorption suggests that the electron transfer is accompanied by the recombination of trapped holes.

Oxidation induced changes on the charge carrier distribution were studied in terms of electrical conductivity and optical absorption as shown in Figure 2. The oxidation treatment was carried out under ambient air by placing the sample into a preheated tube furnace for 45 min. In addition to the aforementioned broad absorbance in the Vis range and enlarged bandgap (Figure 2b, Figure S1) black TiO_2 exhibits exceptionally high conductivity of 150 S/m (Figure 2a). A slight change in the properties was observed upon oxidation at 200 °C followed by more dramatic change for increasing temperatures.

The slight change in the TiO_2 film properties after oxidation at 200 °C is reasonable since the ALD growth was performed at the same temperature. The drastic changes in the electrical

and optical properties correlate perfectly with each other and can be explained by the oxidation of the trapped charge carriers that are responsible for the enhanced conductivity and absorption in the Vis range.

Figure 3 shows scanning electron microscope (SEM) images and grazing-incidence X-ray diffraction (GIXRD) patterns for the oxidized samples. The as-deposited black TiO_2 was found to be amorphous followed by gradual crystallization upon oxidation. In addition to rutile, the crystallized films were found to contain some brookite TiO_2, and quite surprisingly, after oxidation at 350 °C a strong anatase peak appeared. X-ray photoelectron spectroscopy (XPS) reveals that nitrogen (1.8 at. %) is segregated onto the surface at 350 °C that coincides with the formation of the anatase phase (Figure 3c inset). This implies that the small ALD residue concentration of nitrogen plays an important role in the phase stabilization of TiO_2 under these oxidative annealing conditions, although complete crystallization into the most stable rutile TiO_2 via less stable anatase TiO_2 is often observed in the annealing treatments of TiO_2.[13] Furthermore, the nitrogen concentration within the black am-TiO_2 structure is most likely contributing to the broad absorption in a range of 500−900 nm shown in Figure 1 by providing nitrogen induced in-gap states.

SEM images (Figure 3a) reveal that crystallization initiates at 250 °C, which is not yet clear from the GIXRD (Figure 3b). Most importantly, crystallization was found to follow the oxidation of the trapped charge carriers.

The influence of oxidation on the molecular and valence band structure of black TiO_2 was studied with XPS and ultraviolet photoelectron spectroscopy (UPS), respectively. Figure 4 shows photoelectron spectra by comparing the as-deposited and 500 °C oxidized samples. It is evident from the XP survey spectra that the surfaces of ALD grown TiO_2 films are clean with a small concentration of carbon, which is mainly due to impurities from the air exposure, and <0.3 at. % of nitrogen (Figure 4a). The Ti 2p XPS transitions appear as peaks in the binding energy range of 450−480 eV (Figure 4c). The main Ti $2p_{3/2}$ and Ti $2p_{1/2}$ peaks at binding energies of 458.8 and 464.5 eV, respectively, are accompanied by well-known charge transfer shakeup satellite peaks 13 eV above the main peaks.[14] These binding energies and satellite peaks are consistent with the Ti^{4+} state of the TiO_2. In addition, a clear shoulder at the binding energy of 457.5 eV can be seen in the XP spectrum measured from the as-deposited sample. This peak can be assigned to the Ti^{3+}, which can explain the increased absorption in the Vis range[15] and increased conductivity.
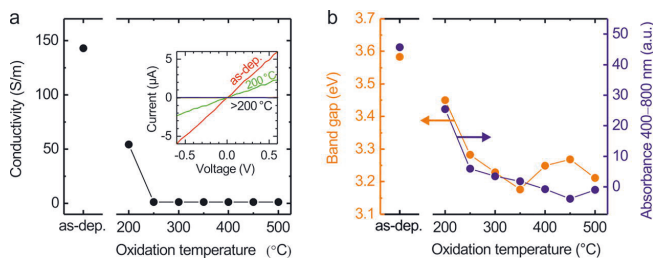

Figure 2. (a) Conductivity and (b) optical band gap and integrated absorbance from 400 to 800 nm for the ALD grown black TiO_2 films after they have been annealed at different oxidation temperatures. Inset in a shows the dramatic change of the $I-V$ characteristics for the as-deposited TiO_2 film and the TiO_2 films after oxidation treatment at 200 °C and higher temperatures.
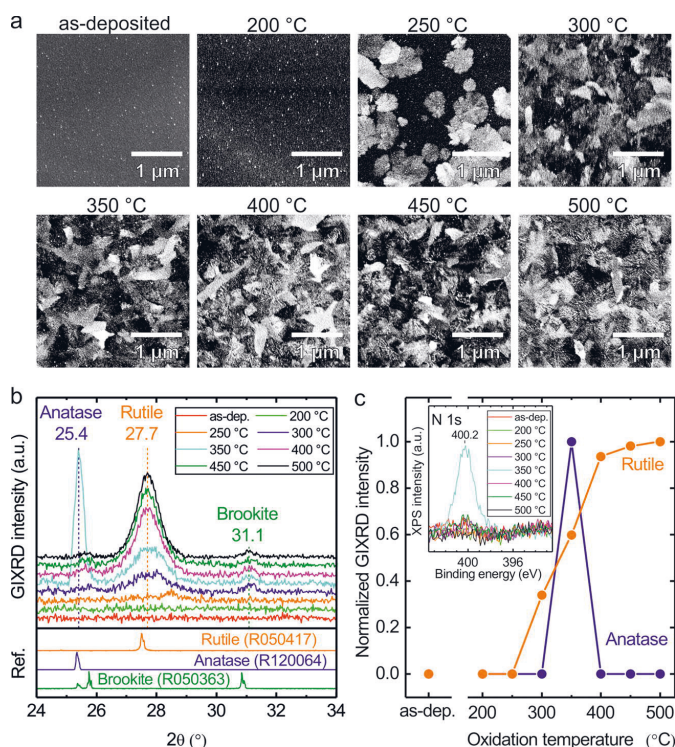
Figure 3. (a) SEM images, (b) GIXRD patterns, and (c) normalized GIXRD intensities of the anatase and rutile peaks for the ALD-grown black TiO$_2$ films at different oxidation temperatures. Inset in c shows XP spectra of N 1s.
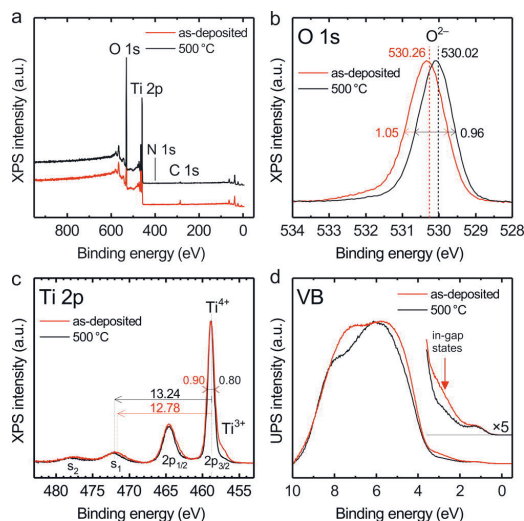

Figure 4. XP (a) survey spectra, (b) O 1s, (c) Ti 2p, and (d) UPS spectra of the valence band (VB) for the ALD-grown black TiO$_2$ film and 500 °C oxidized film.

The O 1s XPS peak is centered at 530 eV as expected for O^{2-} anions of the TiO$_2$ structure[16] and the peak is slightly shifted to a lower binding energy upon oxidation (Figure 4b). This 0.2 eV shift and the decrease in the full width at half-maximum (fwhm) of the O 1s and Ti 2p XPS peaks take place gradually with increasing oxidation temperature (Figure S2) and are a result of the ordering of the amorphous phase to the crystalline rutile phase of TiO$_2$. We note that no such gradual change in neither Ti^{3+} concentration or in O/Ti ratio with temperature was observed (Figure S2a). The majority of Ti^{3+} was oxidized already at 200 °C and the O/Ti ratio was close to 2 throughout the temperature range.

The shakeup satellite peak originates from the excitation of a valence electron to a previously unoccupied state by the outgoing Ti 2p photoelectron according to the sudden approximation of photoemission.[17] Thus, any change in the valence band structure, i.e. Ti−O bonding, may reflect to the charge transfer energy. Indeed, the UPS spectrum of the as-deposited sample (Figure 4d) reveals in-gap states at 2.5 eV that are efficiently removed upon oxidation treatments. Following the removal of in-gap states, the Ti 2p$_{3/2}$ shakeup separation energy was observed to increase with oxidation temperature. The changes in the Ti−O bonding are also evident from the changes in the O 1s binding energy as pointed out above. Therefore, the in-gap states can be assigned to the lattice disorder[18] and the subtle deviations in electronic structure compared to crystalline rutile TiO$_2$ presented above characterize the unique electronic structure of amorphous

ALD TiO$_2$. We note that the careful monitoring of the oxidation-treatment-induced changes in the electronic structure allowed the distinction between the doping,[19] Ti$^{2+/3+}$ defects,[8] oxygen vacancies,[20] and the lattice-disorder-induced in-gap states.

The influence of oxidation on the performance of initially black TiO$_2$ as a photocatalyst for H$_2$O oxidation was studied as shown in Figure 5 and Figure S3. In accordance with our
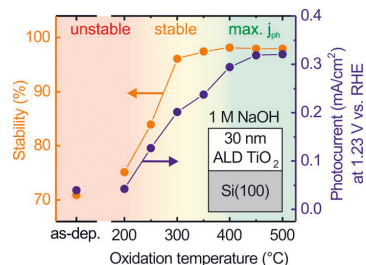

Figure 5. Photoelectrochemical stability and photocurrent (in 1 M NaOH) of the ALD grown, initially black, TiO$_2$ film after oxidation in temperature range from 200 to 500 °C.

previous work,[8] the as-deposited black TiO$_2$ exhibits PEC instability and negligible photocurrent at 1.23 V vs RHE in 1 M NaOH. Only slight change in the PEC stability was observed upon oxidation at 200 °C followed by more dramatic change for increasing temperatures. Therefore, the oxidation of trapped charge carriers at 200 °C does not alone provide an explanation for the PEC stability nor for the increase in photocurrent with oxidation temperature. A reasonable stability is obtained after oxidation at 300 °C and above, whereas photocurrent continues to increase reaching saturation value for samples oxidized at >400 °C. The photocurrent was found to improve with the degree of TiO$_2$ crystallization and reach saturation for crystallized rutile TiO$_2$.

The improvement in PEC stability was found to correlate with crystallization, which supports earlier results that the stability of crystalline TiO$_2$ outperforms the amorphous phase.[21] Albeit the complete crystallization of TiO$_2$ thin film required oxidation at >400 °C, the SEM images (Figure 3a) show that the surface is mostly crystallized already at 300 °C. Thus, the crystallized surface alone is sufficient requirement to endow improved PEC stability to the TiO$_2$ thin film. Although am-TiO$_2$ has been shown to both experimentally and theoretically exhibit several orders of magnitude higher dissolution rates in 1 M NaOH than crystalline polymorphs,[22] we emphasize that the stability of black am-TiO$_2$ can also be improved by controlling the defect distribution.[8]

The unique properties of disordered ALD-TiO$_2$ include controlling the Ti^{3+} self-doping via growth temperature and thermal modification of defect and crystal structure. Recently we showed that annealing in UHV results in increase in Ti^{3+} states in the film and promotes PEC stability via the formation of O$^-$.[8] The facile modification treatments manifest the diversity of ALD-TiO$_2$ in applications ranging from conductive interlayers, to electrically leaky protection layers and photocatalyst materials.

In the present study, we have shown that black TiO$_2$ with enhanced absorbance in the wavelength range of 400−800 nm can be deposited as a conformal amorphous thin film using

ALD. We have demonstrated that the physicochemical properties of TiO$_2$ can be controlled by postannealing treatments either in reductive or oxidative conditions. The black as-deposited TiO$_2$ shows exceptionally high electrical conductivity of 150 S/m, but suffers from poor PEC stability and dissolves in alkaline conditions. Annealing treatment in extremely reductive conditions (UHV) at 500 °C transforms the black as-deposited TiO$_2$ into a photoelectrochemically stable phase of black TiO$_2$ retaining its amorphous structure.[8] On the other hand, oxidation in air at 500 °C crystallizes TiO$_2$ into rutile phase with the maximum efficiency as photocatalyst for photoelectrochemical H$_2$O oxidation. The unprecedented diversity of ALD-TiO$_2$ can be rationalized by the propensity of the molecular structure toward local changes in the bonding configuration that affects the charge carrier densities via modified electronic structure. This unfolds the tremendous optoelectronic properties of TiO$_2$.

■ ASSOCIATED CONTENT

Ⓢ Supporting Information

The Supporting Information is available free of charge on the ACS Publications website at DOI: 10.1021/acsami.8b20608.

UV−vis absorption, XPS, PEC data as a function of oxidation temperature, and experimental details (PDF)

■ AUTHOR INFORMATION

Corresponding Author

*Email: Harri.Ali-Loytty@tut.fi.

ORCID Ⓘ

Harri Ali-Löytty: 0000-0001-8746-7268

Markku Hannula: 0000-0003-1110-7439

Kimmo Lahtonen: 0000-0002-8138-7918

Present Address

Surface Science Group, Laboratory of Photonics, Tampere University of Technology, P.O. Box 692, FI-33101 Tampere, Finland

Notes

The authors declare no competing financial interest.

■ ACKNOWLEDGMENTS

■ REFERENCES

(1) Liu, X.; Zhu, G.; Wang, X.; Yuan, X.; Lin, T.; Huang, F. Progress in Black Titania: A New Material for Advanced Photocatalysis. *Adv. Energy Mater.* **2016**, *6* (17), 1385−1388.

(2) Selcuk, S.; Zhao, X.; Selloni, A. Structural Evolution of Titanium Dioxide during Reduction in High-Pressure Hydrogen. *Nat. Mater.* **2018**, *17* (10), 923−928.

(3) Wang, B.; Shen, S.; Mao, S. S. Black TiO$_2$ for Solar Hydrogen Conversion. *J. Materiomics* **2017**, *3* (2), 96−111.

(4) Yan, X.; Li, Y.; Xia, T. Black Titanium Dioxide Nanomaterials in Photocatalysis. *Int. J. Photoenergy* **2017**, *2017*, No. 8529851.

(5) Hu, S.; Shaner, M. R.; Beardslee, J. A.; Lichterman, M.; Brunschwig, B. S.; Lewis, N. S. Amorphous TiO$_2$ Coatings Stabilize Si, GaAs, and GaP Photoanodes for Efficient Water Oxidation. *Science* **2014**, *344* (6187), 1005−1009.

(6) Sivula, K. Defects Give New Life to an Old Material: Electronically Leaky Titania as a Photoanode Protection Layer. *ChemCatChem* **2014**, *6* (10), 2796−2797.

(7) Yu, Y.; Sun, C.; Yin, X.; Li, J.; Cao, S.; Zhang, C.; Voyles, P. M.; Wang, X. Metastable Intermediates in Amorphous Titanium Oxide: A Hidden Role Leading to Ultra-Stable Photoanode Protection. *Nano Lett.* **2018**, *18* (8), 5335−5342.

(8) Hannula, M.; Ali-Löytty, H.; Lahtonen, K.; Sarlin, E.; Saari, J.; Valden, M. Improved Stability of ALD Grown Amorphous TiO$_2$ Photoelectrode Coatings by Thermally Induced Oxygen Defects. *Chem. Mater.* **2018**, *30* (4), 1199−1208.

(9) Yang, Y.; Ling, Y.; Wang, G.; Liu, T.; Wang, F.; Zhai, T.; Tong, Y.; Li, Y. Photohole Induced Corrosion of Titanium Dioxide: Mechanism and Solutions. *Nano Lett.* **2015**, *15* (10), 7051−7057.

(10) Di Valentin, C.; Pacchioni, G.; Selloni, A. Reduced and N-Type Doped TiO$_2$: Nature of Ti^{3+} Species. *J. Phys. Chem. C* **2009**, *113* (48), 20543−20552.

(11) Burstein, E. Anomalous Optical Absorption Limit in InSb. *Phys. Rev.* **1954**, *93* (3), 632−633.

(12) Yoshihara, T.; Katoh, R.; Furube, A.; Tamaki, Y.; Murai, M.; Hara, K.; Murata, S.; Arakawa, H.; Tachiya, M. Identification of Reactive Species in Photoexcited Nanocrystalline TiO$_2$ Films by Wide-Wavelength-Range (400−2500 Nm) Transient Absorption Spectroscopy. *J. Phys. Chem. B* **2004**, *108* (12), 3817−3823.

(13) Hanaor, D. A. H.; Sorrell, C. C. Review of the Anatase to Rutile Phase Transformation. *J. Mater. Sci.* **2011**, *46* (4), 855−874.

(14) Woicik, J. C.; Weiland, C.; Rumaiz, A. K. Loss for Photoemission versus Gain for Auger: Direct Experimental Evidence of Crystal-Field Splitting and Charge Transfer in Photoelectron Spectroscopy. *Phys. Rev. B: Condens. Matter Mater. Phys.* **2015**, *91* (20), 201412.

(15) Zuo, F.; Wang, L.; Wu, T.; Zhang, Z.; Borchardt, D.; Feng, P. Self-Doped Ti^{3+} Enhanced Photocatalyst for Hydrogen Production under Visible Light. *J. Am. Chem. Soc.* **2010**, *132* (34), 11856−11857.

(16) Naumkin, A. V.; Kraut-Vass, A.; J, C. P. *NIST XPS Database 20*, Version 4.0; National Institute of Standards and Technology, 2008.

(17) Hedin, L.; Lee, J. D. Sudden Approximation in Photoemission and Beyond. *J. Electron Spectrosc. Relat. Phenom.* **2002**, *124* (2), 289−315.

(18) Chen, X.; Liu, L.; Yu, P. Y.; Mao, S. S. Increasing Solar Absorption for Photocatalysis with Black Hydrogenated Titanium Dioxide Nanocrystals. *Science* **2011**, *331* (6018), 746−750.

(19) Asahi, R.; Morikawa, T.; Ohwaki, T.; Aoki, K.; Taga, Y. Visible-Light Photocatalysis in Nitrogen-Doped Titanium Oxides. *Science* **2001**, *293* (5528), 269−271.

(20) Guo, Z.; Ambrosio, F.; Pasquarello, A. Hole Diffusion across Leaky Amorphous TiO$_2$ Coating Layers for Catalytic Water Splitting at Photoanodes. *J. Mater. Chem. A* **2018**, *6* (25), 11804−11810.

(21) Ros, C.; Andreu, T.; Hernández-Alonso, M. D.; Penelas-Pérez, G.; Arbiol, J.; Morante, J. R. Charge Transfer Characterization of ALD-Grown TiO2 Protective Layers in Silicon Photocathodes. *ACS Appl. Mater. Interfaces* **2017**, *9* (21), 17932−17941.

(22) Shkol'nikov, E. V. Thermodynamics of the Dissolution of Amorphous and Polymorphic TiO$_2$ Modifications in Acid and Alkaline Media. *Russ. J. Phys. Chem. A* **2016**, *90* (3), 567−571.